

*Modelling the Biophysics of Pancreatic Ductal Adenocarcinoma On-chip
for Effective Therapeutic Assessment*

Delanyo Kpeglo

Submitted in accordance with the requirements for the degree of

Doctor in Philosophy

The University of Leeds

School of Physics and Astronomy

March 2022

Intellectual Property and Publication Statements

The candidate confirms that the work submitted is their own, except where work which has formed part of jointly authored publications has been included. The contribution of the candidate and the other authors to this work has been explicitly indicated below. The candidate confirms that appropriate credit has been given within the thesis where reference has been made to the work of others

The work in chapter 4 of the thesis appears in the following publication:

Kpeglo, D., Hughes, M. D. G., Dougan, L., Haddrick, M, Knowles, M. A., Evans, S.D. E., and Peyman, S. A. (2022). Modeling the Mechanical Stiffness of Pancreatic Ductal Adenocarcinoma. *Matrix Biology Plus*. 100109.^[1]

- D.K designed, performed the experiments, collected all experimental data, and analysed the data.
- D.K. and M.D.G.H designed the experiments using oscillatory shear rheology and collected the data.
- D.K. and S.A.P wrote the manuscript with input from all authors

This copy has been supplied on the understanding that it is copyright material and that no quotation from the thesis may be published without proper acknowledgement.

The right of Delanyo Kpeglo to be identified as Author of this work has been asserted by her in accordance with the Copyright, Designs and Patents Act 1988.

Acknowledgement

I would like to thank my supervisors, Dr Sally A. Peyman, Prof. Stephen D. Evans, Dr Malcolm Haddrick, and Prof. Margaret A. Knowles, for offering me the opportunity of this Ph.D. I am very grateful for their time, guidance, and support throughout my degree. Many thanks to the Dr Haddrick for the support I received at Medicine Discovery Catapult.

I would like to acknowledge and thank Dr Daniel Baker (Soft Matter research group) and Dr Matthew D. G. Hughes. Without their guidance in the use of shear deformation, a large part of this thesis would not have been completed.

I would like to thank the Peyman research group, the whole of the Molecular and Nanoscale Physics group, and those in the Microbubble research group who offered me advice and support.

I would also like to thank my friends for their encouragement throughout.

Finally, I want to express my gratitude to my mum, sister, and brother, who have offered me nothing but their endless love, and support throughout my degree. Thank you.

Abstract

Pancreatic ductal adenocarcinoma (PDAC) is characterised by a rich fibrotic stroma, which stems from the overproduction of extracellular matrix (ECM), resulting from the cancer-stroma cell interactions. The growing fibrotic stroma, which is additive to the PDAC tumour growth, results in changes to the tissue mechanics, underlining the disease's poor clinical outcome. It is becoming of interest to model the PDAC tumour microenvironment *in vitro* for drug discovery, but there is still a lack of an ideal model that takes into account the cancer-stroma cell interactions and the disease biophysical hallmarks. With the advantage of laminar flow, microfluidic technology offers fluid control capabilities within a defined environment to mimic *in vivo* physiological conditions. However, many microfluidic PDAC cultures perform drug studies when the cultures do not emulate the *in vivo* tissue stiffness and flow conditions. In this thesis, a microfluidic PDAC culture model that recapitulates the disease biophysical characteristics to study novel ways of introducing drugs to the cancer cells is presented.

First, the PDAC tissue biophysical characteristics were investigated with off-chip PDAC cultures to determine the optimum culture conditions required to mimic the tissue mechanics on-chip. Off-chip, PDAC cancer-pancreatic stellate cell (PSC) co-cultures with transforming growth factor- β 1 (TGF- β 1) supplement exhibited *in vivo*-like mechanical stiffness with increasing collagen content. PSCs are central to the PDAC fibrotic stroma from its symbiotic relationship with the cancer cells, and their activity is increased with cytokines such as TGF- β . The presence of hypoxia was then investigated. As *in vivo*, with a rigid collagenous matrix, there is reduced interstitial flow, limiting nutrients and oxygen to cells. Finally, resistance to gemcitabine was explored. On-chip, with a 21-day culture time optimum to mimic the PDAC tissue stroma, stiffness, reduced interstitial flow, hypoxic environment, and chemoresistance, the use of microbubbles and ultrasound to increase gemcitabine efficacy was investigated.

TABLE OF CONTENTS

| | |
|--|-----------|
| Intellectual Property and Publication Statements | 2 |
| Acknowledgement..... | 3 |
| Abstract..... | 4 |
| List of Figures..... | 7 |
| List of Tables | 9 |
| Abbreviations..... | 10 |
| 1. Introduction..... | 11 |
| 1.1. Pancreatic ductal adenocarcinoma..... | 11 |
| 1.2. The tumour microenvironment of pancreatic ductal adenocarcinoma | 13 |
| 1.3. Mechanical assessment of pancreatic ductal adenocarcinoma..... | 18 |
| 1.4. Modelling pancreatic ductal adenocarcinoma | 20 |
| 1.5. Therapeutic strategies for pancreatic ductal adenocarcinoma | 29 |
| 1.6. Project overview and thesis layout..... | 36 |
| 2. Theoretical Background | 39 |
| 2.1. Assessing mechanical stiffness with oscillatory shear rheology | 39 |
| 2.2. Assessing interstitial flow with hydraulic conductivity..... | 41 |
| 2.3. Microfluidic cell culture..... | 43 |
| 2.4. Microbubble stability and production | 46 |
| 3. Experimental Section | 48 |
| 3.1. Cell lines and 2D culture..... | 48 |
| 3.2. Optical microscopy..... | 49 |
| 3.3. Cell labelling with Qtracker™ 585 cell labelling kit | 51 |
| 3.4. Off-chip PDAC cultures..... | 52 |
| 3.5. Mechanical stiffness assessment of the off-chip PDAC cultures | 55 |
| 3.6. Immunostaining off-chip PDAC cultures for collagen and HIF-1 alpha..... | 57 |
| 3.7. Microfluidic device design and fabrication..... | 58 |
| 3.8. The microfluidic PDAC culture | 63 |
| 3.9. Immunostaining on-chip PDAC cultures for collagen and HIF-1 alpha | 64 |
| 3.10. Interstitial flow of the microfluidic PDAC culture | 65 |
| 3.11. Therapeutic assessment of the PDAC cultures | 67 |
| 3.12. Viability assessment of the PDAC cultures..... | 78 |
| 3.13. Statistical analysis | 80 |

| | |
|---|------------|
| 4. The Off-chip Pancreatic Ductal Adenocarcinoma Culture..... | 82 |
| 4.1. Growth of the PDAC cultures..... | 83 |
| 4.2. The mechanical stiffness of the PDAC cultures..... | 88 |
| 4.3. The effect of mechanical stiffness on therapeutic effect..... | 101 |
| 4.4. Conclusion..... | 104 |
| 5. The On-chip Pancreatic Ductal Adenocarcinoma Culture..... | 106 |
| 5.1. Fluid flow assessments..... | 106 |
| 5.2. PDAC culture in the 3-channel and 5-channel microfluidic devices..... | 111 |
| 5.3. The matrix environment of the PDAC culture..... | 116 |
| 5.4. The interstitial flow of the PDAC culture..... | 120 |
| 5.5. Conclusion..... | 123 |
| 6. The effect of Gemcitabine with Microbubbles and Ultrasound on the On-chip Pancreatic Ductal Adenocarcinoma Culture..... | 124 |
| 6.1. The effect of gemcitabine on the PDAC culture..... | 124 |
| 6.2. Effect of microbubbles and ultrasound on the PDAC culture..... | 126 |
| 6.3. Effect of gemcitabine, microbubbles, and ultrasound on the PDAC culture..... | 131 |
| 6.4. Effect of therapeutic microbubbles on the PDAC culture..... | 135 |
| 6.5. Conclusion..... | 140 |
| 7. Conclusion and Future Studies..... | 142 |
| 7.1. Future studies..... | 144 |
| 7.2. Summary..... | 150 |
| References..... | 151 |
| Appendix..... | 183 |
| Hydrostatic pressure driven flow by gravity code..... | 183 |
| Supplementary videos..... | 186 |
| Papers 188 | |

List of Figures

| | |
|---|----|
| Figure 1.1. The development of pancreatic ductal adenocarcinoma | 11 |
| Figure 1.2. The tumour microenvironment | 14 |
| Figure 1.3. The symbiotic relationship between PDAC cancer cells and PSC cells | 15 |
| Figure 1.4. The solid and fluid stress in the PDAC tumour | 16 |
| Figure 1.5. The different techniques for mechanical characterisation | 18 |
| Figure 1.6. Main characteristics of 3D cell cultures..... | 25 |
| Figure 1.7. The mechanism of action of gemcitabine | 31 |
| Figure 1.8. A lipid coated microbubble and its mechanism in drug delivery..... | 34 |
| Figure 1.9. The off-chip and on-chip PDAC culture assessments..... | 37 |
| Figure 2.1. The sinusoidal strain response to shear deformation..... | 40 |
| Figure 3.1. Function of the bright-field and fluorescence microscopy | 49 |
| Figure 3.2. The off-chip PDAC culture set up and culture | 53 |
| Figure 3.3. Exemplar image of the use of the SpheroidSizer program | 54 |
| Figure 3.4. Oscillatory shear deformation of the off-chip PDAC cultures..... | 56 |
| Figure 3.5. CAD of the microfluidic devices for on-chip culture with media reservoirs | 59 |
| Figure 3.6. The rapid prototyping process for the fabrication of the microfluidic devices | 62 |
| Figure 3.7. The interstitial flow assessment of the on-chip PDAC culture | 66 |
| Figure 3.8. Timeline of the therapeutic assessment of the of PDAC cultures | 67 |
| Figure 3.9. The 4 x multiplexed microfluidic device design for microbubble production | 70 |
| Figure 3.10. The perfusion of microbubbles and ultrasound assessments on-chip | 72 |
| Figure 3.11. The therapeutic microbubbles with gemcitabine-loaded liposomes | 75 |
| Figure 4.1. 2D culture of the PANC-1 and PSC cells..... | 82 |
| Figure 4.2. 3D spheroid culture of the off-chip PDAC cultures in ULA plates..... | 83 |
| Figure 4.3. Characterisation of the PANC-1 spheroid growth in the presence of PSC cells | 84 |
| Figure 4.4. Live/dead viability of the PDAC spheroids | 87 |
| Figure 4.5. Metabolic activity of the PDAC spheroids | 87 |
| Figure 4.6. Effect of TGF- β 1 on PANC-1 growth in the presence of PSC cells | 89 |
| Figure 4.7. The off-chip PDAC cultures with TGF- β 1 | 90 |
| Figure 4.8. Examples of the G' and G'' moduli measurement of the off-chip PDAC cultures . | 91 |
| Figure 4.9. Mechanical stiffness characterisation of the off-chip PDAC cultures..... | 92 |
| Figure 4.10. Examples of the frequency sweep measurements | 95 |
| Figure 4.11. Range of normal forces measured by the parallel plate rotary system..... | 96 |

| | |
|--|-----|
| Figure 4.12. Ratio of cells in the off-chip PDAC cultures | 96 |
| Figure 4.13. The mechanical characterisation of BME gel | 97 |
| Figure 4.14. Immunofluorescence stain of collagen type I in PANC-1 cultures with TGF- β 1 .. | 99 |
| Figure 4.15. Immunofluorescence stain of collagen type I in PDAC cultures with TGF- β 1 ... | 100 |
| Figure 4.16. The effect of gemcitabine on the off-chip PDAC cultures with TGF- β 1..... | 102 |
| Figure 5.1. The 3-channel and 5-channel microfluidic device..... | 106 |
| Figure 5.2. Fluid flow assessment in the media channels, between the media reservoirs ... | 110 |
| Figure 5.3. Time for culture media in the inlet and outlet media reservoirs to be equal in volume or height | 112 |
| Figure 5.4. The on-chip PDAC culture with the 3-channel and 5-channel device..... | 114 |
| Figure 5.5. Viability assessments of the on-chip PDAC culture in the 5-channel device | 115 |
| Figure 5.6. Immunofluorescence stain of collagen type I in on-chip PDAC cultures | 117 |
| Figure 5.7. Immunofluorescence stain of HIF-1 alpha in on-chip PDAC cultures | 119 |
| Figure 5.8. The interstitial flow assessment of the on-chip PDAC culture | 121 |
| Figure 5.9. The hydraulic conductivity of the on-chip PDAC culture | 122 |
| Figure 6.1. Timeline of the on-chip PDAC culture treatment with gemcitabine, microbubbles, and ultrasound | 124 |
| Figure 6.2. The effect of gemcitabine on the on-chip PDAC cultures | 125 |
| Figure 6.3. On-chip microbubble production and the size distribution..... | 127 |
| Figure 6.4. Flow of microbubbles in the on-chip PDAC culture | 129 |
| Figure 6.5. On-chip culture viability with microbubbles and ultrasound treatment | 130 |
| Figure 6.6. The effect of ultrasound on BME gel on-chip..... | 132 |
| Figure 6.7. The effect of ultrasound on the 21-day on-chip PDAC culture | 133 |
| Figure 6.8. On-chip culture viability with gemcitabine, microbubbles, and ultrasound treatment..... | 134 |
| Figure 6.9. Viability assessment of 2D PDAC cultures | 136 |
| Figure 6.10. Concentration and size of the gemcitabine-loaded liposomes..... | 137 |
| Figure 6.11. Concentration, size, and effect of the therapeutic microbubbles..... | 139 |

List of Tables

| | |
|--|-----|
| Table 1.1. An overview of the different culture models..... | 21 |
| Table 4.1. Doubling time of the PANC-1 spheroid cultures in the presence of PSC cells | 85 |
| Table 5.1. Fluid flow assessment of microfluidic systems in the literature for cell culture .. | 108 |
| Table 5.2. Dimensions and fluid flow assessments of microfluidic channels for the PDAC culture | 109 |
| Table 5.3. The interstitial flow assessment of the on-chip PDAC culture | 122 |
| Table 7.1. Examples of the types of integrins..... | 148 |

Abbreviations

| | |
|-----------------|---|
| 2D | Two Dimensional |
| 3D | Three Dimensional |
| AFM | Atomic Force Microscopy |
| ATP | Adenosine Triphosphate |
| BME | Basement Membrane Extract |
| CAFs | Cancer Associated Fibroblasts |
| DMEM | Dubelcco's Modified Eagle Media |
| ECM | Extracellular Matrix |
| FBS | Foetal Bovine Serum |
| GEM | Gemcitabine |
| GEMMs | Genetically Engineered Mouse Models |
| HIF-1 alpha | Hypoxia-inducible Factor-1 alpha |
| hENT | Human Equilibrative Nucleoside Transporter |
| IFP | Interstitial Flow Pressure |
| IF _v | Interstitial Flow Velocity |
| LOX | Lysyl Oxidase |
| MBs | Microbubbles |
| MDC | Medicines Discovery Catapult |
| MNP | Molecular and Nanoscale Physics |
| MRP | Multidrug Resistance Proteins |
| PANC-1 | Pancreatic Epithelial Ductal Adenocarcinoma |
| PDAC | Pancreatic Ductal Adenocarcinoma |
| PSCs | Pancreatic Stellate Cells |
| SteCM | Stellate Cell Medium |
| TGF-β1 | Transforming Growth Factor beta 1 |
| ULA | Ultra-Low Attachment |

1. Introduction

1.1. Pancreatic ductal adenocarcinoma

The pancreas is one of the largest glandular organs with complex anatomy. Its complexity and proximity to other anatomical structures make diagnosing and treating pancreatic cancers challenging. Especially pancreatic ductal adenocarcinoma (PDAC), which is the most prevalent and aggressive pancreatic cancer.^[2-6]

The aetiology of PDAC is poorly defined, but epidemiological and genetics studies have provided insight into the disease pathogenesis.^[2, 4, 5, 7, 8] Illustrated in Figure 1.1, PDAC arises from ductal epithelial cells of the exocrine pancreas with the successive accumulation of genetic mutations.^[2, 7, 9, 10] The signature mutations for PDAC development are the proto-oncogene, *KRAS*, and tumour suppressors *CDKN2A*, *TP53*, and *SMAD4*.^[2, 7, 9-11]

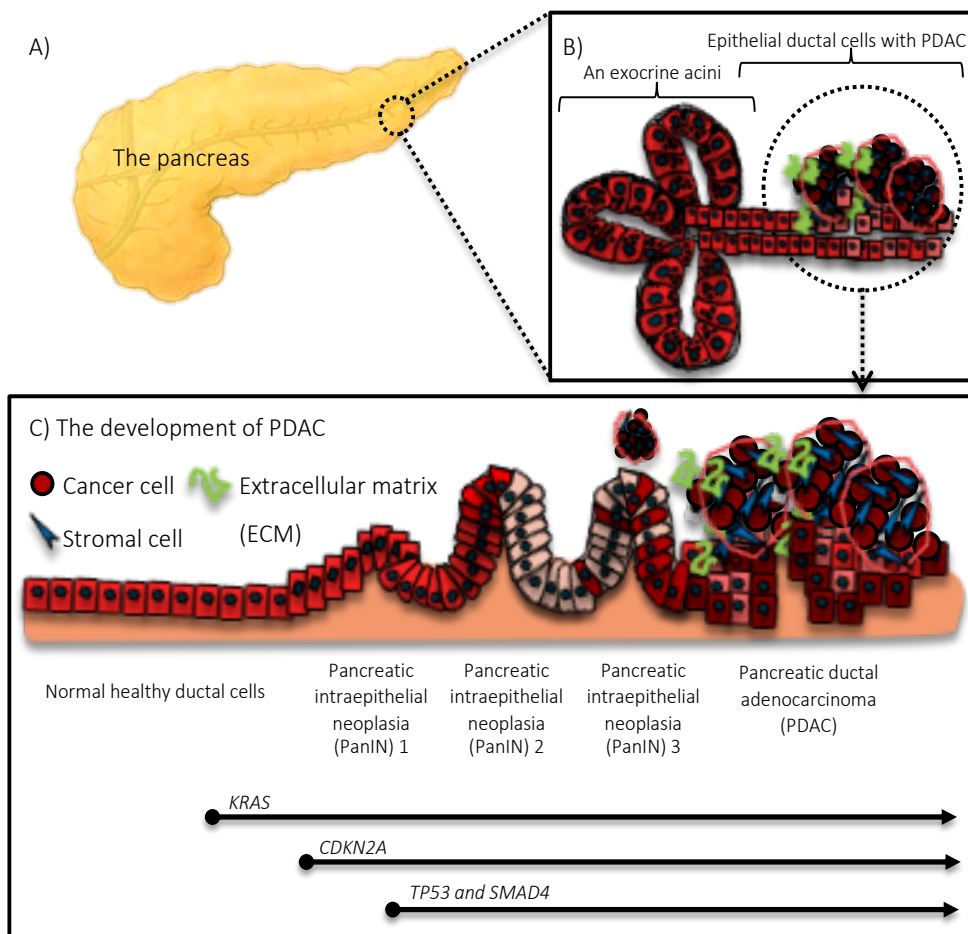


Figure 1.1. The development of pancreatic ductal adenocarcinoma

The pancreas is comprised of the exocrine and endocrine glands. The exocrine pancreas, B) shows a single acinus with acinar and ductal cells. The exocrine acinar produces digestive enzymes secreted via the pancreatic ducts into the duodenum, constituting approximately 99% of the pancreatic tissue. C) Illustrates the genetic mutations that occur for the development of PDAC from pre-cancerous lesions, pancreatic intraepithelial neoplasias (PanINs). Adapted from [9].

The *KRAS* mutation, specifically *KRAS2*, which is observed to have a prevalence of > 90 % in PDAC, is a required malignant lesion to transform pancreatic acinar and epithelial ductal cells into small microscopic pre-cancerous lesions, pancreatic intra-epithelial neoplasia (PanIN), towards PDAC development.^[12-14] *KRAS* promotes cell growth and differentiation as part of the mitogen-activated protein kinase (MAPK) /extracellular-signal-regulated kinase (ERK) pathway.^[2, 7, 9, 10] The loss of *CDKN2A* function, which occurs in 40 % of PanIN towards the development of PDAC, results in cells becoming cancerous as the *CDKN2A* gene provides instruction for making tumour suppressor proteins p16 (INK4A) and p14 (ARF) to regulate cell cycle progression and to keep cells from growing and dividing in an uncontrolled manner.^[2, 7, 9, 10] Moreover, the loss of the *CDKN2A* function results in the inactivation of the TP53 protein, as the p14 (ARF) protein helps to maintain TP53 protein stability. *TP53* is an important tumour suppressor gene for regulating DNA repair and cell division. Its inactivation is found in > 50 % of PDAC.^[2, 7, 9, 10] Loss of function of *SMAD4* occurs late in the development of PDAC. As part of the transforming growth factor- β (TGF- β) signalling family cascade, it regulates cell growth and proliferation.^[2, 9, 10, 15-17]

The genetic alterations underlie the cellular processes and histological changes for the development of PDAC.^[2, 4, 7, 9, 10] Although there have been advancements in the understanding and identifying of hallmarks of the disease to improve treatment outcomes, PDAC remains highly resistant to therapeutics with a 5-year survival rate of about < 9 %.^[3, 4, 6, 9] It accounts for 90 – 95 % of all pancreatic cancer cases.^[9, 17]

PDAC is notable for its desmoplastic stroma, which provides a favourable microenvironment with a niche of cytokines and growth factors for tumour growth. The PDAC stroma exhibits mechanical forces, which define the disease's tissue architecture and morphology, growth, and therapeutic resistance.^[17-22]

In the following sections of this chapter, 1) the PDAC tumour microenvironment with a growing fibrotic stroma and tumour mass is discussed, 2) the biophysical forces that ensue from the growing stroma and tissue mass, and 3) techniques of mechanical assessment and use on PDAC cultures in the literature, are presented. 4) 2D cultures, animal models, and 3D cultures are reviewed with an overview of the *in vivo* and *in vitro* PDAC models in the literature and a focus on their cellular and matrix complexities. 5) The different microfluidic cultures of PDAC in the literature are also presented, and 6) current therapeutic measures against PDAC are discussed. Finally, the scope and aims of the project and thesis layout are presented.

1.2. The tumour microenvironment of pancreatic ductal adenocarcinoma

PDAC is commonly diagnosed in its advanced stages with poor prognosis, as symptoms of the disease are often non-specific. At this stage, a key feature and contributing factor to the disease's therapeutic resistance and poor clinical outcome is the pervasive growth of a dense fibrotic stroma in its tumour microenvironment, which impedes the delivery of therapeutics to the cancer cells.^[17, 23-27] The dense fibrotic stroma is from the excess accumulation of ECM macromolecules (namely fibrillar collagens, proteoglycans, and glycosaminoglycans) produced from interactions between the PDAC cancer cells and stromal cells, including cancer-associated fibroblast (CAFs) and pancreatic stellate cells (PSCs).^[15, 22, 24, 28, 29]

Stromal cells of the PDAC tumour microenvironment include endothelial and tumour infiltrating immune cells. The endothelial cells are needed for vasculature formation in the PDAC tumour tissue. However, the vasculatures formed are dysfunctional and leaky. Immune cells, such as macrophages, in the tumour microenvironment transition into a mesenchymal subtype contributing to the CAF population for the fibrotic stroma. Of the fibroblast cells, PSC cells are essential for the PDAC desmoplastic stroma. Below, the PDAC tumour microenvironment with PSCs central to the PDAC fibrotic stroma is discussed.

1.2.1. Pancreatic stellate cells

Deriving their name from their star-like morphology, PSCs are the primary fibroblast cells of the pancreas. PSCs constitute approximately 4 – 7 % of the pancreatic cell mass. Nonetheless, PSCs have the capacity to mediate the homeostasis of the ECM in healthy and diseased pancreatic tissue.^[15, 24, 26, 28, 30]

PSCs are identified by vitamin A containing lipid droplets in their cytoplasm in the healthy pancreatic tissue. In the presence of PDAC cells, they lose their lipid droplets and activate into myofibroblast-like CAFs expressing alpha-smooth muscle actin (α -SMA) proteins. This key change disrupts the homeostasis of the healthy pancreatic ECM for a tumour facilitatory fibrotic stroma.^[31-33] The activated PSCs proliferate and produce large amounts of ECM by regulating the balance between the synthesis, activity, and degradation of enzymes and proteases, including metalloproteinase (MMPs), tissue inhibitor of metalloproteinase (TIMPs), and lysyl oxidase (LOX), and cytokines such as TGF- β , which further stimulates the activity of PSCs.^[18, 26, 28, 29, 34-36]

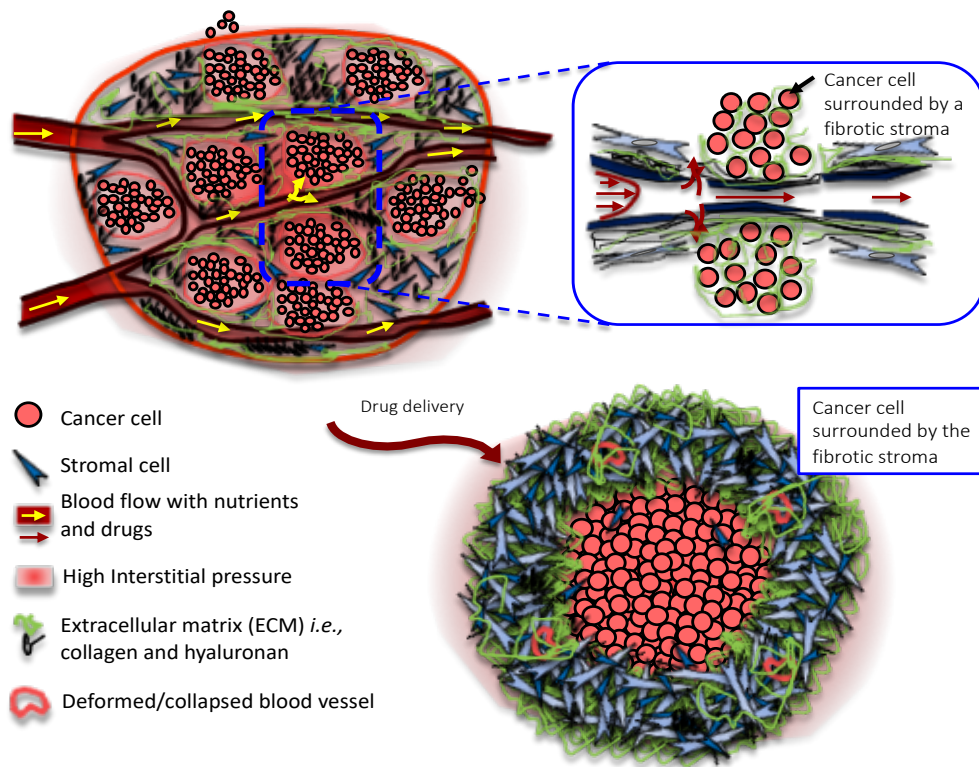


Figure 1.2. The tumour microenvironment

The increased fibrotic stroma and tumour mass, with the accumulation of cancer cells, stromal cells (i.e. fibroblasts), and ECM components, increases tumour tissue rigidity, collapsing vasculatures, which are vital for the delivery of nutrients and drugs to the cancer cells. Adapted from [19].

This makes the ECM a dynamic entity that is continuously remodelled for PDAC growth.^[15, 18, 19, 22, 26, 28, 37] As a result, there are changes to the mechanics of the PDAC tissue, with a growing fibrotic stroma and tumour mass, which makes it difficult to validate therapeutic targets against the PDAC cells.^[21, 23-25, 38-40] Changes in the tumour tissue mechanics are a hallmark of the disease state preceding and driving tumourigenesis, as seen with the PDAC development from PanIN.^[19-22, 41, 42] Figure 1.2 illustrates a schematic of the tumour microenvironment with a rich fibrotic stroma, influencing how nutrients and drugs are delivered to the PDAC cancer cells. Figure 1.3 illustrates the interactions between the PDAC cells and the PSCs. The PDAC cells recruit PSC cells, increasing their growth and proliferation, and in return, the PSCs promote PDAC cell proliferation and survival with a fibrotic stroma.^[15, 19] As the fibrotic stroma grows and the tumour mass increase from the accumulation of cells, there is an increase in matrix and tumour stiffness, which leads to increasing tensional homeostasis.^[17, 19, 41, 43]

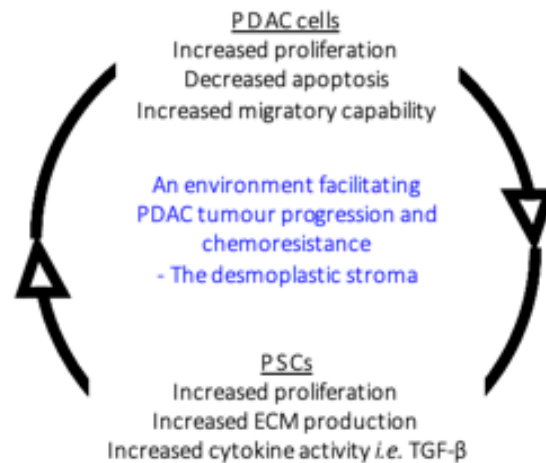


Figure 1.3. The symbiotic relationship between PDAC cancer cells and PSC cells

A summary of the interaction between the PDAC cancer cells and PSC cells illustrating the effects of PDAC cancer cells and PSC cells and vice versa. This interaction is necessary to facilitate an environment for PDAC tumour growth and malignant behaviour. Adapted from [26].

1.2.2. The biophysical forces of the PDAC tumour microenvironment

The tensional homeostasis within the tumour tissue consists of compressive and tensile forces. The PDAC cancer cells sense the mechanical forces through mechanoreceptors and respond by altering their mechanical phenotype with high levels of cell contractility to counteract the stiff environment.^[18, 19, 21, 43-46]

Integrins are the main mechanoreceptors involved in transducing mechanical cues into biomechanical signalling.^[42, 47, 48] Upon activation by a mechanical cue, they activate the Rho GTPase family that regulates cell cytoskeleton arrangement and intracellular contractile forces for the cells to undergo physiological changes in response to the increasing matrix stiffness. The active integrins further stimulate the production of TGF- β from cells which trigger the secretion of MMPs and LOX to remodel the matrix and increase the cross-linking and alignment of collagen fibres.^[42, 48-51] A vicious positive feedback loop of matrix production arises, which is additive to PDAC's tumour stiffness and growth.^[15, 18, 19, 43, 52] Figure 1.4 illustrates the growth-induced stress in the tumour tissue with the compressive and tensile forces.

The ECM components, *e.g.*, collagen and the glycosaminoglycan, hyaluronan (HA), contribute to tumour tissue stiffness, with their propensity to store and transmit stress depending on their mechanical properties.^[18, 19, 41, 43] Collagens provide the basic framework of the ECM

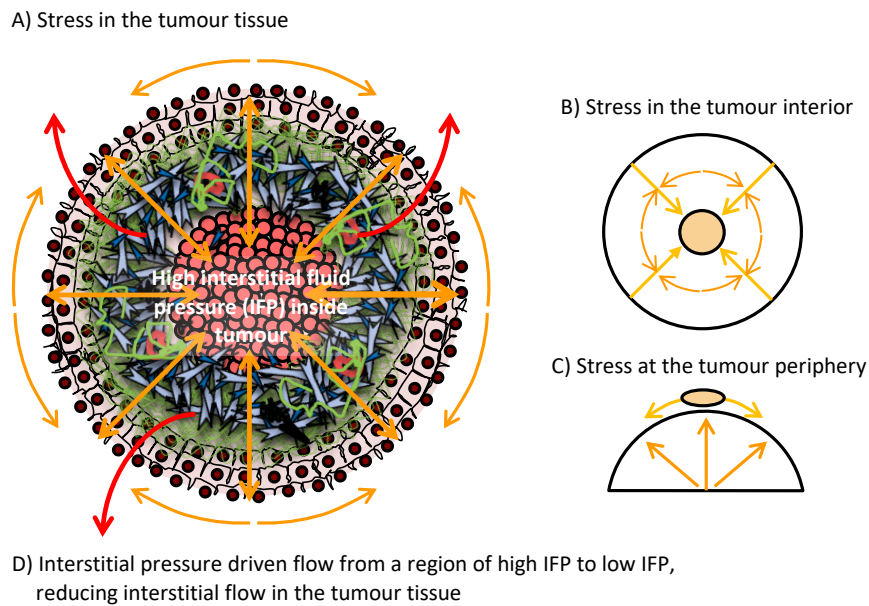


Figure 1.4. The solid and fluid stress in the PDAC tumour

From the accumulation of cells and the fibrotic stroma, A) there is compression and tensile forces and fluid stress from high interstitial fluid pressure in the tumour tissue. B) In the tumour tissue, the solid stress on the cells and ECM components is compressive in the radial and circumferential direction, and C) at the tumour periphery, the solid stress is compressive in the radial direction and tensile in the circumferential direction. D) There is a decrease in the interstitial space for the percolation of fluid, which results in high interstitial fluid pressure (IFP). As a result a steep pressure gradient at the tumour periphery causes interstitial fluid to move out of the tumour into neighbouring tissues. This proves to be an ineffective mechanism for drug delivery to the cells. Orange arrows indicate the solid stress in the tumour. The red arrows indicate the interstitial pressure driven flow of fluids out of the tumour with increasing solid stress. Adapted from [19].

architecture, and collagen type I proteins are the most abundant in the PDAC tumour tissue. Collagens are stiff in tension, providing tensile strength to tissues. At the same time, the negatively charged gelatinous HA provides resistance to the compressive stress with their ability to trap water and swell. Their swelling exerts additional forces on the surrounding cells and stroma, further contributing to the tumour tissue stiffness.^[18, 44, 46, 53-61]

Elevating tissue stiffness reduces the interstitial space available for fluid flow increasing intra-tumour pressure. As shown in Figure 1.4, this creates a steep pressure gradient for the flow of interstitial fluid from a high pressure gradient (the tumour interior) to a low pressure gradient environment (the tumour periphery and neighbouring tissues), a mechanism for the tumour cells to invade neighbouring and distant sites and for the ineffective delivery of drugs to the cancer cells.^[17, 19, 22, 43, 44, 57, 62-65] The increased intra-tumour pressure also results in the deformation of surrounding tissue structures. The tissue structures include blood and lymphatic vasculatures, and their deformation increases interstitial fluid pressure and limits interstitial flow. Interstitial flow is vital for transporting nutrients, oxygen, and drugs to the cancer cells.^[17-19, 24, 41, 43, 63]

Interstitial flow is the movement of intercellular fluid through the intercellular space of tissues. It is an important fluid mechanism for the delivery and formation of gradients of growth factors, chemokines, and also chemotherapeutics to cells. It provides a mechanical environment for the physiological activities of cells and for the physiology and architecture of healthy and disease tissues.^[17, 43, 44, 62-64, 66] A reduced interstitial flow leads to a hypoxic environment, which conversely stimulates the PDAC cell growth and protects them from the effect of the immune cells and drugs.^[17, 19, 24, 43, 67] With a hypoxic environment, cancer cells express genes such as hypoxia-inducible factor-1 alpha (HIF-1 alpha). HIF-1 alpha is a transcriptional factor central to a cell's adaptation to a hypoxic and acidic environment with a lack of nutrients and oxygen.^[68-73] HIF-1 alpha mediates metabolic pathways and responses, including anaerobic glycolysis, due to the inadequate supply of glucose, for cell survival. In effect, there is a high concentration of the glycolytic by-product, lactate, which acidifies the microenvironment, inactivating immune cells and drug effects.^[19, 46, 68, 70-74]

Moreover, with the collapsed vasculatures and reduced interstitial flow, there is the overexpression of pro-angiogenic factors, such as vascular endothelial growth factors (VEGF), for the formation of new blood and tumour vessels. However, the vessels formed become compressed with the growing fibrotic stroma and therefore are leaky and dysfunctional.^[17, 19, 41, 43, 63] The collapsed and dysfunctional vessels elicit fluid accumulation in the interstitial space, which leads to increased fluid flow resistance, particularly by the glycosaminoglycans with their ability to trap water in the tumour tissue.^[18, 19, 41, 43, 59, 63] Decreased fluid flow reduces shear stress on cancer and stromal cells, increasing their motility and activity.

These together, the unorthodox production and accumulation of cells and ECM components, the dense fibrotic stroma that arises with compressive and tensile forces, leading to increasing tissue rigidity, and collapsed vessels, which increases interstitial pressure and decreases the perfusion of nutrients to the cancer cells creating a hypoxic and acidic environment, underlie how the PDAC stroma shields and compromises therapeutic outcomes.^[18, 21, 22, 26, 46, 63]

Understanding the PDAC stroma and the stress and forces it exerts, tissue mechanical stiffness and reduced interstitial flow have provided insights into the mechanism by which tumours progress and evade therapy. However, recapitulating these biophysical forces *in vitro* is critical to further understanding the chemoresistant mechanisms important to effectively assess the efficacy of drugs against PDAC cells. Currently, *in vitro* models in the literature do not encompass the right biophysical characteristics of the PDAC tissue for therapeutic assessment. Section 1.4 discusses the different culture models for PDAC.

1.3. Mechanical assessment of pancreatic ductal adenocarcinoma

The extracellular matrix defines tissue stiffness. Assessing the mechanical stiffness of the healthy and diseased pancreatic tissue *in vivo*, shear wave elastography and magnetic resonance elastography has been used.^[48, 75] *Ex vivo*, multiphoton excitation, and second harmonic imaging techniques have been used to image the PDAC tumour microenvironment to investigate the deposition and alignment of collagen fibres.^[58, 76-80] As illustrated in Figure 1.5, *in vitro*, tension, compression, indentation, atomic force microscopy (AFM), and shear rheology techniques are commonly used to measure cell and culture stiffness.^[48, 79, 81-90]

In tensile and compression testing, a force load is used to pull or press samples to measure their tensile or compressive strength.^[48, 79, 91, 92] Similar to compression tests, in indentation tests, a force load is applied to samples to determine their stress-induced behaviour. With AFM, a scanning force microscopy, a cantilever probe scans, interacts and indents samples to provide information on their mechanical properties.^[83, 86, 87] The rheometer is used to study the flow of samples under shear deformation. It measures the resultant shear response of a sample or a sample's response in resisting a change in shape with sinusoidal shear deformation.^[89, 92-94] Shear rheology is a sensitive method for investigating a sample's mechanical nature and properties without the need for laborious microscopy and imaging

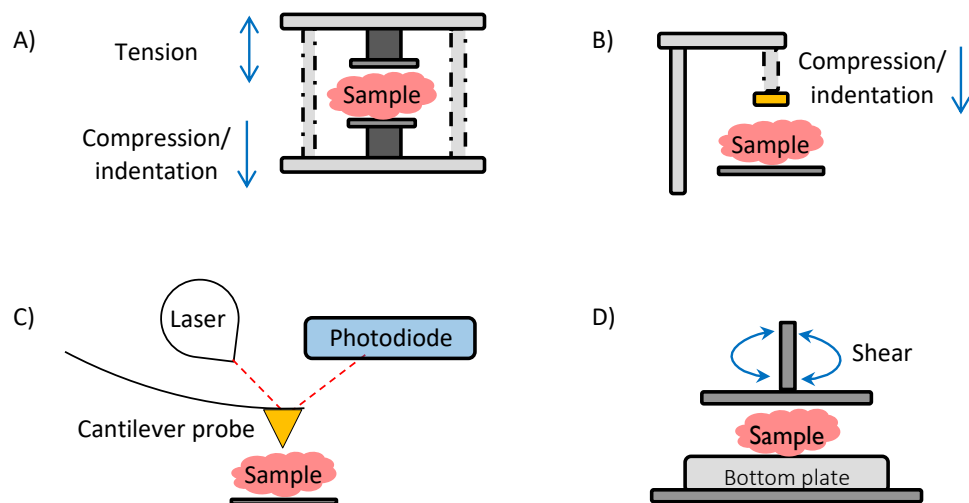


Figure 1.5. The different techniques for mechanical characterisation

Schematic of the commonly used techniques for mechanical assessments. A) and B) tensile, compression, and indentation test with instruments such as the dynamic mechanical analysis, where force is used to pull, press or indent a sample to measure mechanical behaviour. C) The use of the AFM to determine a sample's mechanical stiffness. A cantilever tip with a known geometry probe is used to interact with samples, and the deflection of the cantilever tip as it interacts with the sample is detected by a laser and recorded by photodiodes to inform of sample's mechanical properties. D) Shear rheology with sinusoidal stress at an angular frequency to measure a sample's response to sinusoidal strain to determine sample's stiffness.

techniques. Shear rheology provides information on bulk stiffness, which is the stiffness of samples on average. It takes into account the heterogeneity of samples.^[89, 92-94] Using the indentation approach, as shown in Figure 1.5B, Rubiano *et al.* 2018 investigated and compared the stiffness of patient-derived pancreatitis tissue, patient-derived PDAC tumour tissue, and patient-derived PSC cells grown in collagen matrix and maintained with conditioned media, the supernatant from the 2D culture of murine derived PDAC cancer cells. They found that the PDAC tumour tissues were stiffer than the pancreatitis tissues, and the stiffness of the PSC only cultures was within the range of the stiffness measured for the patient-derived PDAC tumour tissues.^[95] Although they show that mechanical assessment can help to clinically distinguish between different disease tissues and that the *in vitro* culture microenvironment can be tuned to mimic the mechanics of the *in vivo* tissue, mechanical assessment with indentation tests are localised in comparison to the bulk assessment that shear rheology provides.

Rice *et al.* 2017 used the AFM to assess and compare the mechanical stiffness of the mouse pancreatic tissue for normal pancreas, PanIN, and PDAC. They found that as the pancreatic tissue progress from a healthy or normal tissue into PDAC, there is increasing stiffness with increasing collagen production, collagen fibre alignment, and thickness. They also used the AFM to characterise the mechanical stiffness of polyacrylamide gels (based on their assessment with the murine pancreatic tissues) for culturing of PDAC cancer cells to assess how tissue stiffness promotes epithelial-mesenchymal transition (EMT).^[21] EMT is the process where cells lose their cell-cell adhesion properties, with the loss of epithelial proteins such as E-cadherin, and gain migratory and metastatic capabilities.^[96] Although they show how the AFM can be used to assess the mechanical properties of cells and tissues, the models used are murine-derived, and they only characterise the stiffness of their matrix gels for the culturing of PDAC cancer cells. They do not investigate how the cells develop a mechanically stiff environment for growth.^[21] Similar to Rice *et al.*, Nguyen *et al.* 2016 used AFM to measure the mechanical stiffness of different single healthy and PDAC cancer cells, HPDE, Hs766T, MIA PaCa-2, and PANC-1, grown in a petri dish with a thin layer of Matrigel. They assessed how stiffness influences cells' invasive capabilities and found that stiffer cancer cell lines were more invasive.^[20] However, the mechanical assessment was on single PDAC cancer cells only, which is unrepresentative of the mechanical stiffness of the *in vivo* tissue that arises from cell-cell and cell-matrix interactions. Also, they did not include stromal or fibroblast cells in their model.

Shear deformation has been used to characterise the mechanical properties of healthy and diseased pancreatic tissues.^[89] Wex *et al.* 2015 used shear deformation, as illustrated in Figure 1.5D, to assess the mechanical properties of healthy and diseased porcine and human pancreatic tissues. They showed shear rheology can be used to characterise the mechanical properties of different pancreatic tissues and to distinguish between healthy and diseased tissues.^[89]

Mechanobiology is an emerging field focused on learning more about the mechanical properties of cells and tissues and how this affects cell behaviour and disease progression. Cell and tissue mechanics are a hallmark of disease states, and cell and tissue stiffening has been found to precede disease development and drive disease progression.^[21, 42, 46, 80, 90, 97-99] The accumulation of cells and ECM components in the PDAC tissue results in a desmoplastic reaction, which increases the solid and fluid stress in the tissue, affecting therapeutic delivery and effects on the cancer cells. As such, it is essential to model the mechanics of the *in vivo* PDAC tissue to assess the therapeutic efficacy of the cancer cells.^[17, 19, 26, 63, 64, 100]

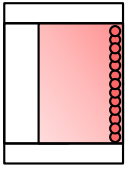
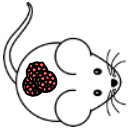
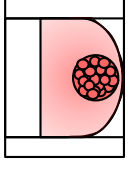
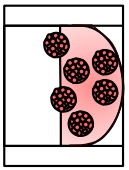
1.4. Modelling pancreatic ductal adenocarcinoma

Therapeutic studies of PDAC have used to date two-dimensional (2D) cell cultures, animal models, and three-dimensional (3D) culture models, in static well formats, which do not adequately represent the physiological conditions observed *in vivo*.^[25, 101-104] *In vitro* and animal models of PDAC have been informative on disease development and progression. However, given that PDAC is often diagnosed in its advanced stages,^[3-5, 105, 106] an adequate model representing the disease in its advanced stage with its biophysical hallmarks is essential for the accurate assessment of therapeutics. Table 1.1 summarises the advantages and limitations of the use of 2D cultures, animal models, and 3D cultures to model tumours.

1.4.1. Two-dimensional cell cultures

2D cell culture is the traditional culture method for providing insight into the physiological behaviour of cells.^[106-108] Its reproducibility, cheap cost, and the efficiency to grow numerous different cell types simultaneously make it a standard culture method for learning about the nature and behaviour of cells. However, 2D cultures involve growing cells on flat and rigid plastic environments with the use of culture dishes and flasks.^[25, 104, 106, 108, 109] This promotes

Table 1.1. An overview of the different culture models

| | 2D monolayer cell cultures | Mouse models | 3D cell culture in suspension | 3D cell culture in matrix scaffold |
|---------------|--|---|--|---|
| Models |  |  |  |  |
| Description | Cells grown with a flat surfaces, example with a polystyrene culture flask or dish | <ul style="list-style-type: none"> GEMMs – introduction of genetic mutation associated with specific tumours CDX and PDX models – developed with the engraftment of human cell lines or tumour tissue | Growth of the aggregate of cells in culture media without a matrix scaffold | Growth of aggregates of cells with a matrix scaffold |
| Advantages | <ul style="list-style-type: none"> Simple technique Cost effective High reproducibility Simple analysis | <ul style="list-style-type: none"> GEMMs – mimics the genetics and phenotype of <i>in vivo</i> tumours, providing the ability to learn and understand tumour development and progression CDX and PDX models – models inexpensive to generate in comparison to GEMMs | <ul style="list-style-type: none"> Closely mimics cell-cell interactions and the 3D organization of <i>in vivo</i> tumour tissues Cellular behaviours with respect to gene expressions, cell and mechanical phenotype, growth, ECM deposition, metabolic state, and drug response representative of <i>in vivo</i> tumours Helps to reduce the use of animal models | <ul style="list-style-type: none"> Closely mimics cell-cell and cell-matrix interactions and the 3D organization of <i>in vivo</i> tumour tissues The use of a matrix scaffold/hydrogel enables the mimicking of the ECM architecture Cellular behaviours with respect to gene expressions, cell and mechanical phenotype, growth, ECM deposition, metabolic state, and drug response representative of <i>in vivo</i> tumours The replacement, reduction, and refinement of the use of animal models |
| Disadvantages | Not representative of the <i>in vivo</i> environments – of the 3D organization of <i>in vivo</i> tumours, their ECM environment, and therapeutic barriers and resistance | Overall, time consuming and expensive to breed and to develop <i>in vivo</i> tumours. Moreover, interspecies differences between mice and humans with respect to drug pharmacokinetics and pharmacodynamics produce results that cannot be translated to humans | Static culture condition that do not reflect the <i>in vivo</i> tumour | Static culture condition that do not reflect the <i>in vivo</i> tumour |

cell-plastic interactions over cell-cell and cell-matrix interactions with the lack of the cellular 3D spatial organisation and the mechanical and biochemical signals conferred by factors of a tumour and its stroma environment. There is also the lack of the *in vivo* physiological fluid flow and shear stress conditions, which affects drug delivery to cells.^[18, 25, 104, 106, 108-112]

2D cell lines can be genetically programmed to reflect the *in vivo* cellular behaviour and interactions.^[106, 108, 113] PDAC cells have been genetically programmed to express transcription factors such as c-Myc, involved in cell differentiation and transformation regulation, to learn about PDAC development and progression.^[106, 113, 114] Conversely, genetic manipulation of cells is often transient in effect. Moreover, genetically programmed 2D cells still lack the biomechanical properties of the native cells and tissues.^[25, 104, 106, 108, 111, 112]

Despite the drawbacks, 2D cultures remain the first approach to growing cells and performing drug studies due to their simplicity and cost-effectiveness in providing insights into the initial cell growth and behaviour. Mukubou *et al.* 2010 assessed the autophagy effects of the chemotherapeutic drug, gemcitabine, with ionising radiation on 2D cultured PDAC cancer cells. They found a synergistic effect of gemcitabine and ionising radiation in reducing culture viability and proposed their potential use in treating pancreatic cancer clinically.^[115] Amrutkar *et al.* 2020 and Bjånes *et al.* 2020 showed gemcitabine-induced cytotoxicity depended on its uptake and activation into an active metabolite using 2D cultured PDAC cancer cells.^[116, 117]

In addition to 2D cultures remaining a standard cell culture procedure, mouse models are commonly used for preclinical drug pharmacokinetics and pharmacodynamic assessments.^[106, 113, 118-120]

1.4.2. Mouse models of pancreatic ductal adenocarcinoma

Mouse models have provided considerable insights into the PDAC pathogenesis, offering strategies to understand the molecular mechanisms underlining the disease.^[113, 118, 121-124] The most commonly used mouse models for PDAC studies are the genetically engineered mouse models (GEMMs) KC and KPC. The GEMMs are produced by the subcutaneous injection of tumour cells, with a genetic mutation generated using conditional and inducible systems.^[106, 113, 118, 125] The KC (KRAS mutation, pancreatic and duodenal homebox 1 (Pdx1) expression for pancreatic cell development, and Cre genetic technique to control where *KRAS* is turned on) and KPC (KRAS and p53 mutation and Cre to control where *KRAS* and *p53* gene are turned on)

models are developed with *KRAS* and *TP53* genetic mutations, and the tumours they develop closely mimics the histology and physiological aspects of the PDAC development, progression, the PDAC desmoplasia with the poor vasculature system, and therapeutic response.^[106, 113, 126, 127] Nonetheless, despite the advantages mouse models present in understanding the PDAC tumour biology and therapeutic response, they come with limitations.

The introduction of genetic mutations to develop GEMMs can lead to off-target pathological effects that can cause harm to the mouse and or result in a disease unrepresentative of the tumour in question.^[106, 113, 118, 126] Moreover, mouse models are expensive and labour intensive to develop and maintain, and the difference in drug metabolism between mice and humans makes the translation of therapeutics to humans cumbersome, underlining why drugs fail in clinical trials.^[106, 108, 118, 121, 128, 129]

The principles of the 3Rs, the replacement, reduction, and refinement of the use of animal models, have presented three-dimensional (3D) models that offer the opportunity and the advantage of emulating the *in vivo* tumour mass and its physiological microenvironment with cell-matrix interactions and the exposure, distribution, and effects of nutrients and oxygen, and drugs.^[25, 104, 110, 111, 130] Particularly as 2D cultures and animal models do not recapitulate the 3D hierarchical complexities of the human tumour tissues or predict effectively and efficiently the pharmacodynamics of the human body.^[11, 131-134]

1.4.3. Three-dimensional cell cultures of pancreatic ductal adenocarcinoma

Drugs fail clinical assessments because of the limitations of 2D cell cultures and animal models. 2D cultures do not emulate the fluid shear stresses and the cell-matrix interactions found in the *in vivo* tissue, and animal models do not reflect the complexities of human tumour tissues for practical drug assessments. 3D culture models offer the opportunity to mimic the human tumour mass and its microenvironment to study drug interactions effectively.

3D cultures are micro-sized aggregates of cells grown with or without a matrix scaffold (Table 1.1). The principle of culturing cells in 3D is based on culture conditions that encourage cell-cell adhesion forces for a relatively compact spherical cellular structure.^[108, 110, 111, 135-138] 3D cells, or spheroids, without a matrix scaffold, are grown using low-adhesion plates, hanging drop, and spinner flasks.^[104, 106, 110, 135, 136] 3D cells with matrix scaffold are grown in hydrogels, which can be natural or synthetic and include collagen, Matrigel, laminin, and agarose to

mimic the ECM and provide cells with the biomechanical and biochemical cues required for growth.^[106, 110-112, 129, 135, 136]

Longati *et al.* 2013 developed a 3D PDAC culture by growing the cancer cells, including BxPC-3, PANC-1, and KPC, in methylcellulose to explore chemoresistance. There was increased collagen production, and their cultures were resistant to the effects of gemcitabine.^[25] Using the liquid overlay technique with agarose-coated wells, Wen *et al.* 2013 developed a 3D pancreatic cancer culture, with MIA PaCa-2 and PANC-1 cells, for drug testing. They treated their PDAC cancer spheroids grown for four days with 5-fluorouracil and gemcitabine. Compared to 2D cultures of the cancer cells, there was reduced sensitivity to the effects of 5-fluorouracil and gemcitabine.^[139] Ware *et al.* 2016 presented a modified hanging drop method using methylcellulose to develop pancreatic cancer spheroids with cells including PANC-1.^[104] Puls *et al.* 2017, grew their pancreatic cancer cells in a collagen-rich matrix to look at the effects of the matrix properties on the cancer cell behaviour and resistance to drugs,^[140] and using patient-derived pancreatic cancer cells and cell-repellent well-based plates to promote cell-cell interactions over cell-substrate interactions, Hou *et al.* 2018 presented a high-throughput screening approach to investigate the effects of a panel of chemotherapeutic drugs, including gemcitabine, on 3D pancreatic cancer cell cultures.^[141] Although the cultures presented in the aforementioned studies inform how 3D models can be used to assess therapeutic response accurately, the models presented were mostly of PDAC cancer cells only without stromal cells, given that stromal cells of the PDAC tumour tissue govern the matrix stroma environment and biophysical hallmarks.^[17, 18, 21, 24]

3D cultures consisting of cancer and stromal cells have the unique capability of modelling the heterogenic gene expressions, cancer-stromal cell interactions, and signalling pathways that promote therapeutic resistance *in vivo* (Cell interactions, Figure 1.6). With the ability to attain diameters of more than 400 μm , 3D cell cultures capture the *in vivo* heterogenic exposure and diffusion of nutrients and oxygen to cells, reflecting the avascular and vascular phases of solid tumours (Metabolic zonal structure, Figure 1.6).^[104, 108, 111, 112, 129, 135, 136]

In the avascular phase, where tumour tissues do not require the process of angiogenesis, there is increased growth with an unlimited source of nutrients and oxygen from surrounding tissues. In the vascular phase, there is the deprivation of nutrients and oxygen and the accumulation of metabolic wastes from tumours, as the tumours outgrow the supply of nutrients and oxygen. This results in the expression of pro-angiogenic factors for vessel formation (e.g., VEGF observed in PDAC) and ECM proteases (e.g., MMP-2 and MMP-9) to

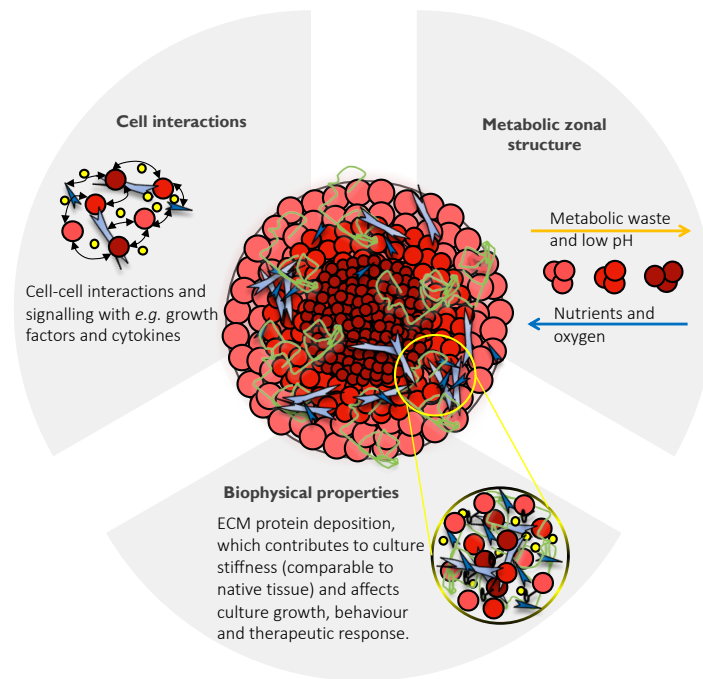


Figure 1.6. Main characteristics of 3D cell cultures

Schematic summarising the fundamental features of solid tumours, mimicked by 3D cell cultures, which account for therapeutic resistance and are crucial for the effective screening of cancer therapeutics. Adapted from [108].

remodel the cell microenvironment for nutrients to the cancer cells for growth and survival.^[7, 43, 108, 111, 129, 135, 136]

In the vascular phase, cells in different metabolic states arise due to the heterogenic diffusion of nutrients and oxygen. The different metabolic states are identified in 3D cultures with proliferative cells at the periphery of the cultures with nutrients and oxygen readily available to them and with quiescent and hypoxic cells within and at the core of the cultures, typically more than 100 μm away from the periphery, deprived of nutrients and oxygen with increased metabolic waste (Metabolic zonal structure, Figure 1.6).^[104, 108, 111, 112, 129, 135, 136] The lack of nutrients and oxygen, and the increased metabolic waste, results in the cells becoming hypoxic and inhabiting an acidic tumour microenvironment of pH 5.6 – 6.8.^[142, 143] The cells adapt by inducing and expressing genes and signalling pathways such as hypoxia-inducible factors and the glycolysis metabolic pathway to obtain nutrients and energy for survival.^[73, 104, 108, 111, 129, 135, 136, 142] Furthermore, the hypoxic and acidic tumour microenvironment confers survival benefits to cancer cells by promoting the activity of stromal cells, impairing the activity of immune cells, and inducing changes in drug properties that influence their cellular uptake and effects.^[19, 43, 69, 73, 111, 129, 142] In addition to the outgrowth of nutrients and oxygen, there is the deposition and accumulation of ECM, which forms a barrier and further limits the

distribution of nutrients and oxygen and therapeutics to the cancer cells (Biophysical properties, Figure 1.6).^[18, 19, 43, 108, 111, 129]

Ware *et al.* 2016 cultured PDAC cancer cells, including BxPC-3, MIA PaCa-2 and PANC-1, with PSCs to model the cancer-stromal cell interactions and investigate its effects on tumour growth. They found increased proliferation of the PDAC cancer cells in the presence of PSC cells. They also found regions of increased collagen deposition and a decrease in the perfusion of drugs to the cells.^[129] Lazzari *et al.* 2018 developed a heterotypic pancreatic cancer spheroid, where pancreatic cancer cells, PANC-1, were cultured with the fibroblast cell, MRC-5, and the endothelial cells, HUVEC, to model the surrounding tumour microenvironment of pancreatic cancer for drug screening. They found increased metabolic activity of the cancer cells, increased spheroid growth, and increased resistance to the effects of gemcitabine compared to mono-pancreatic cancer cell cultures.^[103] Pednekar *et al.* 2021 cultured the PDAC cancer cells, PANC-1, with PSCs and found the cellular arrangement of the PDAC cancer cells with the stroma cells and secreted ECM to mirror that of the *in vivo* tissue. They also found increased cell numbers, collagen regions, and a decrease in the ability of drug molecules to penetrate through dense culture environments.^[144]

In addition, Huang *et al.* 2015, Boj *et al.* 2015 and Tsai *et al.* 2018 developed PDAC organoid cultures with patient-derived pancreatic tumour cells, CAFs, and immune cells. The organoid cultures they developed maintained the histological and genetic properties of the primary tumour and stromal compartment, retained the physiological changes of the PDAC tumour tissue, which includes the expression of hypoxia, and were resistant to gemcitabine.^[107, 145, 146] Organoids, are 3D cultures of stem cells and patient-derived cell lines in a matrix scaffold. The cultures developed with organoids mimic the architecture and the heterogenic phenotypic and genetic characteristics of the tissue of origin, and they have been useful in understanding personalised drug treatment.^[106, 107, 109, 147, 148]

3D cell cultures have become a widely used approach for modelling diseases for pre-clinical assessments due to their capability of capturing the 3D complexities of *in vivo* tumour tissues.^[104, 106, 108, 111, 129, 138] However, most 3D cell cultures of PDAC are often grown in static culture well formats, where the *in vivo* fluid flow and shear stress conditions are lacking to mimic the hallmarks of the PDAC tumour microenvironment.^[25, 102, 103, 133, 135, 137, 149] *In vitro* PDAC models, which focus on the rich tumour stroma and the drug resistance mechanisms that ensue, can advance the understanding of the disease's malignancy and enable the discovery and validation of drugs.

1.4.4. Microfluidic cell culture models of pancreatic ductal adenocarcinoma

Microfluidics, the science of fluid flow confined on the microscale, has become a widely used approach in modelling and studying cells and tissues, including the PDAC tumour.^[131, 133, 149, 150]

With the control of fluid flow within a defined physical environment, microfluidics enables 3D cultures representative of the *in vivo* tissue with physiological fluid pressures and shear stress.

Matrix scaffolds or hydrogels can be used in microfluidics for 3D cell cultures to recreate organ-level multicellular architecture and complexity. Moreover, quantitative and qualitative assessments can be performed on a single device or simultaneously across multiple devices of the same cell culture, and due to the miniature size of the culture systems developed, microvolumes of reagents are used for cell culture and assessments, making microfluidic culture systems an efficient and cost-effective approach for modelling diseases under physiologically relevant conditions.^[133, 134, 149, 151-159]

Huh *et al.* 2015, Kennedy *et al.* 2019, Lai *et al.* 2020, and Nikolaev *et al.* 2020, amongst others, have demonstrated how advantageous and relevant it is to employ microfluidic technology to recapitulate aspects of the healthy and disease tissues to advance diagnoses and treatments.^[39, 131, 152, 155, 156, 160-164] For pancreatic cancers, Drifka *et al.* 2013 developed a 3-channel microfluidic device for culturing the PDAC cancer cells, PANC-1, with PSCs within a collagen-rich matrix for up to seven days. They evaluated the PDAC cancer cell-stroma interaction and the effects of the chemotherapeutic drug paclitaxel. They found increasing ECM contraction and cell-mediated collagen remodelling with the presence of PSCs. They found paclitaxel to be effective in reducing culture viability. However, apart from the collagen matrix used for culture, they do not observe additional collagen deposition with the limited culture time. This can affect how drugs interact with cells as the cultures will not exhibit an *in vivo*-like rich stroma and will be mechanically immature.^[38] Similar to Drifka *et al.*, Lee *et al.* 2018 presented a 7-channel microfluidic device for culturing PANC-1 cells with PSCs to study EMT. They cultured the cells for up to five days and found increasing spheroid formation and EMT-related markers such as low E-cadherin expression levels and increased TGF- β expression of the cancer cells in the presence of PSCs.^[165] Bradney *et al.* 2020 also assessed the EMT of their PDAC on-chip culture. They report a ductal-like tumour microenvironment device to mimic the ductal architecture of the PDAC tumour tissue and the cancer cell-stroma interactions. They seeded murine-derived cancer cells in a collagen-rich matrix into the ductal-like device and cultured them for up to seven days. They found high levels of the zinc finger protein, SNAI1, commonly referred to as Snail, and fibronectin, which are transcription factors

and markers for EMT, and increasing local invasion of their cultures into the stroma. They showed that the intratumoural heterogeneity of PDAC cancer cells affects invasion capabilities, whether the cells are of an epithelial subtype or a mesenchymal subtype. However, the model presented used murine-derived cancer cells, and they did not include fibroblasts cells, which influence the cancer cell-matrix interactions and thus a response to drugs.^[11]

Kramer *et al.* 2019 reported a microfluidic device to assess the reduced interstitial flow in the PDAC tumour microenvironment. Using a 3-channel device for culturing PDAC cancer cells in a collagen matrix, they evaluated the movement of Tetramethyl Rhodamine Iso-Thiocyanate (TRITC)-dextran from a localised spot in the culture chamber of their device. With time-lapse imaging, they found high interstitial flow through the ECM of their cultures and a decrease in cell proliferation from a lack of nutrients.^[166] Although they report their interstitial flow speed within the *in vivo* range, the results found are quite conflicting. With increasing intratumoural pressure in the PDAC tumour tissue, there is reduced interstitial flow with nutrients to the cells reducing cell proliferation. They found high flow speed through their ECM, affecting cell proliferation from high shear stress. This raises the question of whether the culture model they present adequately recapitulates the interstitial flow of the PDAC tumour microenvironment. They also did not include fibroblast or CAF cells in the culture. Moreover, the microfluidic device used, the Organoplate, is based in a 384-well plate, requiring a rocking platform for flow. The use of a well plate format shows that the microfluidic device they present enables static cell culture conditions, as opposed to the advantage of a perfusion culture, provided by microfluidics, to recapitulate the *in vivo* physiological flow conditions.^[167]

Lai *et al.* 2020 also presented a well-based microfluidic device for PDAC cell culture. The InVADE chip is based in a 96-well plate format. Using InVADE, they assessed the interstitial flow of carboxyfluorescein diacetate through their pancreatic tumour co-cultures. They found decreased fluid flow in their PDAC cancer cell cultures with human dermal fibroblast cells. However, their device is in a well plate format, and they did not use fibroblast cells native to the PDAC tissue, which can influence the phenotypic and genetic characteristics of their cultures.^[39]

Microfluidics provides a high degree of control over cell culture conditions representative of *in vivo* tissues. One can have control of the spatial distribution of cells, fluid flow and pressures and establish chemical gradients for drug testing. For pancreatic cancer, most microfluidic cultures focus on the heterogeneity of the disease and the invasive and metastatic behaviour

of PDAC cancer cells.^[11, 39, 165] The studies highlight how the stroma, with PSC cells and ECM, are important for the PDAC cancer-stroma interactions vital for effective drug assessments.^[11, 38, 39, 101, 165] Given how the rigidity of the stroma is central to the therapeutic resistance of the PDAC tissue, there is little research on modelling the rigidity of the *in vivo* PDAC tissue and its effects, on-chip, for therapeutic assessment.^[11, 38, 39, 101, 165, 166, 168]

1.5. Therapeutic strategies for pancreatic ductal adenocarcinoma

Due to the lack of distinctive symptoms and biomarkers, PDAC is commonly advanced at the time of diagnosis. Available and conventional treatments are palliative to relieve symptoms and prolong survival. Treatments include surgery, chemotherapy, immunotherapy, and radiotherapy.^[105, 169-171] Targeting the PDAC stroma has attracted interest as a possible treatment to augment available and conventional therapeutic strategies.^[24, 42, 105, 170-173]

Surgical excision remains the cornerstone treatment for all cancer patients, including PDAC patients. Nevertheless, very few patients, about 10 – 20 %, are eligible,^[3, 9, 105, 171, 174] and the median survival for PDAC patients is approximately 20 months post-surgery.^[105] Adjuvant therapies with chemotherapy, immunotherapy, or radiotherapy, have shown to improve patient survival in comparison to surgery alone.^[9, 105, 169, 171, 174] Radiotherapy allows the local control of the PDAC tumour, increasing the chance of complete tumour removal with surgery.^[9, 171] Immunotherapy has been shown effective in other cancers, including the breast, but in PDAC, the results are conflicting.^[105, 171] However, immune checkpoint inhibitors have shown promise in increasing responses to existing chemotherapeutic drugs.^[9, 105, 171, 175-177]

Chemotherapy remains the main therapeutic option for advanced and metastatic cancers. For patients with PDAC, FOLFIRINOX, a combination of the drugs folinic acid (or leucovorin), 5-fluorouracil, irinotecan, and oxaliplatin, is used to improve patient survival.^[24, 105, 169, 173] However, FOLFIRINOX is only suitable for patients with good performance status due to the increased toxicity effects of the different chemotherapeutic drugs.^[24, 105, 178-181] Gemcitabine, a nucleoside analog, remains the first-line chemotherapeutic drug for PDAC patients.^[24, 105, 170]

1.5.1. The mechanism of action of gemcitabine

Gemcitabine (2',2'-difluoro-2'-deoxycytidine; dFdC; $C_9H_{11}F_2N_3O_3$), with a molecular weight of 263.2 g mol^{-1} , is a hydrophilic nucleoside chemotherapeutic drug and the standard of care for patients with locally advanced and metastatic PDAC.^[24, 105, 170, 182]

Figure 1.7 shows a schematic of the cellular uptake, metabolism, and mechanism of action of gemcitabine. Gemcitabine is a deoxycytidine analog, a prodrug active when transported into cells. As a hydrophilic nucleoside analog, it is transported into cells by a family of integral membrane proteins called the human nucleoside transporters (hNT).^[117, 170, 182, 183] hNTs are vital for the cellular uptake of nucleosides and nucleoside analogs due to the inherent diffusion barrier imposed by their hydrophilic nature. Most gemcitabine uptake is mediated by the human equilibrative nucleoside transporter (hENT) 1.^[105, 170, 182] Once inside the cell cytoplasm, gemcitabine (dFdC) is either deaminated into 2',2'-difluoro-2'-deoxyuridine (dFdU), a process catalysed by cytidine deaminase (CDA), or it is phosphorylated into gemcitabine monophosphate (dFdCMP), a rate-limiting step catalysed by deoxycytidine kinase (dCK).^[170, 182-184] As dFdCMP, gemcitabine can be dephosphorylated by 5' nucleotidases (5'-NTs) to dFdC, phosphorylated by the enzyme, pyrimidine nucleoside monophosphate (UMP-CMP) kinase, to gemcitabine diphosphate (dFdCDP), or inactivated by deoxycytidylate deaminase (dCTD) into dFdU monophosphate (dFdUMP), which inhibits the activity of thymidylate synthase.^[170, 182-184] Thymidylate synthase plays an important role in providing precursors for the deoxynucleotide triphosphate (dNTP) pool, which is vital for DNA synthesis. If thymidylate synthase is inhibited, there is an imbalance of deoxynucleotides, resulting in DNA damage and, therefore, cell death.^[170, 182, 183] When dFdCMP is dephosphorylated by 5'-NTs, phosphorylation by dCK is compromised, affecting the metabolism and the overall beneficial cytotoxicity of gemcitabine. However, if dFdCMP is phosphorylated into dFdCDP by UMP-CMP, dFdCDP inactivates ribonucleotide reductase (RR) by covalently binding to its active site, and it is further phosphorylated, by nucleoside diphosphate kinase, into gemcitabine triphosphate (dFdCTP).^[170, 182-184] RR is a protein also vital for the dNTP pool. RR inactivation decreases the dNTP pool, reduces dCTD activity, and drives cells to uptake nucleosides (including gemcitabine) to increase the dNTP pool.^[170, 182-184]

Phosphorylation of dFdCDP to dFdCTP is the final phosphorylation for the effect of gemcitabine as a nucleoside chemotherapeutic drug.^[170, 182, 183] dFdCTP masquerades as cytidine, which is incorporated onto DNA strands during DNA synthesis. This results in a mask chain termination, where dFdCTP incorporation disrupts DNA synthesis and causes irreparable

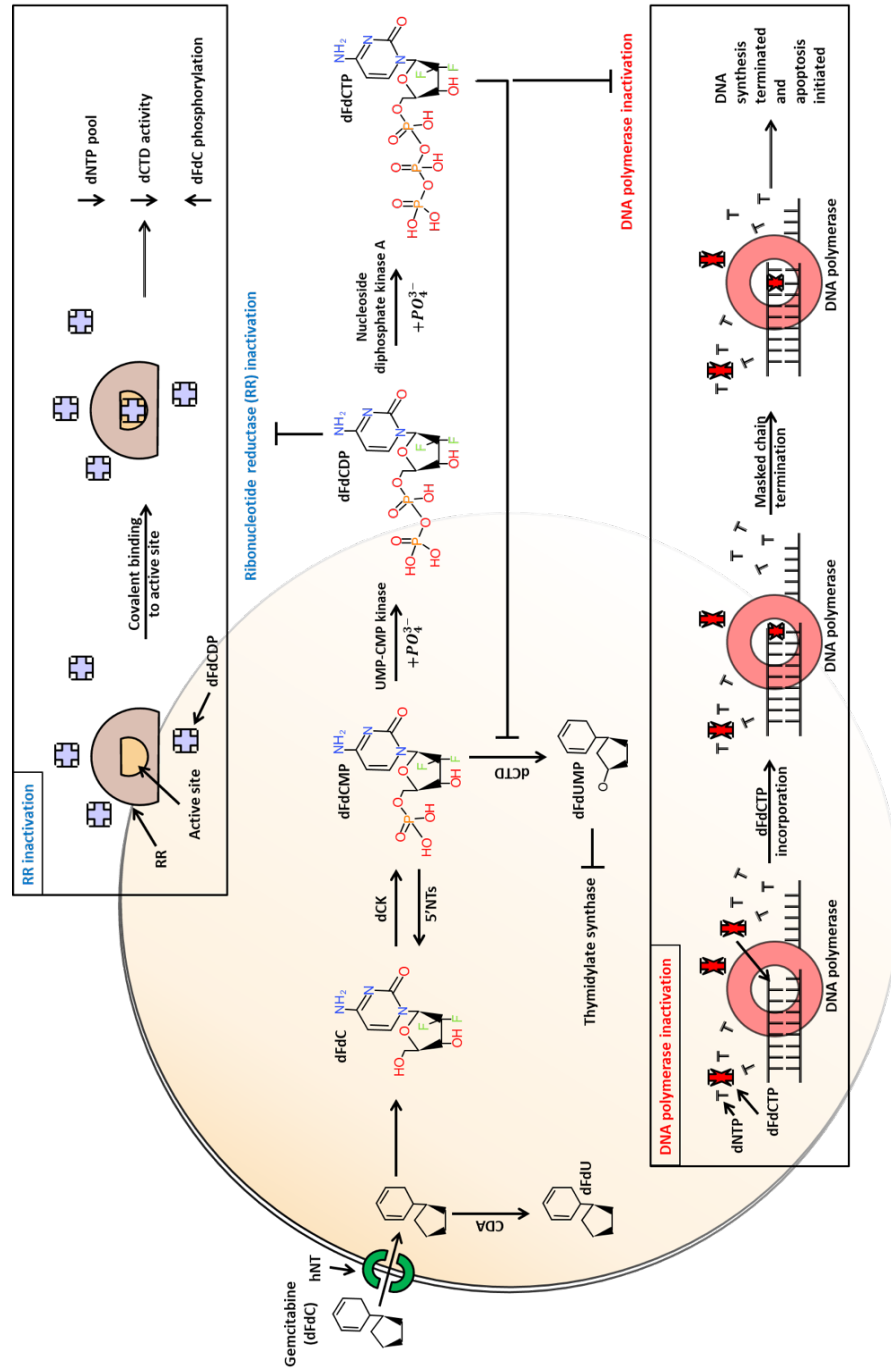


Figure 1.7. The mechanism of action of gemcitabine

Gemcitabine (dFdC) is taken into cells actively by the hNTs. Once inside cells, dFdC is phosphorylated into dFdCMP by dCK, or deaminated by CDA. If phosphorylated into dFdCMP, it can be inactivated by 5' NTPs, deaminated by dCTD or phosphorylated into dFdCDP by UMP-CMP kinase. dFdCDP covalently binds and inactivates RR, which is essential for the dNTP pool for DNA synthesis, dFdCDP is phosphorylated into dFdCTP for gemcitabine, dFdC, to act as deoxyxycytidine analog. Gemcitabine masquerades as a cytidine, and it is incorporated onto the DNA strand, which results in DNA synthesis stopping and cancer cell apoptosis. Adapted from [170].

DNA damage leading to cancer cell death.^[170, 182, 183]

Gemcitabine increases patient survival to approximately 18 months with a substantial improvement in relieving symptoms, but as a chemotherapeutic drug, its side effects prove to be an ineffective means of treatment. Moreover, the dismal prognosis of PDAC is high chemoresistance due to the dense fibrotic stroma in the tumour microenvironment.^[17, 22, 24, 173, 185]

1.5.2. Mechanisms of therapeutic resistance and targeting the PDAC stroma

Using 2D cultures of PDAC cell lines, Bjånes *et al.* 2020 demonstrated hENT1, a determinant of gemcitabine uptake and retention.^[117] Kramer *et al.* 2019 found high levels of multidrug resistance proteins (MRPs) with interstitial flow in their cultures, which resulted in a minimal response to the anti-proliferative effects of gemcitabine.^[166] MRPs are expressed in tissues and act as efflux transporters for endobiotic and xenobiotics, influencing the extrusion of chemotherapeutic drugs out of cells,^[186-188] as shown by Kramer *et al.* Referred to as fibroblast drug scavenging, Hessman *et al.* 2018 found high intracellular levels of the gemcitabine metabolite, dFdCTP, with no effect on their viability, in CAFs and PSC cells.^[179] This entrapment of active gemcitabine by the fibroblast cells contributes to the limited availability of gemcitabine to the cancer cells. Also, Dalin *et al.* 2019 showed the PSC cells secrete large amounts of the nucleoside deoxycytidine (which is important for maintaining the dCTP pool for DNA synthesis) into the tumour microenvironment to compete with gemcitabine for uptake by the PDAC cancer cells.^[189, 190] Pednekar *et al.* 2021 show with PSC, with the release and accumulation of cells and the ECM such as collagen, there is a dense stromal barrier to the penetration of drugs.^[144, 189, 191] Using an integrin $\alpha 5$ (ITGA5) antagonistic peptide, AV3, to inhibit the activation of PSC and thus the production of ECM macromolecules,^[192] there was an influx of drug molecules to the PANC-1 cells. Hessman *et al.*, Dalin *et al.*, and Pednekar *et al.* show how central PSC cells are to gemcitabine resistance. Studies with mouse models show that gemcitabine is sequestered in the PDAC stroma, limiting its availability to the cancer cells, and drugs that target the PDAC stroma, suppressing the activity of PSCs and the ECM production, aim to enhance the delivery of drugs to the cancer cells.^[22, 24, 170, 185]

Studies on improving the delivery of drugs to the PDAC cancer cells have resulted in the reengineering of the PDAC stroma with and including the inactivation and depletion of PSC cells, the targeting of hyaluronan and the crosslinking of collagen fibrils, or relieving

vasculature compression.^[22, 42, 65, 192, 193] However, vessel patency is reported to have shown early time-points of drug administration and accumulation and does not correlate with drug pharmacokinetics and pharmacodynamics.^[179] The depletion of fibroblasts, collagen and hyaluronan, although has proven to reduce fibrosis and increase drug delivery and response,^[192-196] consequently has shown to increase tumour growth and aggressiveness.^[22, 42, 197, 198]

Studies combining chemotherapeutic drugs with stroma targets in mice, by regulating the hedgehog (HH) signalling mechanisms, for example, have shown an increase in the delivery of drugs to the PDAC cancer cells, reducing metastasis and prolonging survival.^[22, 105, 173, 185, 199, 200] The HH signalling pathway plays a pivotal role in PDAC development, promoting cancer cell survival and desmoplasia formation. As such, HH is of interest in repressing PDAC development and progression.^[105, 170, 173, 185] Reported in Olive *et al.* 2009 the HH inhibitor, IPI-926, has a synergistic effect with gemcitabine, where the intratumoural concentration of gemcitabine and delivery to cancer cells is enhanced, increasing overall mice survival. However, in patients, the results have been conflicting, leading to reduced patient survival.^[105, 170, 173, 180, 185, 201] Matrix metalloproteinase inhibitors have also been tested to determine their effects on increasing the therapeutic efficacy of gemcitabine. Nonetheless, high expressions of MMPs, such as MMP1, 2, 7, and 11, are associated with poor prognosis.^[42, 173, 185, 202]

On-going and emerging studies are on decreasing the high interstitial fluid pressure (IFP) in the PDAC tumour tissue to increase the hydraulic conductivity of the interstitial space and enhance drug transport to cancer cells.^[44, 57, 196, 200, 203] Angiotensin II type 1 receptor blockers (ARBs) have shown promising results in relieving solid stress and IFP. Candesartan and losartan have shown evidence of suppressing the activation of PSC cells, reducing the production of ECM macromolecules, and prolonging patient survival.^[105, 172, 199, 200, 204, 205] Also, the use of PEGylated recombinant hyaluronidase (PEGPH20) to degrade HA, and therefore deplete HA accumulation in the tumour microenvironment, in combination with gemcitabine, has been shown to relieve solid stress and IFP with better mice survival.^[22, 105, 173, 185, 195, 196, 200, 206]

Altogether, the desmoplastic tumour stroma is central to the malignancy of PDAC, and novel approaches are required to enhance drug delivery to the cancer cells. The use of ultrasound contrast agents, microbubbles, has shown to increase cellular drug uptake. Owing to their sonoporation effects, creating transient pores in cell membranes to increase drug uptake, their therapeutic potential is widely studied in the context of targeted drug delivery.^[117, 207-212]

1.5.3. Using microbubbles to assist drug delivery to PDAC cells

Microbubbles are phospholipid shell encapsulating gas core bubbles of 1 – 10 μm diameter. Their oscillation and bursting with ultrasound imposes shear stress on cell membranes to

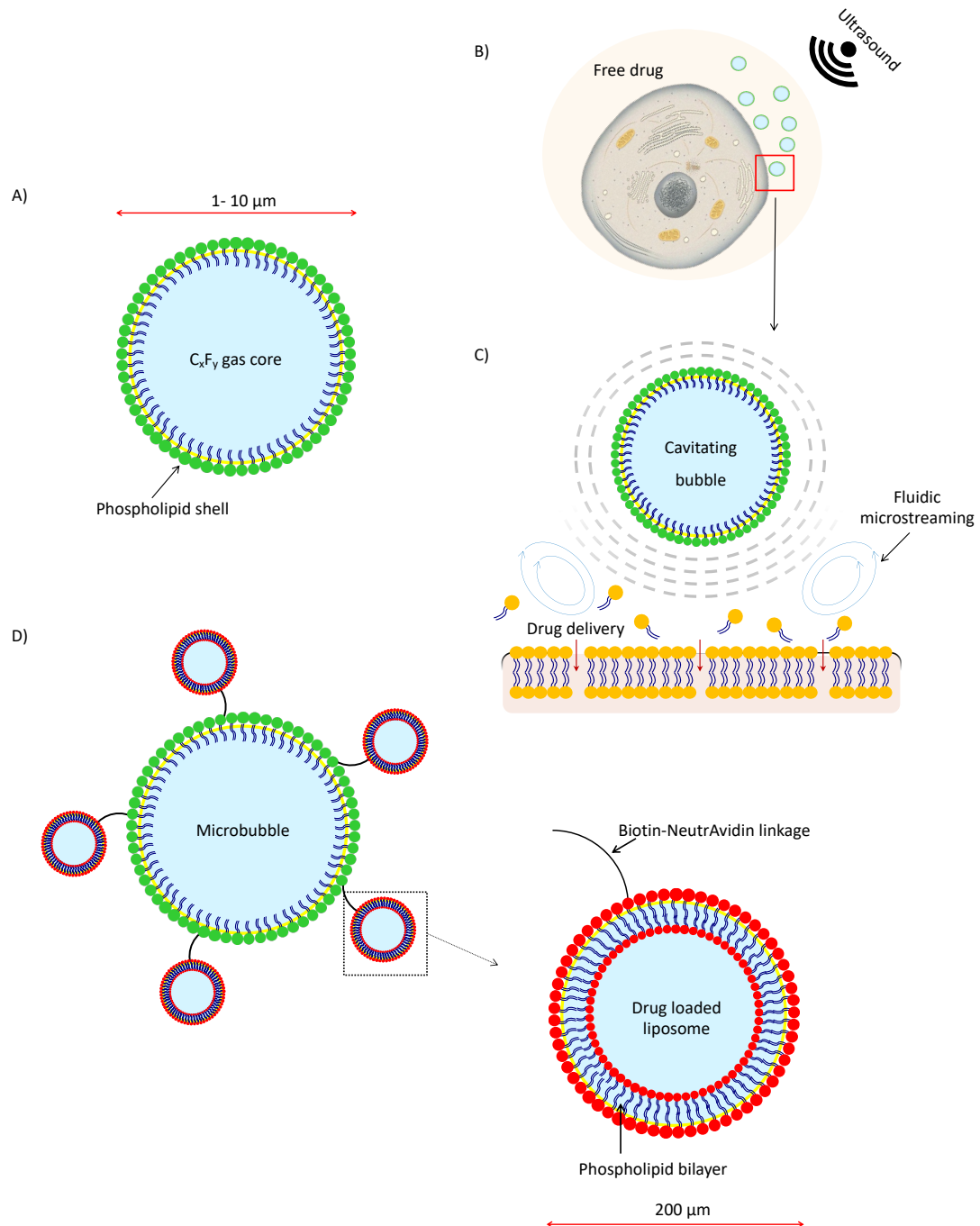


Figure 1.8. A lipid coated microbubble and its mechanism in drug delivery

An illustration of A) the structure of the microbubble with a phospholipid monolayer shell and a perfluorocarbon gas core, and B) a mechanism by which microbubbles with ultrasound increase drug delivery to cells. The oscillation of cavitation or microbubbles under ultrasound exposure induces fluid microstreaming, causing shear stress on cell membranes. This results in increase cell membrane permeability from the formation of transient pores in the cell membranes. An increase in cell membrane permeability enhances the uptake of drugs by cells. D) Schematic of a therapeutic microbubble composed of a microbubble conjugated to drug-loaded liposomes of up to 200 nm in diameter.

make them permeable for drug uptake.^[117, 207, 208, 211, 213-217] Figure 1.8 illustrates the structure of a microbubble and a mechanism of sonoporation.

The use of microbubbles with ultrasound has been shown to enhance drug uptake and their effects on PDAC.^[209, 218, 219] McEwan *et al.* 2015 investigated the effect of oxygen-loaded microbubbles *in vitro* with 2D PDAC cancer cell cultures and *in vivo* with orthotopic models of PDAC. They assessed how oxygen delivered with microbubbles could generate reactive oxygen species and therefore sensitise hypoxic cells to the effects of sonodynamic therapy using a rose bengal sensitiser. They found microbubbles with ultrasound to effectively deliver oxygen to the hypoxic cells, decrease cell viability, and decrease tumour volume in the orthotopic models.^[67] Following this, the same group and Nesbitt *et al.* 2018 investigated the effects of the oxygen-loaded microbubbles with ultrasound on sensitising PDAC cancer cells to the effects of 5-fluorouracil and gemcitabine. They demonstrated that sonodynamic therapy in conjunction with the oxygen-loaded microbubbles conjugated to 5-Fluorouracil and gemcitabine enhanced cell cytotoxicity and significantly reduced tumour growth in the mouse models.^[218, 219] Bressand *et al.* 2019 investigated the effectiveness of nab-paclitaxel with microbubbles and ultrasound also on 2D cultures and orthotopic models of PDAC. They showed that microbubble and ultrasound increased the effects of nab-paclitaxel with a decrease in cell viability and tumour volume.^[220] Clinically, Dimcevski *et al.* 2016 demonstrated the use of microbubbles and ultrasound with gemcitabine to treat patients with inoperable pancreatic cancers. There was an increase in mean patient survival.^[209] These studies show microbubbles with ultrasound promote the effective transport of drugs into cells for therapeutic effects.

Microbubbles can also be adapted by modifying the composition of the phospholipid shell or the gas core into drug-carrying vesicles to form therapeutic microbubbles. Such as with the attachment of drug-loaded liposomes to enhance drug delivery and effectiveness at target sites.^[221-224] Liposomes are biocompatible sphere-shaped phospholipid vesicles of more than one lipid bilayer enclosing a known liquid solution, and their sizes are typically tens to hundreds of nanometers in diameter (Figure 1.8D).^[221, 223-225] The oscillation of therapeutic microbubbles under ultrasound allows the shedding of liposomes into the environment of the target site. With the opening of cell membranes transiently, the released liposomes from the conjugates are taken up the cells allowing high drug dosage to be delivered into cells. Studies with gemcitabine-loaded liposomes, including Celano *et al.* 2004, Kim *et al.* 2018, Tucci *et al.*

2019, Li *et al.* 2019, and Ruan *et al.* 2021, show an effective gemcitabine delivery to PDAC cancer cells, reducing cell and tumour growth.^[222, 226-230]

Microbubbles are well established and commonly used clinically as contrast agents. As therapeutic agents, microbubbles are used due to their ability to increase cell membrane permeability for drug delivery into cells. The idea of microbubbles oscillating and bursting under ultrasound can be exploited to investigate ways of disrupting the PDAC stroma to increase drug delivery to the PDAC cancer cells. Therapeutic assessments on *in vitro* PDAC cultures that reflect the disease's biophysical hallmarks with microbubbles and ultrasound can shed light on targeting PDAC cells effectively to improve treatment outcomes.

1.6. Project overview and thesis layout

The aim of this project was to develop a microfluidic PDAC culture model for therapeutic assessment with microbubbles and ultrasound. The growing PDAC fibrotic stroma, with increasing tumour rigidity, high intratumoural pressure, and collapsed vasculatures, poses a physical barrier to the delivery of drugs to the cancer cells.^[17, 18, 46, 80] PDAC culture models in the literature do not adequately emulate these biophysical hallmarks for effective therapeutic studies. Here, the PDAC culture model presented focuses on the disease's fibrotic stroma, tissue mechanical stiffness, reduced interstitial flow, and chemoresistance for assessment with microbubbles and ultrasound.

The PDAC fibrotic stroma, mechanical stiffness, and chemoresistance were investigated off-chip to determine the optimum culture conditions to mimic these features on-chip. Microfluidics was used for culture as it enables fluid flow control within a defined physical microenvironment to recapitulate *in vivo* conditions. On-chip, the interstitial flow nature of the PDAC culture and the use of microbubbles and ultrasound to enhance gemcitabine effects were assessed. The PDAC culture consisted of the PDAC cancer cells, PANC-1, with PSCs and TGF- β 1 supplement.

As the primary aim was to model the PDAC tumour tissue mechanics and to investigate the role of the PDAC tumour mechanics in therapeutic resistance, PSCs were used in the culture model as they are the primary fibroblast and stromal cells central to the PDAC desmoplastic. PANC-1 cancer cell lines were used as a representative PDAC cancer cell line in the culture model. Figure 1.9 illustrates the mechanical stiffness assessment of the off-chip PDAC cultures

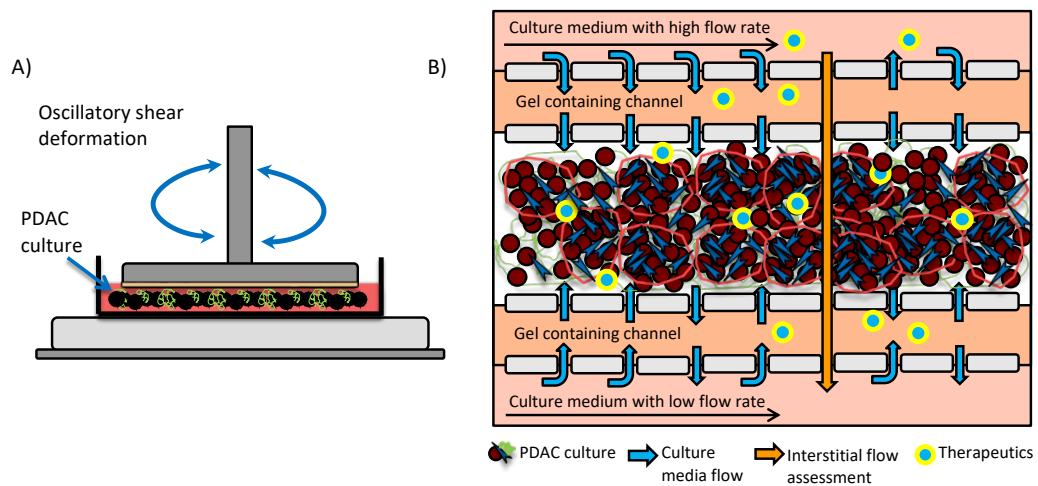


Figure 1.9. The off-chip and on-chip PDAC culture assessments

A) Oscillatory shear deformation of the off-chip PDAC cultures to assess their mechanical stiffness, and B) the on-chip PDAC cultures with the interstitial flow and therapeutic assessment (gemcitabine, microbubbles, and ultrasound treatment together).

with oscillatory shear deformation and the interstitial flow and therapeutic assessments of the on-chip PDAC cultures.

Based on these assessments, this thesis is structured as follows:

- Chapter 1 presented an overview of PDAC and its tumour microenvironment. Different techniques used to assess the mechanical stiffness of cells and tissues, the different culture models of PDAC, and the therapeutic measures against PDAC, were discussed.
- Chapter 2 describes the theoretical background underlying the use of oscillatory shear rheology to investigate mechanical stiffness, the assessment of the interstitial flow nature of the on-chip PDAC cultures, the use of microfluidics for cell culture, and the stability and production of microbubbles.
- Chapter 3 presents the experimental procedures, the materials and techniques used for the mechanical characterisation of the off-chip PDAC cultures, the development of the microfluidic device and the on-chip PDAC culture set-up, the therapeutic assessment of the cultures, and data acquisition and analyses.
- Chapter 4 presents results on the off-chip PDAC culture. The growth and mechanical properties of the cultures and the effect of gemcitabine only treatment.

- Chapter 5 describes and presents the microfluidic device, the on-chip PDAC culture, and the interstitial flow assessment as the culture develops mechanically.
- Chapter 6 presents results on the therapeutic assessment of the on-chip PDAC culture with gemcitabine, microbubbles, and ultrasound together.
- Chapter 7 summarises the main findings presented in this thesis, providing an outlook for future studies toward improving PDAC treatment outcomes.

2. Theoretical Background

This chapter contains the theoretical background on the use of oscillatory shear rheology to investigate the mechanical stiffness of the PDAC cultures, the assessment of the interstitial flow nature of the on-chip PDAC cultures, the use of microfluidics for cell culture, and the stability and production of microbubbles.

2.1. Assessing mechanical stiffness with oscillatory shear rheology

Mechanical stiffness is the extent to which a sample can resist mechanical deformation, with commonly used techniques described in section 1.3.^[83, 94, 231] The response to deformation can be elastic (*e.g.* as with steel) or inelastic (*e.g.* as with a rubber band), and it is expressed as a modulus. The modulus is the ratio between the stress and strain measurement of a sample, informing of a sample's degree of elasticity, the maximal force required to distort the sample. The modulus is expressed mathematically as

$$\text{Modulus} = \frac{\sigma}{\gamma} \quad (1)$$

where σ is stress (Pa), which describes the magnitude of the force per unit area during deformation, and γ is strain (dimensionless), which describes the extent to which a sample deforms under the force applied. The unit of modulus is Pascals (Pa; or N m^{-2}).^[46, 94, 231]

With shear deformation, the extensional stress is applied perpendicular to the direction of strain. Shear oscillatory rheology is an ideal technique to probe the mechanical behaviour of biological systems such as tissues, as such systems are often viscoelastic. Ideal solid materials are perfectly elastic, *i.e.*, returning all energy input once the applied deformation is removed. In contrast, ideal viscous materials are perfectly inelastic, *i.e.*, returns none of the input energy once the applied deformation is removed. However, viscoelastic materials, such as biological systems, are neither purely elastic nor purely viscous exhibiting cells, ECM, and structural proteins, which have elastic and viscous behaviours.^[54, 93, 94, 232] In shear rheology, the elastic and inelastic components of materials mechanics can be investigated by considering the phase lag of the strain compared to applied sinusoidal shear stress (Figure 2.1). If the material was ideally elastic, then the sample strain and stress would be proportional and always in phase ($\delta = 0$). The modulus would be defined by its elastic behaviour (storage modulus). If the material was ideally viscous, then the sample's strain would be proportional to the rate of stress

deformation and out of phase ($\delta = \pi/2$). Its modulus then would be defined by its viscous behaviour (loss modulus). For viscoelastic materials, the strain response would be both in phase and out of phase due to its elastic and viscous components. The strain response would be in a phase shift to the stress deformation ($0 < \delta < \pi/2$), and the modulus of the viscoelastic material would be defined by the complex sum of both its elastic and viscous moduli components.^[46, 93, 94, 231]

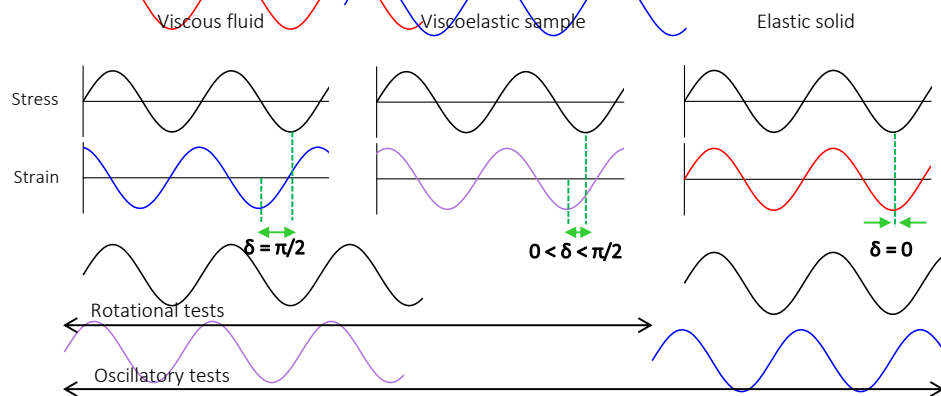


Figure 2.1. The sinusoidal strain response to shear deformation

The measured strain to oscillatory shear stress for a viscous, viscoelastic, and elastic samples. The strain response of a viscous fluid moves out of phase by 90° ($\delta = \pi/2$) to applied shear stress. Viscoelastic samples are, however, in phase with an applied shear stress either by less than 45° ($\delta < \pi/2$) for a solid-like sample or by more than 45° ($\delta > \pi/2$) for a liquid-like sample. An elastic solid is in phase ($\delta = 0$) with the movement of the applied shear stress. Depending on how viscous or elastic a sample is, a rotational or oscillatory test can be used to determine the sample's shear deformation. Adapted from [93].

All units in Pascals (Pa), G' is the storage or elastic modulus, which is the energy stored by the sample from a change in geometry under shear deformation, recoverable when the deformation is removed, and G'' is the loss or viscous modulus (G'') which is the energy lost or used when the sample is recovering into its original geometry.^[46, 93, 94, 231] The storage and loss moduli are respectively represented mathematically as

$$G' = \frac{\sigma}{\gamma} \times \cos \delta \quad (2)$$

$$G'' = \frac{\sigma}{\gamma} \times \cos \left(\delta - \frac{\pi}{2} \right) = \frac{\sigma}{\gamma} \times \sin \delta \quad (3)$$

The complex shear modulus (G^*) is the complex sum of the storage and loss moduli measurements.^[83, 93, 94, 231] It is represented mathematically as

$$G^* = G' + iG'' \quad (4)$$

In this work the complex shear modulus was used as a measure of the stiffness of the *in vitro* PDAC cultures. The Elastic Young's modulus informs of the maximal force required to deform a sample with tensile or compressive stress, *i.e.*, extensional stress applied parallel to the strain. Using the AFM, tensile and compressive stress, has been previously used to investigate the mechanical properties of pancreatic tissues.^[21] In this work, shear oscillatory rheology is used to probe the mechanical characteristics of *in vitro* PDAC cultures.^[89] The extracted shear moduli from the rheological characterisations can be compared to previously measured Elastic Young's modulus using the relation outlined in *Equation 2*,

$$E = 2G^* (1 + \nu) \quad (5)$$

where E is the Elastic Young's modulus (Pa), G^* is the complex shear modulus (Pa), and ν is the Poisson ratio. The Poisson ratio is approximated as 0.5 for hydrogels due to their volume expansion under compression. The Poisson ratio is the measure of the expansion of a material in directions perpendicular to the force applied.^[90, 233, 234]

2.2. Assessing interstitial flow with hydraulic conductivity

Interstitial fluid flow can be measured by assessing the hydraulic conductivity of the interstitial space in a matrix environment to fluid flow.^[19, 43, 63, 64, 235] The interstitial space is the fluid-filled areas surrounding cells composed of a fluid phase of water, electrolytes, and nutrients, and the ECM, which is made up of a network of fibrillar proteins, glycoproteins, and glycosaminoglycans. As the ECM influences the architecture of the interstitial space, it governs interstitial fluid flow.^[236-239] The interstitial flow is the ease at which fluid moves through the matrix environment. It is an important mechanism for transporting nutrients and removing waste from cells.^[19, 43, 203, 238]

The accumulation and properties of the different ECM components result in a dense and tortuous matrix network that limits the conductivity of interstitial fluid flow. For example, cross-linkage of fibrillar collagens builds a scaffold, which reduces the size of the porous structure of the matrix and hence restricts the diffusion of fluids through the matrix. While glycosaminoglycans, which have the propensity to trap fluid and swell, increase interstitial tissue pressure and reduce the space for fluid flow.^[44, 59, 236-238, 240]

In vitro, the hydraulic conductivity can be assessed by measuring the rate of fluid extrusion per unit pressure drop across a unit area of a porous fibrous sample of unit thickness.^[237, 238, 240] The hydraulic conductivity (*Equation 7*) can be defined from Darcy's law (*Equation 6*) for low Reynolds number flow through a porous fibrous medium.^[19, 235-238, 240]

$$Q = \frac{K \times A \times \Delta P}{L \times \eta} \quad (6)$$

$$K' = \frac{K}{\eta} = \frac{Q}{(A/L) \times \Delta P} \quad (7)$$

where Q is the volumetric flow rate of the fluid ($\text{m}^3 \text{s}^{-1}$), K is the hydraulic conductivity ($\text{m}^2 \text{s}^{-1} \text{Pa}^{-1}$) of a porous medium, A is the cross-sectional area (m^2) of the porous medium, L is the distance (m) of fluid flow, η is the dynamic viscosity (Pa.s) of the fluid, and ΔP is the pressure-gradient (Pa) driving the hydraulic flow through the porous medium.

The hydraulic conductivity depends on the intrinsic permeability of the porous medium. The intrinsic permeability, specific hydraulic conductivity, or Darcy's permeability (K in m^2) is the property of the porous medium. It defines the capacity and ability of the porous medium to conduct fluids. It can be determined from *Equation 6* or *7* as

$$K = \frac{Q \times \eta}{(A/L) \Delta P} \quad (8)$$

With the hydraulic conductivity, the interstitial fluid velocity (*Equation 9*) can also be determined by applying Darcy's law.^[19, 43, 235]

$$IF_v = -K \times \nabla P \quad (9)$$

where IF_v is the interstitial fluid velocity ($\mu\text{m s}^{-1}$), K is the hydraulic conductivity ($\text{m}^2 \text{s}^{-1} \text{Pa}^{-1}$) of a porous medium, and ∇P (or ΔP in *Equations 6 - 8*) is the pressure-gradient (Pa) driving fluid flow through the porous medium. The higher the hydraulic conductivity, the higher the interstitial fluid velocity through the interstitial space and *vice versa*.

In the fibrotic tumour tissue, as illustrated in Figure 1.4, increasing IFP leads to decreasing interstitial fluid flow and fluid flows from the tumour into the tumour periphery and neighbouring tissues. This promotes the metastasis and invasion of cancer cells. Moreover, a reduced hydraulic conductivity or interstitial flow in the tumour tissue means low shear stress across the tumour tissue, increasing the tumourigenic activity of cancer cells and stromal cells.^[17, 43, 44, 62-64, 97] Low shear stress increases the activity and motility of stromal cells (*i.e.*,

fibroblasts), which are responsible for the production and structure of the ECM.^[16, 17, 43, 48, 64, 241, 242] In this work, the hydraulic conductivity of the on-chip PDAC culture was investigated with the flow of fluorescein in culture media solution. This was to determine whether the on-chip PDAC cultures reflected the reduced interstitial flow of the tumour tissue, resulting from a fibrotic stroma and increasing mechanical stiffness, compared to the healthy pancreatic tissue.

2.3. Microfluidic cell culture

There is the initial complexity of designing channels optimal and operational for culture, with the culture set-up, fluid control and analysis challenging at times. Nonetheless, microfluidics has transformed how healthy and disease tissues can be modelled and studied in 3D to recapitulate the *in vivo* microenvironment and investigate biological, chemical, and physical mechanisms.^[149, 164, 243-248] This section gives an overview of the use of polydimethylsiloxane (PDMS) in making devices and the equations governing the nature of fluid flow in microfluidic devices and which must be taken into account when designing devices.

2.3.1. PDMS based microfluidic devices

To fabricate microfluidic devices, a silicon master mould with a photoresist pattern of microchannels based on a computer-aided design (CAD) is made using ultraviolet (UV) light. This process is referred to as photolithography. Then, elastomeric techniques or soft lithography of polydimethylsiloxane (PDMS) is used to mould numerous replicas of the microchannel patterns into a solid substrate.^[131, 133, 149, 151, 153, 158, 159] Section 3.7.2 describes the photolithography and soft lithography process in more detail. Figure 3.6 illustrates the photolithography and soft lithography process.

Silicon and glass materials were used in the development of early microfluidic devices. However, silicon and glass-based microfluidic devices are expensive and brittle to fabricate and handle for cell culture.^[133, 149, 150, 153, 159] The ease of handling and performing biological experiments must be considered when designing and fabricating microfluidic devices for cell culture. First used by Whitesides in 1988, PDMS-based microfluidic devices have become a widely used material for moulding patterns of intricate microchannels for cell culture.^{[149, 150,}

^{159, 249]} PDMS-based microfluidic devices are cheap and easy to set up, and PDMS is an optically transparent gas permeable elastomer material, which is good for cell culture.

The optical transparency of PDMS allows for imaging cell cultures at high resolution, and the gas permeable feature of PDMS permits gaseous exchange for cell culture. However, PDMS is a hydrophobic material, and its porosity results in the absorption of lipids and small molecules and the evaporation of reagents.^[133, 149, 150, 153, 159, 249-251] Nonetheless, PDMS is used for microfluidic cell cultures due to its biocompatibility. To reduce any effects of absorption and the evaporation of reagents, culture media reservoirs can be used, and cultures can be placed in an environment with high humidity, such as a cell culture incubator.^[149, 251, 252] With media reservoirs, there is continuous or perfusion culture, but stable flow velocities are needed to avoid high shear stress, which affects the viability of cells.

2.3.2. Reynolds number

Determining and knowing the fluid flow regime in microfluidic channels is important for viable cell cultures.^[249, 252-257] The fluid flow regime is governed by Navier-Stoke equation^[258]

$$\overset{Mass}{\tilde{\rho}} \cdot \overbrace{\left(\frac{\partial \mathbf{v}}{\partial t} + \mathbf{v} \times \nabla \mathbf{v}\right)}^{Acceleration} = \overbrace{\rho \mathbf{g} - \nabla p + \eta \nabla^2 \mathbf{v}}^{Force} \quad (10)$$

where ρ is the fluid density for the mass component, the acceleration component looks at \mathbf{v} , the fluid velocity, over time, and the force component takes into account any gravity and electromagnetic effect, pressure gradient, and the viscous effect of fluid with η being the dynamic fluid viscosity. Here, the equation denotes for an incompressible, Newtonian fluid.

Due to Poiseuille flows in microfluidic channels, *Equation 10* can be written as

$$\nabla p = \eta \nabla^2 \mathbf{v} \quad (11)$$

where p is the pressure driving fluid flow, η is the dynamic fluid viscosity (Pa.s), and \mathbf{v} is the velocity (m s⁻¹) of the fluid flow. The flow of fluids in microfluidic channels is assumed to be in the laminar flow regime, which is determined with the measure of the Reynolds number.

The Reynolds number is a dimensionless number that defines the ratio of inertial forces to viscous forces to determine the fluid flow regime.^[249, 254-256, 259] Reynolds number is defined by

the length of a channel in which fluid travels, the velocity at which the fluid travels, and the density and dynamic fluid viscosity. It is calculated as

$$Re = \frac{\text{inertial forces}}{\text{viscous forces}} = \frac{\rho \times V \times D}{\eta} \quad (12)$$

where Re is the dimensionless Reynolds number, ρ is the fluid density in kg m^{-3} , V is the fluid linear velocity (m s^{-1}), D is the hydraulic diameter in meters for a rectangular pipe channel, and η is the dynamic fluid viscosity (Pa.s).

The hydraulic diameter, D , is calculated as

$$D = \frac{4A}{P} = \frac{2 \times w \times h}{w + h} \quad (13)$$

where A is the cross sectional area of the microfluidic channel, P is the wetted perimeter of the channel, and w and h are the channel width and height in metres, respectively.

For a laminar flow regime, where the Reynolds number is < 2000 , there is a streamline or steady flow of fluid particles with dominant viscous forces and negligible inertial forces. For microfluidic cell culture, the laminar flow regime is required as this offers the fine control of fluids to be able to have the physiological flow conditions, *i.e.*, fluid flow pressures and shear stress, representative of the *in vivo* tissue. Where the Reynolds number is > 4000 , there is irregular movement of fluid particles with high fluid velocity and dominant inertial forces over viscous forces. This is referred to as turbulent flow. When the Reynolds number is in range of $2000 - 4000$, flow is defined as in the transitional flow regime, as flow is unstable with an onset of turbulence.^[249, 254-256]

2.3.3. Hydraulic flow resistance

Determining the flow regime in a microfluidic channel is important to ensure viable cell culture. Moreover, the flow resistance, and pressure drop in channels, must be considered when designing microfluidic devices to achieve a desirable flow rate for culture.^[256, 258, 259] They can be defined mathematically as

$$\Delta P = QR_{hyd} \quad (14)$$

Where ΔP is the pressure drop (Pa) across a microfluidic channel, Q is the volumetric flow rate ($\text{m}^3 \text{s}^{-1}$) in the device, and R_{hyd} is the hydraulic resistance (Pa.s m^{-3}).

The volumetric flow rate is the volume of fluid which passes through a surface per unit time. As it remains constant throughout the device, irrespective of channel dimensions, it is commonly used rather than the linear velocity (m s^{-1}) when calculating and describing flow rate in devices, and it is given by

$$Q = \text{linear velocity} \times \text{channel cross sectional area} \quad (15)$$

ΔP is proportional to Q , and R_{hyd} can be defined as the proportional coefficient. Therefore, R_{hyd} quantifies the hydraulic pressures along microfluidic channels and can be used to describe and understand the effects of channel dimensions on flow conditions when designing a device.

The flow hydraulic resistance for a rectangular microfluidic channel is given by ^[258]

$$R_{hyd} = \frac{12 \times \eta \times L}{w \times h^3} \cdot \frac{1}{1 - 0.63 \frac{h}{w}} \quad (16)$$

where R_{hyd} is the hydraulic resistance for a rectangular channel in Pa.s m^{-3} , η is the fluid dynamic viscosity (Pa.s), L , h , and w are the length, height and width of a rectangular channel in metres, respectively.

2.4. Microbubble stability and production

Illustrated in Figure 1.8, microbubbles are gas-filled bubbles stabilised by a phospholipid shell. The first class of microbubble agents produced, to resolve the stability of air-filled bubbles in an electrolyte solution, had a relatively rigid shell corresponding to a decrease in the scattering of acoustic waves for ultrasound imaging. This led to the development of microbubble ultrasound contrast agents with a phospholipid shell.^[217, 260] The phospholipid shell, encapsulating the gas core, forms a resistive barrier against the diffusion of the gas from inside to outside of the microbubble. This eliminates interfacial tension, offering bubbles a stabilised gas core against Laplace pressure-driven dissolution.^[217, 260] The Young-Laplace equation describes the equilibrium pressure difference between the inside and outside of a surface interface and is given by ^[261]

$$\Delta P (P_i - P_o) = \gamma \frac{2}{R} \quad (17)$$

where ΔP is Laplace pressure, the pressure difference between the inside (P_i) and outside (P_o) of the bubble, which is governed by the interfacial surface tension (γ) at the lipid shell, and R is the radius of the microbubble.

The decreased interfacial tension and improved microbubble stability are enhanced with high molecular weight and low water-soluble perfluorocarbon gas core, which leads to increased microbubble elimination half-life, and, thus, duration of contrast imaging.^[215, 217, 260, 262, 263]

The effectiveness of microbubbles as contrast agents is due to the acoustic impedance mismatch between the microbubbles and the surrounding liquid.^[215, 260, 262, 264, 265] As microbubbles resonate, oscillating volumetrically, their gas cores contract and expand in response to the pressure changes of the acoustic waves. This results in the effective scattering of acoustic waves, which enhances contrast during ultrasound imaging. For therapeutics, as illustrated in Figure 1.8C, the volumetric oscillation of the microbubbles sensitises cell membranes to influence the transport and uptake of drugs. Clinically, with a diameter ranging between 8 – 10 μm for capillaries, it is vital microbubbles are less than 10 μm in diameter to avoid embolism. Moreover, a diameter of less than 10 μm allows microbubbles to pulsate at their natural frequency with resonance frequencies between 1 – 10 MHz, the typical frequency range used in diagnostic ultrasound.^[211, 260, 262, 266]

Microbubbles are commonly made with the dispersion of a perfluorocarbon or a sulphur hexafluoride gas core into a phospholipid suspension under high shear mixing.^[208, 211, 260, 262, 263] Microbubbles can be produced using mechanical agitation or with microfluidics. Mechanical agitation is the conventional approach of making microbubbles. The process requires a solution of phospholipid to be placed in a vial, and the remaining head space of the vial is then filled with a low soluble gas for the microbubble gas core. The vial is then placed in a mechanical agitator for microbubble production. Although the microbubble concentration can be approximately $10^9 - 10^{10}$ bubbles per mL,^[267-269] there is poor control on the microbubble size. The mechanical agitation approach results in a heterogeneously sized microbubble population, where a majority of microbubbles are close to 10 μm in diameter, which can cause embolisms.^[267, 268, 270] The use of microfluidics for the formation of microbubbles offers the advantage of control over microbubble size.

In this project, microbubbles are formed with a phospholipid mixture and perfluorocarbon gas using a multiplexed microfluidic device. The multiplexed microfluidic device allows for the rapid production of homogeneously sized microbubbles in comparison to mechanical agitation.^[268] With a microbubble concentration of $\sim 10^{10}$ bubbles per mL, a majority of the microbubbles formed with the multiplexed device were $< 3 \mu\text{m}$. Section 3.11.3 describes the formation of microbubble using the multiplexed device in more detail. Figure 3.9 illustrates the CAD of the device used for microbubble formation.

3. Experimental Section

The experimental procedures described below were carried out in the research laboratories of the School of Physics and Astronomy, University of Leeds. Where specified, the experiments were carried out at the Medicines Discovery Catapult (MDC).

3.1. Cell lines and 2D culture

The human pancreatic epithelial ductal adenocarcinoma cell line, PANC-1 (ECACC 87092802)^[7], was acquired from Sigma-Aldrich supplied by the European Collection of Authenticated Cell Cultures (ECACC). The PANC-1 cells were maintained in Dulbecco's Modified Eagle Medium (DMEM; Thermo Fisher Scientific) with 10 % foetal bovine serum (FBS; Sigma-Aldrich) supplemented with 1 % Penicillin Streptomycin (P/S; Sigma-Aldrich) and 1 % GlutaMAX Supplement (Thermo Fisher Scientific), which will be referred to as DMEM/10 % FBS culture medium.

The human pancreatic stellate cells (HPaSteC or PSCs) and respective culture reagents and supplements were acquired from ScienCell™ Research Laboratories supplied by Caltag Medsystems Ltd. The PSCs were maintained and expanded in Stellate Cell Medium (SteCM) with 10 % FBS supplemented with 1 % of Stellate Cell Growth Supplement and 1 % P/S, which will be referred to as SteCM/10 % FBS culture medium.

The PANC-1 and PSC cells were cultured with their respective culture media, DMEM/10 % FBS or SteCM/10 % FBS, in either a 25 or 75 cm² culture flask under humidified conditions (95 – 99%) at 37°C with 5 % CO₂. The cells were passaged from culture with 1 mL TrypLE Express Enzyme (1 ×) no phenol red (Thermo Fisher Scientific) and used once ≥ 70 % cell confluence was achieved. For the PSCs, the culture flasks were coated with poly-l-lysine (ScienCell™ Research Laboratories) incubated at 37°C for at least 1 hour, and passages between 2 and 6 were used in the cultures.

For mycoplasma testing, a pellet of 1×10^6 cells mL⁻¹ PANC-1 and PSC cells were prepared in 1 mL Dulbecco's phosphate-buffered saline (DPBS; Thermo Fisher Scientific) by centrifugation at 13,000 r.p.m at room temperature for 5 minutes and sent to MDC for PCR testing. For cryopreservation of the cells, 1×10^6 cells mL⁻¹ of the PANC-1 and PSC cells were prepared in their respective culture media, supplemented with 10 % dimethyl sulfoxide (DMSO; Sigma-

Aldrich), and dispensed into cryovials for storage in cryogenic storage dewars. All cell count were performed by preparing 40 μL of Trypan Blue-treated cell suspension and applying 20 μL to a haemocytometer.

3.2. Optical microscopy

Images of cultured PANC-1 and PSC cells, off-chip with the ULA plates and in culture dishes with BME gel and on-chip with microfluidic devices, were taken with bright-field, and confocal and epifluorescence microscopy. At MDC, the PANC-1 and PSC cells were labelled and co-cultured for live cell imaging using the IncuCyte[®] S3 Live-Cell Analysis System (Sartorius, Essen BioScience). Below are details of the use of the different microscopy systems to image the PANC-1 and PSCs in culture. All acquired images and videos were analysed with ImageJ. Figure 3.1 illustrates how the bright-field, epifluorescence, and confocal microscopy works.

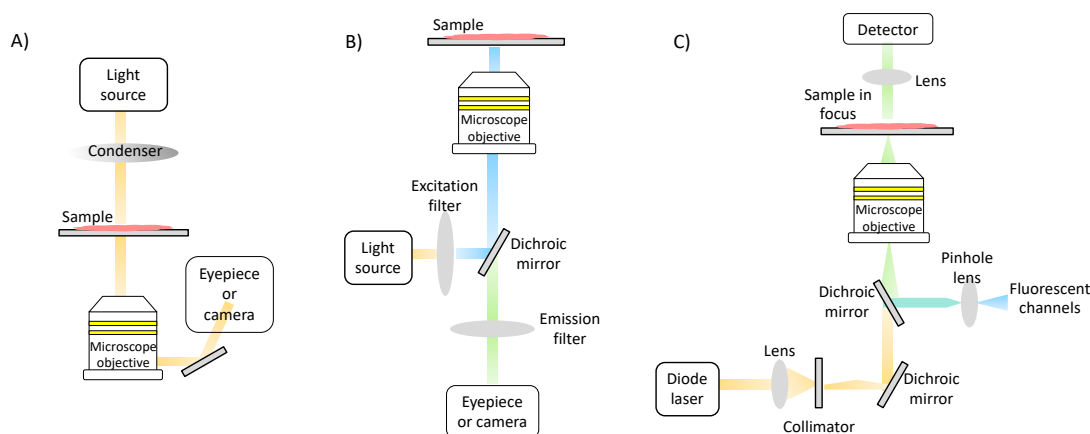


Figure 3.1. Function of the bright-field and fluorescence microscopy

The performance of A) a bright-field microscope, B) an epifluorescence microscope, and C) a confocal microscope, where pinhole lens system allows for high spatial resolution and imaging contrast.

3.2.1. Bright-field microscopy

An inverted phase contrast microscope (VWR VisiScope[®] IT404) with 4 \times and 10 \times objectives was used to image and monitor the growth of the PANC-1 and PSC cells in culture.

Bright-field microscopy is the simplest, standard optical microscopy to illuminate samples. As illustrated in Figure 3.1A, the illumination source travels through a condenser to the sample.

The contrast in bright-field is generally low, and it is caused by a reduction in the amount of light transmitted through dense areas of samples. The transmitted light travels through an objective lens to the eyepiece/camera to view sample images.

The PANC-1 and PSC cells were maintained and expanded in culture flasks. The cells were harvested once they were $\geq 70\%$ confluent and seeded for 3D culture using ultra-low attachment (ULA) plates, culture dishes with basement membrane extract (BME) gel, and microfluidic devices. Sections 3.4 and 3.8 describe the seeding and culturing procedures using these platforms.

3.2.2. Epifluorescence microscopy

Epifluorescence microscopy, with an upright and inverted microscope (Ti-U and E600, Nikon, Tokyo, Japan), were used to evaluate fluid flow through the on-chip PDAC (co-culture of the PANC-1 and PSC cells) cultures and to characterise microbubble size and population, as described in section 3.10 and section 3.11.3, respectively. Epifluorescence microscope permits simple fluorescence imaging. As shown in Figure 3.1B, the incident light from a lamp is focused through an excitation filter, and the excitation wavelength of interest is permitted and reflected by a dichromatic mirror onto the sample. Fluorescent dye in the sample fluoresces, passing through the emission filter to illuminate the area of interest.^[271-274] Images and videos of the on-chip cultures with the microscope were taken with a 4 × objective, FITC setting, an autogain of 1.00, and exposure between 600 ms – 1 s.

3.2.3. Confocal microscopy

An inverted confocal laser scanning microscopy system (SP8, Leica Microsystems GmbH, Wetzlar, Germany) was used for high-resolution fluorescence microscopy of the off- and on-chip PDAC cultures (seeding of the cells for the cultures is described in sections 3.4 and 3.8, respectively) following incubation with fluorescent dyes. Figure 3.1C shows a schematic of the optics of the confocal microscope. The confocal microscope uses a pinhole system in the optical pathway to focus laser light onto a defined region of interest in the sample at a specific depth. The pinhole system excludes light from the focal plane, eliminating background fluorescence. As a result, only the fluorescence signals from the illuminated region of interest enter the light detector. As the pinhole allows images from one focal plane to be captured,

images of different focal planes can be captured and rendered into a 3D map of the sample.^[271, 272, 274-276]

The Leica confocal fluorescence microscope used was equipped with 405 nm, 488 nm, 552 nm, and 638 lasers. Following incubation of the PDAC cultures with fluorescent dyes, the cultures were imaged with the confocal microscope using a 10 × objective and pinhole of 1.00 AU. Assessing the flow of ATTO 488 microbubbles through the on-chip PDAC cultures (described in section 3.11.4), time-lapse series were taken with a 30-second interval for an average of 250 frames. The fluorophores used in imaging the cultures with the fluorescence dyes and microbubbles were Hoechst 33324 and DAPI, Calcein AM, Propidium iodide, ATTO 488, and Alexa Fluor 488 and Alexa Fluor 647.

3.2.4. Live cell imaging with the IncuCyte® live-cell analysis system

Live cell imaging of the off-chip PANC-1 only, PSC only and PDAC cultures, and on-chip PDAC cultures, was done using the IncuCyte® S3 Live-Cell Analysis System at MDC. With IncuCyte live cell analysis, viable cultures of the PANC-1 and PSC cells were measured *in situ* in a physiologically relevant environment (37°C with 5 % CO₂ and 90 – 99 % humidity) inside an incubator with bright-field and fluorescent channels. The IncuCyte live cell analysis enabled continuous analysis of the growth, aggregation of the cells into 3D, and the cellular interactions between the PANC-1 and PSC cells in co-culture.

Labelled (described in section 3.3) and unlabelled PANC-1 and PSC cells were seeded into 96-well standard culture plates, 96-well ULA plates (described in section 3.4.1), and 5-channel microfluidic devices (described in section 3.8) and placed into the IncuCyte system for bright-field and fluorescence imaging with a 10 × objective. For the on-chip culture using the 5-channel microfluidic devices (Figure 3.5B illustrates a CAD schematic of the device), imaging was performed with a 4 × objective using a Corning® 12-well culture plate setting.

3.3. Cell labelling with Qtracker™ 585 cell labelling kit

The PANC-1 cells were labelled with Qtracker® 585 Cell Labelling Kit (Thermo Fisher Scientific) for live-cell imaging with the IncuCyte system (as described in section 3.2.4). The cells were labelled to investigate cell behaviour and interactions between the PANC-1 and PSC cells in

co-culture. The Qtrackers are designed to load cultured cells with highly fluorescent quantum dot nanocrystals for intense, stable fluorescence labelling for long-term imaging.^[277, 278]

As per the manufacturer's instruction, the protocol for using the Qtracker labelling kit was optimised to use with the PANC-1 cells. Qtracker labelling solution was prepared by mixing equal volumes (1 μL) of the Qtracker nanocrystals with the Qtracker carrier. The pre-mix solution was incubated for 5 minutes at room temperature. 200 μL of DMEM/10 % FBS was added to the pre-mix solution, and the solution was vortexed for 30 seconds. PANC-1 cells at a concentration of 1×10^6 cells mL^{-1} were harvested and incubated with the Qtracker labelling solution for 1 hour at 37°C. After incubation, the cells were washed twice with culture medium. The labelled PANC-1 cells were seeded with PSC cells in a 1: 3 seeding ratio into the 96-well plate, ULA plate, and the 5-channel microfluidic device for culture and imaging with the IncuCyte system.

3.4. Off-chip PDAC cultures

Once the PANC-1 and PSC cells, maintained and expanded in culture flasks, were ≥ 70 % confluent, the cells were harvested for spheroid culture. The cells were seeded into Corning® 96-well clear round bottom ULA plates (Costar 7007s; Scientific Laboratory Supplies) for spheroid culture in suspension. Or, seeded into 21.5 cm^2 Nunclon Delta surface treated cell culture Petri dishes (Thermo Fisher Scientific) with 6 – 9 mg mL^{-1} of Cultrex® Basement Membrane Extract (BME) gel (R&D Systems, Bio-Techne) for spheroid culture with a hydrogel.

Figure 3.2A illustrates the seeding of the cells into the ULA plates. The wells of the ULA plates are covalently coated with a non-ionic, neutrally charged hydrogel making the surface hydrophilic. This enhances cell-cell interactions over cell-substrate interactions for spheroid formation and culture. Figure 3.2B illustrates the seeding of the cells into the culture plates with basement membrane extract (BME) gel. With a hydrogel, here the BME gel, spheroids are formed by natural aggregation closely mimicking the tumour microenvironment.

3.4.1. Off-chip PDAC cultures with ultra-low attachment plates

The PANC-1 and PSC cells were seeded into the ULA plates for PSC only, PANC-1 only and PDAC spheroid cultures at a seeding density of 250, 500, and 1000 cells per well.

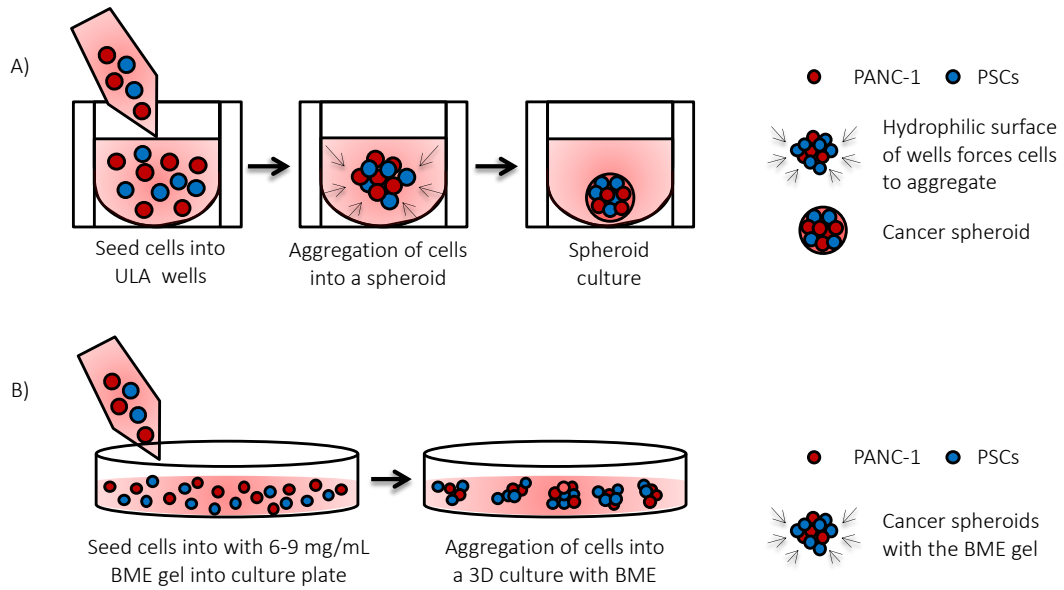


Figure 3.2. The off-chip PDAC culture set up and culture

A) The spheroid culture of the PANC-1 and PSC cells in ULA plates. The wells of the ULA plate are hydrophilic, forcing the cells to be in a suspended state and to aggregate into a spheroid. B) The spheroid culture of PANC-1 and PSC cells with a hydrogel. Cells are seeded with BME gel, and due to the ECM environment, the BME gel provides, the cells naturally aggregate into a 3D structure.

For the PDAC spheroid cultures, the PANC-1 and PSC cells were seeded together at a seeding density of 1:2 or 1:3 for biological relevance.^[165] The spheroids were cultured with DMEM/10 % FBS culture medium under humidified conditions at 37°C with 5 % CO₂. The culture medium was refreshed once a week by a half volume media change using the colour of the media as a guide to pH. Culture media was changed when its colour appeared orange-yellow.

Images were taken daily using the inverted microscope (VWR VisiScope® IT404), and the size in width (µm) and volume (mm³) of the spheroids were analysed using a MATLAB-based SpheroidSizer program^[279] to monitor their growth. Figure 3.3 shows an exemplar image of the use of the SpheroidSizer program to assess the size of the spheroids. The width and volume estimates were used in Equation 18 below to determine the growth and doubling time of the spheroids. Similar to determining the doubling time of single cells, the doubling time of the spheroids was defined as the time it takes for the spheroid size to double in volume.

$$\text{Doubling time} = \frac{\text{time} * \ln(2)}{\ln(\text{final volume}/\text{initial volume})} \quad (18)$$

where *time* was culture time in days, *final volume*, in mm³, was the spheroid volume at the end of culture, and *initial volume*, in mm³, was the volume 24 hours after seeding when the cells had aggregated into a spheroid.

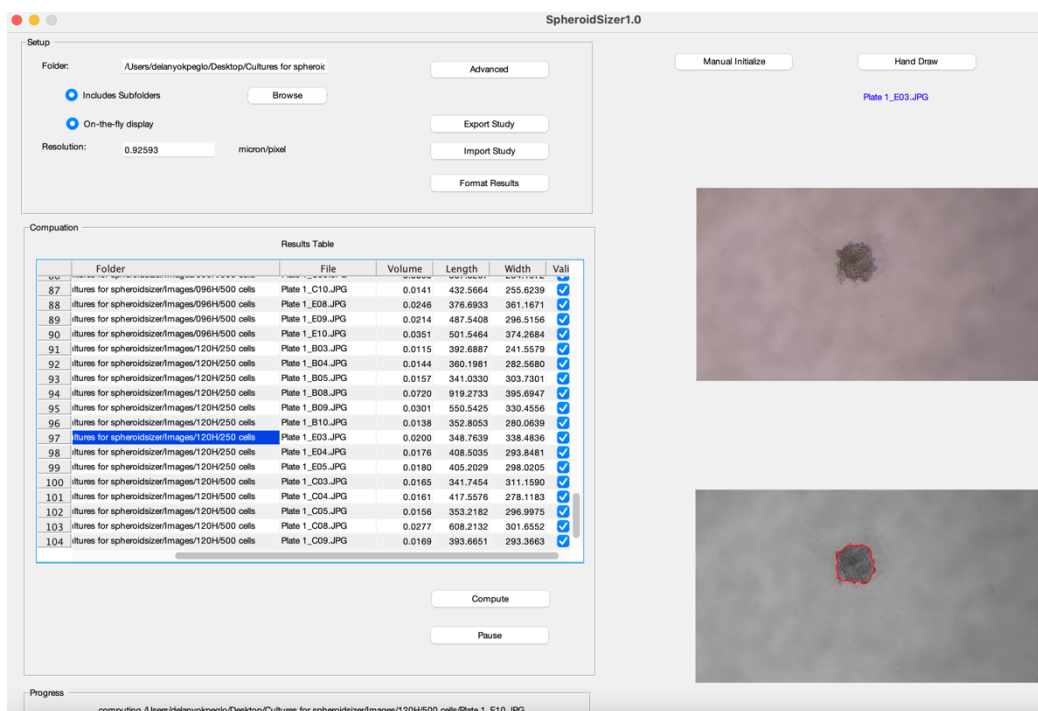


Figure 3.3. Exemplar image of the use of the SpheroidSizer program

Morphology and size assessment of the off-chip PDAC spheroids with the MATLAB based SpheroidSizer program.

3.4.2. Off-chip PDAC cultures with basement membrane gel

PANC-1 and PSC cells were seeded at a concentration of 1×10^6 cells mL^{-1} into cell culture dishes with 6 – 9 mg mL^{-1} of BME gel, which includes laminin and type IV collagen^[280], for PANC-1 only, PSC only and PDAC (PANC-1 and PSC co-culture in a 1: 3 seeding ratio) spheroid cultures with an ECM environment. The PANC-1 only, PSC only, and PDAC spheroid cultures with BME gel will be referred to as PANC-1 only, PSC only, and PDAC cultures, respectively. Matrigel or basement membrane extract was used for the 3D culturing of the cells as it is a commonly used hydrogel or scaffold for 3D cell culture, including pancreatic cancer cells.^[107, 146, 148, 281, 282] Basement membrane was chosen to allow the cells to naturally engineer an environment as opposed to a synthetic hydrogel, which often lacks the presence of structured proteins and fails to capture the biophysical structures and cues of the cellular microenvironment.^[283-285] With BME gel, collagen deposition from the cells as they naturally engineer their environment was monitored by staining for collagen as described in section 3.6.

The PANC-1 only, PSC only, and PDAC cultures were grown with 10 ng mL^{-1} of transforming growth factor beta (TGF- β 1) supplement^[286-288] in DMEM/10 %FBS culture medium under humidified conditions at 37°C with 5 % CO_2 for mechanical stiffness assessment. The cultures were maintained with TGF- β 1 to mimic the fibrotic stroma as the TGF- β 1 signalling pathway is reported to promote solid stress, increasing cell and tumour tissue stiffness.^[15-17, 22, 42, 43, 199, 289] TGF- β 1 was purchased from Sigma-Aldrich, mixed with 1 mL of sterile water and 2 mg mL^{-1} of bovine serum albumin (BSA; Sigma Aldrich), in phosphate-buffered saline (PBS) for a stock solution of $1 \text{ } \mu\text{g mL}^{-1}$. The TGF- β 1 solution was aliquoted into Eppendorfs (100 μL per Eppendorf) and stored at -20°C for use.

3.5. Mechanical stiffness assessment of the off-chip PDAC cultures

Oscillatory shear deformation was performed with an Anton Parr MCR 302 stress-controlled rheometer to assess the mechanical stiffness of the off-chip PANC-1 only and PDAC cultures (PANC-1 and PSC cell co-culture in a 1: 3 seeding ratio) with and without TGF- β 1 supplement (10 ng mL^{-1}). The seeding of the cells for culture is as described in section 3.4.2; Figure 3.2B.

Oscillatory shear rheology measures the elastic or storage (G') and viscous or loss (G'') moduli response exhibited by a sample in resisting a change in shape under oscillatory shear deformation (Figure 3.4A). With these measurements, the complex shear modulus (G^*), as shown in *Equation 4*, is used to determine their mechanical stiffness, the extent to which the sample resists deformation.^[89, 94]

Figure 3.4B shows a schematic of the rheometer set-up used to assess the mechanical stiffness of the cultures with oscillatory shear deformation. Replicate cultures of the PANC-1 only and PDAC cultures were grown for up to 45 days with and without TGF- β 1 supplement. For shear deformation assessment, the cultures were taken from the incubator and placed on the bottom plate of the rheometer. A 50 mm diameter parallel plate, with anti-slip material to prevent sample slippage on the surface^[89], was brought into contact with the cultures at a working gap of 0.8 mm. Pseudo-strain controlled shear deformation time sweeps were performed at a shear strain of 2 % and a frequency of 0.5 Hz for 600 seconds. As the gap was set to 0.8 mm, normal force was measured to ensure contact between the parallel plate and the culture samples. Frequency sweep measurements from 10 Hz to 0.1 Hz, with a constant shear strain of 2 %, were also performed to determine the long-term structural stability of the cultures under deformation.

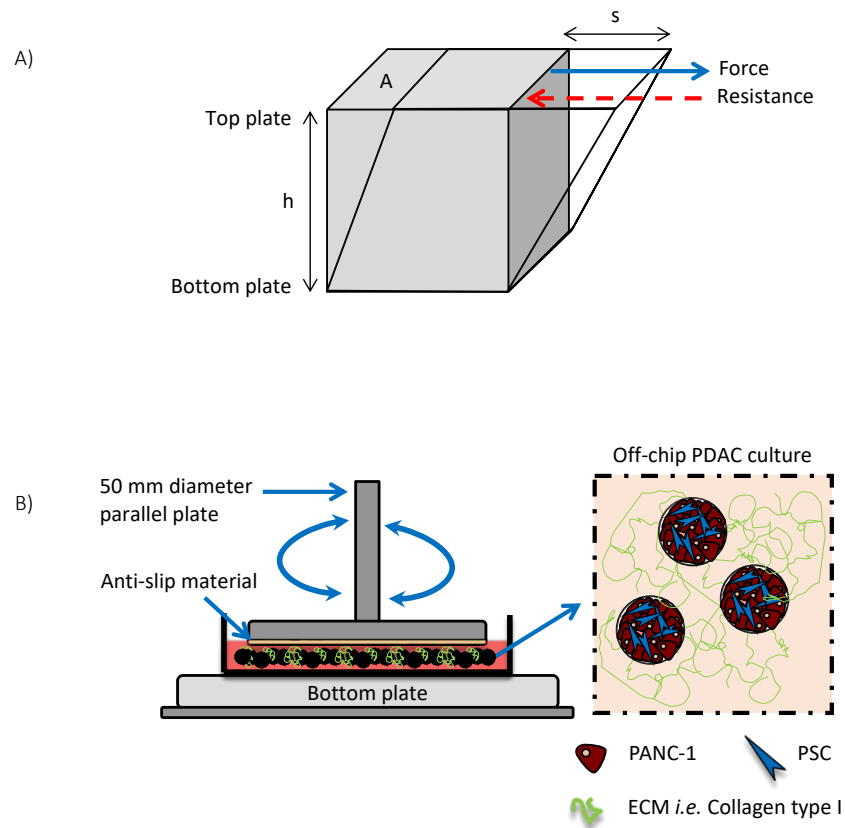


Figure 3.4. Oscillatory shear deformation of the off-chip PDAC cultures

A) Schematic of the shear deformation of a sample, where within a defined shear area (A) and a working gap height (h) between two shear plates, shear force is applied, and there is a change in shape (s) resisted by the sample. Data on the sample's resistance to change shape informs of the storage and loss moduli components to determine the sample's mechanical properties. B) A 50 mm parallel plate rotary system was used for the shear deformation of the PANC-1 only and PDAC cultures with and without TGF- β 1 supplement (10 ng mL^{-1}) to determine their storage (G') and loss (G'') moduli components, and their mechanical stiffness, G^* .

After shear deformation, the parallel plate geometry was released from contact with the cultures, and the G' and G'' for the different culture conditions, PANC-1 only with and without TGF- β 1 supplement, and PDAC with and without TGF- β 1 supplement, were determined by averaging their steady-state measurements over the measurement time (600 seconds) from the time sweep curves. The G' and G'' measurements for the different cultures were used in Equation 4 to determine their complex shear modulus, G^* .

Images were taken daily using the inverted microscope (VWR VisiScope® IT404) to assess the effects of the presence of PSC and TGF- β and determine if the measured mechanical stiffness was due to an increase in cell number, size, or increase in the number of spheroids. The Binary function in ImageJ was used to assess the effect of cell number, size, and or spheroid number on the measured mechanical stiffness of the cultures.

3.6. Immunostaining off-chip PDAC cultures for collagen and HIF-1 alpha

The PSC only, PANC-1 only, and PDAC cultures with and without TGF- β 1 supplement (seeding of the cells for culture is described in section 3.4.2. Figure 3.2B illustrates the cultures) were fixed with formaldehyde 4 % aqueous solution (VWR; kindly provided by Dr Zhang Y. Ong) in ibidi chambered tissue culture-treated slides (8-well chamber, removable; ibidi) for 30 minutes at room temperature, and permeabilised with 0.2 % Triton X-100 (Sigma Aldrich) in 1 % BSA (Sigma Aldrich), 5 % FBS (Sigma Aldrich) solution for 1 hour at room temperature. After incubation, the cultures were washed 2 \times with PBS for 5 minutes each time at room temperature on a shaker.

The cultures were then stained for collagen and HIF-1 alpha with recombinant anti-collagen 1 antibody (rabbit monoclonal [EPR22894-89] to collagen I) and recombinant anti-HIF-1 alpha antibody (rabbit monoclonal [EPR16897] to HIF-1 alpha), respectively, overnight at 4°C. The staining of collagen was to establish the deposition of ECM, where collagen type 1 is the most abundant, and HIF-1 alpha staining was to show a hypoxic environment in the cultures. HIF-1 alpha is central to the regulation of cellular adaptation to hypoxia. The primary antibodies, collagen and HIF-1 alpha, were prepared in 1 mL of PBS containing 1 % BSA at 1/250 and 1/500 dilution, respectively. As a control, replicate cultures were incubated with 1 mL of PBS containing 1 % BSA without the primary antibodies. After incubation with the primary antibodies, the cultures were washed 3 \times with PBS. Each time for 5 minutes at room temperature in the dark on a shaker.

Secondary antibody staining was performed with goat anti-rabbit Alexa Fluor™ 488 (ab150077) for 1 hour at room temperature in the dark on a shaker, together with phalloidin-iFluor 647 to stain for F-actin. The secondary antibody and actin stain were prepared in 1 mL of PBS containing 1 % BSA at 1/100 and 1/500 dilution, respectively. After incubation with the secondary antibody and actin, the cultures were washed 3 \times with PBS for 5 minutes each time at room temperature in the dark on a shaker.

The cultures were then incubated with 1 μ g mL⁻¹ DAPI solution for 5 – 15 minutes in the dark. After incubation, the cultures were washed 2 \times with PBS for 5 minutes each time at room temperature in the dark on a shaker. The primary and secondary antibodies, and actin stain, were all sourced from Abcam, UK. DAPI was sourced from Boster Biological Technology, USA.

The silicon gasket of the chamber slides was removed with tweezers. Coverslips (24 mm \times 60 mm microscope coverslips for chambers; ibidi) were prepared by washing with 70 % ethanol

and mounted with Histomount histology mounting media (National Diagnostics) onto the chamber slides with the cultures stained for collagen, HIF-1 alpha, actin, and nuclei, prior to imaging. Confocal microscopy was performed as described in section 3.2.3.

3.7. Microfluidic device design and fabrication

Figures 3.5A and 3.5B show a schematic of the computer-aided design (CAD) of the 3-channel and the 5-channel device used for the on-chip PDAC culture. A 3-channel device was initially used for the on-chip PDAC cultures and provided insight for the inclusion of gel-containing channels.^[11, 290] A 5-channel device was then used for an efficient 21-day culture of the PDAC cells (co-culture of the PANC-1 and PSC cells in a 1: 3 seeding ratio) for subsequent assessments. The 3-channel and 5-channel devices were designed using Autodesk's AutoCAD® software, and their layouts were edited with WieWeb's CleWin5 software for fabrication using photo and soft lithography.

3.7.1. Microfluidic device design

The 3-channel device (Figure 3.5A) consisted of a central culture chamber of 1 mm × 5 mm (w × L) and two 100 μm wide media channels for the supply of nutrients (or therapeutics) to the cells in the culture chamber. The 5-channel device (Figure 3.5B) also featured a central culture chamber of 1 mm × 6 mm (w × L) and two 100 μm wide media channels, and 275 μm wide gel-containing channels^[11, 19, 43, 290] between the culture chamber and media channels. Separating the channels for both the 3- and 5-channel devices were pillars (Figures 3.5C) of 80 μm × 40 μm (w × L), with a 5 μm interspace, for the perfusion of culture media into the culture chamber at a stable gradient by diffusion. The height of both the 3- and 5-channel devices was 100 μm.

The devices were designed for culture with media reservoirs at the inlet and outlet of the media channels. The media reservoirs, designed by Matthew Bourn, eliminated the issue of using a cumbersome syringe pump and tubing in a cell culture incubator to grow the PDAC cells on-chip.^[291] The media reservoirs also provided the advantage of culturing the cells under flow, which is representative of the physical environment of cells in tissues. Figure 3.5D shows a schematic of the on-chip culture with media reservoirs. Figure 3.5E shows a schematic of a media reservoir. The media reservoirs, fabricated with a 16 mm diameter Sustanat®

polycarbonate rod (Engineering & Design Plastics), were approximately 32 mm high with an inner diameter of 10 mm and a 2 mm wide spout at its bottom to allow the interface with the 2 mm wide inlet and outlet of the culture media channels. The lids of the media reservoirs were composed of a Delrin (Par-group) ring with a 0.22 μm polytetrafluoroethylene (PTFE) filter for sterile culture.

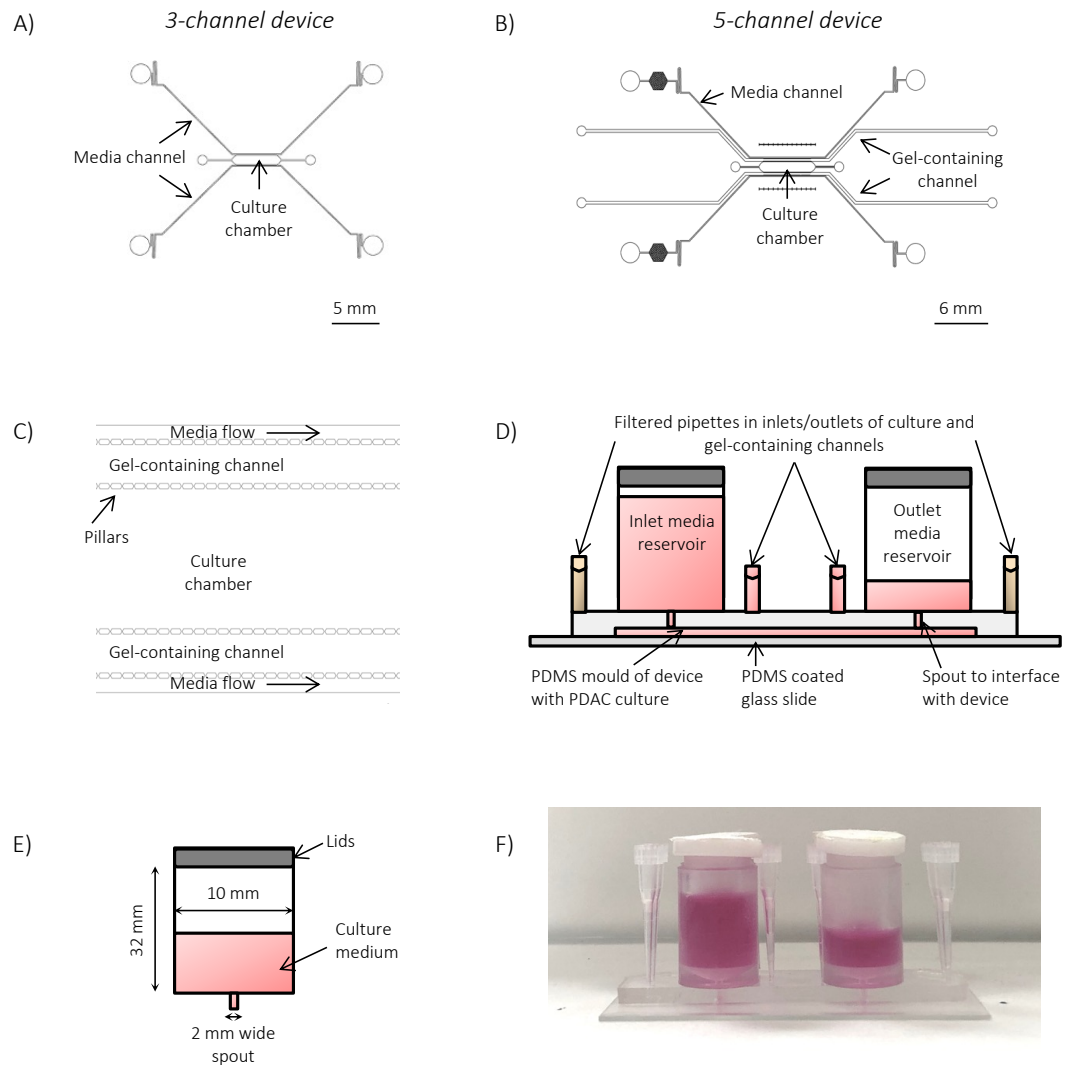


Figure 3.5. CAD of the microfluidic devices for on-chip culture with media reservoirs

A) The 3-channel device is composed of a culture chamber with dimensions of 1 mm \times 5 mm ($w \times L$) and media channels with dimensions of 100 μm \times 40 mm ($w \times L$). B) The 5-channel device is composed of a culture chamber with dimensions of 1 mm \times 6 mm ($w \times L$), gel-containing channels of 275 μm \times 66 mm ($w \times L$), and media channels with dimensions of 100 μm \times 43 mm ($w \times L$). C) Separating the channels, a close up of the 5-channel device in B), are pillars, which are 5 μm apart, to permit culture medium and waste into and out of the culture chamber. D) An illustration of the media reservoirs used for the on-chip PDAC culture with the 5-channel device. E) Schematic of the culture media reservoirs, which are 32 mm high with an inner diameter of 10 mm and a 2 mm wide spout to interface with the devices for cell culture. F) Image of the culture media reservoirs with the 5-channel device as illustrated in the D).

The flow of culture media through the media channels with the media reservoirs was $0.5 \mu\text{L min}^{-1}$. This was determined from a range of linear velocities calculated (using *Equations 14 – 16*) from devices reported in the literature for microfluidic cell culture.^[131, 134, 257, 292-297] This is described in more detail in chapter 5, section 5.1. The rate of $0.5 \mu\text{L min}^{-1}$ with the dimensions for the media channels permitted a laminar flow regime with a Reynolds number of 0.02 for culture. The Reynolds number was calculated with *Equation 12*.

With the dimensions of the media reservoirs and media flow rate of $0.5 \mu\text{L min}^{-1}$, a MATLAB code (Appendix, *Hydrostatic pressure driven flow by gravity*, adapted from a hydrostatic MATLAB code by Matthew Bourn) was scripted to determine how often to replenish culture medium. The code was written with the equations below, based on *Equations 14 – 16*.

The hydraulic resistance equation used is as seen in *Equation 16* and below

$$R_{hyd} = \frac{12 \times \eta \times L}{w \times h^3} \cdot \frac{1}{1 - 0.63 \frac{h}{w}}$$

where R_{hyd} is the hydraulic resistance for a rectangular channel in Pa.s m^{-3} , η is the dynamic viscosity of the culture media ($6.99 \times 10^{-4} \text{ Pa.s}$ at 37°C), L is the length of the media channel in metres, and h and w are the media channel height and width in metres, respectively.

The equation for the volumetric flow rate, as a function of time, used is given by

$$Q(t) = \frac{Q_0 \times 10^9 \times e^{-2 \rho g t}}{R_{hyd} \pi \left(\frac{d}{2}\right)^2} \quad (19)$$

where $Q(t)$ is the final volumetric flow rate ($\text{m}^3 \text{s}^{-1}$), Q_0 is the initial volumetric flow rate ($\text{m}^3 \text{s}^{-1}$), ρ is the density of culture media (993.3 kg m^{-3} at 37°C), g is the gravitational acceleration (9.81 m s^{-2}), t is time in seconds, R_{hyd} is the hydraulic resistance for a rectangular channel calculated using *Equation 16*, π is the ratio of the reservoir circumference to its diameter (3.14), and d is the inner diameter of the media reservoirs in metres.

The equation for the hydraulic fluid pressure, as function of time, used is given by

$$P_{hyd} = \left(\frac{Q(t)}{10^9}\right) \cdot R_{hyd} \quad (20)$$

where P_{hyd} is the hydraulic pressure, $Q(t)$ is the final volumetric flow rate as a function of time ($\text{m}^3 \text{s}^{-1}$), calculated using *Equation 20*, and R_{hyd} is the hydraulic resistance for a rectangular channel calculated using *Equation 19*.

Culture medium was replenished approximately every three days, but flow through the culture media channels were checked daily to identify and resolve any blockages.

3.7.2. Microfluidic device fabrication – photo and soft lithography

In-house, photo- and soft lithography (Figure 3.6) was used to fabricate the devices for the on-chip PDAC culture. Photolithography was used to make an SU-8 master silicon wafer mould (Figure 3.6A) of the CAD of the devices in Figure 3.5, and PDMS soft lithography was used to mould the devices (Figure 3.6B) for the on-chip culture.^[298]

As illustrated in Figure 3.6, SU-8 2075 photoresist (Microchem, Newton, MA) was warmed at room temperature for 30 minutes. At the same time, a 3 or 4-inch silicon wafer was warmed in the oven at a temperature of 200°C. Approximately 3 mL of the SU-8 2075 was spin-coated onto the wafer at a spin rate of 500 r.p.m for 10 seconds and 1, 500 r.p.m for 60 seconds to achieve an SU-8 coat depth of 100 µm. The SU-8 2075 coated wafer was then placed onto a hot plate to soft bake at 55°C for 90 minutes to evaporate the solvent on the top surface of the SU-8 photoresist.^[298] After this, the wafer on the hot plate was set to cool down to 25°C, taking approximately 2 hours.

The CAD designs, processed with CleWin5, were exposed onto the SU-8 coated wafer with a laser power of 375 nm at a resolution of 2 µm using a direct-write laser system (MicroWriter™, Durham Magneto Optics, Durham, UK). After exposure, the SU-8 patterned master silicon wafer of the CAD designs was placed onto a hot plate for post-exposure bake at 55° C for 90 minutes to polymerise and cross-link the SU-8.^[298] After this, the wafer on the hot plate was set to cool down to 25°C, taking approximately 2 hours. The SU-8 patterned master mould was developed with an ethylene carbonate (EC) solvent bath (Microposit™, DOW, Midland, MI, USA) for up to 20 minutes to remove any unpolymerised SU-8.^[298] The developed SU-8 patterned master silicon wafer of the CAD designs was then washed with Isopropanol (IPA) and dried using an air gun.

Base PDMS and crosslinking agent (Sylgard™ 184 Silicon Elastomer Kit, Dow Chemical, Midland, MI, USA) were mixed at a weight ratio of 10: 1, centrifuged at 4000 r.p.m for 1 minute to remove air bubbles and poured onto the SU-8 patterned master silicon wafer in a standard 90 mm Petri dish. The PDMS covered wafer was then degassed for at least 1 hour under vacuum to remove dissolved gases in the PDMS, and the PDMS covered wafer was placed in

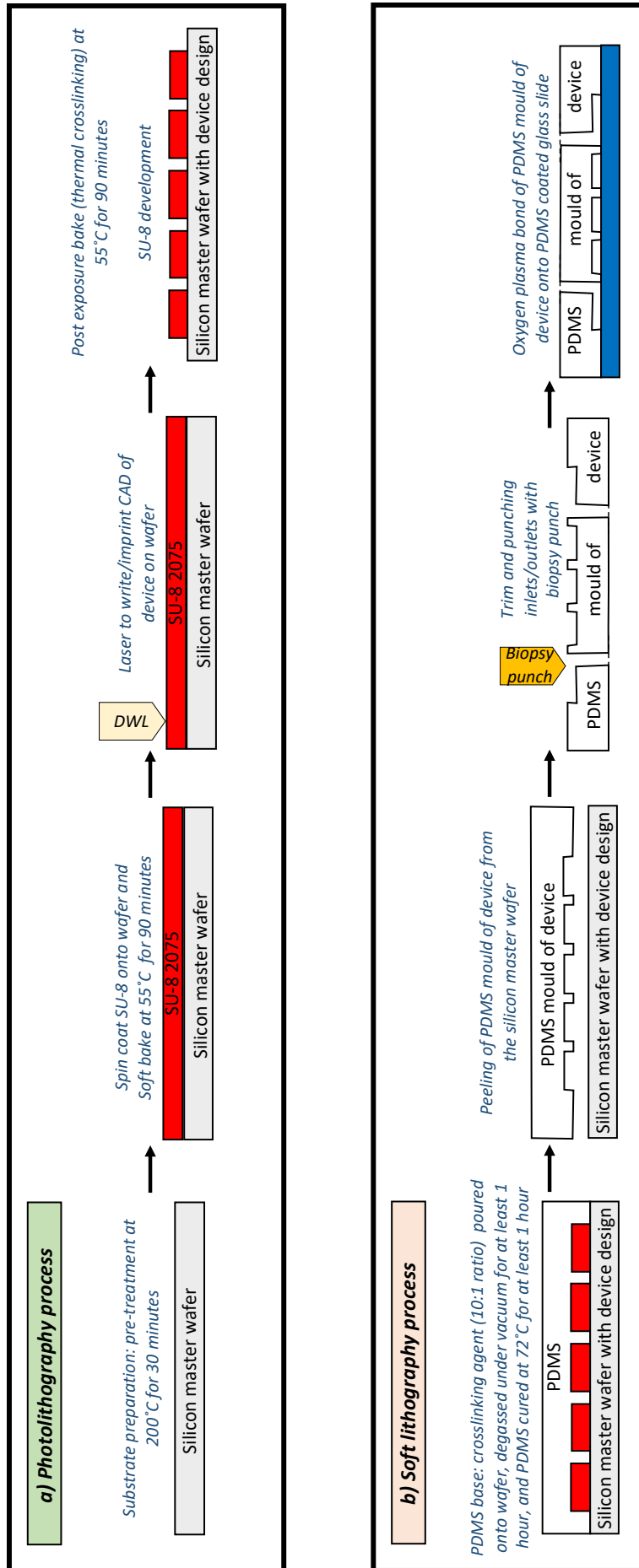


Figure 3.6. The rapid prototyping process for the fabrication of the microfluidic devices

The fabrication of the microfluidic devices were done using photolithography and PDMS soft lithography, the CAD of the devices were imprinted on an SU-8 2075 coated silicon wafer with a direct write laser (DWL). B) soft lithography, the devices are moulded from the SU-8 master mould with PDMS. Adapted from [298].

an oven at approximately 72°C to cure the PDMS for at least 1 hour.^[298] After curing, the PDMS was separated from the wafer, individual devices were cut out, and the inlets and outlets of the channels formed using a 1 and a 2 mm diameter biopsy punch. The PDMS device moulds were then bonded onto PDMS coated (50 µm thick) glass slides using oxygen plasma treatment. The oxygen plasma treatment removes hydrocarbons from the surfaces of the PDMS mould and PDMS coated glass slides, and increases the number of silanol (Si-O-H) groups on the surfaces of the PDMS mould and coated glass slides. These form covalent siloxane (Si-O-Si) bonds when the two PDMS surfaces are pressed together.^[298, 299]

The PDMS coated glass slides were made by coating large microscope glass slides (75 × 50 mm) with PDMS (base PDMS and crosslinking agent at a 10:1 ratio) at a spin rate of 800 r.p.m, for 5 seconds, and 2000 r.p.m, for 20 seconds. The glass slides were washed with isopropanol before coating with PDMS. The coated glass slides were placed onto a hotplate at 95°C for approximately 10 minutes to cure the PDMS. PDMS coated glass slides were used to provide one surface for cell culture and to prevent cells from favouring one surface to another, *i.e.*, glass surface versus PDMS.

The bonded devices were placed into an oven at approximately 72°C to finalise the bonding. The devices were autoclaved at 120°C for 30 minutes prior to cell culture. The media reservoirs used for cell culture were also autoclaved at 120°C for 30 minutes, and together with lids on their underside, further sterilised with ultraviolet (UV) light for 30 minutes.

3.8. The microfluidic PDAC culture

PANC-1 and PSC cells were harvested, prepared at 1: 3 seeding ratio and a concentration of 1×10^6 cells mL⁻¹, mixed with 6 – 9 mg mL⁻¹ BME for a cell-gel suspension, pipetted into the culture chamber of the devices, and incubated at 37°C, 5 % CO₂, for approximately 30 minutes. After incubation in the 5-channel device, 9 – 12 mg mL⁻¹ of BME was pipetted into the gel-containing channels, and the devices were placed into the incubator for another 30 minutes to polymerise the gel. The gel-containing channels were to prevent cells from growing into the media channels. After incubation, media reservoirs were placed into the respective inlets and outlets of the media channels with 2 mL and 200 µL of DMEM/10 % FBS, respectively, supplemented with TGF-β₁ (10 ng mL⁻¹). The inlets and outlets of the culture chamber and gel-containing channels were sealed with the filtered pipettes (illustrated in Figure 3.5D and shown in Figure 3.5F) used in injecting the cells and BME gel into the channels.

The on-chip PDAC cultures were grown in an incubator at 37°C with 5 % CO₂ for 21 days. Culture medium was changed approximately every three days, and culture medium flow was checked daily, ensuring consistent media flow in the device. The absence of culture medium flow with nutrients would have been detrimental to the viable culture of the PDAC cells. During the 21-day culture, culture viability was assessed with live/dead stain and by quantifying ATP content. Assessment of culture viability is described in section 3.12.

3.9. Immunostaining on-chip PDAC cultures for collagen and HIF-1 alpha

Similar to the immunofluorescence stain of the off-chip cultures for collagen and HIF-1 alpha, the on-chip PDAC cultures with TGF-β1 supplement were fixed and stained for collagen and HIF-1 alpha. Collagen staining was performed on day 7, day 14, and day 21 of culture. For HIF-1 alpha, staining was day 21 only. The staining of collagen was to demonstrate the mechanical development of the on-chip cultures with the deposition of collagen into the culture environment. The staining of HIF-1 alpha was to assess for a hypoxic environment, which affects therapeutic efficacy.

All reagents were introduced on-chip via the media channels using the reservoirs. The inlet reservoirs were filled with 500 μL of the reagents and the outlet reservoir with 100 μL of the reagents. With reference to Kim and Ingber. 2013^[162], the on-chip cultures were first washed with PBS for 5 – 10 minutes at room temperature. The cultures were then fixed with formaldehyde 4 % aqueous solution (VWR; provided by Dr Zhang Y. Ong) for 10 – 15 minutes at room temperature and permeabilised with 0.2 % Triton X-100 (Sigma Aldrich) in 1 % BSA (Sigma Aldrich) and 5 % FBS (Sigma Aldrich) solution for 10 – 15 minutes at room temperature.

The cultures were washed with PBS for 5 – 10 minutes at room temperature, and then incubated with primary antibodies from Abcam, recombinant anti-collagen 1 antibody (rabbit monoclonal [EPR22894-89] to collagen I) and recombinant anti-HIF-1 alpha antibody (rabbit monoclonal [EPR16897] to HIF-1 alpha), on day 7, 14, or 21 of culture for 45 minutes to 1 hour at room temperature. The collagen and HIF-1 alpha primary antibodies were prepared in 1 mL of PBS containing 1 % BSA at 1/250 and 1/500 dilution, respectively. As a control, replicate cultures were incubated with 1 mL of PBS containing 1 % BSA without the primary antibodies. After incubation, the cultures were washed with PBS for 5 – 10 minutes at room temperature.

Secondary antibody staining was performed with goat anti-rabbit Alexa Fluor™ 488 (Abcam) again for 45 minutes to 1 hour in the dark at room temperature, together with phalloidin-iFluor 647 to stain for F-actin. The secondary antibody and phalloidin stain were prepared in 1 mL of PBS containing 1 % BSA at 1/100 and 1/500 dilution, respectively. After incubation with the secondary antibody and actin stain, the cultures were washed with PBS for 5 – 10 minutes at room temperature.

The cultures were then incubated with 1 $\mu\text{g mL}^{-1}$ DAPI solution (Boster Biological Technology) for 5 – 15 minutes in the dark at room temperature. After incubation, the cultures were washed with PBS for 5 – 10 minutes in the dark at room temperature before imaging with the confocal microscopy. Confocal microscopy was performed as described in section 3.2.3.

3.10. Interstitial flow of the microfluidic PDAC culture

The reduced interstitial flow of the PDAC tissue, with increasing intratumoural pressure, was assessed by investigating the hydraulic conductivity^[19, 43, 237, 238] of the developing on-chip PDAC culture. As illustrated in Figure 3.7, a syringe pump was used to perfuse 5(6)-carboxyfluorescein in DMEM/10 % FBS culture medium (1: 10 volume ratio) through the on-chip PDAC culture. The 5(6)-carboxyfluorescein in DMEM/10 % FBS culture medium will be referred to as fluorescein in media solution. The syringe pump was used to accurately create a pressure gradient across the culture chamber and, therefore, determine the interstitial flow nature of the PDAC cultures.

The on-chip PDAC cultures were imaged using an epifluorescence microscope as described in section 3.2.2. Two 1 mL glass syringes (SGE gas-tight syringes Luer Lock, Sigma Aldrich) were loaded with fluorescein in media solution or culture media only, and a syringe pump (PHD ULTRA™ Syringe Pump Infuse/With Programmable, Harvard Apparatus) was used to perfuse the solutions through the media channel inlets at a flow rate of 0.5 and 0.1 $\mu\text{L min}^{-1}$, respectively. The time taken for the fluorescein in media solution to permeate through the PDAC culture was determined. As a control, the flow of the fluorescein in media solution was assessed with just 6 – 9 mg mL^{-1} BME gel in the culture chamber.

Darcy's equation for fibrous medium subject to low *Reynolds* number^[19, 43, 235, 237, 238], as shown in *Equation 6*, was applied to determine the hydraulic conductivity and thus interstitial flow with *Equation 7* and *9*, respectively, of the on-chip PDAC culture.

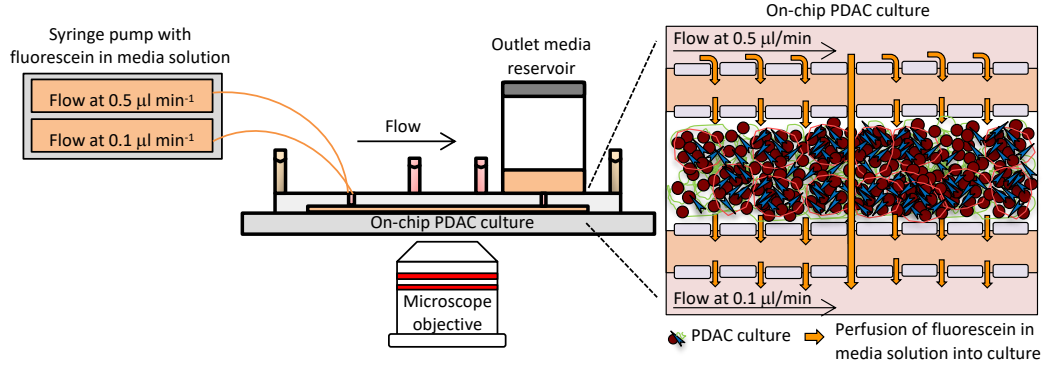


Figure 3.7. The interstitial flow assessment of the on-chip PDAC culture

An illustration of the perfusion of fluorescein in media solution through the PDAC culture in the culture chamber to assess the interstitial flow nature of the culture, in mimicking the interstitial flow of the PDAC tissue.

The pressure-gradient (Pa) driving the hydraulic flow through the porous medium was calculated using Bernoulli's equation

$$P_1 + \frac{1}{2}pv_1 + pgy_1 = P_2 + \frac{1}{2}pv_2 + pgy_2 \quad (21)$$

where P is pressure (Pa), p is the density of culture media (993.3 kg m^{-3} at 37°C), g is the gravitational acceleration (9.81 m s^{-2}), and y is the height (m) of the culture media channel.

As the device height, irrespective of channel, was $100 \text{ }\mu\text{m}$, and DMEM/10 % FBS culture medium was used for the fluorescein in media solution, Equation 21 was rearranged into

$$\begin{aligned} &= P_1 + \frac{1}{2}pv_1 = P_2 + \frac{1}{2}pv_2 \\ &= P_1 - P_2 = \frac{1}{2}pv_1 - \frac{1}{2}pv_2 \\ &= \nabla P = \frac{1}{2}\rho(v_2 - v_1) \end{aligned} \quad (22)$$

where ∇P (Pa) is the pressure-gradient; v_2 and v_1 , the flow velocity (m s^{-1}) in the respective media channels.

Moreover, as hydraulic conductivity depends on the porosity of the BME gel or the on-chip PDAC culture, the percolation threshold or the intrinsic permeability^[238] of the BME gel and PDAC culture was determined with Equation 8.

Furthermore, fluid shear stress on the PDAC culture in the culture chamber was approximated with the wall-shear rate model for a rectangular channel,^[300, 301] which is given by

$$\tau = \frac{6 \times \eta \times Q}{w \times h^2} \quad (23)$$

where τ is the shear stress (Pa) converted to dyne cm^{-2} , η is the dynamic viscosity of the culture medium (6.99×10^{-4} Pa.s at 37°C), Q is the volumetric fluid flow rate ($\text{m}^3 \text{s}^{-1}$), and w and h are the width and height of the channel in metres, respectively.

3.11. Therapeutic assessment of the PDAC cultures

On-chip PDAC cultures supplemented with TGF- β 1 were treated with gemcitabine, microbubbles, and ultrasound. For this, the optimum gemcitabine concentration, determined off-chip, was defined as the concentration resulting in a percentage viability of approximately 70 %. This provided sufficient cellular viability to assess further viability decreases of gemcitabine with microbubbles and ultrasound. Determining the optimum gemcitabine concentration is described in chapter 4, section 4.3. The flow of microbubbles into the culture chamber with the PDAC culture, and the effect of microbubbles and ultrasound on the PDAC culture prior to assessments with gemcitabine, were also investigated. With the optimum gemcitabine concentration determined and conditions for the application of microbubbles and ultrasound optimised, the effect of gemcitabine with microbubbles and ultrasound on the on-chip PDAC culture was assessed. Gemcitabine was purchased from Sigma, dissolved to 5 mg mL^{-1} stock solution in dimethyl sulfoxide (DMSO; Sigma-Aldrich), and stored at -20°C for use.

Figure 3.8 shows a timeline of the seeding of the cells for culture, treatment with gemcitabine, microbubble, and ultrasound, and their viability assessment. Assessments with 2D cultures of the PDAC cells were done to compare results with the on-chip PDAC cultures.

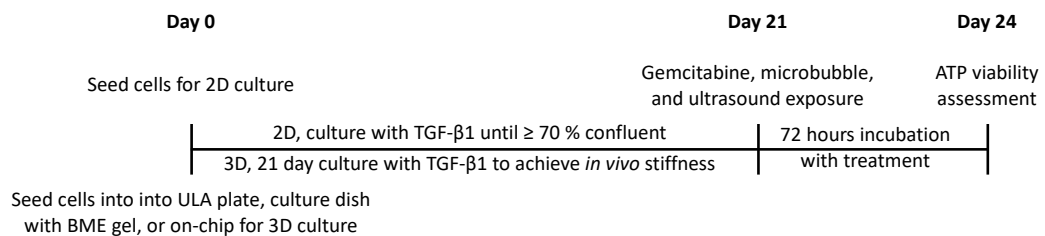


Figure 3.8. Timeline of the therapeutic assessment of the of PDAC cultures

Timeline of the seeding of the PDAC cells off-chip and on-chip for culture and their ATP viability assessment following treatment with gemcitabine, microbubbles, and ultrasound.

3.11.1. Therapeutic assessment of the off-chip PDAC cultures with gemcitabine

The PANC-1 and PSC cells were seeded into ULA plates for PSC only, PANC-1 only, and PDAC spheroid cultures at a seeding density of 250 cells per well (seeding as described in section 3.4.1, Figure 3.2A). The spheroid cultures were maintained with and without TGF- β 1 supplement (10 ng mL⁻¹) for 21 days, and treated with gemcitabine, between 0.09 – 500 μ M in a 2-fold dilution series, for 72 hours for the cytotoxic effect of gemcitabine^[222] prior to ATP viability quantification (described in section 3.12.2). Viability was normalised to positive and negative controls with the treatment of adjacent cultures with 10 % DMSO for total cell kill treatment and 0.01 % DMSO, respectively, to determine the optimum gemcitabine concentration to use on-chip with the PDAC culture.

The PANC-1 and PSC cells were then seeded with 6 – 9 mg mL⁻¹ BME gel into the culture petri dishes for PSC only, PANC-1 only, and PDAC cultures at a seeding density of 1×10^6 cells mL⁻¹ (seeding as described in section 3.4.2, Figure 3.2B). The cultures were maintained with and without TGF- β 1 supplement (10 ng mL⁻¹) for 21 days, and treated with 7.8, 31.25, and 250 μ M of gemcitabine (following the assessment with the spheroid cultures) for 72 hours, prior to ATP viability quantification (described in section 3.12.2). Viability was normalised to positive controls (10 % DMSO treated cultures) and negative controls (0.01 % DMSO treated cultures) in determining the optimum gemcitabine concentration to use on the on-chip PDAC cultures.

3.11.2. Therapeutic assessment of the on-chip PDAC culture with gemcitabine

PANC-1 and PSC cells were seeded into the 5-channel device with 6 – 9 mg mL⁻¹ BME gel at a seeding density of 1×10^6 cells mL⁻¹ for a 21-day culture with TGF- β 1 supplement (10 ng mL⁻¹) (seeding as described in section 3.8). The on-chip PDAC cultures were treated with 31.25 μ M of gemcitabine for 72 hours. From the off-chip PDAC culture assessment with gemcitabine, 31.25 μ M was found as an optimum gemcitabine concentration to use on-chip with the PDAC culture. ATP viability (described in section 3.12.2) was assessed, and the viability was normalised to positive controls (10 % DMSO treated cultures) and negative controls (0.01 % DMSO treated cultures) to determine the effect of gemcitabine on the on-chip PDAC culture.

3.11.3. Microbubble production

Figure 1.8A shows a schematic of the phospholipid coated microbubble used. For microbubble production, 1,2-dipalmitoyl-sn-glycero-3-phosphocholine (DPPC), 1,2-distearoyl-sn-glycero-3-phosphoethanolamine-N-[amino(polyethylene glycol)-2000] (DSPE-PEG₂₀₀₀), and ATTO 488-DOPE lipids were mixed together in a molar ratio of 95%: 4.9%: and 0.1%, respectively for a 2mg mL⁻¹ final lipid solution concentration. The lipid solution was dried under a steady stream of nitrogen for 40 minutes then left under vacuum overnight to remove any remaining chloroform: methanol storage solvent. The DPPC and DSPE-PEG₂₀₀₀ lipids were purchased from Avanti Polar Lipids (USA). ATTO 488 DOPE lipid, for fluorescent imaging of the microbubbles, was purchased from ATTO-TEC (Germany). The lipids were dissolved in chloroform and methanol (1:1 ratio) and stored at -20°C to use.

After drying, the DPPC: DSPE-PEG₂₀₀₀: ATTO 488 lipid solution was resuspended in 2 mL of 4mg mL⁻¹ sodium chloride (NaCl) solution containing 1 % glycerol (vol/vol) for a final lipid solution concentration of 2 mg mL⁻¹. The lipid solution was sonicated in a water bath for a cloudy and homogenous mix. Microbubbles were produced with the microspray regime by combining the lipid solution and perfluorocarbon gas (C₄F₁₀; Sigma Aldrich) in a 4 × multiplexed microfluidic device^[268] at flow rate of 80 μL min⁻¹ and a gas pressure of 1000 mbar. Figure 3.9 shows a CAD schematic of the poly(methyl methacrylate) (PMMA) multiplexed microfluidic device used for microbubble production. The lipid inlet and gas inlet channels together branch into 4 separate channels with flow focusing nozzles. Up to the flow focusing nozzles, the device height is 25 μm. Pass the flow focusing nozzles, the height of the device is increased by 25 μm to facilitate a rapid pressure drop. This results in an atomisation effect for the production of the microbubbles in the microspray regime. The multiplexed microfluidic device with the microspray regime approach allows the production of polydisperse microbubbles at a concentration of $\geq 1 \times 10^8$ microbubbles per mL, with a majority (99%) of the microbubbles with a diameter of 2 μm.^[268, 302]

Where the multiplexed microfluidic device was unavailable, mechanical agitation was used to produce microbubbles. For mechanical agitation, 1 mL of the lipid solution was combined with C₄F₁₀ in a vial at a gas pressure between 250 – 300 mbar for at most 2 minutes. The vial was then sealed with parafilm and shaken vigorously for 45 seconds at a rate of 4300 oscillations per minute with an amalgamator (3M™ CapMix™ Capsule Mixing device – 230V/50 Hz, GB).

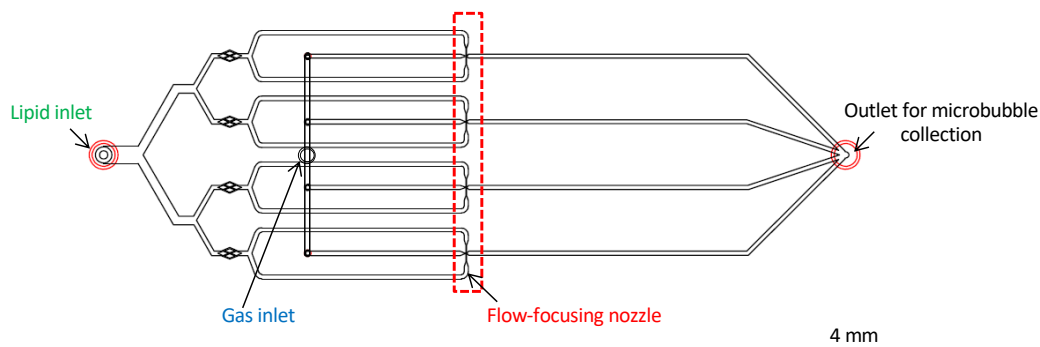


Figure 3.9. The 4 × multiplexed microfluidic device design for microbubble production

A schematic of the CAD device of the 4 × multiplexed device for microbubble production. The device consists of four identical flow-focusing nozzles for the rapid production of homogeneously sized microbubbles. The device was designed and developed by Dr Sally Peyman detailed in reference [268]. Image of CAD adapted with permission from Dr Peyman.

After production, the ATTO 488 DOPE lipid tag, and the size and concentration of the microbubbles were characterised optically using an epifluorescence microscope. The size and concentration of the microbubbles were analysed using a MATLAB-based Microbubble Population Analysis code program.^[303]

The microbubbles were washed to remove excess fluorescent lipids and reduce background fluorescence for imaging. With a protocol and centrifugation column provided by Jordan Tinkler, 1 mL of the microbubbles were added to the centrifugation column with 4 mL of PBS. The centrifugation column consisted of a 5 mL syringe (without the plunger) with a 1-way tap at the end of the syringe. The centrifugation tube with the microbubble: PBS solution was sealed with parafilm and placed into a 50 mL falcon tube for centrifugation at $300 \times g$ for 10 minutes. After, the centrifugation column was removed from the falcon tube and suspended with a clamp to gradually drain the infranatant of the microbubble: PBS solution until 1 mL of the solution remained. 4 mL of PBS was added to the centrifugation column, placed into a falcon tube for centrifugation again at $300 \times g$ for 10 minutes. The centrifugation column with the microbubble: PBS solution was suspended with clamp, and the supernatant of washed microbubbles were pipetted into a 1 mL Eppendorf tube with a wide bore 1000 μL pipette.

3.11.4. The perfusion of microbubbles into the on-chip PDAC culture

After washing the DPPC: DSPE-PEG₂₀₀₀: ATTO 488 microbubbles, to assess the microbubbles permeating and flowing through the culture chamber with the PDAC culture, the microbubbles were diluted with DMEM/10 %FBS culture media in a 1: 10 ratio and pipetted directly into a media channel via the inlet through an inlet reservoir spout. The rest of the microbubbles diluted with culture media were pipetted into the reservoir, and its respective outlet reservoir was filled with 200 μ L of culture media to permit flow through the media channel. The other inlet and outlet reservoirs were filled with approximately 200 μ L of culture media for little to no flow in the respective media channel to induce a pressure gradient across the culture chamber with the PDAC cells and allow microbubbles in and through the culture chamber.

Figure 3.10A illustrates the perfusion of the microbubbles into the on-chip PDAC culture. As a control, the flow of the microbubbles was assessed with 6 – 9 mg mL⁻¹ BME gel only in the culture chamber. Images of the perfusion of the microbubbles into the culture chamber with the PDAC culture or BME gel only was performed with confocal fluorescence microscopy, as described in section 3.2.3, using a 10 \times objective and a pinhole of 1.00 AU with the respective excitation and emission wavelengths for the ATTO 488 lipid (Ex/Em: 500/520 nm). All images were analysed with ImageJ.

3.11.5. Effect of microbubbles and ultrasound on the on-chip PDAC culture

Figure 3.10C illustrates the application of ultrasound to the on-chip PDAC cultures with DPPC: DSPE-PEG₂₀₀₀: ATTO 488 microbubbles. For ultrasound work, the 5-channel device for the PDAC culture was moulded with PDMS to a thickness of approximately 1 mm (Figure 3.10B). Additional 4 – 5 mm thick PDMS were made and bonded onto the PDMS moulded 5-channel device. The additional PDMS was to ensure optimum culture with the media reservoirs.

DPPC: DSPE-PEG₂₀₀₀: ATTO 488 microbubbles were made as described in section 3.11.3 and diluted with DMEM/10 % FBS culture media in a 1: 10 ratio. The microbubbles in media solution was pipetted into the media channel via the inlet through the inlet reservoir spouts. The remaining microbubbles in media solution were pipetted into the inlet reservoirs and the outlet reservoirs were filled with 200 μ L of culture media for microbubble flow through the media channel and into the culture chamber with the 21-day on-chip PDAC culture.

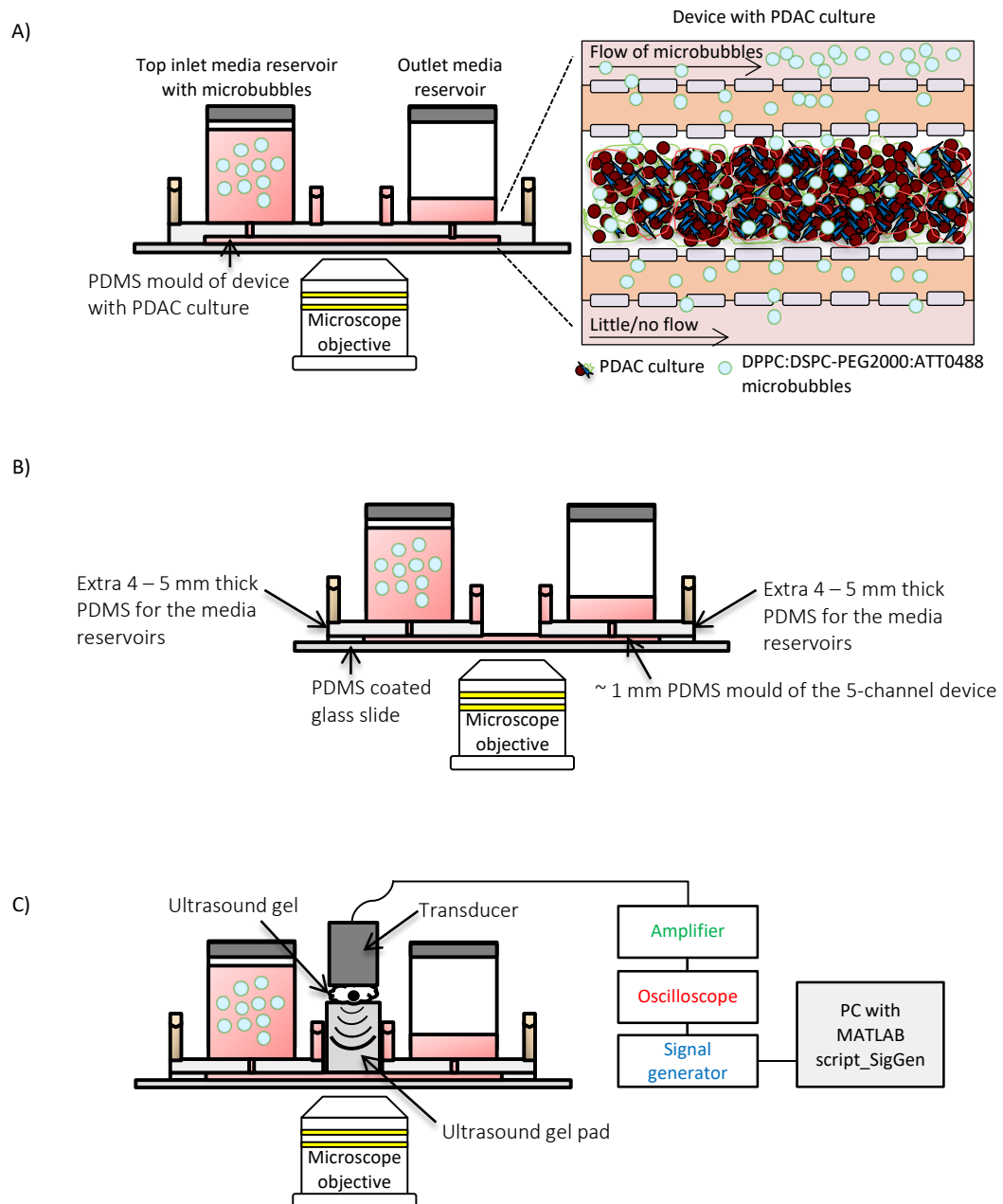


Figure 3.10. The perfusion of microbubbles and ultrasound assessments on-chip

An illustration of A) the perfusion of ATTO488 microbubbles through the on-chip PDAC culture, B) of the 5-channel PDMS moulded to a ~ 1 mm thick device with extra PDMS mould of 4 – 5 mm thickness bonded to the device around the reservoirs, and C) ultrasound application to the on-chip PDAC culture with microbubbles.

After approximately 2 hours with the microbubbles on-chip with the PDAC culture, the effect of the microbubbles only (no ultrasound and gemcitabine) and the effect of ultrasound with and without microbubbles (no gemcitabine) on the on-chip PDAC cultures were assessed by quantifying ATP content as described in section 3.12.2.

Shown in Figure 3.10C, a 3 cm × 1.5 cm ultrasound gel pad (Aquaflex®, Parker Laboratories, Inc. USA) was positioned between the pipette tips placed at the inlet and outlet of the culture chamber for coupling. A blob of ultrasound transmission gel (Anagel®, Ana Wiz Ltd) was placed onto the gel pad, and a 0.25 inch (6.35 mm) diameter 2.25 MHz V323-SM single element ultrasonic transducer (Olympus, Tokyo, Japan) was placed onto the ultrasound gel. Using a MATLAB-based signal generator the 2.25 MHz frequency ultrasound was applied to the on-chip culture for a total duration of 5 seconds and comprised of a mechanical index of 0.6, a pulse repetition frequency of 1 kHz, and a duty cycle of 1 % to avoid damage to the transducer.

The MATLAB signal generator script was written by Damien Batchelor and connected to a signal generator (TG5011, Aim & Thurlby Thandar Instruments, UK) to produce the signal. The signal generator was connected to an oscilloscope (WaveRunner LT342L, LeCroy Cooperation, USA). With the oscilloscope the parameters for the frequency was checked to ensure the set-up was correct. The oscilloscope was connected to a +53 dB amplifier (A150, Electronics & Innovation, Rochester, USA), which was connected to the transducer to generate the ultrasound signal to the on-chip PDAC cultures (Figure 3.10C).

As a control, the effect of ultrasound on-chip with just 6 – 9 mg mL⁻¹ BME gel in the culture chamber with and without microbubbles was assessed. Imaging to assess the effect of ultrasound for all conditions on the chip-based PDAC cultures was performed with the Leica confocal fluorescence microscope (described in section 3.2.3) using a 10 × objective and a pinhole of 1.00 AU with the respective excitation and emission wavelengths for the ATTO 488 lipid (Ex/Em: 500/520 nm).

3.11.6. Therapeutic assessment of on-chip PDAC cultures with gemcitabine, microbubbles and ultrasound

PANC-1 and PSC cells were seeded into the 5-channel device for ultrasound assessment (Figure 3.10B) with 6 – 9 mg mL⁻¹ BME gel at a seeding density of 1 × 10⁶ cells mL⁻¹ for a 21-day culture with TGF-β1 supplement (10 ng mL⁻¹) (seeding as described in section 3.8).

DPPC: DSPE-PEG₂₀₀₀: ATTO 488 microbubbles were made as described in section 3.11.3 and diluted with DMEM/10 % FBS culture media with 31.25 μM of gemcitabine in a 1: 10 ratio. After 21 days of culture, microbubbles in DMEM/10 %FBS/31.25 μM of gemcitabine solution were pipetted directly into the media channels via the spout of the reservoirs. The rest of the

reservoirs were filled with the DMEM/10 %FBS/31.25 μ M of gemcitabine solution. Ultrasound was applied after approximately 2 hours, using the 0.25 inch (6.35 mm) diameter 2.25 MHz transducer at a mechanical index of 0.6, a pulse repetition frequency of 1 kHz, a duty cycle of 1 %, for a total duration for 5 seconds. The cultures were incubated for a further 72 hours. ATP viability (described in section 3.12.2) was assessed, and this was normalised to positive controls (10 % DMSO treated cultures) and negative controls (0.01 % DMSO treated cultures) to determine the effect of gemcitabine with microbubbles and ultrasound on the on-chip PDAC culture.

3.11.7. Effect of therapeutic microbubbles on the on-chip PDAC culture

Similar to Abou-Saleh *et al.* 2020, Ruan *et al.* 2021, and Xu *et al.* 2014^[228, 230, 270], and with the help of Dr Nicola Ingram, gemcitabine-loaded liposomes were prepared at 40 mg mL⁻¹ lipid concentration using DPPC:DSPE-PEG₂₀₀₀: Cholesterol: DSPE-PEG₂₀₀₀-Biotin:ATTO590 at a molar concentration of 60:5:30:5:0.01 %, respectively. The lipid solution was dried under a steady stream of nitrogen for 1 hour and left under vacuum overnight to remove any remaining chloroform: methanol storage solvent. DPPC, DSPE-PEG₂₀₀₀, and DSPE-PEG₂₀₀₀-Biotin were purchased from Avanti Polar Lipids (USA). The ATTO 590 DOPE lipid, to label the liposomes, was purchased from ATTO-TEC (Germany). Cholesterol was purchased from Sigma-Aldrich. The lipids were dissolved in chloroform and methanol (1:1 ratio) and stored at -20°C to use.

After drying, the DPPC: DSPE-PEG₂₀₀₀: Cholesterol: DSPE-PEG₂₀₀₀-Biotin: ATTO 590 thin film was hydrated in 500 μ L of 250 mM ammonium sulphate ((NH₄)₂ SO₄). The lipids in (NH₄)₂ SO₄ solution was vortexed for about 3 minutes, incubated in a water bath at 41°C (the transition temperature of the predominant lipid, DPPC) for 1 hour, and underwent a 5 \times freeze-thaw-vortex cycle using the water bath and liquid nitrogen, each time for 5 minutes, to help with the resuspension of the lipids and the encapsulation of gemcitabine into the liposomes.^[230] The (NH₄)₂ SO₄ solution was used to actively load gemcitabine into the liposomes and increase the encapsulation efficiency (EE %) of gemcitabine.^[222, 230, 304] As shown in Figure 3.11C, the presence of (NH₄)₂ SO₄ creates a balanced pH gradient between the internal and external environment of the liposome with the protonation of gemcitabine to increase EE %, which is the percentage of drug entrapped into the liposomes defined as^[222, 230]

$$EE \% = \frac{\text{total drug amount entrapped}}{\text{total drug amount used in preparation}} \times 100 \% \quad (24)$$

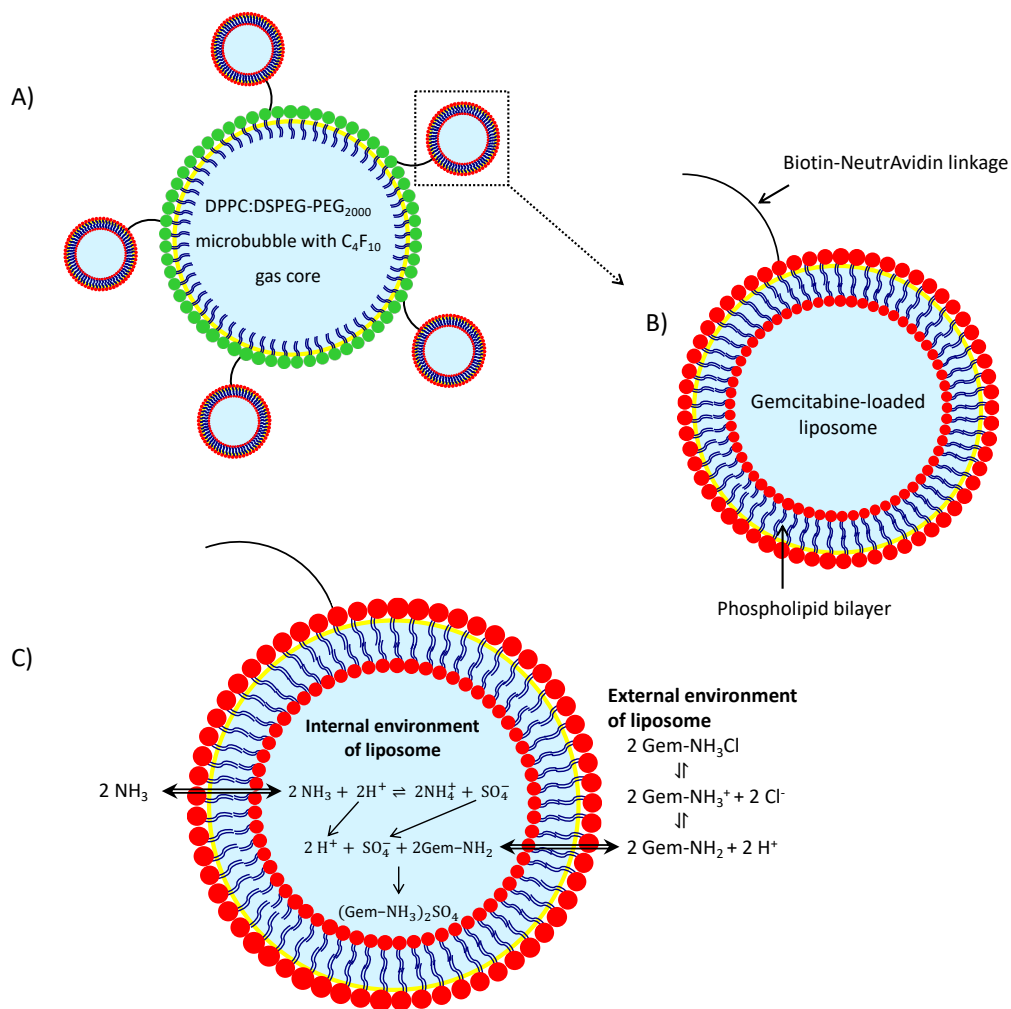


Figure 3.11. The therapeutic microbubbles with gemcitabine-loaded liposomes

A) Schematic diagram of therapeutic microbubbles or liposome-microbubble complex. Biotinylated liposomes containing gemcitabine as seen in B) are attached to the surface of the microbubbles with biotin-NeutrAvidin linkage. B) Schematic of the liposome structures with gemcitabine encapsulated. C) Schematic of the gemcitabine encapsulation process in the liposomes, where the presence of ammonium sulphate ($(\text{NH}_4)_2\text{SO}_4$) creates a pH gradient with the protonation of gemcitabine.

The homogenous lipid solution was extruded at room temperature through a 200 nm pore size polycarbonate membrane 11 × using a sterilised Avanti mini extruder system (Alabaster, AL, USA). Excess lipids and $(\text{NH}_4)_2\text{SO}_4$ from the solution were cleaned by ultracentrifugation at $60,000 \times g$ for 1 hour at 4°C . After centrifugation, the liposomes were incubated in a water bath at 41°C with $30 \mu\text{L}$ of 5 mg mL^{-1} (16.68 mM) gemcitabine (anhydrous purchased from Sigma-Aldrich and dissolved in PBS) for at least 3 hours. For comparison, blank liposomes were made by incubating the liposomes with $30 \mu\text{L}$ of PBS for at least 1 hour. The liposomes after

incubation were centrifuged at $60,000 \times g$ for 1 hour at 4°C to remove any unencapsulated gemcitabine. After centrifugation, the liposomes were resuspended in PBS and stored at 4°C for use.

The liposome size distribution and concentration were measured on a NanoSight NS300 (Malvern Panalytical, UK). The liposomes were diluted $10,000 \times$ in PBS for characterisation. The concentration of gemcitabine in the liposomes was characterised on a UV-vis spectrometer (Agilent, UK). Gemcitabine concentrations ranging from $0.19 - 50 \mu\text{g mL}^{-1}$ ($0.65 - 166.85 \mu\text{M}$), in a 2-fold dilution, were used to calibrate and generate a standard curve (Figure 6.10C) to determine the amount of gemcitabine in the liposomes. $600 \mu\text{L}$ of the different concentrations of gemcitabine in methanol was pipetted into a quartz cuvette (Hellma Analytics, UK; kindly provided by Joel Whipp) for absorbance reading on the UV-vis spectrometer. The gemcitabine-loaded liposomes were mixed with methanol in a $10,000 \times$ dilution to break the liposomes and release the encapsulated gemcitabine, centrifuged, and the supernatant collected into the quartz cuvette for absorbance reading with the UV-vis spectrometer.

For the therapeutic microbubbles, gemcitabine-loaded liposome-microbubble complex (Figure 3.11A), approximately $100 \mu\text{L}$ of the gemcitabine-loaded liposome solution was incubated with $8 \mu\text{L}$ of 2.5 mg mL^{-1} stock NeutrAvidin (Avidin, NeutrAvidin™ biotin-binding protein, Thermo Fisher Scientific) for 20 minutes at room temperature. Microbubble lipid (DPPC: DSPE-PEG₂₀₀₀: ATTO 488) solution were prepared and produced as described in section 3.11.3, and 1 mL of the microbubbles were incubated with the liposomal solution for 20 minutes at room temperature. After incubation, the size and concentration of the therapeutic microbubbles were characterised optically using an epifluorescence microscope. The size and concentration of the microbubbles were analysed using the MATLAB-based Microbubble Population Analysis code program.^[303]

For treatment with the on-chip PDAC cultures, the therapeutic microbubbles was mixed in a 1: 10 ratio with DMEM/10 %FBS culture media, and PDAC cells grown on-chip for 21-days were treated with the therapeutic microbubble: DMEM/10 %FBS culture medium solution. After approximately 2 hours with the therapeutic microbubble: DMEM/10 %FBS culture medium solution, ultrasound was applied using the 0.25 inch diameter 2.25 MHz transducer at a mechanical index of 0.6, a pulse repetition frequency of 1 kHz, a duty cycle of 1 %, for a total duration for 5 seconds. As controls, the 21-day on-chip PDAC cultures were treated with therapeutic microbubbles of blank liposomes conjugated to the DPPC: DSPE-PEG₂₀₀₀: ATTO

488 microbubbles and incubated for 72 hours. ATP viability assessment was performed and normalised to positive controls (10 % DMSO treated cultures) and negative controls (0.01 % DMSO treated cultures) to determine the effect of the therapeutic microbubbles on the on-chip cultures.

3.11.8. Therapeutic assessment of 2D PDAC cultures with gemcitabine, microbubbles and ultrasound

To compare, the effect of gemcitabine, microbubbles and ultrasound were assessed on the 2D culture of the PDAC cells. PANC-1 and PSC cells at a ratio of 1: 3, were prepared to a cell suspension of $5 - 7 \times 10^5$ cells mL⁻¹, and the cells were seeded into a 96-well or into ibidi μ -Slide (VI 0.4, iBidi, Germany) microfluidic devices. Each of the ibidi μ -Slide devices consists of 6 individual channels with a channel height of 0.4 mm and a length of 17 mm designed for the culturing of adherent cells. 40 μ L of the cells were seeded into the ibidi μ -Slide devices and incubated for at least 2 hours, and 60 μ L of culture media were added to each reservoir simultaneously for static cell culture.

The PDAC cells in the 96-well or the ibidi μ -Slide devices were cultured with DMEM/10 % FBS culture media with TGF- β 1 supplement (10 ng mL⁻¹) until ≥ 70 % confluent and exposed to gemcitabine, microbubbles and ultrasound. The 2D PDAC cultures were also treated with therapeutic microbubbles and ultrasound. DMEM/10 %FBS/31.25 μ M of gemcitabine solution, DPPC: DSPE-PEG₂₀₀₀: ATTO 488 microbubble solution, the microbubbles in DMEM/10 %FBS/31.25 μ M of gemcitabine solution, or the therapeutic microbubble (gemcitabine-loaded liposomes or blank liposomes conjugated onto DPPC: DSPE-PEG₂₀₀₀: ATTO 488 microbubbles): DMEM/10 %FBS culture medium solution was added to the wells of the 96-well plate or a reservoir chamber of each channel of the ibidi μ -Slide devices to induce flow for treatment. Ultrasound was applied with and without gemcitabine and microbubbles using the 0.25 inch (6.35 mm) diameter 2.25 MHz transducer at a mechanical index of 0.6, a pulse repetition frequency of 1 kHz, a duty cycle of 1 %, for a total duration for 5 seconds, and the cultures were incubated for 72 hours. Viability was assessed as described in section 3.12. ATP viability results were normalised to positive controls (10 % DMSO treated cultures) and negative controls (0.01 % DMSO treated cultures) to determine the effect of gemcitabine with microbubbles and ultrasound application on the 2D cultures.

3.12. Viability assessment of the PDAC cultures

The viability of the off-chip and on-chip PDAC cultures was assessed with live/dead viability assay and by quantifying their ATP content. Live/dead viability assessment of the off-chip and on-chip PDAC cultures was done with 2 μM Calcein AM, 4 μM ethidium homodimer-1 (EthD-1) and 5 $\mu\text{g mL}^{-1}$ of Hoechst 33342, or with ReadyProbes™ Cell Viability Imaging Kit, Blue/Red, which consists of Hoechst and propidium iodide. The live/dead viability reagents were all sourced from Thermo Fisher Scientific and performed according to the manufacturer's instructions. ATP content of the 2D cultures and off-chip and on-chip 3D PDAC cultures were quantified with CellTiter-Glo® 2D cell viability assay and CellTiter-Glo® 3D cell viability assay, according to the manufacturer's instructions. The 2D and 3D cell viability assay were sourced from Promega UK Ltd.

3.12.1. Live/dead viability assay

The off-chip PDAC spheroid cultures were treated with 2 μM Calcein AM, 4 μM EthD-1 and 5 $\mu\text{g mL}^{-1}$ of Hoechst 33342 and incubated at 37 °C with 5 % CO_2 for at least 30 minutes before imaging. Hoechst binds to the cell nucleus of live cells to fluoresce blue, Calcein AM is enzymatically converted (hydrolysed via the intracellular esterase activity) to the fluorescent green calcein in live cells, and EthD-1 binds to the nucleic acid of dead cells, cells that have lost their plasma integrity, to fluoresce red.

The 2D cultures of the PDAC cells grown in the ibidi μ -Slide microfluidic devices were incubated with a solution of the ReadyProbes™ Cell Viability Imaging Kit, Blue/Red, prepared according to the manufacturer's instructions. The on-chip PDAC cultures were also treated with the ReadyProbes™ Cell Viability Imaging Kit. Two drops of NucBlue® Live (Hoechst stain) and propidium iodide, which binds to the nucleic acid of dead cells, were added to 1 mL of culture media, and 120 μL of the solution was pipetted into a reservoir chamber of each channel of the ibidi μ -Slide devices to induce flow and stain the 2D cultured cells. For the on-chip PDAC cultures, two drops of the NucBlue® Live (Hoechst stain) and propidium iodide were added to the inlet media reservoirs with 1 mL of DMEM/10 % FBS culture media. The 2D and on-chip 3D PDAC cultures were incubated for 15 – 30 minutes prior to imaging.

All imaging were performed with the Leica confocal fluorescence microscope (described in section 3.2.3) using a 10 \times objective and a pinhole of 1.00 AU with the respective excitation

and emission wavelengths for Calcein AM (Ex/Em: 494/517 nm), EthD-1 (Ex/Em: 528/617 nm), Hoechst (Ex/Em: 350/461 nm), NucBlue® Live (Ex/Em: 360/460 nm), and propidium iodide (Ex/Em: 535/617 nm). All acquired images were analysed with Image J.

3.12.2.ATP viability assay

The metabolic activity of the 2D PDAC cultures, and the off-chip and on-chip 3D PDAC cultures were assessed by quantifying their ATP content with CellTiter-Glo® 2D and 3D reagent. The CellTiter-Glo® 3D reagent is optimised for 3D culture assessment as it is a highly concentrated lytic reagent to penetrate the core of 3D cultures. The CellTiter-Glo® 2D and 3D reagent were used to measure the luminescence signal from the 2D and 3D cultures, proportional to their ATP content and, therefore, culture viability.

For the 2D PDAC cultures, when the PDAC cells reached approximately $\geq 70\%$ confluency, in a 1: 1 volume ratio DMEM/10 % FBS culture media was mixed with CellTiter-Glo® 2D reagent, and 200 μL of the DMEM/10 % FBS/CellTiter-Glo® 2D reagent solution was added to the wells of the 96-well plate or 120 μL of the DMEM/10% FBS/CellTiter-Glo® 2D reagent solution was added to a reservoir of the channels of the ibidi μ -Slide devices. The 96-well plate and ibidi μ -Slides with the PDAC cultures were placed on an orbital shaker at room temperature for about 20 minutes to induce lysis. The lysed cultures from the 96-well plate and the ibidi μ -Slide devices were transferred by pipetting into 96-well opaque-walled plates (BD Falcon) and incubated further at room temperature for 10 minutes to stabilise the luminescent signal.

For the off-chip 3D cultures grown in the ULA plates, single spheroids were transferred by pipetting into 96-well opaque-walled plates (BD Falcon) for treatment with the CellTiter-Glo® 3D reagent. For both the single spheroids, transferred into the opaque plate, and the cultures grown with BME gel in culture dishes, in a 1: 1 volume ratio, equal to the culture media present in each well or culture dish, CellTiter-Glo® 3D reagent was added. The well plate and culture dishes were then placed on an orbital shaker at room temperature for 5 minutes to induce lysis. The lysed cultures grown with BME gel were transferred into 96-well opaque-walled plates. Then, both opaque plates, with the lysed single spheroids or cultures grown with BME gel, were placed at room temperature for an additional 20 – 25 minutes to stabilise the luminescent signal.

For the on-chip PDAC cultures, in a 1: 1 volume ratio, equal to the culture media present in the inlet media reservoirs, a volume of CellTiter-Glo® 3D reagent was added, and the cultures incubated for at most 30 minutes. Cells were then retrieved by pipetting from all outlets of the device into a 96-well opaque-walled plate for recording of the luminescence signal.

Luminescence signal for the 2D PDAC cultures and the off-chip and on-chip 3D PDAC cultures were recorded with a SpectraMAX M2 microplate reader (Molecular Devices).

3.12.2.1. Percentage viability assessment

Following treatment of the off-chip and on-chip PDAC cultures with gemcitabine only or gemcitabine with microbubbles and ultrasound, the viability of the cultures was assessed as described above, and percentage viability was assessed by normalising to positive controls (10 % DMSO treated cultures) and negative controls (0.01 % DMSO treated cultures). The percentage viability of the cultures was assessed with *Equation 25* below, where RLU is the relative luminescence unit reading from the microplate reader. Subtracting readings of the positive control from readings of the test compound and negative control takes into account any further background noise and variability in measurement as luminescence reading for positive controls cannot result in a zero value^[305]

$$\frac{RLU \text{ of test sample} - RLU \text{ content of positive control}}{RLU \text{ content of negative control} - RLU \text{ content of positive control}} \times 100\% \quad (25)$$

3.13. Statistical analysis

All data were expressed as the mean or average \pm standard error (SE) from biological and experimental repeats. Moreover, using OriginPro software, statistical significance was assessed. Paired Sample T-Test was used to assess the effect of TGF- β 1 on the stiffness of the cultures. Student's t-test as well as the parametric test one-way analysis of variance (ANOVA), followed by Tukey's test, were also used to assess the effect of gemcitabine, microbubbles and ultrasound treatment on the cultures and to determine the effect of the on-chip culture mechanics on interstitial flow. $p \leq 0.05$, was considered statistically significant.

3.13.1. Z-factor index

Z-factor score was calculated to measure the quality of the ATP cell viability assessments in determining the effect of gemcitabine on the off-chip and on-chip PDAC cultures. The Z-factor is a statistical measure of the suitability or the quality of an assay for use in a high throughput screen.^[306-310] The Z-factor was calculated as

$$Z = 1 - \frac{3(\sigma_p - \sigma_n)}{|\mu_p - \mu_n|} \quad (26)$$

where, σ and μ are the standard deviation and mean of both the positive (p) and negative (n) control samples, respectively. For a quality assay, the Z-factor score must be between 0.5 and 1.0.^[305, 306, 308, 309]

4. The Off-chip Pancreatic Ductal Adenocarcinoma Culture

Some of the content of this chapter can be found in the manuscript *Kpeglo, D., Hughes, M. D. G., Dougan, L., Haddrick, M, Knowles, M. A., Evans, S.D. E., and Peyman, S. A. (2022). Modeling the Mechanical Stiffness of Pancreatic Ductal Adenocarcinoma. Matrix Biology Plus. 100109.*

The optimal culture conditions to mimic the growth and mechanical behaviour of the PDAC tissue on-chip were investigated with off-chip cultures. The PDAC cancer cells, PANC-1, and pancreatic stellate cells (PSCs) were seeded into ultra-low attachment (ULA) plates and culture dishes with basement membrane extract (BME) gel and cultured with transforming growth factor- β 1 (TGF- β 1) supplement (as described in section 3.4). BME gel was used to permit the culturing and growth of the cells in 3D and for the cells to naturally engineer an environment that reflects that of the PDAC tissue with the laying down of collagen and other ECM into the surrounding matrix. Figure 4.1 shows images of the PANC-1 and PSC cells expanded in culture flasks for seeding into the ULA plates or culture dishes with BME gel.

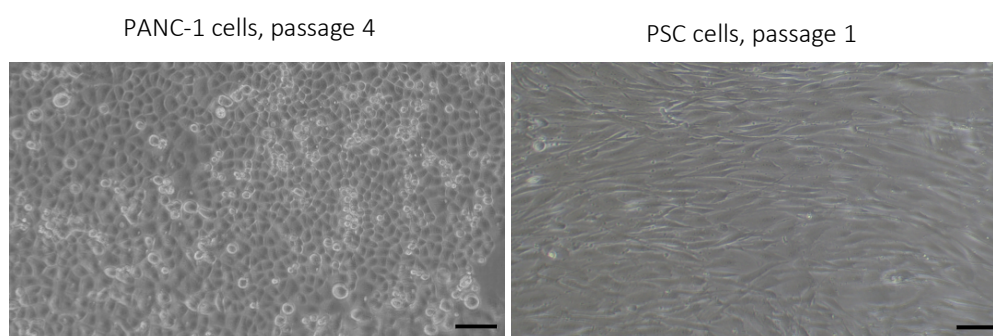


Figure 4.1. 2D culture of the PANC-1 and PSC cells

Bright-field images of the PANC-1 and PSC cells cultured in 25 cm² culture flasks in their respective culture media. Both cell lines were > 70 % confluent. Scale bar: 100 μ m.

PANC-1 cells were chosen as the cell line for the PDAC model as they were derived from a patient with an adenocarcinoma of the pancreatic head with metastases to the pancreatic lymph nodes – characteristics of PDAC.^[3, 7, 105, 171] PSCs, the main fibroblast cells of the pancreas, were chosen as they are central to the increased deposition and cross-linking of matrices, which results in the heterogeneous, dense, and hypovascularized PDAC fibrotic environment, exacerbated by the overexpression of TGF- β .^[15, 100, 311-317]

In this section, the growth and mechanical stiffness of the PANC-1 cells in the presence of PSCs and TGF- β are presented.

4.1. Growth of the PDAC cultures

PANC-1 and PSC cells were seeded into ULA plates for PSC only, PANC-1 only, and PDAC spheroid cultures. For the PDAC spheroid cultures, PANC-1 and PSC cells were seeded together at a 1: 2 ratio or a 1: 3 ratio to determine the optimum seeding ratio between the PANC-1 and PSC cells. The seeding ratio of 1: 2 and 1: 3 were used as they were reported to have biological relevance.^[318]

The spheroids were allowed to grow for 14 days or 21 days to gain a spheroid size that resembled the metabolic stratification of the tumour tissue. Daily images were taken to monitor their diameter and volume and assess spheroid growth. Figure 4.2 shows the cells cultured in the ULA plates from the day of seeding to day 7 of culture. Supplementary videos 1 – 3 show the aggregation of the PSC only cells, PANC-1 only cells, and PDAC (PANC-1 and PSCs) cells in the ULA plates from the day of seeding to day 3 of culture. The videos were acquired with the IncuCyte® S3 Live-Cell Analysis System at MDC (described in section 3.2.4). Twenty-four hours after seeding, the cells aggregated into a spherical-like structure. With the hydrophilic coating of the wells of the ULA plates, cell-cell interactions dominate over cell-plastic interactions, thus facilitating spheroid formation. By day 7, the cells are compact within the 3D spheroid structure.



Figure 4.2. 3D spheroid culture of the off-chip PDAC cultures in ULA plates

Representative bright-field images of the PANC-1 and PSC cells seeded into ULA plate for spheroid culture. Due to the hydrophilic coating of the ULA plate, the cells aggregate into a spheroid structure. Scale bar 200 μ m.

Figure 4.3 shows images of the different culture conditions, PSC only, PANC-1 only, and PDAC (PANC-1 and PSCs in a 1: 2 seeding ratio) spheroids (without TGF- β 1 supplement) on day 14 of culture, and their respective diameter at two cell seeding densities, 500 and 1000 cells per

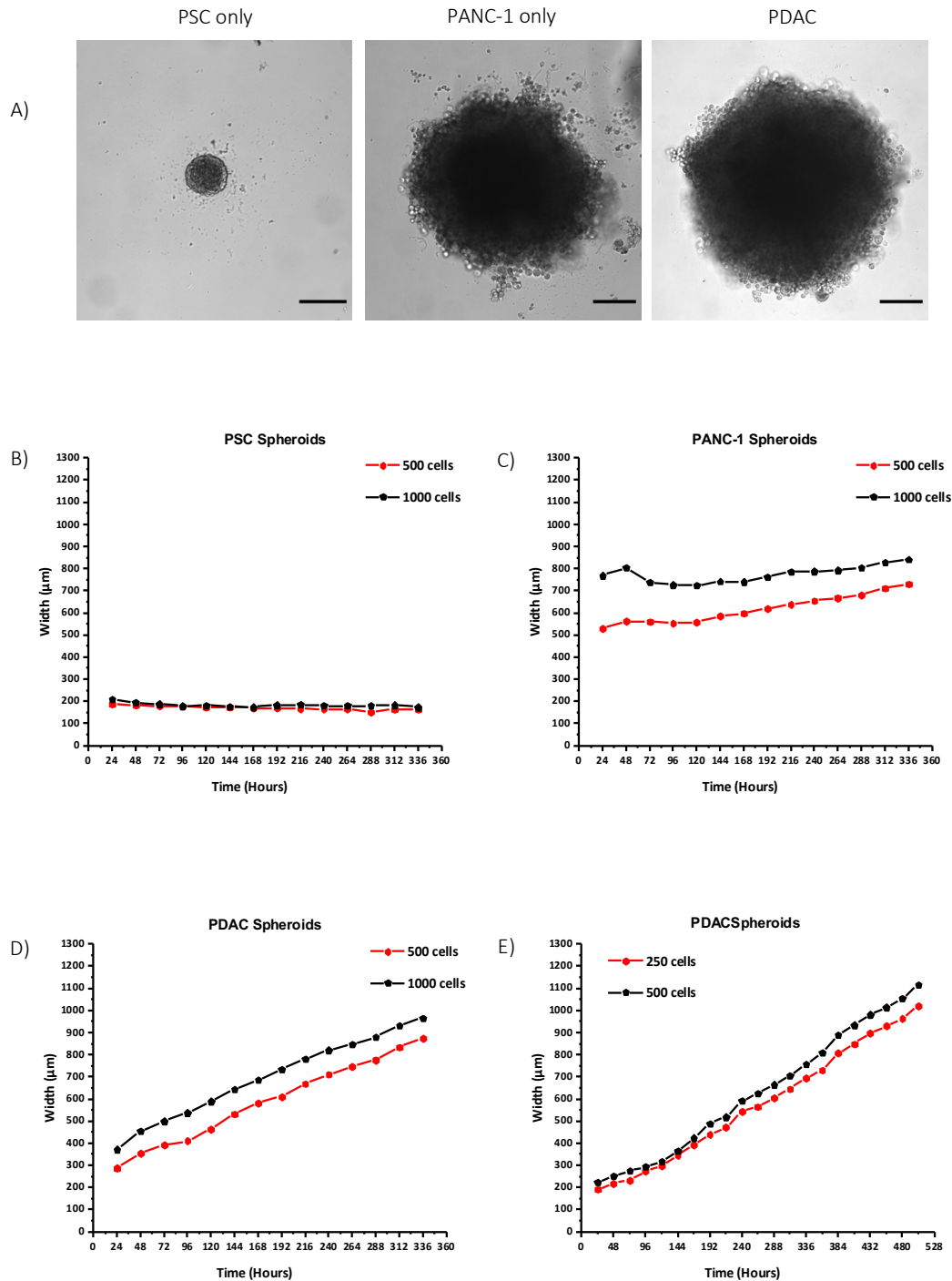


Figure 4.3. Characterisation of the PANC-1 spheroid growth in the presence of PSC cells

A) Bright-field images of the PSC only, PANC-1 only, and PDAC (PANC-1 and PSC, 1: 2 seeding ratio) spheroid cultures on day 14 of culture. Cell seeding density for each of the different spheroid conditions: 1000 cells per well. Scale bar, 200 µm. The diameter of the B) PSC only spheroids for cell seeding densities of 500 and 100 cells per well, and C) PANC-1 only spheroids for cell seeding densities of 500 and 100 cells per well, and D) PDAC spheroids with PANC-1 and PSC cells in a 1: 2 seeding ratio for cell seeding densities of 500 and 100 cells per well, over the 14-day culture period, and the diameter of E) PDAC spheroids with the PANC-1 and PSC cells in a 1: 3 seeding ratio for cell seeding densities of 250 and 500 cells per well, over a 21-day culture period. N = 3 – 9 spheroids generated from 2 separate seeding settings.

well, over the 14-day culture period. The PSC only spheroids were observed to be inactive over the 14-day culture period with no significant growth regardless of seeding density (Figure 4.3B). The PSCs are reported to be quiescent and active only when in co-culture with cancer cells.^[26, 28, 35, 316, 319, 320] The PANC-1 only increased in diameter by 40 % and approximately 14 %, from 500 μm and 700 μm , 24 hours after seeding, to 700 μm and 800 μm , by day 14 of culture, for seeding densities of 500 and 1000 cells per well, respectively (Figure 4.3C). The growth of the PANC-1 spheroids with PSCs, the PDAC spheroids (Figure 4.3D), increased in diameter by > 100 % in comparison to the PSC only and PANC-1 only spheroid cultures. The PDAC spheroid diameter was 290 μm and 370 μm , 24 hours after seeding, and 880 μm and 960 μm , by day 14 of culture, for 500 and 1000 cell seeding densities, respectively. The PDAC spheroid growth rate, the time it takes for the spheroid size to double in volume, was approximately 3 days, irrespective of seeding density and seeding ratio between the PANC-1 and PSCs (Figure 4.3D and E, and Table 4.1).

The effect, increasing compactness and growth, of the PSC cells on the PANC-1 spheroids are in line with findings from Ware *et al.* 2016 and Pednekar *et al.* 2021.^[104, 129, 144] Ware *et al.* cultured PDAC cancer cells with PSC cells to model the stromal constituent of the PDAC tissue, and they found spheroids with increasing structural integrity – more compact – with high Ki67 expression, a proliferation marker. Pednekar *et al.* presented a PANC-1: PSC culture model with the cellular arrangement and genetic profile of the PDAC tumour tissue and counted the number of cells in the cultures. They found the number of cells significantly increased in cultures with PSC cells in comparison to the PANC-1 only cultures.

*Table 4.1. Doubling time of the PANC-1 spheroid cultures in the presence of PSC cells
The doubling time in days of the PDAC spheroid cultured for 14 or 21 days, n = 3 to 9 spheroids
generated from 2 separate seeding settings*

| Culture | Seeding density | Seeding ratio between PANC-1 and PSC cells | Cultured for [in days] | Mean volume [mm³] on day 1 (24 hours after seeding) | Mean volume [mm³] on day 14 or 21 of culture | Mean doubling time [in days] |
|----------------|------------------------|---|-------------------------------|---|--|-------------------------------------|
| PDAC | 250 | 1: 3 | 21 | 0.005 ± 0.001 | 0.62 ± 0.04 | 2.91 ± 0.06 |
| PDAC | 500 | 1: 3 | 21 | 0.009 ± 0.002 | 0.84 ± 0.10 | 3.08 ± 0.07 |
| PDAC | 500 | 1: 2 | 14 | 0.017 ± 0.005 | 0.37 ± 0.01 | 2.91 ± 0.29 |
| PDAC | 1000 | 1: 2 | 14 | 0.034 ± 0.003 | 0.50 ± 0.02 | 3.34 ± 0.13 |

A seeding ratio of 1: 3 between the PANC-1 and PSC cells for culture was chosen for subsequent assessments. In Figure 4.3E, the PDAC spheroids were cultured for 21 days to investigate the long-term effect of the PSC cells on the PANC-1 spheroid growth. Supplementary video 4 shows incuocyte videos of the co-culture of labelled PANC-1 cells (labelled with Qtracker dye as described in section 3.3) and unlabelled PSC cells in the ULA plate. Labelled PSC cells were not used for culture as the Qtracker dye was observed not to retain well in the cells. With PSC cells, most of the PANC-1 cells were observed to be at the centre of the spheroids, and the PANC-1 spheroid growth increased steadily and mirrored the nutrient availability and oxygen gradient of the PDAC tissue as a solid tumour.

Figure 4.4 shows the live/dead viability assessment of the PDAC spheroid cultures using Hoechst, Calcein AM, and ethidium homodimer-1 (EthD-1). The live/dead viability assessment was used to investigate the viability of the PDAC spheroids cultured for 21 days. However, with the ability of spheroids to mimic the gradients of nutrients and oxygen in solid tumours,^[40, 104, 108, 111] the PDAC spheroids exhibited an outer region of proliferative cells, shown with the Calcein Am stain in green, where the cells had enough nutrients to undergo cell division, a region of quiescent cells, shown with Hoechst stain in blue, where the cells were alive but did not have enough nutrients and oxygen for cell division, and a central hypoxic environment with dead cells shown with EthD-1 stain in red, where there was a limited supply of nutrients and oxygen.

With the PSC cells surrounding the PANC-1 cells, and due to the activity of the PSC cells on the PANC-1 cells, where there is increasing compactness and growth, there was a limited perfusion of nutrients and oxygen through the spheroids, rendering the cells to be in different metabolic states. Again, these findings are in line with observations by Ware *et al.* 2016, Zanoni *et al.* 2016, and Pednekar *et al.* 2021.^[104, 112, 144] Ware *et al.* and Zanoni *et al.* present spheroids of which there were non-viable cells at the spheroid core, highly proliferative cells at the culture periphery, and cells in a quiescent state in between. Pednekar *et al.* looked at the cellular arrangement of PDAC tumour tissues and observed the pancreatic duct, with CK19 expression, surrounded by high amounts of α -SMA expressing cells (CAFs/PSC cells). They, therefore, based their PANC-1: PSC cultures on this cellular arrangement, where pancreatic cancer cells were surrounded by PSC cells.

Figure 4.5 shows the metabolic activity, ATP viability assessment, of the PDAC spheroids, over the 21-day culture period. Over the 21-day culture period, there was an increase in the ATP content of the PDAC spheroids, showing the cultures were viable.

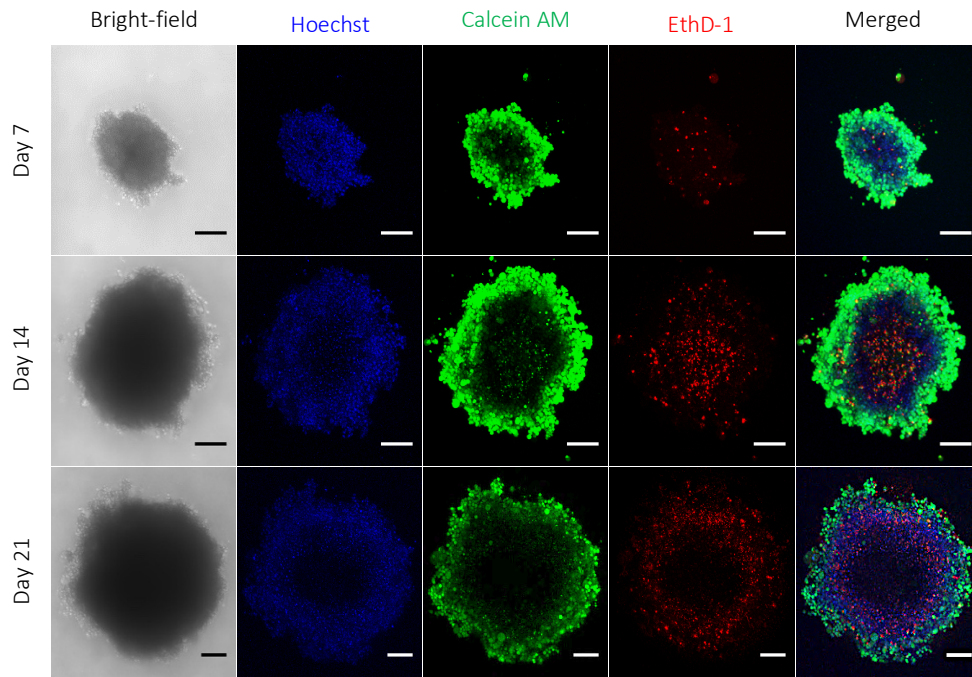


Figure 4.4. Live/dead viability of the PDAC spheroids

Confocal images of the live/dead viability assessment of the PDAC spheroids (PANC-1 and PSC cells in a 1:3 seeding ratio) of a seeding density of 250 cells per well, cultured for 21 days, with Hoechst for the cell nucleus in blue, Calcein Am for live cells in green, and Ethidium homodimer-1 (EthD-1) for dead cells in red. Scale bar 200 μ m.

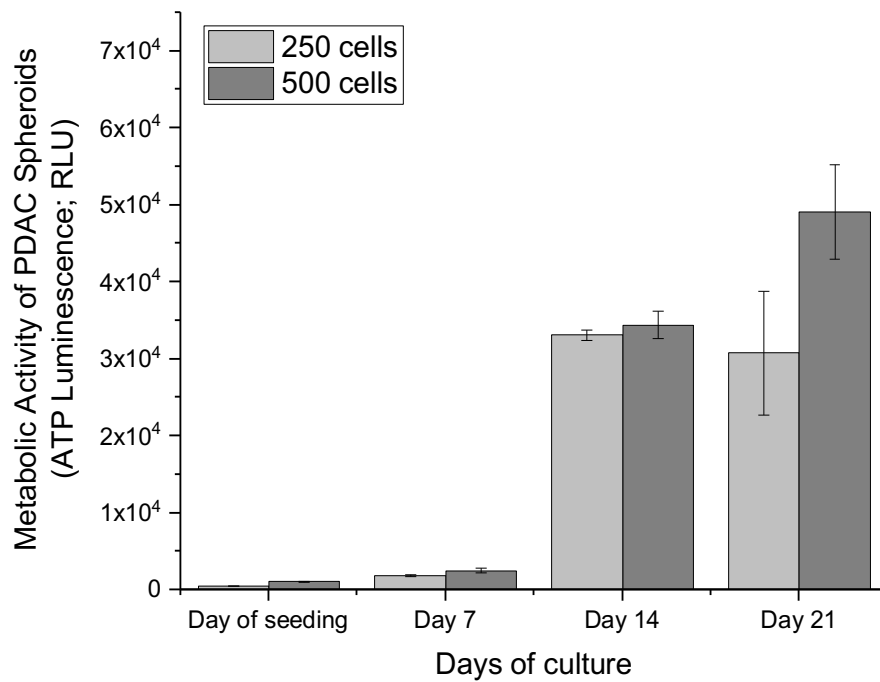


Figure 4.5. Metabolic activity of the PDAC spheroids

ATP viability assessment of the PDAC (PANC-1 and PSC cells in a 1: 3 seeding ratio) of seeding densities of 250 cells and 500 cells per well, from the day of seeding until day 21 of culture .

In vivo, PSC cells are reported to increase the growth of the PDAC cancer cells, and this is shown here with the size and growth assessments of the cultures. In the presence of PSC cells (irrespective of size or seeding ratio between the cells), the PANC-1 size and growth were enhanced. This shows that the PANC-1 culture with PSCs mimics the growth behaviour of the PDAC tumour tissue. Assessments on how viable the cultures were also confirmed that not only were the spheroid growth increasing but also attained the stratified metabolic activity of the tumour tissue.

4.2. The mechanical stiffness of the PDAC cultures

PANC-1 and PSC cells were seeded into culture dishes with 6 – 9 mg mL⁻¹ BME gel for PANC-1 only, and PDAC cultures with and without TGF-β1 supplement (10 ng mL⁻¹), and their mechanical stiffness was characterised with oscillatory shear rheology. Seeding of the cells with BME gel for culture with TGF-β1 and for mechanical assessment is as described in sections 3.4.2 and 3.5, respectively.

Prior to characterising the culture mechanical stiffness, the effect of TGF-β1 on the growth of the PDAC cultures was assessed. The cells were seeded into ULA plates and cultured with TGF-β1. Figure 4.6 shows the growth of the spheroid cultures with and without TGF-β1. Again, the PSCs in the PSC only spheroids were inactive with and without TGF-β1. The growth of the PANC-1 only spheroids with TGF-β1 was increased in comparison to PANC-1 only spheroids without TGF-β1. The PANC-1 spheroid cultures without TGF-β1 had a percentage size increase of > 100 % from day 5 of culture (spheroid diameter of 500 μm) to day 21 of culture (spheroid diameter of 1110 μm), but when supplemented with TGF-β1, the percentage size increase was 42 % between day 5 of culture (spheroid diameter of 823 μm) and day 21 of culture (spheroid diameter of 1172 μm). TGF-β1 is reported to increase the activities of cells. However, the increase in spheroid size does not appear to be as significant as with the PDAC spheroids without TGF-β1. The percentage size increase was about 70 % between day 5 of culture (spheroid diameter of 688 μm) and day 21 of culture (spheroid diameter of 1172 μm), and with the PDAC spheroids with TGF-β1, the percentage size increase of about 26 % between day 5 of culture (spheroid diameter of 977 μm) and day 21 of culture (spheroid diameter of 1237 μm). This could be as a result of the effect of TGF-β1 on ECM production, which affects how dense and compact a spheroid is. TGF-β1 increases the activity of PSCs for the overproduction of, *i.e.*, collagen, which increases the solid stress in the spheroids. This makes

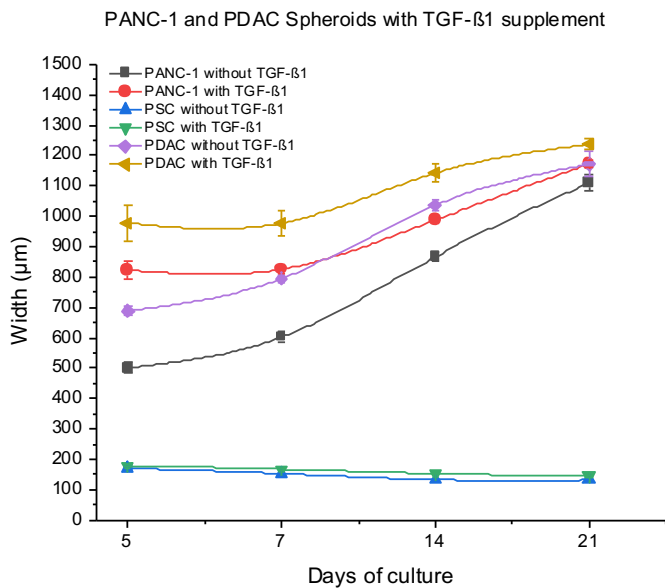


Figure 4.6. Effect of TGF-β1 on PANC-1 growth in the presence of PSC cells

The spheroid diameter of the PSC only, PANC-1 only, and PDAC (PANC-1 and PSC cells in a 1: 3 seeding ratio) spheroids with and without 10 ng mL^{-1} TGF-β1 growth factor supplement. $N = 6$ spheroids per culture condition generated from 2 separate seeding settings.

the cells contract, and as such, the spheroids become dense and compact. Therefore, the overall size increase for the PDAC cultures with TGF-β1 does not appear to be as significant as the PDAC cultures without TGF-β1 by day 21 of culture, which are not as compact.

Figure 4.7A shows images of the PDAC cultures in BME gel with TGF-β1 supplement. With the BME gel, the cells aggregated into 3D structures. Figure 4.7B shows the metabolic activity, ATP viability assessment, of the different culture conditions grown in BME gel with TGF-β supplement on day 21 of culture. As the cultures become complex, *i.e.*, co-culture of the PDAC cells with TGF-β1 supplement, there was an increase in the ATP content.

TGF-β signalling promotes the growth, invasion, and metastasis of PDAC by enhancing the activity of PSC cells. This influences the PDAC cancer-PSC cell interactions for a favourable tumour microenvironment,^[311, 314, 321-323] and therefore the increased growth (size) and metabolic activity of the PANC-1 spheroids in the presence of PSC cells and TGF-β, in comparison to the PSC only cultures and the PANC-1 only cultures with and without TGF-β supplement.

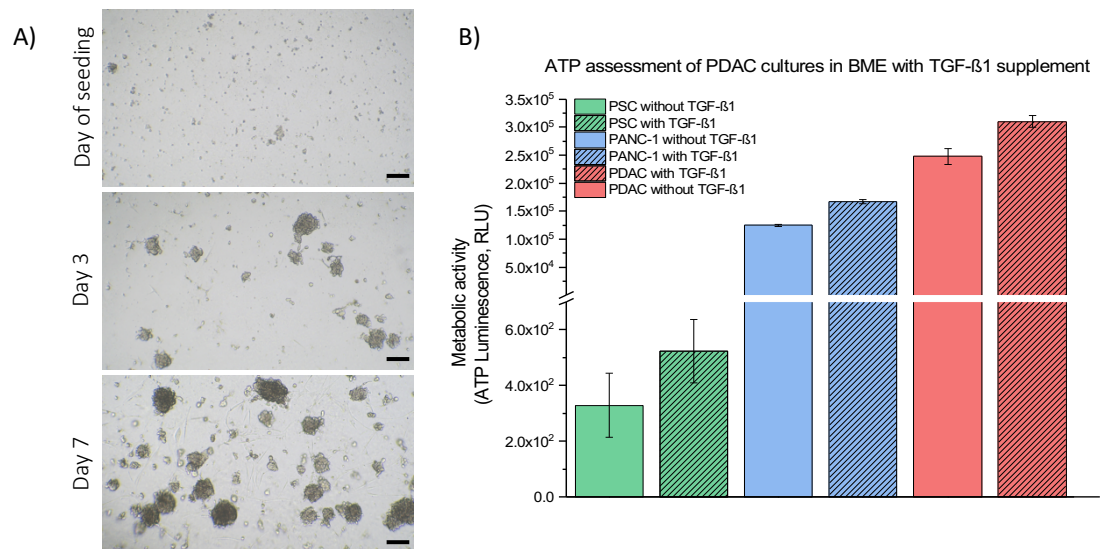


Figure 4.7. The off-chip PDAC cultures with TGF-β1

The culturing and viability assessment of the off-chip PDAC cultures. A) Representative bright-field images of the PANC-1 and PSC (at a 1: 3 seeding ratio) cells seeded into culture dishes with BME gel (6 – 9 mg mL⁻¹) for culture with TGF-β1 (10 ng mL⁻¹) supplement. With the BME gel the cells aggregated together into a 3D structure by day 7 of culture. Scale bar: 200 μm. B) The metabolic activity, ATP viability assessment, of the different culture conditions grown in BME gel with the TGF-β1 supplement on day 21 culture. N = 2 culture plate per culture condition generated from 2 separate seeding settings.

For mechanical stiffness characterisation, the PANC-1 only and PDAC cultures, grown for 45 days with and without TGF-β1, were assessed using oscillatory shear deformation. As the PSC only cultures were inactive on their own (Figures 4.3A and 4.6), their mechanical stiffness was not characterised. The storage or elastic modulus (G') and the loss or viscous modulus (G'') components of the PANC-1 only and PDAC cultures with and without TGF-β1 were measured, and steady state values of G' and G'' measurements were extracted from the time sweep curves as described in section 3.5.

Figure 4.8 shows exemplar plots of the time sweep curves with the G' and G'' measurements for the PDAC cultures with and without TGF-β1 supplement, and exemplar box magnification of the steady-state measurements on day 0 for the PDAC cultures without TGF-β1 and day 45 for the PDAC cultures with TGF-β1, where the G' and G'' measurements were extracted. Figure 4.9A and B show plots of the average of the extracted G' and G'' measurements for the different culture conditions over culture time. It shows an increase in the elastic component and the viscous components of the cultures, corresponding to the mechanical properties of the ECM produced and that of the resulting mechanical effect on the cells, with increasing culture time. On day 45, there is a decrease in the loss modulus with an increase in the storage

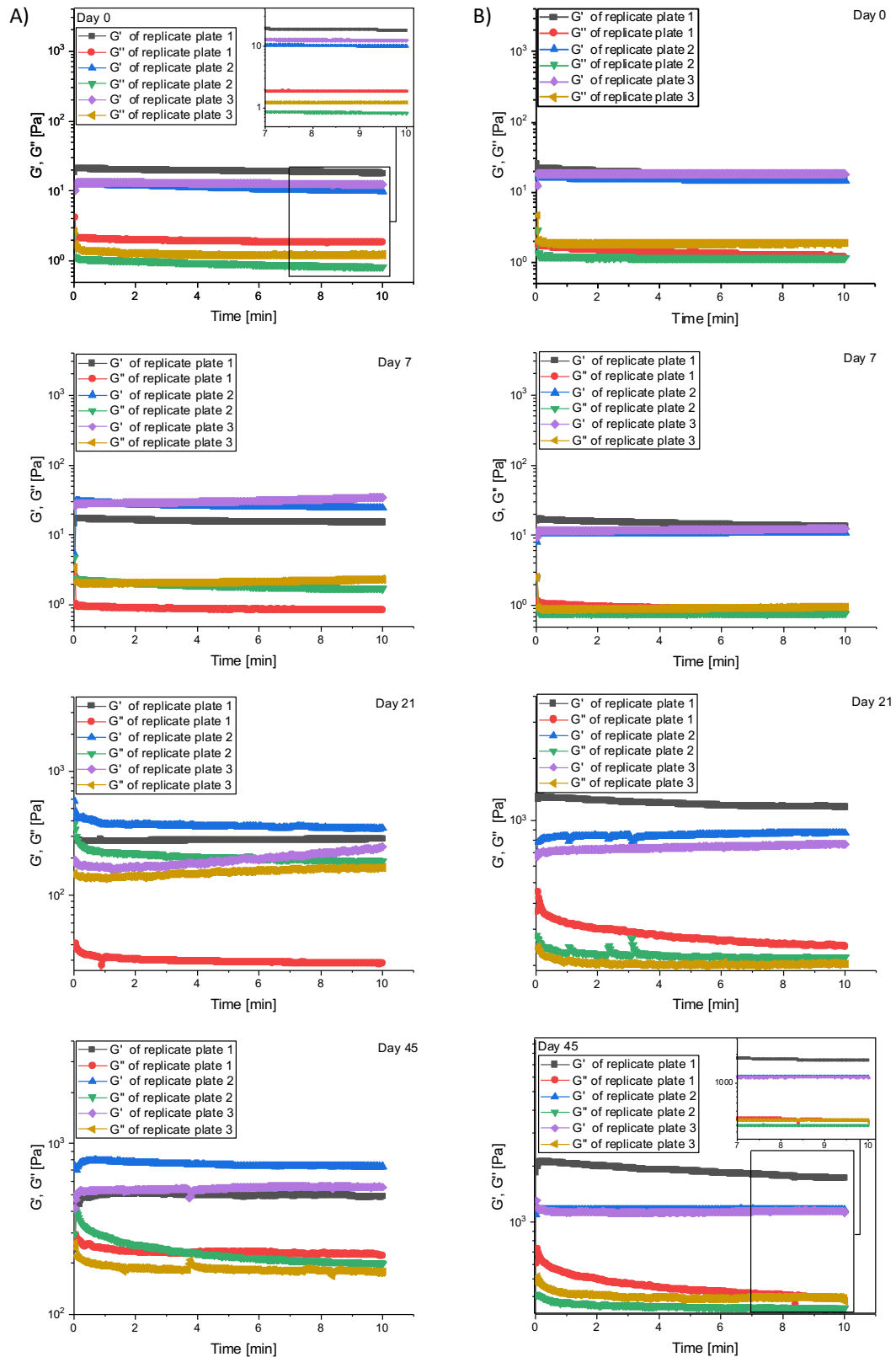


Figure 4.8. Examples of the G' and G'' moduli measurement of the off-chip PDAC cultures

The G' and G'' measurements of the PDAC cultures A) without and B) with TGF- β 1 on day 0 (3 – 4 hours after seeding), day 7, day 21, and day 45 of culture, of which an average of their steady state measurement over time, as seen in the box magnification for the PDAC cultures without TGF- β 1 on day 0 and for the PDAC cultures with TGF- β 1 on day 45 of culture, was used to determine their complex shear modulus, G^* .

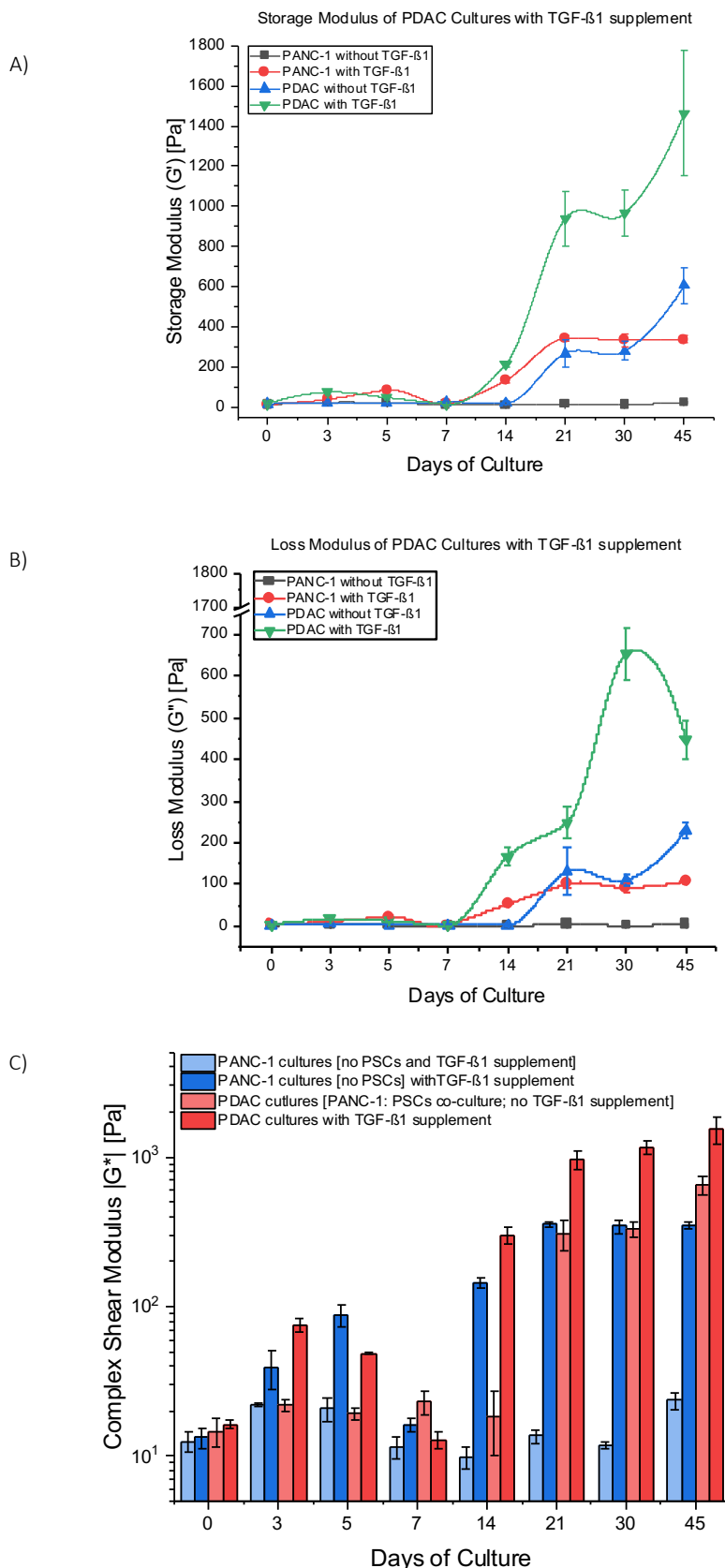


Figure 4.9. Mechanical stiffness characterisation of the off-chip PDAC cultures

The average A) storage (G'), and B) loss (G'') moduli measurements of the PANC-1 only cultures and PDAC (PANC-1 and PSC co-culture at a seeding ratio of 1: 3) cultures with and without TGF- β 1 (10 ng mL^{-1}) supplement, extracted from the time sweep curves. C) The complex shear modulus G^* , mechanical stiffness, of the PANC-1 only and PDAC cultures with and without TGF- β 1. $N = 9$ culture plates per culture condition generated from three separate seeding settings.

modulus. The increase storage modulus on day 45 in comparison to the decrease loss modulus could be as a result of increasing cross-linking of, *i.e.*, collagen fibres from increasing ECM deposition. It has been shown that an increase elastic modulus is proportional to the cross-linking degree of fibres, which results in a dense network structure contributing to overall stiffness.^[324, 325] Therefore, the energy stored in the cultures with deformation (section 2.1) on day 45 was greater, accounting for the increased and decreased storage and loss modulus, respectively, observed. Using the G' and G'' measurements with *Equation 4* (section 2.1), the complex shear modulus for the different culture conditions was calculated. Figure 4.9C shows the mechanical stiffness, the complex shear modulus G^* , calculated.

The PANC-1 only cultures and PDAC cultures, in the absence of TGF- β 1 growth factor supplement, were observed to have a G^* of 13 Pa (± 2) and 15 Pa (± 3), respectively, 3 – 4 hours after seeding. After a 45-day culture, the G^* of the PANC-1 only and PDAC cultures was 23 Pa (± 3) and 650 Pa (± 9), respectively. With TGF- β 1, on day 45 of culture, G^* of the PANC-1 cultures increased to 350 Pa (± 18). However, the G^* of the PDAC cultures on day 21 of culture was 970 Pa (± 143), a value corresponding to an Elastic Young's modulus (E) of 2.9 kPa (using *Equation 5*, section 2.1) and approaching the mechanical stiffness measured for the *in vivo* PDAC tissue. The Elastic Young's modulus of solid tumours, including the PDAC tumour tissue, is reported to range between 1 – 68 kPa in comparison to normal tissue rigidity, which ranges between 0.38 – 7 kPa.^[21, 46, 89, 326, 327] Rice *et al.* 2017 and Wex *et al.* 2014 investigated the mechanical stiffness of healthy and fibrotic or pancreatic cancer tissues. Rice *et al.* measured an Elastic Young's modulus ranging between 3 – 4 kPa for PDAC tissues, and Wex *et al.* measured a complex shear modulus ranging between 1 – 3 kPa for human fibrotic pancreatic tissues.^[21, 89] Here, on day 45 of culture, G^* of the PDAC cultures with TGF- β 1 was 1500 Pa (± 310). A decrease in G^* between day 5 and day 14 of culture was likely due to the secretion of enzymes and proteases by the cells, mediated by PSCs, for the remodelling of the matrix environment for a fibrotic stroma to support their growth.^[17, 26, 28, 46, 48, 58, 313]

Rice *et al.* showed with increased collagen density, during the progression of the disease pancreas from a premalignant lesion (PanIN) to PDAC, there is increasing tissue stiffness.^[21] Lai *et al.* 2020, using microfluidics as a platform for their culture model and second harmonic generation (SHG) imaging, also showed increased collagen deposition with fibroblast or PSC cells and TGF- β 1, corresponding to increasing culture stiffness.^[39] Robinson *et al.* 2016 showed PSCs to be central to the remodelling of the matrix environment of their cultures, where increased PSC cell number correlated with increased collagen alignment in the matrix

environment.^[58] With PSC cells, and TGF- β 1, there is increasing ECM production, *i.e.*, collagen, increasing fibre cross-linking and thus in mechanical stiffness as measured for the cultures.

Frequency sweep measurement was done to assess the time-dependent behaviour of the cultures. Frequency sweep measurements show the physical strength and cohesiveness of a sample in a time dependent manner. Figure 4.10 shows exemplar plots of the frequency sweep measurements with the G' and G'' components of the PDAC cultures with and without TGF- β 1. It shows that the G' measurements were greater than the G'' measurements, indicating that the culture samples were more structurally elastic. Moreover, with both measurements relatively constant, it shows the G' and G'' components of the cultures were independent of frequency. These show the networks in the cultures – of the matrix environment, cell-cell interactions, and cell-matrix interactions – were structurally stable during the oscillatory shear deformation.

Figure 4.11 shows a plot example of the range of normal forces measured by the parallel plate rotary system to ensure contact with the cultures during deformation. The range of normal forces – low, medium, high range – measured indicates that when there was a change in the volume (an expansion or contraction) of the culture samples as a result of a temperature change or moisture loss, for example, the rotary system was able to adapt (increase or decrease) the gap between the parallel plate geometry and culture to ensure continuous contact for deformation.

Figures 4.12A and B show exemplar bright-field and binarized images, respectively, used to assess the ratio of cells versus matrix between the different culture conditions with increased culture time, Figure 4.12C. Bright-field images of the PANC-1 only and PDAC cultures with and without TGF- β 1 were analysed with ImageJ to determine if the measured mechanical stiffness (Figure 4.9C) was due to differences in cell number, size or number of the spheroid cultures. Figure 4.12C shows the ratio of cells versus matrix against the day of culture for the different culture conditions. The relative volume occupied by the cells versus matrix gel environment did not differ between the different culture conditions with increasing culture time. This shows the mechanical stiffness measured was not due to the number of cells present, which increased with culture time. Moreover, Figure 4.13 shows G' , G'' , and G^* , and frequency sweep measurements of just BME gel over a 21-day incubation period. An overall decrease in G^* , over the 21-day culture period, demonstrates the measured mechanical stiffness for the PANC-1 cultures in the presence of PSC and TGF- β 1 supplement could have been due to the cells remodelling their matrix for an environment to support their growth.

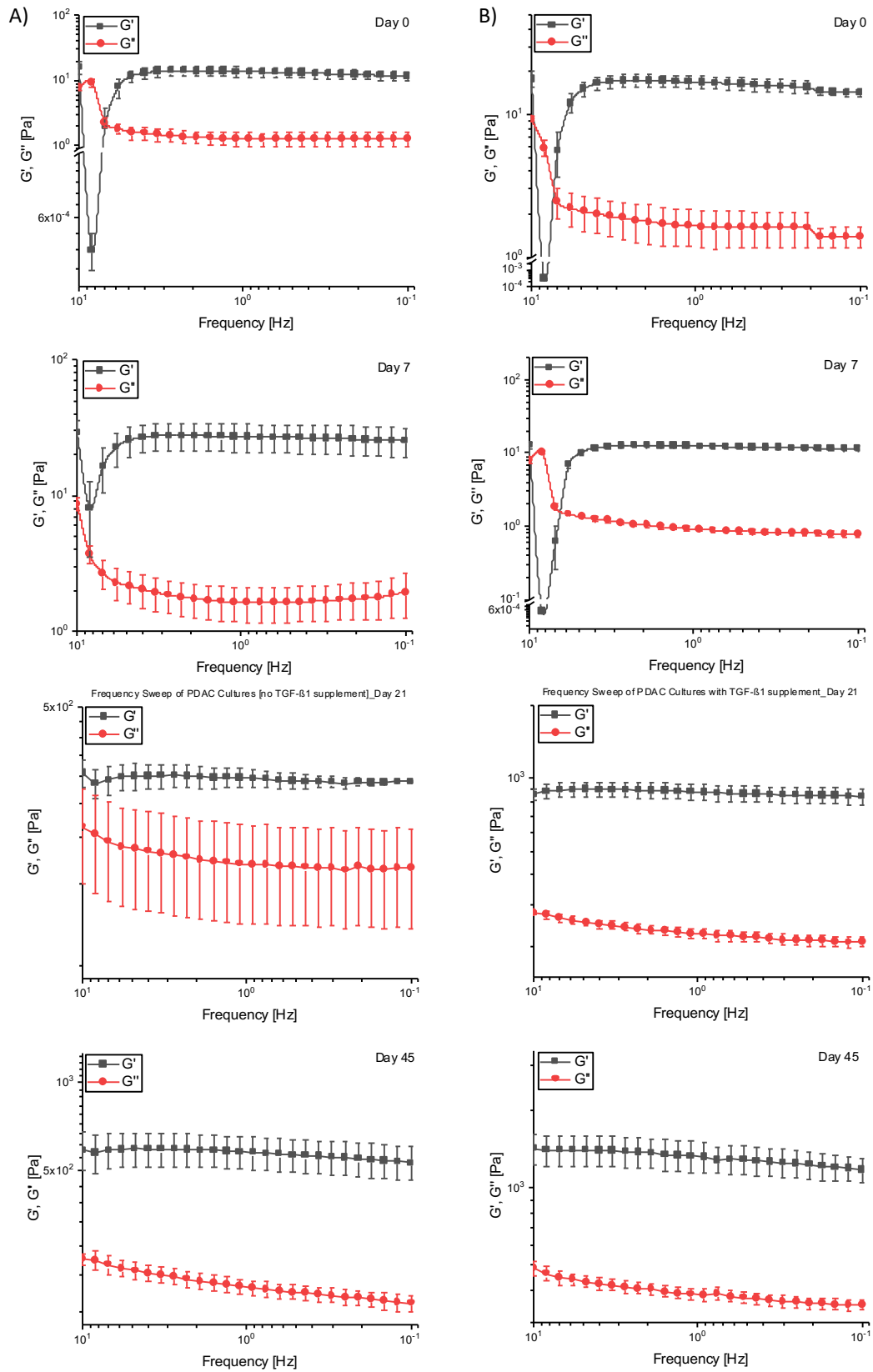


Figure 4.10. Examples of the frequency sweep measurements

The frequency sweep measurements of the G' and G'' measurements of the PDAC cultures A) without and B) with TGF- β 1 on day 0 (3 – 4 hours after seeding), day 7, day 21, and day 45 of culture at 2 % shear strain.

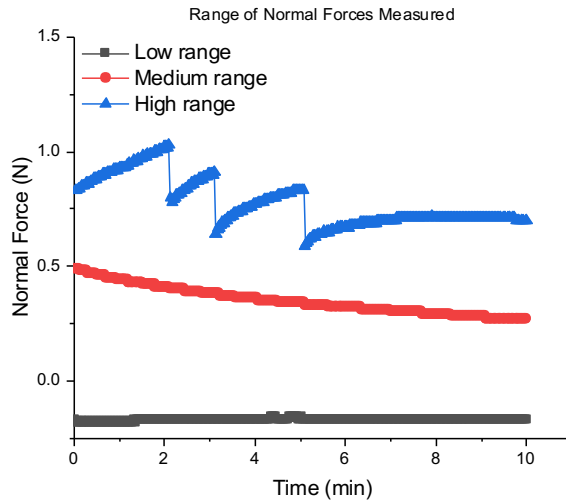


Figure 4.11. Range of normal forces measured by the parallel plate rotary system

Examples of the range of normal forces measured by the parallel plate rotary system to ensure contact with the cultures during oscillatory shear deformation with the rheometer.

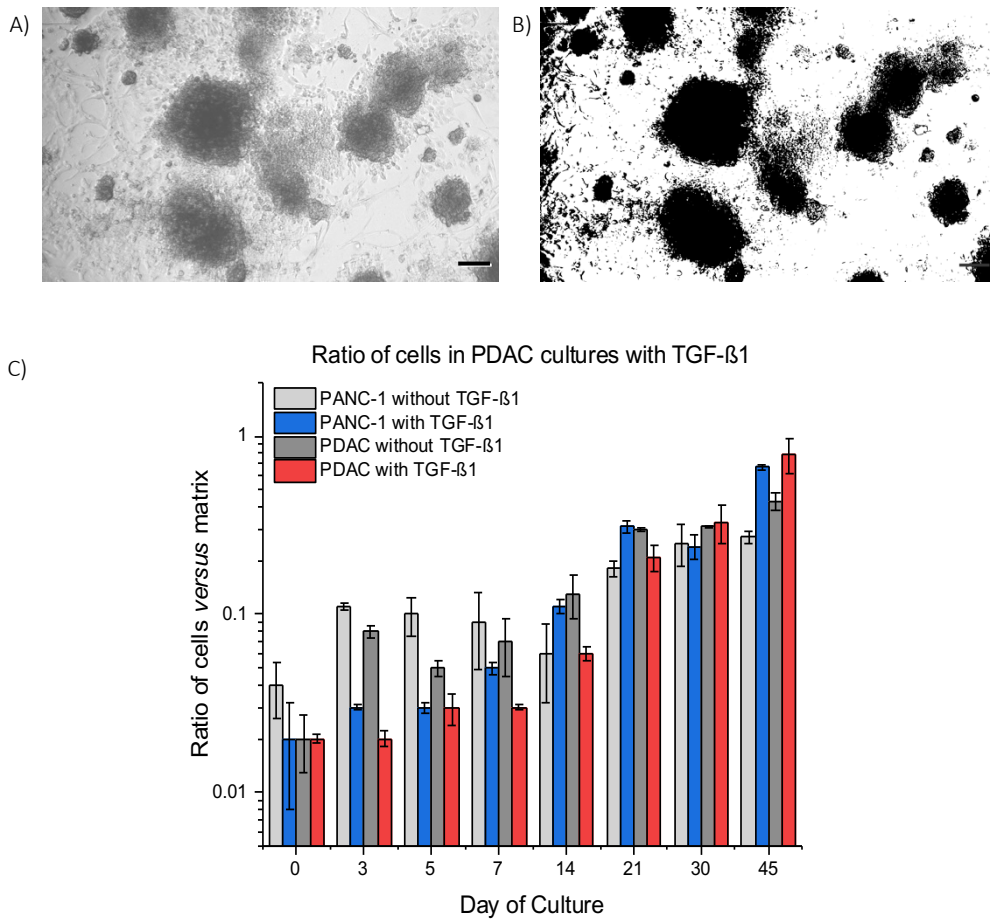


Figure 4.12. Ratio of cells in the off-chip PDAC cultures

A) Representative bright-field and B) its binarized image of off-chip PDAC culture with TGF-β1 on day 21 of culture to determine the C) ratio of cells in the different culture conditions versus the matrix environment. N = 3 – 5 images from the 9 culture plates from 3 separate seeding settings in Figure 4.9. Scale bar: 200 μm.

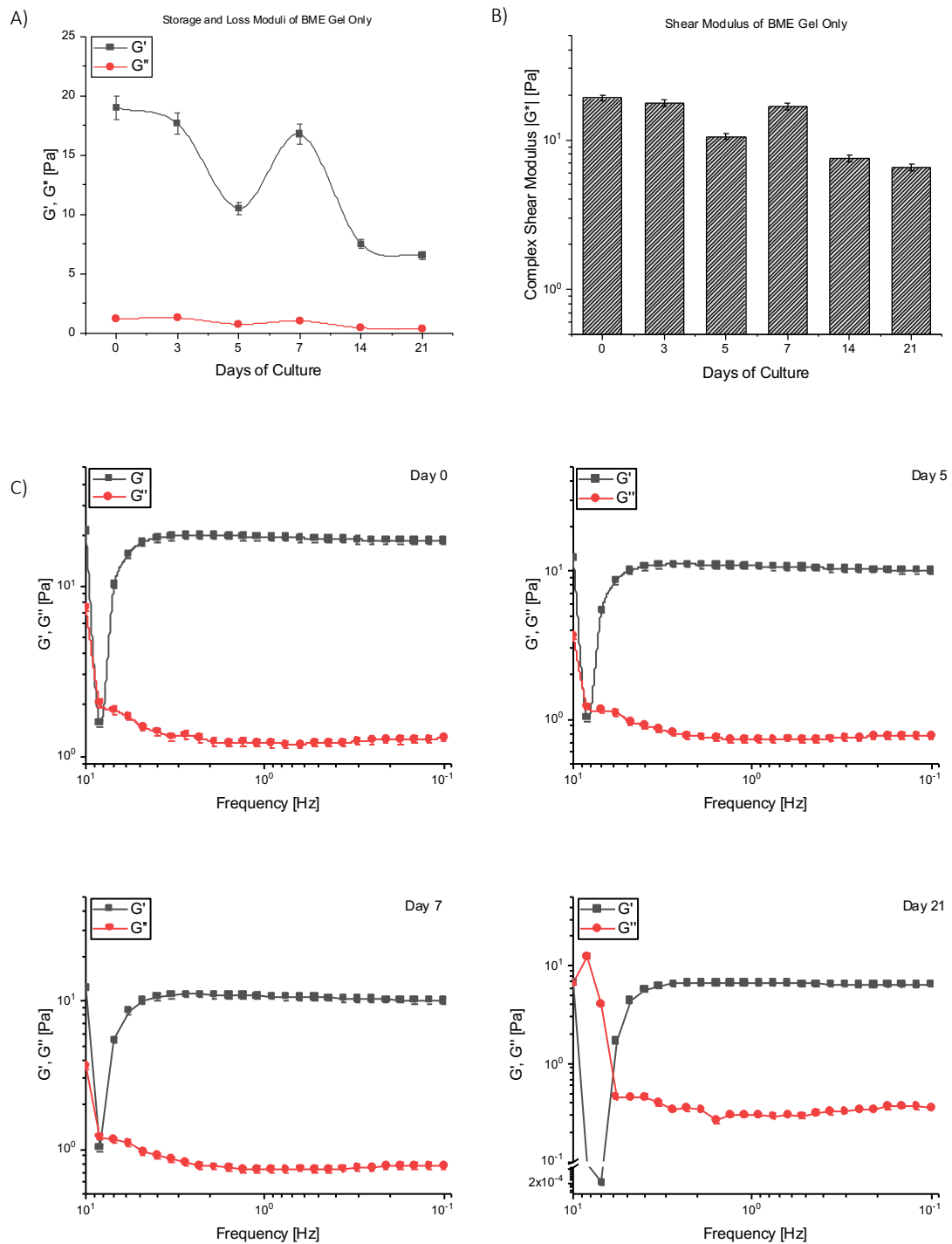


Figure 4.13. The mechanical characterisation of BME gel

The A) G' , G'' and B) G^* , and C) frequency measurements at 2% shear strain of $6 - 9 \text{ mg mL}^{-1}$ of BME gel over a 21-day incubation period.

To determine if the measured mechanical stiffness was due to the production of ECM, accounting for the fibrotic-like structures in the matrix environment (Figure 4.12A), the PANC-1 only cultures, and PDAC cultures with and without TGF- β 1 (10 ng mL⁻¹) supplement, were fixed and stained for collagen type I on day 7, 14, 21, and 30 of culture. The immunofluorescence stain for collagen type I is as described in section 3.6. Figure 4.14 and Figure 4.15 show images of the immunofluorescence stain for collagen in the PANC-1 only and PDAC cultures with and without TGF- β 1. Without TGF- β 1, the PANC-1 only cultures showed no evidence of collagen in their matrix environment. Collagen was seen mostly at the culture periphery. With TGF- β 1, collagen was also mostly observed at the culture periphery of the PANC-1 cultures (Figure 4.14). In the PDAC cultures without TGF- β 1, some collagen was observed in the matrix environment by day 30 of culture, but with TGF- β 1, the PDAC cultures exhibited more collagen in the matrix environment by day 21 of culture, which was much more on day 30 of culture (Figure 4.15). This shows with the presence of PSC cells and TGF- β 1 supplement, there is the overproduction of ECM macromolecules, which is exacerbated by TGF- β 1,^[26, 34, 35, 42, 48] and this accounted for the increasing mechanical stiffness measured for the cultures (Figure 4.9C) and reflected in their increasing elasticity and viscosity (Figures 4.9A and B).

The increase in elasticity and viscosity are due to the concentration, organisation, and mechanical properties of ECM components. Fibrillar collagen and elastin account for the elasticity and stiffness of the ECM, providing cells and tissues with the structure, strength, and extensibility they require to grow and develop. Whereas, glycosaminoglycans, such as hyaluronans, with their ability to absorb fluid and swell, account for the viscosity of the ECM.^[44, 54, 57, 60, 328, 329] Together, the elastic and viscous behaviour of the cultures show the cells sense and adapt to the mechanical forces exerted from the growing heterogeneous ECM.^[42, 45-47, 49-51, 54, 99, 328]

The PDAC tumour tissue exhibit a stroma where collagen type I is the most abundant providing the tumour tissue with its stiffness, and this was achieved here with the culturing of the PANC-1 cells in the presence of PSCs and TGF- β for 21 days.

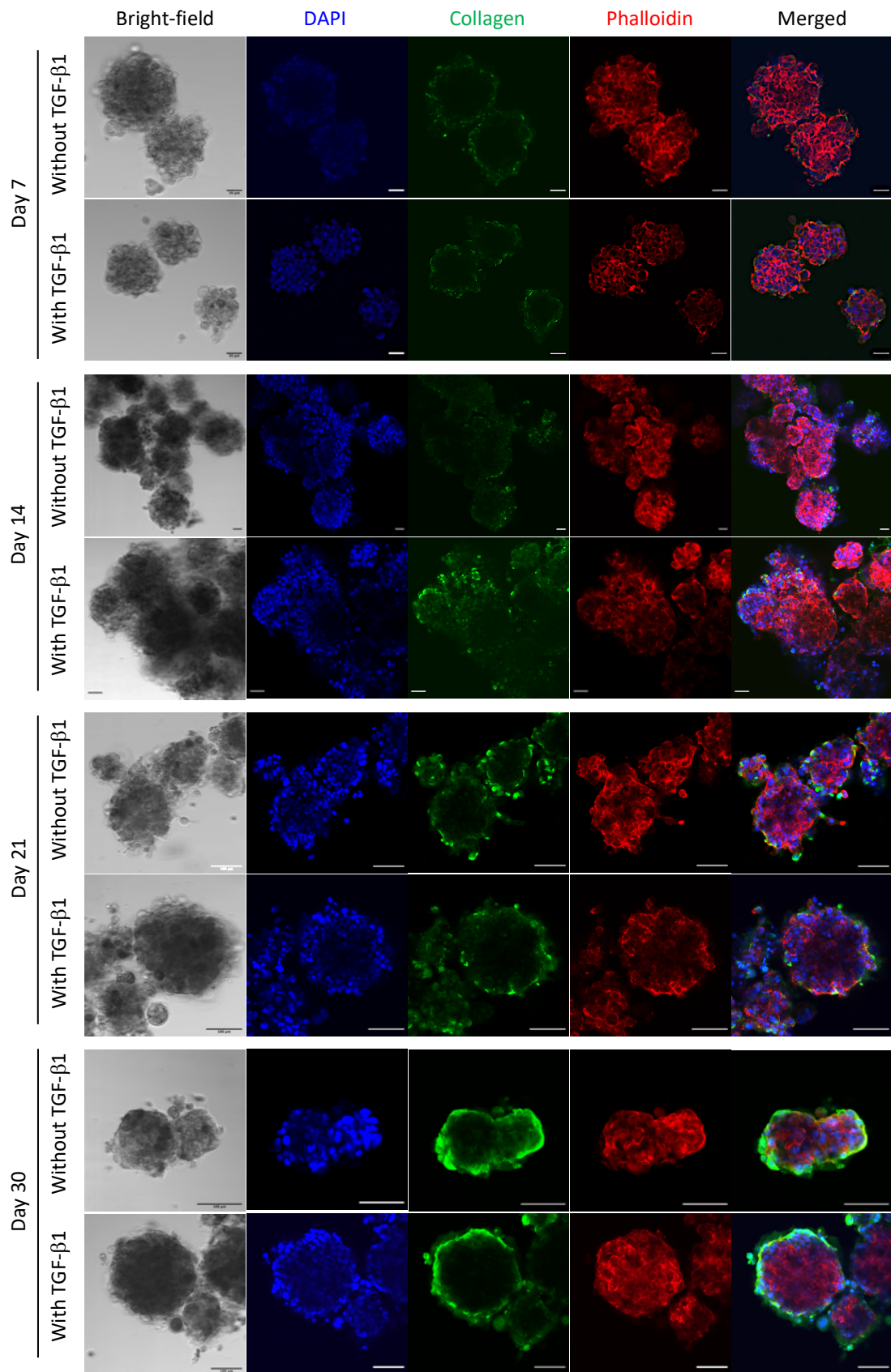


Figure 4.14. Immunofluorescence stain of collagen type I in PANC-1 cultures with TGF- β 1

Representative confocal images of the collagen type I stain in the PANC-1 only cultures with and without TGF- β 1 supplement on day 7, 14, 21, and 30 of culture. Nuclei stained with DAPI in blue, collagen in green, and actin with phalloidin in red. Scale bar on day 7 and 14, 50 μ m. Scale bar on day 21 of culture and 30 of culture, 100 μ m.

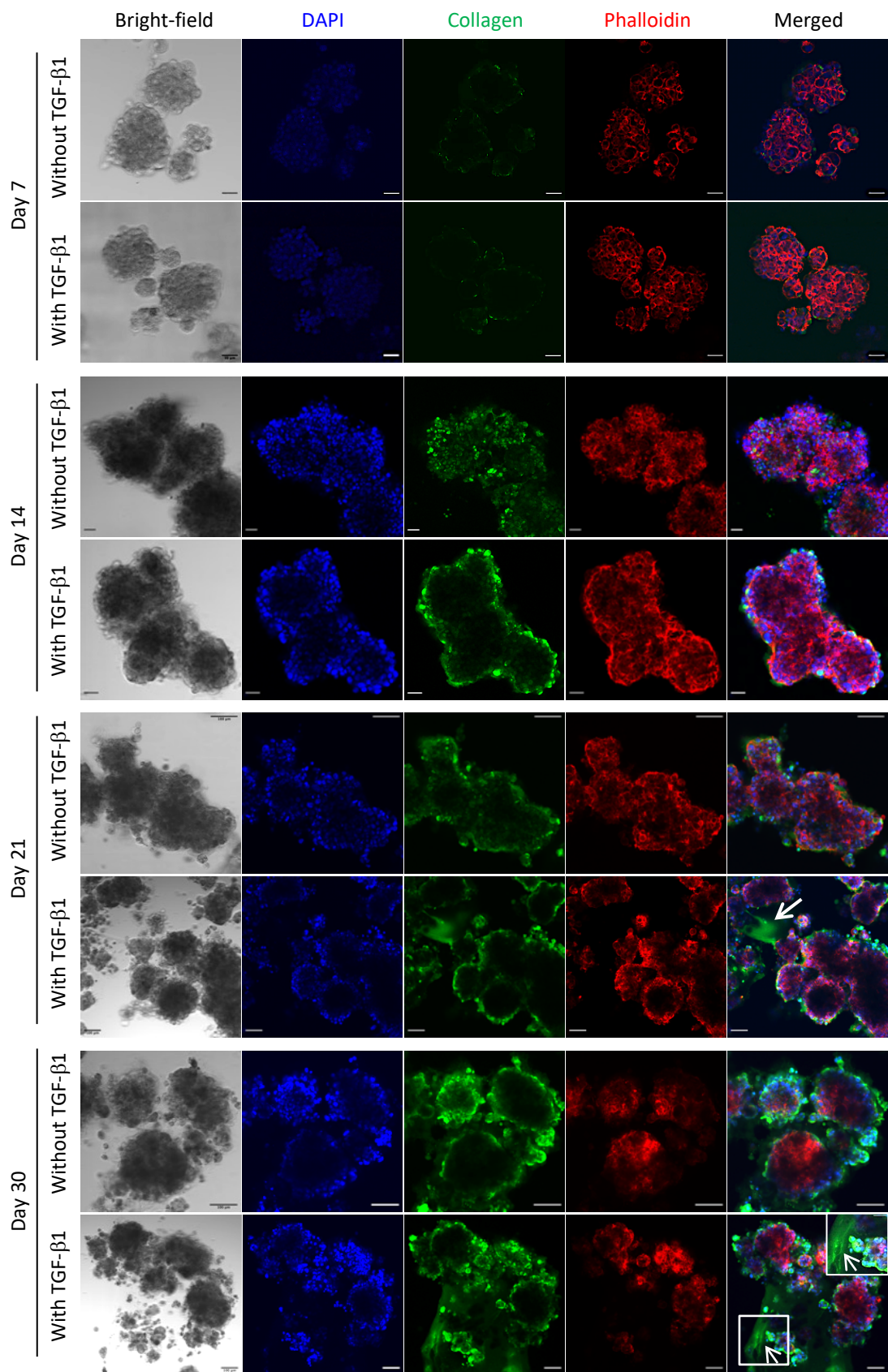


Figure 4.15. Immunofluorescence stain of collagen type I in PDAC cultures with TGF-β1

Representative confocal images of the collagen type I stain in the PDAC (PANC-1: PSCs co-culture in a seeding ratio of 1: 3) cultures with and without TGF-β1 supplement on day 7, 14, 21, and 30 of culture. Nuclei stained with DAPI in blue, collagen in green, and actin with phalloidin in red. Scale bar on day 7 and 14, 50 μm. Scale bar on day 21 and 30 of culture, 100 μm.

4.3. The effect of mechanical stiffness on therapeutic effect

As the fibrotic stroma and resulting tissue rigidity affects the delivery and effect of chemotherapeutics, [17, 18, 21, 24, 46, 105] the effect of gemcitabine on the off-chip PDAC cultures was assessed. First, PANC-1 and PSCs were seeded into ULA plates at a seeding density of 250 cells per well for PSC only, PANC-1 only, and PDAC spheroid cultures with and without TGF- β 1 supplement (10 ng mL⁻¹). The spheroids were grown for 21 days to mimic the PDAC tumour fibrotic stroma and mechanical stiffness. After the 21-day culture, the spheroid cultures were treated with gemcitabine at different concentrations for 72 hours, and their ATP viability was assessed. The seeding of cells into ULA plates for spheroid culture to assess with gemcitabine is described in section 3.11.1. ATP viability assessment is as described in section 3.12.2.

Figure 4.16A shows the timeline of the seeding of the cells for culture, incubation of the cultures with gemcitabine, and ATP viability assessment. Figure 4.16B shows the percentage viability (normalised to controls) versus the different gemcitabine concentrations (in log scale) used. There was a decrease in percentage viability for the different culture conditions with an IC₅₀ of 1.5 (\pm 0.06), 1.4 (\pm 0.06), 1.5 (\pm 0.07), 1.7 (\pm 0.08), 2.1 (\pm 0.09), and 2.08 μ M (\pm 0.13) for the PSC only spheroids without and with TGF- β 1, the PANC-1 only spheroids without and with TGF- β 1, and the PDAC spheroids without and with TGF- β 1, respectively. Z-factor score for the PSC only cultures without and with TGF- β 1, the PANC-1 only cultures without and with TGF- β 1, and the PDAC cultures without and with TGF- β 1 was 0.8, 0.6, 0.8, 0.9, 0.6, and 0.7, respectively. The Z-factor score values between 0.5 – 1.0 show the quality of the ATP assay assessment of the efficacy of gemcitabine on the mechanically stiff cultures was good. [306, 308, 309]

The PDAC spheroids without TGF- β 1 were observed to be resistant to a decrease in percentage viability in comparison to the PDAC spheroid cultures with TGF- β 1 until treated with high gemcitabine concentrations (250 and 500 μ M, log 2.4 and 2.7, respectively). This was believed to be related to the inability of gemcitabine to effectively permeate into and through the spheroid cultures. As seen in Supplementary video 4, most of the PANC-1 cells were at the centre of the spheroids. This was also shown in Pednekar *et al.* 2021, with α -SMA expressing cells surrounding PDAC cancer cells. [144, 189, 191] Moreover, with PSC cells whose activity is increased with TGF- β , the spheroids become compact, and there is increase ECM, which all together limits the perfusion of nutrients and oxygen and of drugs through the culture. This likely accounted for the high gemcitabine concentration required to decrease culture viability. Also, the lack of nutrients and oxygen results in a hypoxic, acidic environment

which also affects the effects of drugs. [68, 71, 73, 108, 330] Even if gemcitabine could permeate through the culture, its activity and effect would be inhibited by the hypoxic and acidic environment.

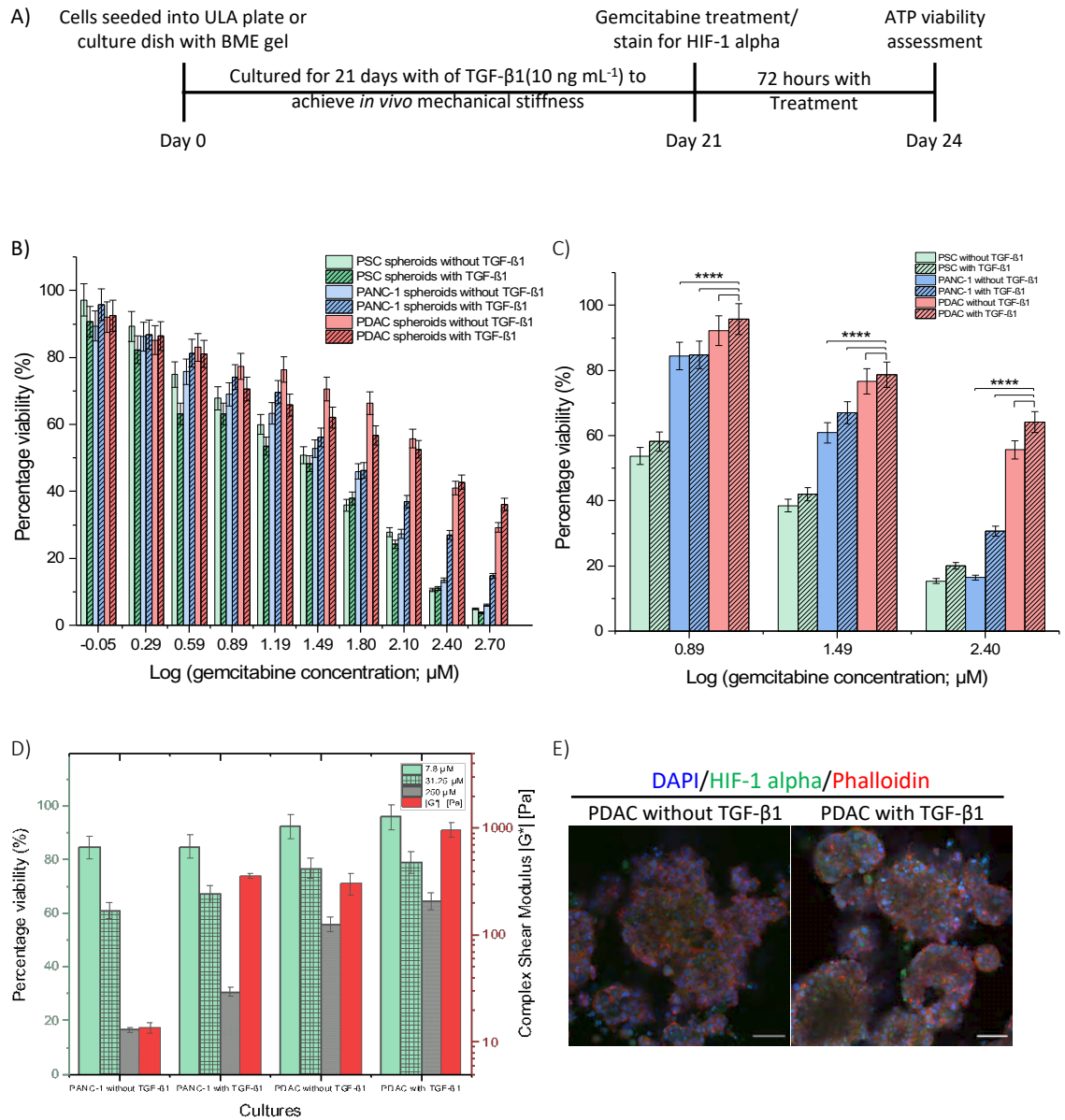


Figure 4.16. The effect of gemcitabine on the off-chip PDAC cultures with TGF-β1

Gemcitabine effect on the PSC only, PANC-1 only, and the PDAC (PANC-1 and PSC co-culture in a 1: 3 seeding ratio) culture with and without TGF-β1 supplement (10 ng mL⁻¹). A) Timeline of the seeding of the PANC-1 and PSC cells for culture to assess with gemcitabine. B) The percentage viability of the different spheroid culture conditions versus the log scale of the different gemcitabine concentrations used. N = 12 spheroids per culture condition generated from two separate seeding settings. C) The percentage viability assessment of the different culture (cells seeded with BME gel) conditions versus the log scale of the gemcitabine concentrations used. N = 4 culture plates generated from two separate seeding settings. D) The percentage viability versus the PANC-1 only and PDAC cultures in C) and their corresponding complex shear modulus measured from Figure 4.9C. E) The PDAC cultures grown in BME gel with and without TGF-β1 supplement stained for HIF-1 alpha on day 21 of culture. Nuclei stained with DAPI in blue, HIF-1 alpha in green, and actin with phalloidin in red. Scale bar, 100 μm. ****p < 0.001, two-way ANOVA followed by Tukey's multiple comparison test.

Investigating further, how mechanical stiffness affects gemcitabine efficacy, PANC-1 and PSCs were seeded into culture dishes with 6 – 9 mg mL⁻¹ BME gel for PANC-1 only, and PDAC cultures with and without TGF-β1 (10 ng mL⁻¹). The cultures were grown for 21-days to achieve *in vivo* mechanical stiffness (Figure 4.9C). The cultures were treated with 7.8, 31.25, and 250 μM of gemcitabine for 72 hours, and their ATP viability were assessed. The seeding of cells into culture plates with BME gel to assess the effect of gemcitabine is described in section 3.11.1. ATP viability assessment is as described in section 3.12.2. Again, Figure 4.16A shows the timeline of the seeding of the cells for culture, incubation of the cultures with gemcitabine, and ATP viability assessment. Figure 4.16C shows the percentage viability (normalised to controls) versus the 7.8, 31.25, and 250 μM of gemcitabine (in log scale) used.

The IC₅₀ for the PSC only cultures without and with TGF-β1, the PANC-1 only cultures without and with TGF-β1, and the PDAC cultures without and with TGF-β1 was 1.1 (± 0.05), 1.2 (± 0.06), and 1.7 (± 0.03), 1.9 (± 0.07), 2.5 (± 0.14), and 2.8 μM (± 0.21), respectively. Z-factor score for the PSC only cultures without and with TGF-β1 was 0.5 and 0.3, respectively. The Z-factor score for the PANC-1 only cultures without and with TGF-β1, and the PDAC cultures without and with TGF-β1 was 0.9. The Z-factor value of 0.3 for the PSC only cultures shows the assay quality was marginal in determining the efficacy of gemcitabine of the PSC only cultures with TGF-β1. Again, the Z-factor score values between 0.5 – 1.0 shows the quality of the ATP assay assessment of the efficacy of gemcitabine on the PANC-1 and PDAC cultures without and with TGF-β1 was good.

The percentage viabilities measured for the cultures were compared to their mechanical stiffness measured in Figure 4.9C. Figure 4.16D shows the percentage viabilities for the cultures compared to their measured mechanical stiffness, and with a mechanical stiffness of 970 Pa for the PDAC cultures with TGF-β1, culture viability decreased to approximately 60 % when treated with a high gemcitabine concentration (250 μM, log 2.4). This shows the PDAC cultures with TGF-β1 were resistant to a decrease in culture viability. With the presence of PSCs and TGF-β1, there is the accumulation of ECM proteins (collagen observed in the culture environment, Figure 4.15), which increases the density of the fibrotic stroma and culture mechanical stiffness. This reduces the permeation of drugs through the cultures, resulting in less cells exposed to drugs, and hence the effect of gemcitabine observed on the PDAC cultures. From this assessment, 31.25 μM (log 1.49) was found as an optimum gemcitabine concentration to use on-chip with the PDAC culture, as it resulted in a percentage viability of

approximately 70 %, providing sufficient cellular viability to assess the further viability decreases of gemcitabine with microbubbles and ultrasound.

In addition, the PDAC cultures with and without TGF- β 1 were fixed and stained for hypoxia-inducible factor-1 alpha (HIF-1 alpha) to determine if they exhibited a hypoxic environment based on previous assessments (Figures 4.4 and 4.16B). A hypoxic and acidic environment, further to the physical barrier posed by the fibrotic stroma and mechanical stiffness for the delivery of drugs to the cancer cells, inactivates the effect of drugs with the concentrated glycolytic by-product, lactate.^[68, 70-73, 108, 330] The fixing and staining of the cultures for HIF-1 alpha is as described in section 3.6. Figure 4.16E shows images of the immunofluorescence stain of the cultures for HIF-1 alpha in green. The expression of HIF-1 alpha shows the PDAC cultures were hypoxic with no difference with and without TGF- β 1 supplement. This accounted for the effect of gemcitabine observed for the PDAC spheroid cultures without and with TGF- β 1 in Figure 4.16B. With cancer cells deprived of nutrients and oxygen, the cancer cells adapt, mediated by HIF-1 alpha, for metabolic pathways and responses, such as the anaerobic glycolysis, for survival. As a result, there is the production of the glycolytic by-product lactate in the microenvironment, which inactivates any therapeutic effect.^[19, 46, 68, 70-74, 330]

4.4. Conclusion

The presence of PSCs, whose activity is compounded with TGF- β , in *in vitro* PDAC cultures is important to modelling the tumour growth, fibrotic stroma, and rigidity of the PDAC tissue. PSC cells are central to the PDAC tissue mechanics with the overproduction of ECM macromolecules in the tumour microenvironment, and TGF- β stimulates PSCs activity with the secretion of enzymes including LOX and MMPs for a fibrotic stroma.^[26, 28, 42, 48, 51] Studies show how important PSCs are,^[15, 17, 100, 129, 316] but most *in vitro* PDAC studies do not include PSC cells or TGF- β to recapitulate the fibrotic stroma and the tumour tissue rigidity central to the malignancy and therapeutic resistance of the PDAC tissue.

The PDAC culture, PANC-1 cells in the presence of PSC cells and TGF- β , mimics the biophysical hallmarks of the *in vivo* PDAC tissue. There is a steady increase in the PANC-1 cell growth (Figure 4.3, 4.5, and 4.6) and a mechanical stiffness (Figure 4.9C) within *in vivo* range, with an increased deposition of collagen type I and the expression of hypoxia in the culture matrix environment (Figures 4.15 and 4.16E), which accounted for high drug concentrations required

to reduce culture viability (Figure 4.16). These findings highlight PSCs and TGF- β promote a desmoplastic, stiff tumour microenvironment and resistance to the effects of therapeutics.

Investigating the growth, mechanical stiffness, presence of a fibrotic stroma, and the effect of culture stiffness on how gemcitabine affected the cells off-chip, the optimum culture conditions to mimic PDAC's biophysical nature on-chip was determined. A 21-day culture is optimum to mimic the PDAC tissue fibrotic stroma, mechanical stiffness, and resistance to gemcitabine. Current conventional models do not include stromal elements of the PDAC tumour tissue (i.e., PSC cells and TGF- β), do not grow their cultures for 21 days, and therefore do not capture these biophysical hallmarks. This makes them unrepresentative as models of PDAC for therapeutic assessments.

5. The On-chip Pancreatic Ductal Adenocarcinoma Culture

A 3-channel device (as described in section 3.7, and seen in Figure 5.1A below), was initially used for the on-chip PDAC culture. The 3-channel device provided insight for the design of a 5-channel microfluidic device (Figure 5.1B) to culture the PDAC cells with DMEM/10 %FBS culture media supplemented with TGF- β 1 (10 ng mL⁻¹) for 21 days. The design of the 3-channel and 5-channel device, both with a height of 100 μ m, was based on microfluidic organ-on-chip systems reported in the literature to adequately recapitulate a microenvironment for cell culture.^[38, 131, 132, 162, 165, 331-333]

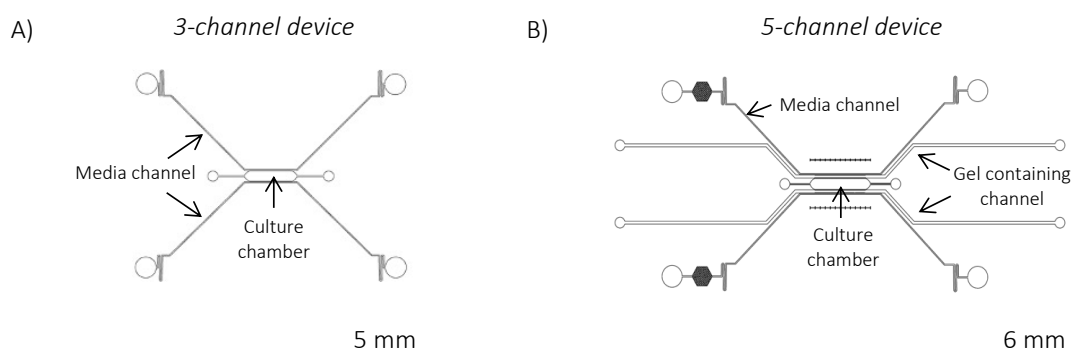


Figure 5.1. The 3-channel and 5-channel microfluidic device

The A) 3-channel device composed of a culture chamber and culture media channels, and B) the 5-channel device composed of a culture chamber, gel-containing channels and culture media channels.

In this chapter, fluid flow assessments of channels for the design and fabrication of the 3-channel and 5-channel device and with media reservoirs, PDAC cell culture in the 3-channel and 5-channel device, immunofluorescence assessment for collagen and HIF-1 alpha, and the interstitial flow assessments of the on-chip PDAC culture are presented.

5.1. Fluid flow assessments

Before designing the 3-channel and 5-channel device, the linear velocities of channels in microfluidic systems, reported in the literature for cell culture under constant flow^[131, 162, 257, 293-295, 297, 334], were investigated to determine an optimal laminar flow regime to use for the culturing of the PDAC cells. The height, width, and volumetric flow rate (in m³ s⁻¹) of the

channels of the reported microfluidic systems were used to determine a range of linear velocities, using *Equation 14 – 16*, and to calculate fluid flow regimes using *Equation 12*.

Table 5.1 shows a list of the channel dimensions of reported microfluidic devices, the linear velocities, and the fluid flow regime calculated. A laminar flow regime of ≤ 0.2 , and a media flow rate of $0.5 \mu\text{L min}^{-1}$ for the media channels, were deemed optimal for the viable cell culture of the PDAC cells. A flow regime of ≤ 0.2 , and a media flow rate of $0.5 \mu\text{L min}^{-1}$, indicated a steady diffusion and transport of nutrients and analytes, with control of the shear stresses induced in the device with media flow.^[38, 162, 165, 332, 335-337] Based on the laminar flow regime and media flow rate of ≤ 0.2 and $0.5 \mu\text{L min}^{-1}$, respectively, the optimal channel dimensions for the 3-channel and 5-channel device was assessed.

Table 5.2 shows the dimensions of the different channels for the 3-channel and 5-channel devices, the linear velocities, hydraulic resistance, flow regime, and microchannel wall shear stress, calculated based on the flow regime and culture media flow rate of ≤ 0.2 and $0.5 \mu\text{L min}^{-1}$, respectively. The microchannel wall shear stress was calculated using *Equations 23*. Investigating the linear velocities, hydraulic resistance, flow regime, and microchannel wall shear stress for the 3- and 5-channel device, was important in determining (particularly for the culture chamber) channel dimensions optimal for viable cell culture. An optimal channel dimension was deemed to have a flow regime of ≤ 0.2 , a hydraulic resistance less than $1.0 \times 10^{-13} \text{ Pa.s m}^{-3}$, and a microchannel wall shear stress of $\leq 0.5 \text{ dyne cm}^{-2}$ as this meant a steady flow of fluids to enable an *in vivo*-like physiological behaviour and adhesion properties of cells crucial for viable cell culture.^[101, 337, 338] With the optimal channel dimensions, the 3-channel and 5-channel devices were designed and fabricated for culture, as described in sections 3.7 and 3.8.

In addition, the flow of culture media in the media channels with media reservoirs was investigated. This was to establish how often to replenish culture media in the media reservoirs. A MATLAB code was scripted with the hydraulic resistance and pressure equations (*Equations 16, 19, and 20*). The Appendix, *Hydrostatic pressure driven flow by gravity*, shows the code, using the culture media channel length for the 5-channel device. Figure 5.2 shows the volumetric flow rate, the pressure difference, and culture medium height between the inlet and outlet media reservoir versus time in hours for culture medium in the inlet and outlet media reservoirs to be equal in volume or height.

Table 5.1. Fluid flow assessment of microfluidic systems in the literature for cell culture

| Literature | Channel dimensions [m] | | Cross section [m ²] | Volumetric flow rate [m ³ s ⁻¹] | Linear velocity [m s ⁻¹] | Hydraulic diameter [rectangular channel; m] | Flow regime [Re] ^{g*} |
|---|-------------------------|------------------------|---------------------------------|--|--------------------------------------|---|--------------------------------|
| | Height | Width | | | | | |
| Huh <i>et al.</i> , 2013 ^{a*} | 1.0 × 10 ⁻⁴ | 4.0 × 10 ⁻⁴ | 4.0 × 10 ⁻⁸ | 5.6 × 10 ⁻¹² | 1.4 × 10 ⁻⁴ | 1.6 × 10 ⁻⁴ | 0.03 |
| Huh <i>et al.</i> , 2013 ^{b*} | 1.5 × 10 ⁻⁴ | 1.0 × 10 ⁻³ | 1.5 × 10 ⁻⁷ | 8.3 × 10 ⁻¹² | 5.6 × 10 ⁻⁵ | 2.6 × 10 ⁻⁴ | 0.02 |
| Liu <i>et al.</i> , 2016 ^{c*} | 1.2 × 10 ⁻⁴ | 2.0 × 10 ⁻⁴ | 2.4 × 10 ⁻⁸ | 3.3 × 10 ⁻¹¹ | 1.4 × 10 ⁻³ | 1.5 × 10 ⁻⁴ | 0.30 |
| Liu <i>et al.</i> , 2016 ^{c*} | 1.2 × 10 ⁻⁴ | 6.0 × 10 ⁻⁴ | 7.2 × 10 ⁻⁸ | 3.3 × 10 ⁻¹¹ | 4.6 × 10 ⁻⁴ | 2.0 × 10 ⁻⁴ | 0.13 |
| Sugimoto <i>et al.</i> , 2018 ^{c*} | 3.0 × 10 ⁻⁴ | 2.0 × 10 ⁻⁴ | 6.0 × 10 ⁻⁸ | 3.3 × 10 ⁻¹⁰ | 5.6 × 10 ⁻³ | 2.4 × 10 ⁻⁴ | 1.91 |
| Sugimoto <i>et al.</i> , 2018 ^{c*} | 3.0 × 10 ⁻⁴ | 5.0 × 10 ⁻⁴ | 1.5 × 10 ⁻⁷ | 6.7 × 10 ⁻¹⁰ | 4.4 × 10 ⁻³ | 3.8 × 10 ⁻⁴ | 2.39 |
| Sugimoto <i>et al.</i> , 2018 ^{d*} | 3.0 × 10 ⁻⁴ | 3.0 × 10 ⁻⁴ | 9.0 × 10 ⁻⁸ | 3.3 × 10 ⁻⁹ | 3.7 × 10 ⁻² | 3.0 × 10 ⁻⁴ | 15.94 |
| Annabi <i>et al.</i> , 2013 ^{e*} | 1.5 × 10 ⁻⁴ | 5.0 × 10 ⁻⁵ | 7.5 × 10 ⁻⁹ | 2.5 × 10 ⁻¹⁰ | 3.3 × 10 ⁻² | 7.5 × 10 ⁻⁵ | 3.59 |
| Annabi <i>et al.</i> , 2013 ^{e*} | 1.5 × 10 ⁻⁴ | 5.0 × 10 ⁻⁵ | 7.5 × 10 ⁻⁹ | 2.8 × 10 ⁻¹⁰ | 3.8 × 10 ⁻² | 7.5 × 10 ⁻⁵ | 4.07 |
| Silva <i>et al.</i> , 2013 ^{e*} | 1.25 × 10 ⁻⁴ | 3.0 × 10 ⁻⁴ | 3.8 × 10 ⁻⁸ | 1.1 × 10 ⁻¹⁰ | 3.0 × 10 ⁻³ | 1.8 × 10 ⁻⁴ | 0.75 |
| Kim and Ingber, 2013 ^{e*} | 1.5 × 10 ⁻⁴ | 1.0 × 10 ⁻³ | 1.5 × 10 ⁻⁷ | 8.3 × 10 ⁻¹² | 5.6 × 10 ⁻⁵ | 2.6 × 10 ⁻⁴ | 0.02 |
| Maoz <i>et al.</i> , 2018 ^{f*} | 1.0 × 10 ⁻³ | 1.0 × 10 ⁻³ | 1.0 × 10 ⁻⁶ | 1.7 × 10 ⁻¹¹ | 1.7 × 10 ⁻⁵ | 1.0 × 10 ⁻³ | 0.02 |
| Maoz <i>et al.</i> , 2018 ^f | 2.0 × 10 ⁻⁴ | 1.0 × 10 ⁻³ | 2.0 × 10 ⁻⁷ | 1.7 × 10 ⁻¹¹ | 8.3 × 10 ⁻⁵ | 3.3 × 10 ⁻⁴ | 0.04 |
| Hassell <i>et al.</i> , 2017 ^{f*} | 1.0 × 10 ⁻³ | 1.0 × 10 ⁻³ | 1.0 × 10 ⁻⁶ | 1.7 × 10 ⁻¹¹ | 1.7 × 10 ⁻⁵ | 1.0 × 10 ⁻³ | 0.02 |
| Hassell <i>et al.</i> , 2017 ^{f*} | 2.0 × 10 ⁻⁴ | 1.0 × 10 ⁻³ | 2.0 × 10 ⁻⁷ | 1.7 × 10 ⁻¹¹ | 8.3 × 10 ⁻⁵ | 3.3 × 10 ⁻⁴ | 0.04 |

^{a*}Lung-on-a-chip culture chamber dimensions; ^{b*}Gut-on-a-chip culture chamber dimensions; ^{c*}Fluid/flow distribution channel dimensions; ^{d*}Gelation channel dimensions; ^{e*}Culture channel dimensions; ^{f*}dimensions; top and bottom culture chamber channel, respectively.

^gDensity and dynamic viscosity of water at 37°C, used for the density and dynamic viscosity of the culture media used for the on-chip culture: 993.3 kg m⁻³ and 6.92 10⁻⁴ Pa.s, respectively.

Table 5.2. Dimensions and fluid flow assessments of microfluidic channels for the PDAC culture

| Device | Channel dimensions [m] | | | Cross section [Height x width m ²] | Volumetric flow rate [m ³ s ⁻¹] | Linear velocity [m s ⁻¹] | Hydraulic diameter [rectangular channel; m] | Hydraulic resistance [rectangular channel; Pa.s m ⁻³] | Flow regime [Re] ^{g*} | τ [dyne cm ⁻²] |
|------------------------|------------------------|------------------------|-----------------------|---|--|---|--|--|-----------------------------------|----------------------------|
| | Height | Width | length | | | | | | | |
| 3-channel ¹ | 1.0 × 10 ⁻⁴ | 2.0 × 10 ⁻⁴ | 2.5 × 10 ² | 2.0 × 10 ⁻⁸ | 8.3 × 10 ⁻¹² | 4.2 × 10 ⁻⁴ | 1.3 × 10 ⁻⁴ | 1.5 × 10 ⁻¹² | 0.08 | 0.17 |
| 3-channel ² | 1.0 × 10 ⁻⁴ | 1.0 × 10 ⁻³ | 5.0 × 10 ³ | 1.0 × 10 ⁻⁷ | 8.3 × 10 ⁻¹² | 8.3 × 10 ⁻⁵ | 1.8 × 10 ⁻⁴ | 1.1 × 10 ⁻¹¹ | 0.02 | 0.03 |
| 5-channel ¹ | 1.0 × 10 ⁻⁴ | 1.0 × 10 ⁻⁴ | 4.3 × 10 ² | 1.0 × 10 ⁻⁸ | 8.3 × 10 ⁻¹² | 8.3 × 10 ⁻⁴ | 1.0 × 10 ⁻⁴ | 9.7 × 10 ⁻¹² | 0.12 | 0.35 |
| 5-channel ² | 1.0 × 10 ⁻⁴ | 1.0 × 10 ⁻³ | 6.0 × 10 ³ | 1.0 × 10 ⁻⁷ | 8.3 × 10 ⁻¹² | 8.3 × 10 ⁻⁵ | 1.8 × 10 ⁻⁴ | 9.5 × 10 ⁻¹¹ | 0.02 | 0.03 |
| 5-channel ³ | 1.0 × 10 ⁻⁴ | 2.8 × 10 ⁻⁴ | 4.5 × 10 ² | 2.8 × 10 ⁻⁸ | 8.3 × 10 ⁻¹² | 3.0 × 10 ⁻⁴ | 1.5 × 10 ⁻⁴ | 1.8 × 10 ⁻¹² | 0.06 | 0.13 |

¹ Culture media channel; ² culture chamber channel; ³ gel-containing channel; * Density and dynamic viscosity of water at 37°C, used for the density and dynamic viscosity of the culture media used for the on-chip culture: 993.3 kg m⁻³ and 6.92 · 10⁻⁴ Pa.s, respectively.

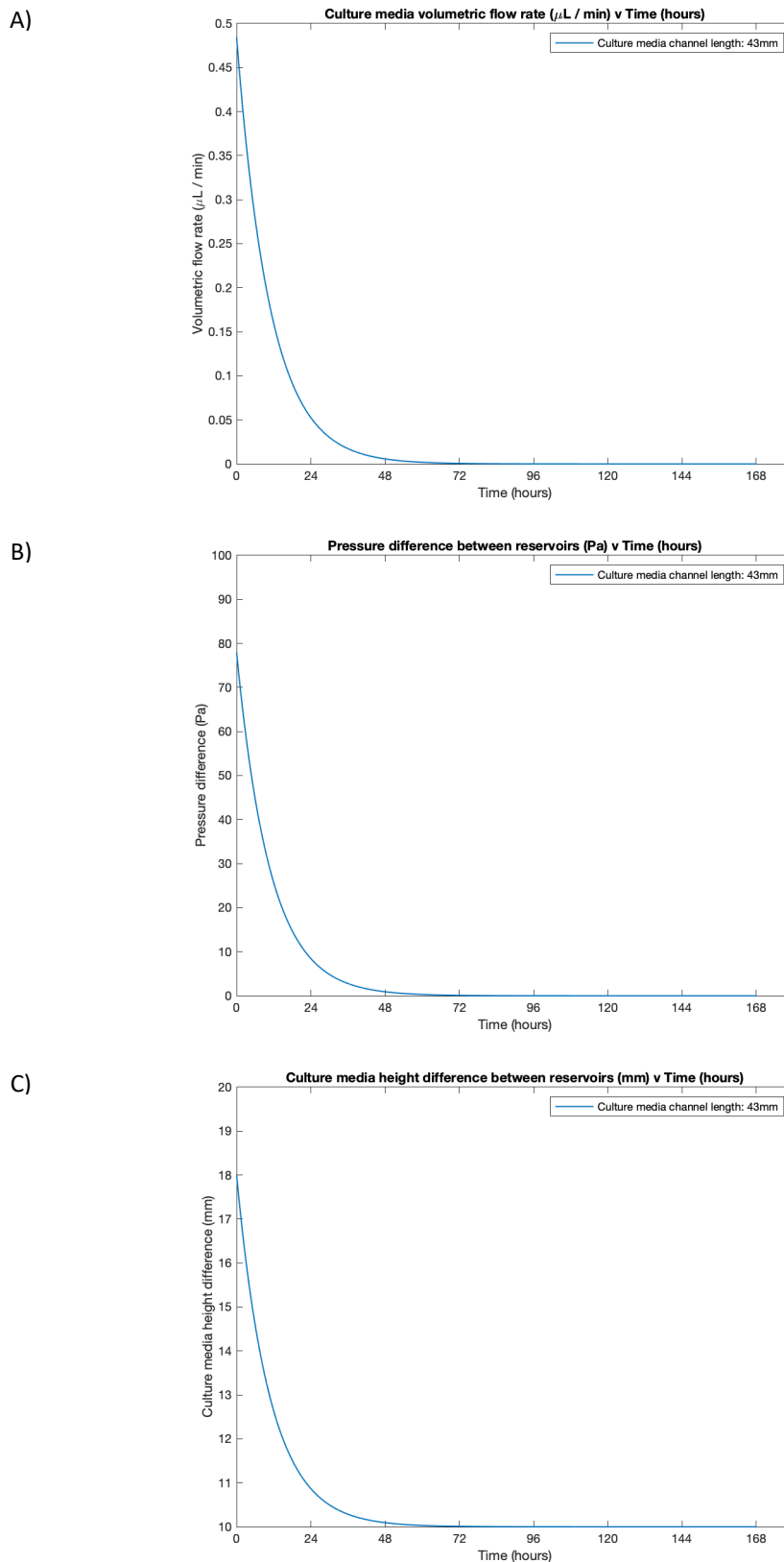


Figure 5.2. Fluid flow assessment in the media channels, between the media reservoirs

A) The volumetric flow rate of culture media in the media channels of, here, the 5-channel device with a media channel length of 43 mm. B) The pressure difference between the inlet and outlet media reservoirs, which drives culture medium flow in the media channels. C) The difference in culture media height between the media reservoirs. All versus time in hours, to determine how long it takes for media in the reservoirs to be equal in volume or height to change culture media.

With a flow rate of approximately $0.5 \mu\text{L min}^{-1}$, a pressure difference of 80 Pa and a culture media height difference of 18 mm (height of 2 mL of culture medium in the inlet reservoir is approximately 20 mm, and height of 200 μL of culture medium in the outlet reservoir is approximately 2 mm), it took about 72 hours for culture media in the inlet and outlet media reservoirs to be equal in volume or height.

Figure 5.3 shows the experimental assessment of the time it took for culture media in the media reservoirs to be equal in volume or height. Using the 5-channel device and BME gel only, the inlet and outlet media reservoirs were filled with DMEM/10 %FBS culture medium (2 mL and 200 μL , respectively), and the time it took for medium in the reservoirs to be equal in volume or height was observed. It took 72 hours, and this was in agreement with the theoretical assessment shown in Figure 5.2. As shown in Figures 5.2 and 5.3, the pressure difference from the culture media volume, thus height difference, in the inlet and outlet media reservoirs drives the passive flow of medium in the media channels at a constant flow rate allowing for long term cell culture.^[167, 337, 339]

5.2. PDAC culture in the 3-channel and 5-channel microfluidic devices

PDAC cells were seeded into the culture chamber of the 3-channel or 5-channel device for a 21-day culture with DMEM/10 %FBS culture media supplemented with TGF- β 1 (10 ng mL⁻¹). Figure 5.4A shows bright-field images of the PDAC cells in the culture chamber of the 3-channel device on the day of seeding, day 7, and 14 of culture. The cells were cultured for 14 days rather than 21 days, as by day 14, cells were observed to grow into the media channels.^[340, 341] With cells in the media channels by day 14 of culture, the flow of media into the culture chamber for a 21-day culture of the PDAC cells will be impeded, which will be detrimental to the growth and drug treatment of the cells. As a result of cells growing into the media channels of the 3-channel device, the device was optimised, by including gel-containing channels for a 5-channel device. The gel-containing channels put a distance between the culture chamber and media channels to prevent cells from growing into the media channel with a 21-day culture.

Microfluidic devices for pancreatic cancer studies in the literature culture pancreatic cancer cells for approximately 7 – 10 days. If the PDAC cells here were cultured for 7 – 10 days, the mechanical stiffness achieved would be < 300 Pa (Figure 4.9C), unrepresentative of the PDAC tumour tissue stiffness.

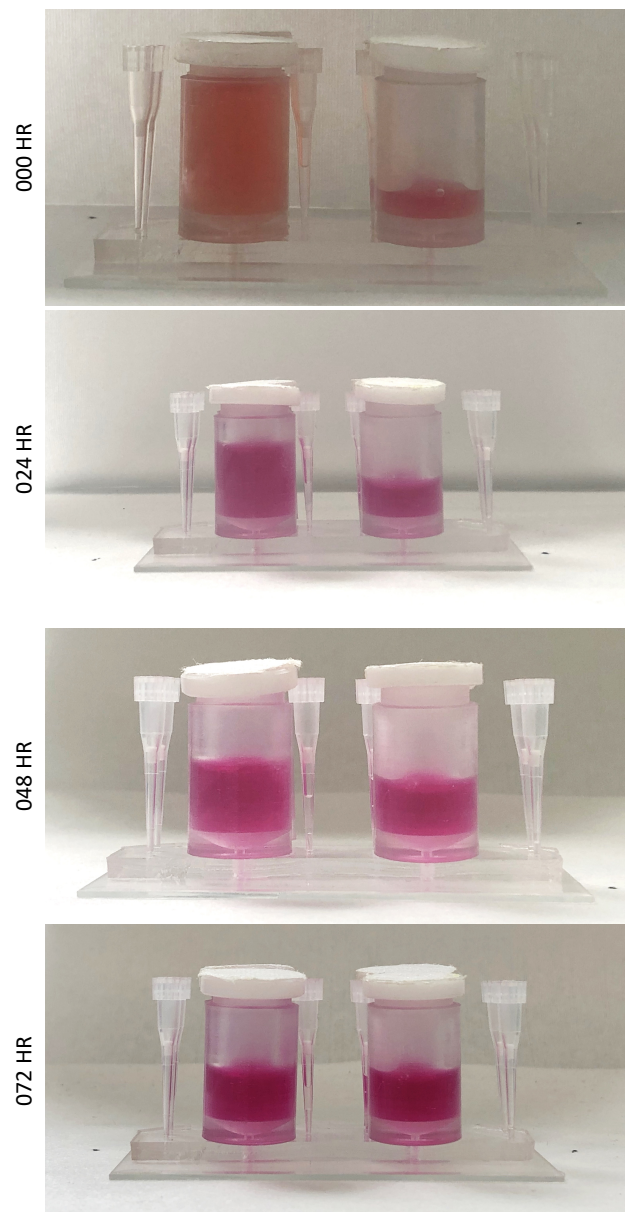


Figure 5.3. Time for culture media in the inlet and outlet media reservoirs to be equal in volume or height
Representative images showing the inlet and outlet media reservoirs with DMEM/10 %FBS culture media, and the time it took for the inlet and outlet reservoirs to have the same volume of media. It took approximately 72 hours for culture media in the reservoirs to be equal in volume/height. The pressure difference, from a difference in the volume or height of culture media in the respective media reservoirs, drives the passive flow of DMEM/10 %FBS in the media channels.

Drifka *et al.* 2013, Lee *et al.* 2018, and Bradney *et al.* 2020 report a 3-channel, 7-channel (3 channels for cell culture and 4 channels for media flow), and a ductal-like channel, respectively, for a 5 – 10 day culture to study the stroma-cancer microenvironment and epithelial-mesenchymal transition (EMT) to evaluate the efficacy of potential therapeutics.^[11, 38, 165] The reason for the 5 – 10 day culture is likely they did not consider recapitulating the

PDAC tumour mechanics as shown here, where the cells grow and remodel their environment for a stiff matrix (Figures 4.9 and 4.15, respectively).^[26, 48, 58, 313]

Figure 5.4B shows bright-field images of the PDAC cells in the culture chamber of the 5-channel device on the day of seeding, day 7, 14, and day 21 of culture. The field of view of the PDAC culture, with a 4 × objective, was between the 275 µm gel-containing channels. The cells were seen confluent in the culture chamber and gel-containing channels. Very few cells were observed in the media channels by day 21 of culture (Figure 5.4C), demonstrating the suitability of the design of the 5-channel device for a 21-day culture. Figure 5.5 shows the live/dead stain and ATP viability assessment of the PDAC cells grown in the 5-channel device during the 21-day culture. Live/dead stain of the on-chip culture was performed with ReadyProbes™ Cell Viability Imaging Kit, Blue/Red as described in section 3.12.1. The ReadyProbes™ Cell Viability Imaging Kit consists of NucBlue® Live (Hoechst stain) for live cells and propidium iodide (PI), which binds to DNA of dead cells to fluoresce red. ATP viability assessment of the on-chip culture is as described in section 3.12.2. The live/dead stain (Figure 5.5A) with less PI staining in comparison to the DAPI staining showed, qualitatively, the on-chip PDAC cultures were viable. This is supported with the ATP viability assessment (Figure 5.5B), which showed quantitatively, the cultures were viable, with increasing ATP luminescence, which is proportional to the ATP content of the culture, with increasing culture time. Few dead cells were observed, mostly around the gel-containing channels and the media channels (Figure 5.5A). This could be due to the shear stress imposed with the flow of culture medium in the media channels. Shear stress of 0.35 dyne cm⁻² was determined for the media channels (Table 5.2). This was low in comparison to the physiological shear stress, which ranges between 0.5 – 120 dyne cm⁻² for blood and lymphatic vessels and tissues.^[338] However, this induced mechanical forces on cells proximal to the media channels, which might have affected their viability, as seen in Figure 5.5A.

Beer *et al.* 2017 and Lai *et al.* 2020^[39, 253] show the culturing of pancreatic cancer cells with dielectrophoresis (DEP) and in devices (InVADE) of a multi-well plate format similar to the Organoplate, respectively. DEP was used to selectively assemble viable cells for culture, but long term culture with DEP has shown to cause cell damage, albeit in bacterial cells.^[342] InVADE, microfluidic devices based on a multi-well plate format, requires a rocking platform for the perfusion of media,^[39, 155] permitting static culture conditions, which do not emulate the *in vivo* physiological flow conditions.^[167]

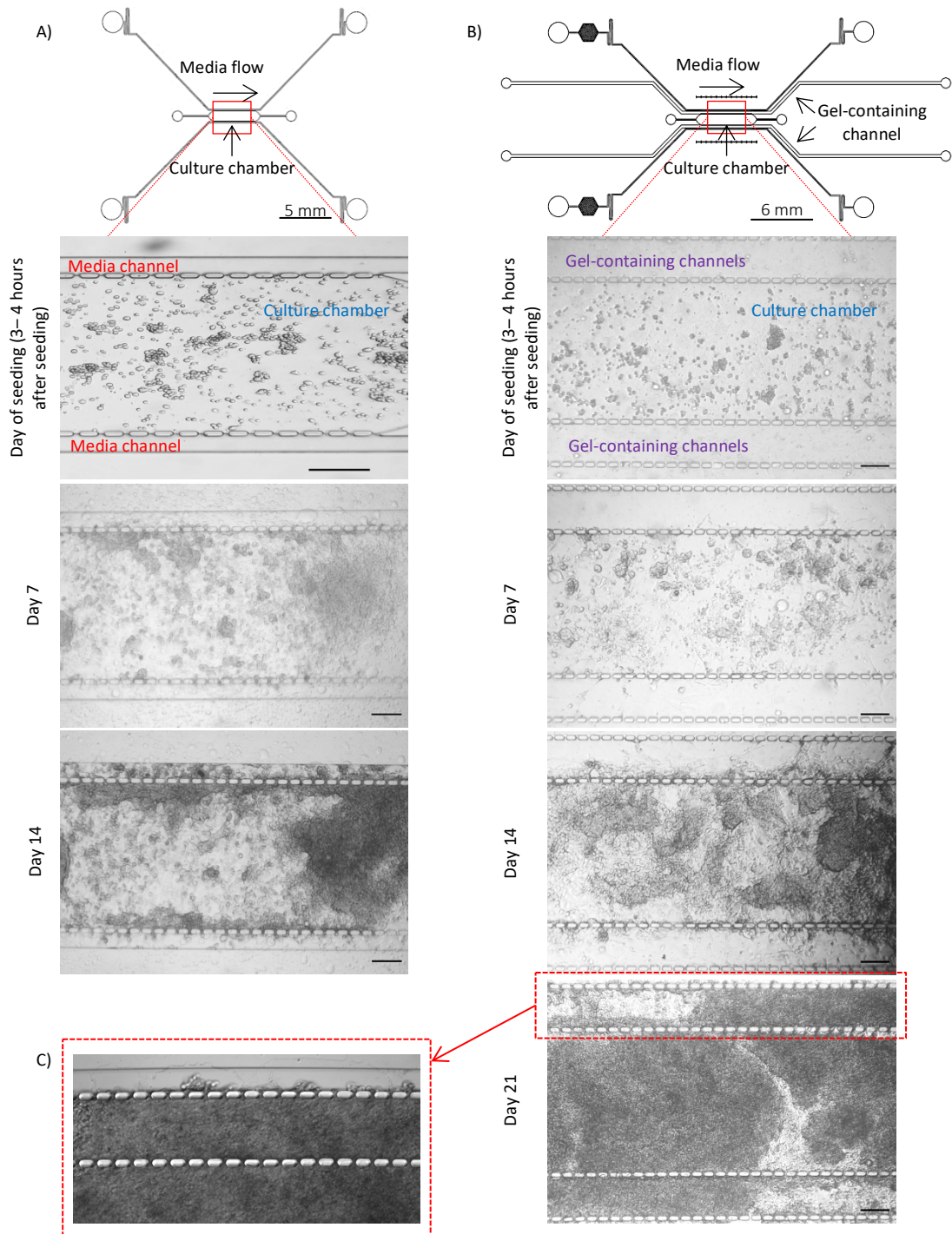


Figure 5.4. The on-chip PDAC culture with the 3-channel and 5-channel device

Representative images of the on-chip culture of the PDAC cells (PANC-1 and PSC cells in a 1:3 seeding ratio) with TGF-β1 (10 ng nL⁻¹) in A) the 3-channel and B) the 5-channel device on day 7, 14, and 21 of culture. C) An example image of the media channel of the 5-channel device with very few cells. Scale bar, 200 μm.

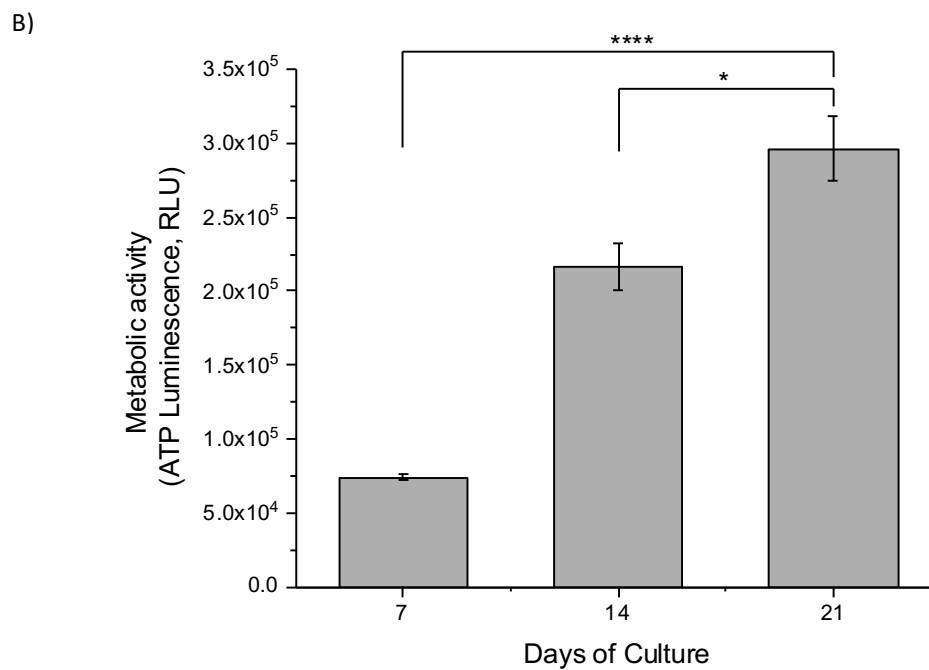
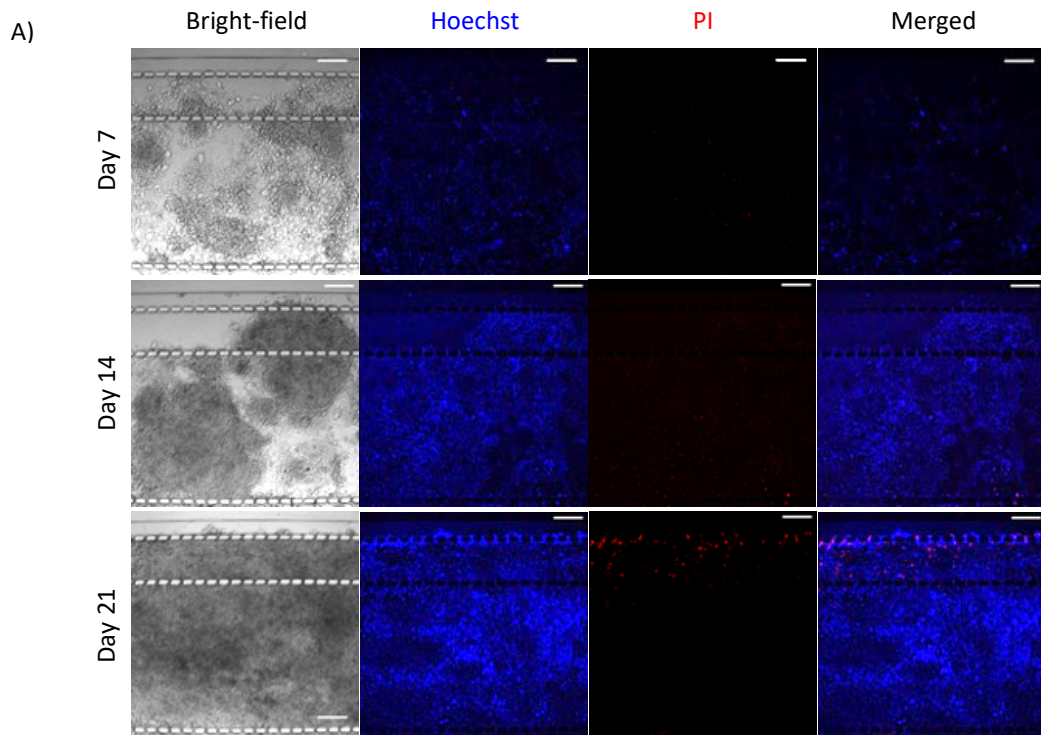


Figure 5.5. Viability assessments of the on-chip PDAC culture in the 5-channel device

A) Representative confocal images of the live/dead viability assessment of the on-chip PDAC (PANC-1 and PSC cells in a 1:3 seeding ratio) with TGF- β 1 (10 ng nL⁻¹) culture on day 7, 14, and 21 of culture with Hoechst for live cells in blue, and propidium iodide for dead cells in red. Scale bar, 200 μ m. B) ATP viability assessment of the on-chip PDAC culture on day 7, 14, and 21 of culture. N = 18 devices per day of culture generated from three separate seeding settings. **** $p < 0.001$, and * $p < 0.5$, one-way ANOVA followed by Tukey's multiple comparison test.

The IncuCyte® S3 Live-Cell Analysis System at MDC (described in section 3.2.4) was used to observe the PDAC cells in the 5-channel device. The labelling of the cells is described in section 3.3. As mentioned in section 4.1, labelled PSC cells were not used as they did not retain the Qtracker dye. The IncuCyte® videos of the PDAC cells on-chip, Supplementary 5 and 6, could only capture up to 2 days and 18 hours of culture. The presence of bubbles in the culture media channels was detrimental to the flow of culture media into the culture chamber for the PDAC culture, and there were focusing issues on the culture chamber with the IncuCyte®. This was improved by placing the PDMS moulds of the 5-channel device approximately 1 cm away from the edge of PDMS coated glass slides. However, the videos show cells aggregating in 3D and forming structure networks.

The 21-day on-chip culture of the PDAC cells with TGF- β 1 supplement was to achieve the *in vivo*-like mechanical growth and behaviour of the PDAC tissue for therapeutic assessment. To ensure the on-chip culture reflected the mechanical behaviour and growth of the PDAC tissue, first, the on-chip PDAC cultures were fixed and stained for collagen type I and HIF-1 alpha. Second, reduced interstitial fluid flow, resulting from a dense fibrotic ECM ^[41, 63, 238, 343], was assessed.

5.3. The matrix environment of the PDAC culture

As shown in Supplementary videos 5 and 6 of the on-chip cultures forming a network, the on-chip cultures were stained to investigate the collagen network. Immunofluorescence assessment of the cultures for collagen type I and HIF-1 alpha is described in section 3.9.

In comparison to Beer *et al.* 2017, Bradney *et al.* 2020, and Lee *et al.* 2018, which embed pancreatic cancer cells in a collagen matrix to mimic the tumour microenvironment of PDAC for a 5 – 10 day culture, Figure 5.6 shows the production and accumulation of collagen as the PDAC cells grows and develop mechanically (Figure 4.9), on-chip. Figure 5.6 show the immunostained images of the cultures for collagen on day 7, 14, and 21 of culture. On day 7 and 14 of culture, collagen was found mostly around the cells and not in the surrounding matrix environment. This is in line with what was observed for the collagen levels in the surrounding culture environment for the off-chip cultures (Figure 4.15) and the measured mechanical stiffness (Figure 4.9), where on day 7 and day 14 of culture, there was a decrease in the complex shear modulus of the PDAC cultures from less amount of collagen deposited

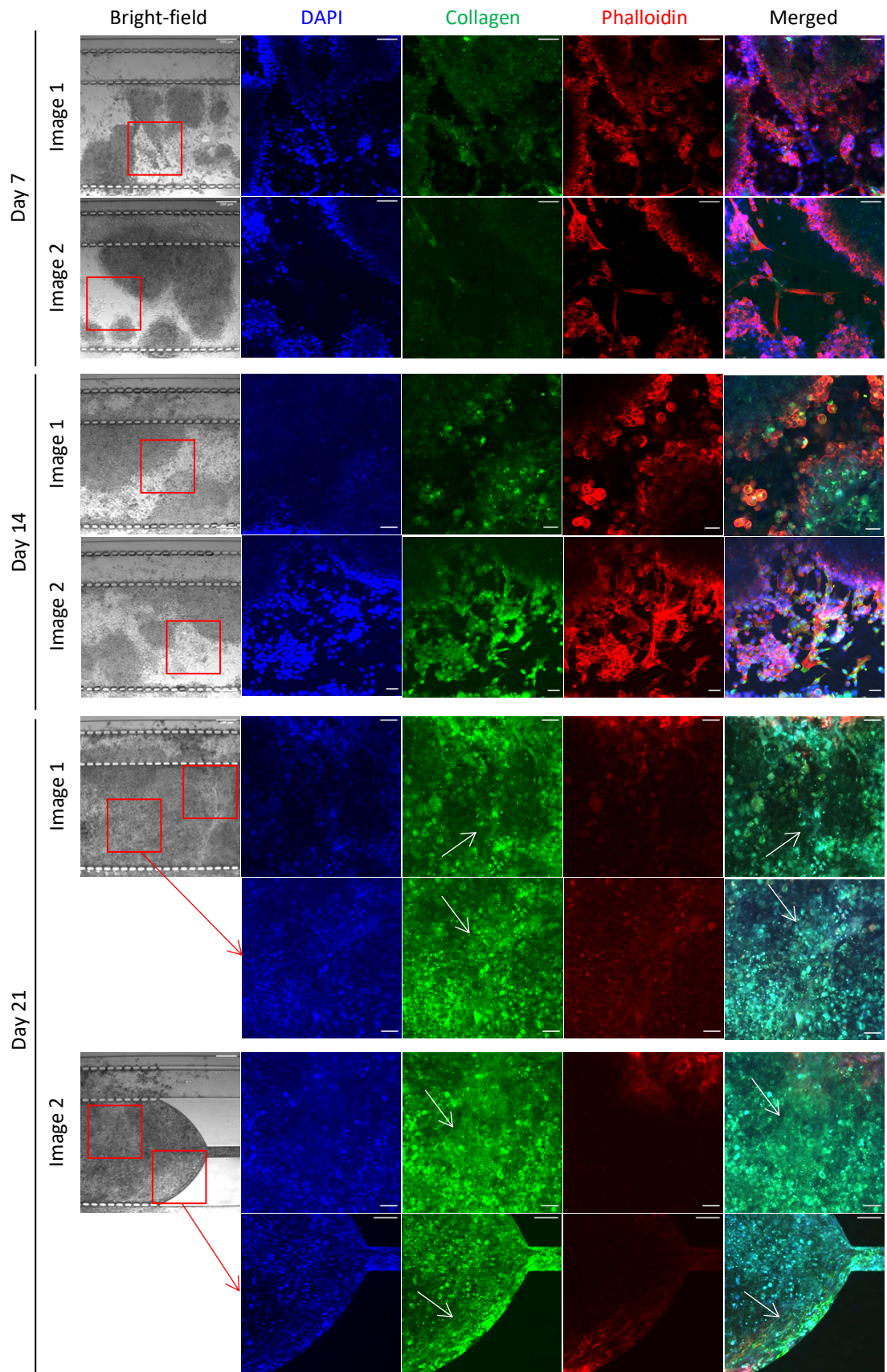


Figure 5.6. Immunofluorescence stain of collagen type I in on-chip PDAC cultures

Representative confocal images of the collagen stain in the on-chip PDAC (PANC-1: PSCs in a seeding ratio of 1: 3) cultures with TGF- β 1 supplement on day 7, 14, and 21 of culture. Nuclei stained with DAPI in blue, collagen in green, and actin with phalloidin in red. DAPI, collagen, phalloidin, and merged images are magnified images of the red box in the bright-field images. White arrows indicate collagen fibres. Scale bar of the magnified images on day 7, 100 μ m. Scale bar of the magnified images on day 14, 50 μ m. Scale bar on day 21 of culture, 50 μ m for image 1 and 100 μ m for image 2.

into the surrounding culture environment. Again, comparable to the off-chip cultures on day 21 of culture (Figures 4.9 and 4.15), there were increased amounts of collagen on-chip. This showed the 21-day on-chip cultures were mechanically mature, mimicking the *in vivo* PDAC tissue stiffness.^[21, 344]

With a growing dense, fibrotic stroma and tissue stiffening, vasculatures collapse, resulting in high interstitial pressure for an ineffective fluid flow intratumourally with nutrients and oxygen or drugs. This results in a hypoxic and acidic environment in which the cancer cells thrive.^[19, 24, 68] Reported microfluidic devices on modelling tumour hypoxia show the contributing effect of hypoxia on chemoresistance.^[345-349] Palacio-Castaneda *et al.* 2020 report a 3-channel microfluidic platform to study the hypoxic tumour microenvironment, where hypoxia is induced by blocking the diffusion of oxygen into cultures with the addition of polymethyl methacrylate (PMMA) to PDMS moulds of the device.^[348] Refet-Mollof *et al.* 2021 culture spheroids of more than 750 µm in diameter for the natural expression of hypoxia to study the role of hypoxia in drug resistance.^[349] Palacio-Castaneda *et al.* characterised hypoxia levels with oxygen-sensitive dye probes. High intensity levels of the probe correlated with lower oxygen concentration in the cultures. Refet-Mollof *et al.* immunostained for the expression of carbonic anhydrase IX (CAIX), which is downstream of HIF-1 alpha in the hypoxia responsive element pathway and correlates with poor cancer prognosis.^[350-353] Here, the 21-day on-chip cultures were stained for HIF-1 alpha, a key regulator of cellular and systemic responses to hypoxia,^[74, 350, 351, 353-355] to determine if the cultures were hypoxic.

Figure 5.7 shows the immunostained images of the 21-day on-chip cultures for HIF-1 alpha. HIF-1 alpha expression shows the on-chip PDAC cultures developed a hypoxic environment. This is considered to be in response to the restricted access of nutrients and oxygen from collagen accumulation (Figure 5.6). With large amounts of ECM resulting in tissue rigidity, the availability of nutrients and oxygen to cells becomes scarce, a hypoxic, acidic environment develops, and the PDAC cells adapt by expressing HIF-1 alpha, shifting metabolic activity from oxidative phosphorylation to glycolysis to survive.^[351, 356-358] In turn, with the development of hypoxia, there is the upregulation of LOX protein which oxidises lysine residues in collagen, thereby increasing the cross-linking of collagen fibres for a fibrotic, rigid stroma, correlating to overall poor survival.^[48, 351, 359-361] The adaptive response by PDAC cells to hypoxia results in malignant behaviour and therapeutic resistance as previously observed off-chip (Figure 4.16).

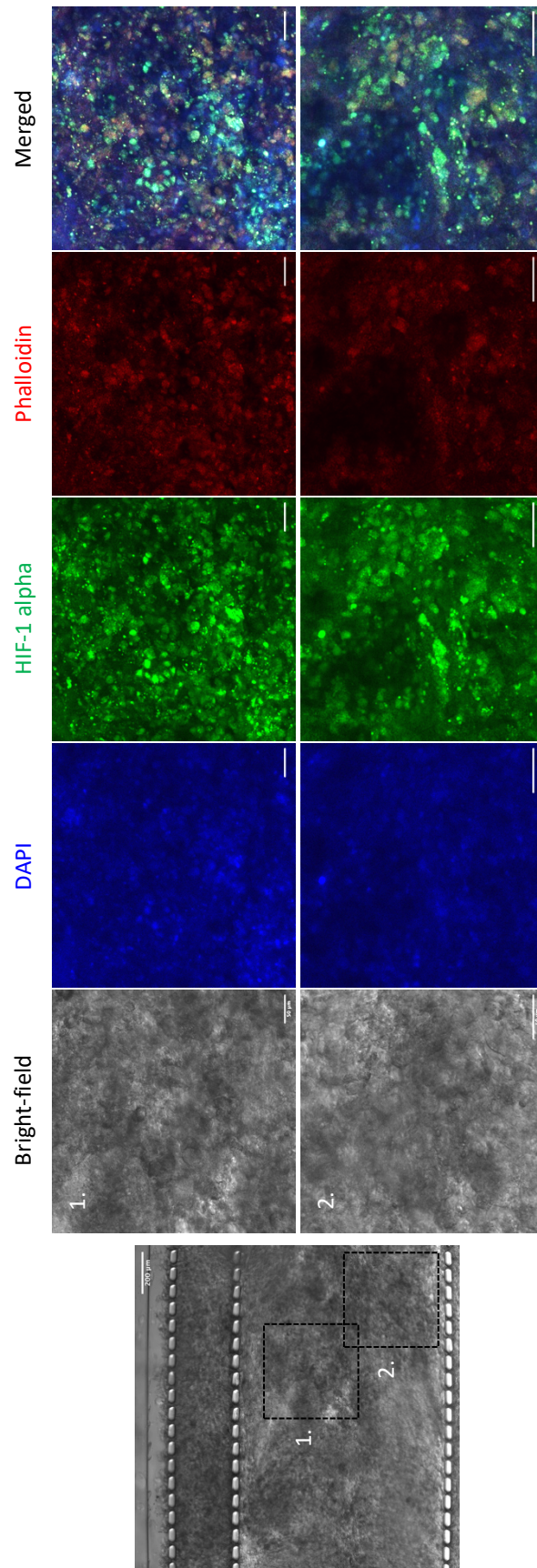


Figure 5.7. Immunofluorescence stain of HIF-1 alpha in on-chip PDAC cultures

Representative confocal images of the HIF-1 alpha stain for the on-chip PDAC (PANC-1: PSCs in a seeding ratio of 1: 3) cultures with TGF- β 1 supplement on day 21 of culture. Section of the bright-field image of the culture chamber is magnified to observed the nuclei stained with DAPI in blue, actin with phalloidin in red, and HIF-1 alpha expression, in green, of the PDAC cells. Scale bar of the magnified images, 50 μ m.

5.4. The interstitial flow of the PDAC culture

The accumulation of collagen and expression of HIF-1 alpha showed the 21-day on-chip PDAC culture mimicked the biophysical traits of the PDAC tissue – accumulation of collagen proteins, resulting in tissue stiffening and a hypoxic environment. A hypoxic environment meant reduced interstitial flow with nutrients and oxygen. Therefore, the nature of interstitial fluid flow in the 21-day on-chip PDAC culture was assessed.

The interstitial flow nature of the on-chip PDAC culture was assessed by investigating the perfusion of 5(6)-carboxyfluorescein in DMEM/10 % FBS culture medium (1: 10 volume ratio), referred to as fluorescein in media solution. As a control, the perfusion of fluorescein in media solution was assessed with BME gel on-chip. The assessment of the interstitial flow with fluorescein in media solution is described in section 3.10. The perfusion of the fluorescein in media solution through the device culture chamber with BME gel or the 21-day PDAC culture was captured with an epifluorescence microscope. Supplementary videos 7 and 8 show the flow through the BME gel and the 21-day PDAC culture, respectively, and Figure 5.8 shows images of the perfusion flow (Figure 5.8B) and the plot of the fluorescein intensity versus the distant travelled by the solution over time (Figure 5.8C). In comparison to the flow of the solution through the BME gel on-chip, it took more than 90 minutes for the intensity of the fluorescein in media solution to be the same throughout the culture chamber with the 21-day on-chip PDAC culture. This demonstrated a reduced interstitial flow due to the accumulation of collagen in the culture. With increasing collagen content, the cultures become dense, compact and rigid as seen off-chip, which reduces the size of the porous structure in the culture matrix, restricting flow. Lai *et al.* 2020 investigated interstitial flow through their on-chip PDAC cultures, grown in the InVADE chip, using carboxyfluorescein diacetate (CFDA).^[39] They found a decrease in the flow of CFDA solution through denser areas (with high collagen accumulation) of their cultures.

To quantify the interstitial flow, the hydraulic conductivity of the BME gel or the PDAC culture with the flow of the fluorescein in media solution, using Darcy's law (*Equation 6*), was calculated. Shown in Table 5.3 and Figure 5.9, the hydraulic conductivity (K) of the BME gel and the developing on-chip PDAC culture (day 7 and 14 of culture) were $1.9 \times 10^{-9} \pm 6.3 \times 10^{-11}$, $5.0 \times 10^{-9} \pm 1.2 \times 10^{-9}$, and $4.2 \times 10^{-9} \pm 8.4 \times 10^{-10} \text{ m}^2 \text{ s}^{-1} \text{ Pa}^{-1}$, respectively. In comparison to the hydraulic conductivity for the 21-day on-chip PDAC culture, which was $9.1 \times 10^{-10} \pm 6.9 \times 10^{-11} \text{ m}^2 \text{ s}^{-1} \text{ Pa}^{-1}$, this showed that there was an increased perfusion of the fluorescein in media

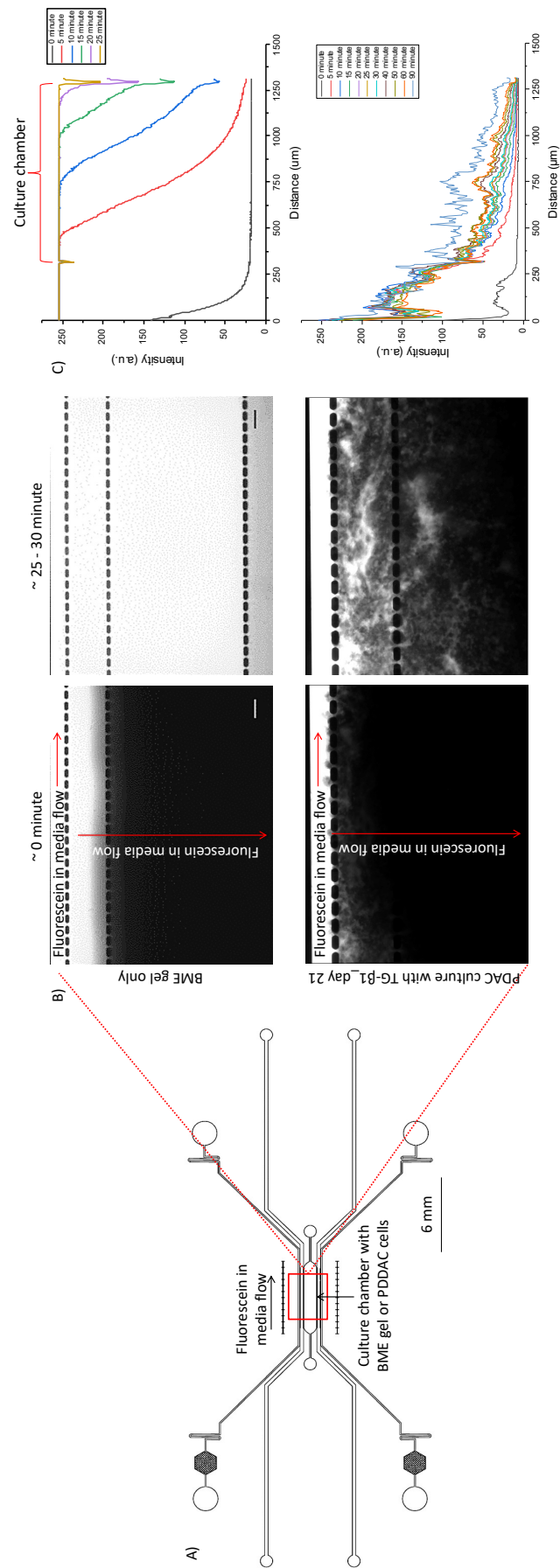


Figure 5.8. The interstitial flow assessment of the on-chip PDAC culture

The perfusion of fluorescein in media solution through the A) 5-channel device with B) BME gel only or the on-chip PDAC culture on day 21 of culture at 0 minute and 20 – 30 minutes after perfusion. C) The intensity profile of the perfusion of the fluorescein in media solution versus the distance travelled in the device over 25 – 90 minute period.

Table 5.3. The interstitial flow assessment of the on-chip PDAC culture

The hydraulic conductivity, interstitial flow velocity and shear stress with the perfusion of fluorescein in culture media solution in the culture chamber with BME gel only or PDAC culture. N = 3 or 4 devices for the BME gel only and the on-chip PDAC per day of culture from three separate seeding settings

| Culture | Ks [m ²] | K' [m ² s ⁻¹ Pa ⁻¹] | IF _v [μm s ⁻¹] | τ [dyne cm ⁻²] |
|----------------------|---|---|---|--|
| BME gel only | 1.3 × 10 ⁻¹² ± 4.4 × 10 ⁻¹⁴ | 1.9 × 10 ⁻⁹ ± 6.3 × 10 ⁻¹¹ | 6.3 × 10 ⁻⁴ ± 2.1 × 10 ⁻⁵ | 2.6 × 10 ⁻⁸ ± 8.7 × 10 ⁻¹⁰ |
| PDAC culture _Day 7 | 3.5 × 10 ⁻¹² ± 8.5 × 10 ⁻¹³ | 5.0 × 10 ⁻⁹ ± 1.2 × 10 ⁻⁹ | 1.6 × 10 ⁻³ ± 4.1 × 10 ⁻⁴ | 6.9 × 10 ⁻⁸ ± 2.3 × 10 ⁻⁸ |
| PDAC culture _Day 14 | 2.9 × 10 ⁻¹² ± 5.8 × 10 ⁻¹³ | 4.2 × 10 ⁻⁹ ± 8.4 × 10 ⁻¹⁰ | 1.4 × 10 ⁻³ ± 2.7 × 10 ⁻⁴ | 5.8 × 10 ⁻⁸ ± 1.2 × 10 ⁻⁸ |
| PDAC culture _Day 21 | 6.3 × 10 ⁻¹³ ± 4.8 × 10 ⁻¹⁴ | 9.1 × 10 ⁻¹⁰ ± 6.9 × 10 ⁻¹¹ | 3.0 × 10 ⁻⁴ ± 2.3 × 10 ⁻⁵ | 1.2 × 10 ⁻⁸ ± 9.6 × 10 ⁻¹⁰ |

Ks, specific hydraulic conductivity; K', hydraulic conductivity; IF_v, interstitial flow velocity; τ, shear stress

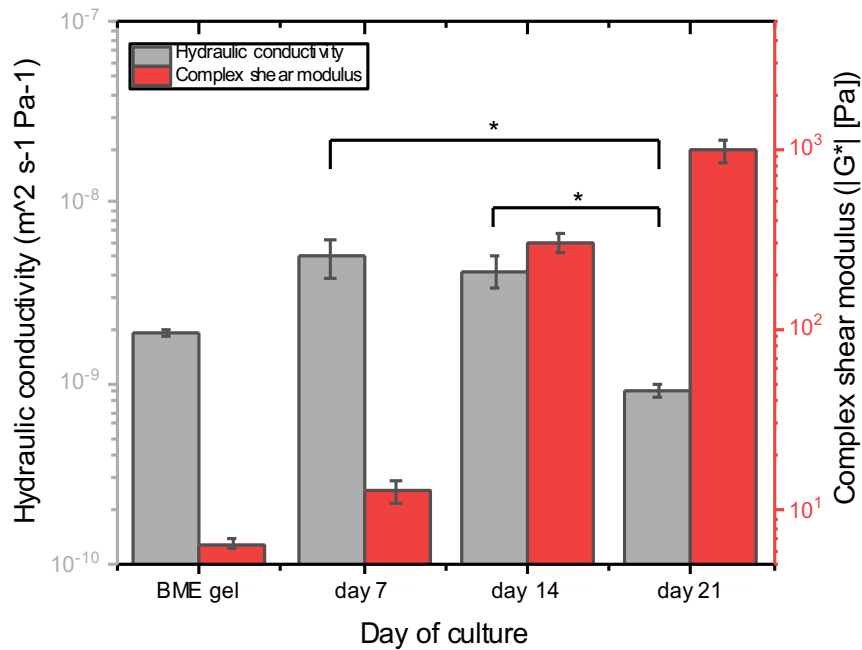


Figure 5.9. The hydraulic conductivity of the on-chip PDAC culture

The hydraulic conductivity of BME gel only and the on-chip PDAC culture on day 7, 14, and 21 of culture compared to the measured complex shear modulus (Figure 4.9). N = 3 or 4 devices for the BME gel only and the on-chip PDAC per day of culture generated from three separate seeding settings. * p < 0.5, one-way ANOVA followed by Tukey's multiple comparison test.

solution in the developing on-chip culture. Increased perfusion indicates the matrix environment for the BME gel and the developing on-chip PDAC cultures were not dense and therefore rigid. This then resulted in increased intrinsic permeability (K_s) to allow the flow of the fluorescein in media solution, resulting in increased K and, therefore, high interstitial flow (IF_v). High interstitial flow also means high shear stress (τ), which affects culture viability. Kramer *et al.* 2019 reported reduced cell proliferation in their PDAC cultures grown in the Organoplate. The rocking platform required for flow (the Organoplate is based in a well-plate format permitting static cell culture) likely resulted in high shear stress, which affected the proliferation of their cells.^[166] For the 21-day culture, with the collagenous, rigid matrix environment, there is increasing cross-linking of fibres, which decreases the size of the porous structure of the matrix, resulting in reduced K_s , IF_v, and τ .^[236-238, 240, 362]

The reduced interstitial flow for the 21-day on-chip PDAC culture is in agreement with the HIF-1 alpha expression (Figure 5.7), as with reduced flow there is limited perfusion of nutrients and oxygen to the cells.

5.5. Conclusion

The 5-channel device was optimal, compared to the 3-channel device, in culturing the PDAC cells (PANC-1 and PSC co-culture) with TGF- β for 21 days. In developing the 5-channel device, it was important to investigate the linear velocities of reported microfluidic devices in the literature to determine optimum channel dimensions and flow regime to ensure continuous flow for the culturing of the PDAC cells. With the optimum channel dimensions and flow regime, the PDAC cells were seeded with BME gel for a 21-day culture. Using collagen hydrogel to mimic the PDAC stroma, Bradney *et al.* 2020, Lee *et al.* 2018, and Lai *et al.* 2020 grew their PDAC cells for up to 10 days. However, they failed to allow the cells to remodel their matrix into a rigid, hypoxic environment with reduced interstitial flow. They did not include stromal cells and cultured their cells in a static culture conditions. Here, with the 21-day culture, the PDAC cells remodelled their ECM into an environment that supported their growth. They mimicked the hallmarks of the PDAC tumour tissue – a fibrotic, hypoxic environment with reduced interstitial transport – for effective therapeutic studies.

6. The effect of Gemcitabine with Microbubbles and Ultrasound on the On-chip Pancreatic Ductal Adenocarcinoma Culture

In this chapter, results of gemcitabine treatment with microbubbles and ultrasound exposure investigated on the on-chip PDAC culture are presented. The viability of the 21-day on-chip culture treated with gemcitabine only, the ability of microbubbles to penetrate through the on-chip culture, and the effect of microbubbles only, ultrasound only, and combined, and the efficacy of gemcitabine with microbubbles and ultrasound together, are presented. Figure 6.1 shows a timeline of the culturing of the 21-day PDAC culture and assessments with gemcitabine, microbubbles, and ultrasound exposure.

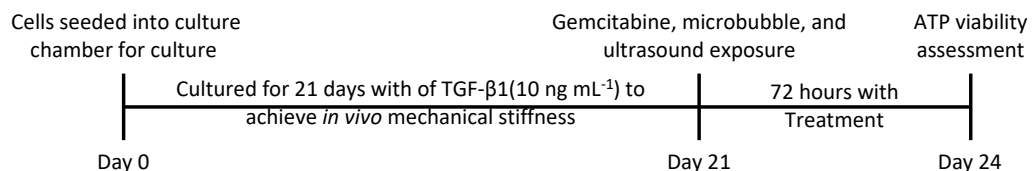


Figure 6.1. Timeline of the on-chip PDAC culture treatment with gemcitabine, microbubbles, and ultrasound
Timeline of the seeding of the PDAC cells on-chip for a 21-day culture, and the ATP viability assessment of the on-chip cultures following treatment with gemcitabine, microbubbles, and ultrasound.

6.1. The effect of gemcitabine on the PDAC culture

Figure 6.2 compares the ATP metabolic activity of the on-chip PDAC cultures with and without gemcitabine. The ATP metabolic activity of the on-chip cultures without gemcitabine is also shown in Figure 5.5B. As shown in Figure 6.1 above, the PANC-1 and PSC cells were seeded on-chip, grown with TGF-β1 for 21 days, and treated with 31.25 μM of gemcitabine for 72 hours. The concentration of gemcitabine used was found to be optimum as it resulted in sufficient cellular viability to assess further viability decreases with gemcitabine, microbubbles, and ultrasound together. The concentration was determined from the effect of varying gemcitabine concentrations used on the off-chip PDAC cultures (section 4.3).

With gemcitabine, the ATP luminescence of the on-chip cultures decreased by about 10%. Lai *et al.* 2020, with the InVADE platform, exposed their cultures to 1 μM of gemcitabine for 96 hours and observed no cytotoxic effects.^[39] They observed cell viability of approximately >

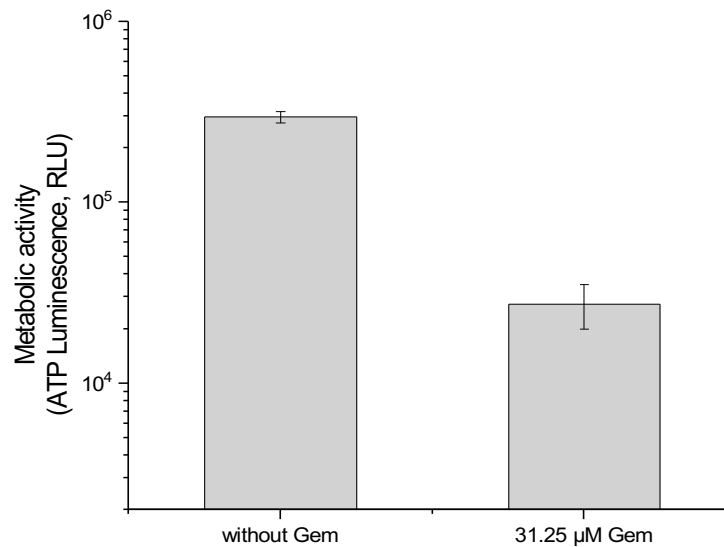


Figure 6.2. The effect of gemcitabine on the on-chip PDAC cultures

ATP viability assessment of the on-chip PDAC culture (PANC-1 and PSC co-culture in a 1: 3 seeding ratio with TGF-1 supplement [10 ng mL⁻¹] with and without gemcitabine, normalised to controls. N = 18 devices generated from three separate seeding settings for the on-chip cultures without gemcitabine treatment. N = 12 devices from three separate seeding settings for the on-chip cultures treated with 31.25 µM gemcitabine.

70 % for their fibroblast only, pancreatic tumour organoid (PDAC cancer cells only), and co-cultures (the pancreatic tumour organoids and fibroblast cells) in Matrigel solution. This could be due to the low gemcitabine concentration used, but Lee *et al.* 2018 exposed their co-cultures (PANC-1 and PSC in collagen solution) to 1 mM of gemcitabine for 72 hours, and 80 – 90 % of tumour cells were still viable.^[165] Kramer *et al.* 2019, with the OrganoPlate platform, exposed their PDAC cells grown in collagen rich solution to varying concentrations of gemcitabine (0 – 64 nM) for 72 hours and observed lower sensitivity.^[166] Lai *et al.*, Lee *et al.*, and Kramer *et al.* cultured their cells for up to 10 days, and they used contrasting concentrations of gemcitabine and different to the 31.25 µM of gemcitabine used here for the 21-day on-chip PDAC cultures. However, the effect of gemcitabine observed demonstrates the impediment of the dense, collagenous PDAC stroma on the cytotoxic effects of gemcitabine (Figure 4.16). Gemcitabine molecule has a longer dimension of around 1.1×10^{-4} µm (11Å),^[363] and this indicates the stroma of the 21-day on-chip PDAC culture might have a pore size of less than 1.1×10^{-4} µm to impede the interstitial transport of gemcitabine. As such, it was perceived disrupting the stroma and inducing delivery and uptake of gemcitabine would increase its efficacy.

6.2. Effect of microbubbles and ultrasound on the PDAC culture

Before treatment with gemcitabine, the ability of microbubbles to permeate through the on-chip PDAC culture, its effect on the culture viability, and the effect of ultrasound exposure with and without microbubbles on culture viability was evaluated.

6.2.1. Microbubble production

As described in section 3.11.3, microbubbles were produced on-chip and with mechanical agitation. Mechanical agitation was used where the multiplexed device used for microbubble production on-chip was unavailable. The multiplexed microfluidic device was developed by Dr Sally A Peyman.^[268, 302] Figure 6.3A shows a schematic of the multiplexed device, with a focus on one of the flow focusing nozzles, where there is an atomisation effect for the production of microbubbles in the microspray regime. Figure 6.3B shows bright-field and ATTO 488 fluorescent images of the microbubbles produced with the multiplexed microfluidic device diluted 10 × with PBS for size and concentration analysis. Figure 6.3C shows a typical population distribution data for the microbubble concentration and size characterisation. The concentration and size of the microbubbles produced on-chip were $2.3 \times 10^9 \pm 4.93 \times 10^8$ bubbles per mL and $2 \pm 1.5 \mu\text{m}$ in diameter, respectively. Shown in Figure 6.3D, compared to microbubbles produced on-chip, microbubbles produced by mechanical agitation were more polydispersed,^[267, 302] but with sizes still within the clinical range of 1 – 10 μm .^[211, 260, 262, 266] The concentration and size of the microbubbles were $8.43 \times 10^8 \pm 3.34 \times 10^8$ bubbles per mL and $2.46 \pm 2.3 \mu\text{m}$ in diameter, respectively.

6.2.2. Microbubble perfusion and effect on the on-chip PDAC culture viability

As described in section 3.11.4 and illustrated with Figure 3.10, the ability of microbubbles to permeate through the on-chip PDAC culture was investigated. DPPC: DSPE-PEG₂₀₀₀: ATTO 488 microbubbles were made as described in section 3.11.3, diluted with DMEM/10 %FBS culture media in a 1: 10 ratio, and introduced into the device with the 21-day on-chip PDAC culture. As a control, the flow of microbubbles was assessed with BME gel only on-chip. Imaging was performed with confocal microscopy, using a 10 × objective and a pinhole of 1.00 AU with the respective excitation and emission wavelengths for the ATTO 488 lipid (Ex/Em: 500/520 nm).

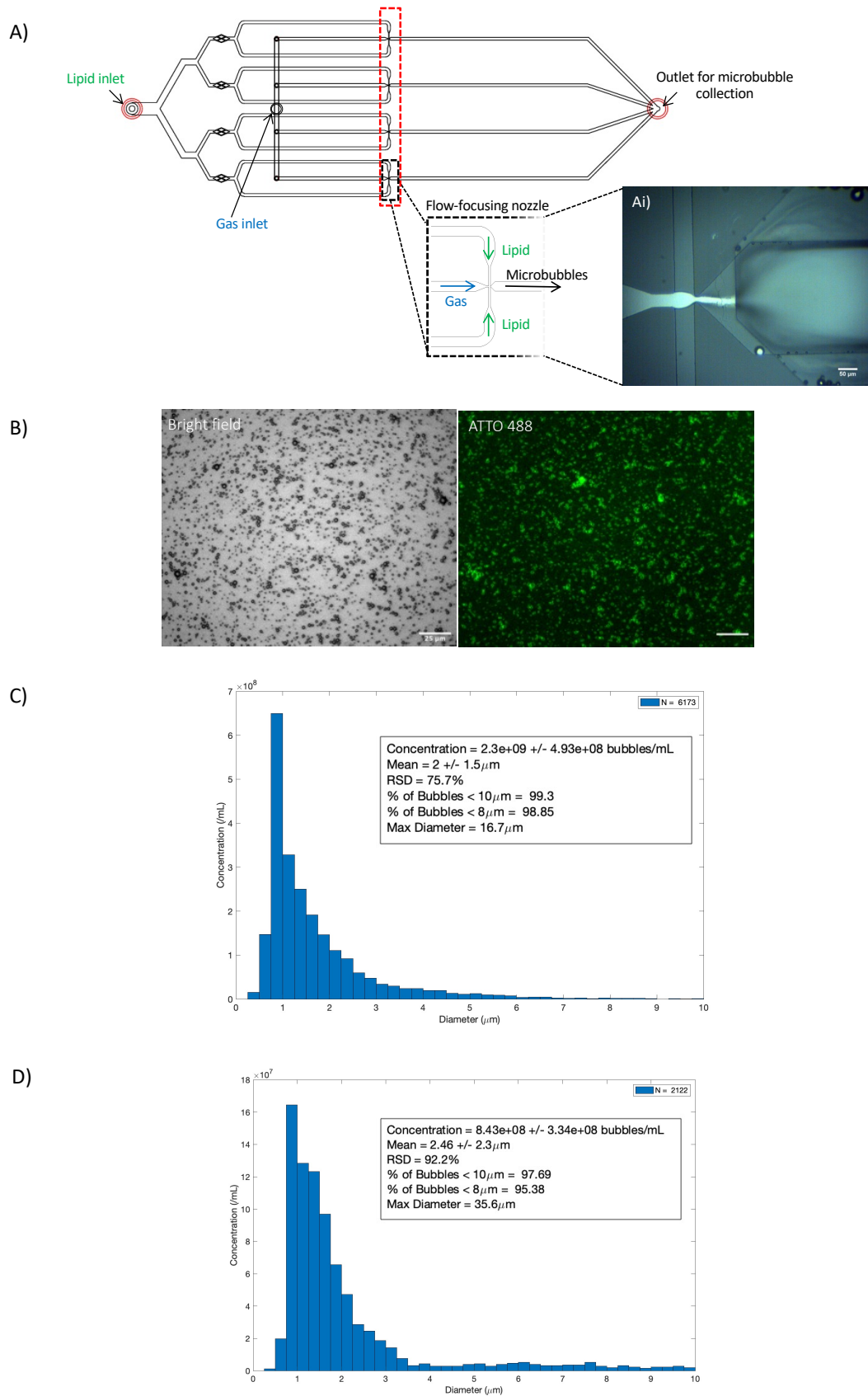


Figure 6.3. On-chip microbubble production and the size distribution

A) CAD of the multiplexed microfluidic device for microbubble production in the microspray regime. The device was designed and developed by Dr Sally A. Peyman detailed in reference [268]. Image of CAD adapted with permission from Dr Peyman. B) Bright-field and ATTO 488 images of the DPCC: DSPE-PEG₂₀₀₀: ATTO 488 microbubbles produced on-chip. C) and D) data on the microbubble concentration and size produced on-chip and with mechanical agitation, respectively.

Figure 6.4 shows the microbubbles in the device with BME gel only and the 21-day on-chip culture. The microbubbles used in the assessments had an average size of 2 μm , as shown in the exemplar population distribution graphs (Figures 6.3C and D). Supplementary videos 9 to 12 show the bright-field and ATTO 488 fluorescent videos of the flow of microbubbles passing between the pillars into the device with the BME gel only and 21-day on-chip PDAC culture. They show the microbubbles were able to flow between the pillars, permeating through the porous structure of the BME gel only (Figure 6.4A) and the dense, collagenous matrix of the PDAC culture (Figure 6.4B).

Pednekar *et al.* 2021 assessed the penetration of 100 nm silica nanoparticles in their PANC-1: PSC cultures with a dense ECM and grown in 4 or 5 mg mL^{-1} of collagen. Fisher *et al.* 2018 analysed the pore size of their 3D collagen matrix scaffolds and found a median pore size of 10.99 μm and 6.84 μm for 1.5 mg mL^{-1} and 3.0 mg mL^{-1} of collagen, respectively.^[144, 364] For the microbubbles to permeate through the BME gel only and the 21-day on-chip PDAC culture, in comparison to Pednekar *et al.* and Fisher *et al.*, the size of the matrix pore could have been < 5 μm . SEM images of the BME gel only and the culture environment of the PDAC cultures could have been used to confirm the pore structure and size given more experimental time. Moreover, with a reduced hydraulic conductivity measured (Figure 5.9), it is likely less than a majority of the microbubbles flowing in the media channels entered into the culture chamber with the PDAC culture.

Figure 6.5 shows the effect of the microbubbles only on the viability of the 21-day on-chip PDAC culture. With microbubbles only, the viability of the 21-day on-chip PDAC culture was about 84 %. A decrease in viability in comparison to the on-chip culture without treatment could be a result of the effects of the lipid preparation for the microbubble production. The phospholipids are biocompatible^[365, 366] and were prepared under aseptic conditions. However, the lipids were prepared in a chemistry laboratory, where the lipid solution could have been contaminated, as oppose to its preparation in a tissue culture lab under sterile conditions.

6.2.3. The effect of ultrasound with and without microbubbles on the on-chip PDAC culture viability

For ultrasound application, as described in section 3.11.5, the 5-channel device for the on-chip culture was made to a 1 mm thickness.

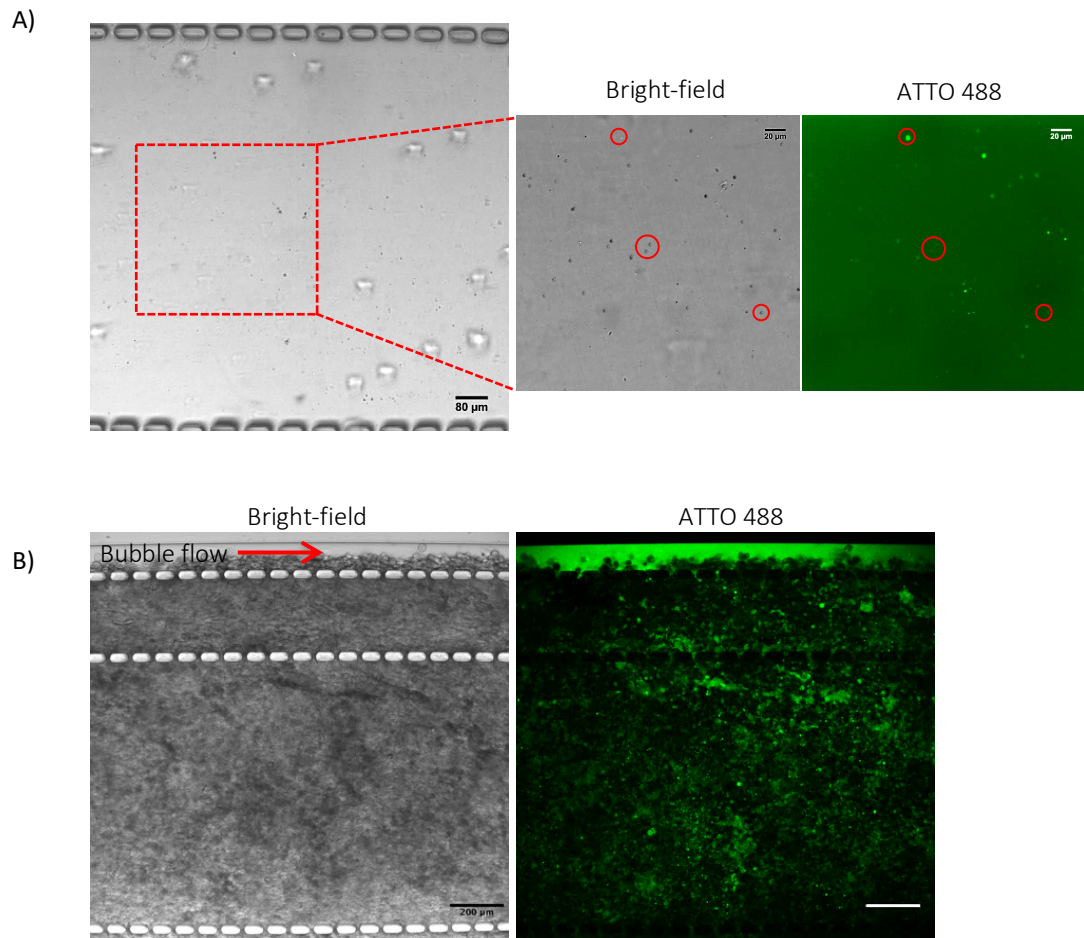


Figure 6.4. Flow of microbubbles in the on-chip PDAC culture

DPPC: DSPE-PEG₂₀₀₀: ATTO 488 microbubbles were perfused into the device with A) BME gel only and B) the 21-day on-chip culture. The microbubbles were observed in the culture chamber of the device with the BME gel 21-day on-chip PDAC culture. Red circles in A) show microbubbles in the gel. Scale bar 200 μm .

This was to reduce the attenuation of the ultrasound signals travelling through the PDMS to the culture chamber.^[367] For optimal culturing with the media reservoirs, additional PDMS of 4 to 5 mm in thickness was bonded onto the inlet and outlet media regions of the device (Figures 3.10B).

DPPC: DSPE-PEG₂₀₀₀: ATTO 488 microbubbles were made, diluted in a 1: 10 ratio with DMEM/10 % FBS culture media, and introduced into the device with the 21-day on-chip PDAC culture. After approximately 2 hours, with the microbubbles in the culture chamber with the PDAC culture, ultrasound was applied. Confocal imaging and ATP viability assessments were performed (described in sections 3.2.3 and 3.12.2, respectively) to determine the effect of

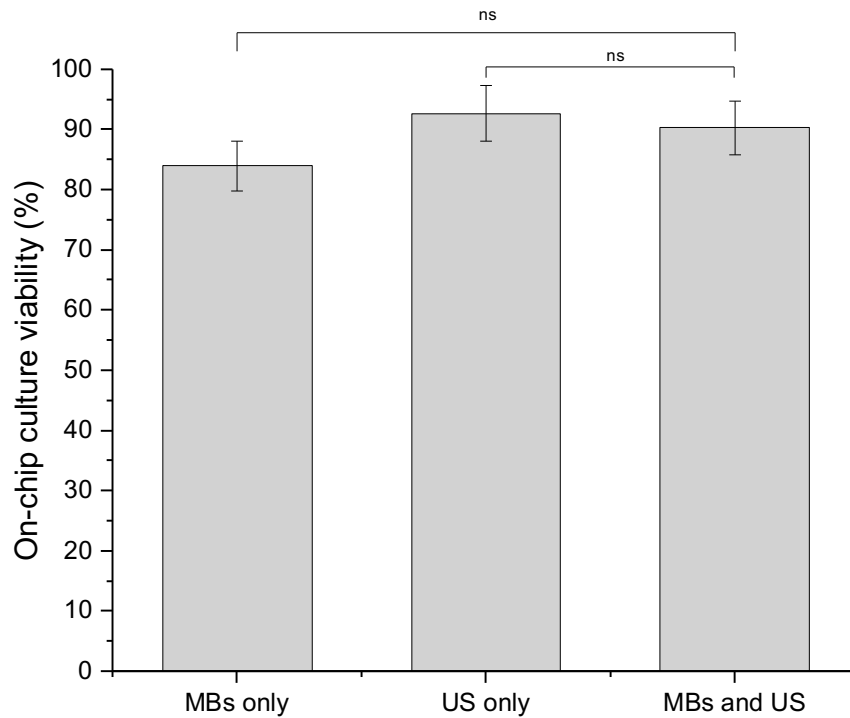


Figure 6.5. On-chip culture viability with microbubbles and ultrasound treatment

ATP viability assessment for the 21-day on-chip PDAC cultures treated with microbubble only (MBs only), ultrasound only (US only) and microbubble and ultrasound together (MBs and US). $N = 6 - 8$ devices per treatment generated from three separate seeding settings. ns, $p > 0.5$, one-way ANOVA followed by Tukey's multiple comparison test.

ultrasound with and without microbubbles on the cultures. As a control, the effect of ultrasound application with and without microbubbles was assessed on BME gel only.

Figure 6.6 shows images of the effect of ultrasound with and without microbubbles on the BME gel only and the 21-day on-chip culture. Figure 6.6A, there was no effect observed when ultrasound only (no microbubbles) was applied to the BME gel only on-chip. The only effect observed was to do with the confinement of the BME gel around the pillars, between the media channel and the gel channel (Figure 6.6Aii). There was an expansion of the BME gel into the media channel, and this was likely to do with the expansion of air pockets (from no fluid flow in the media channel), which affected the integrity of the confined BME gel. With microbubbles, Figure 6.6B, the structure of the BME gel in the culture chamber seemed disturbed. The stiffness of the BME gel over a 21-day incubation period was 10 – 15 Pa (Figure 4.13) and, therefore, the oscillation and bursting of the microbubbles with ultrasound application may have easily disrupted the BME gel structure.

Figure 6.7 shows images of the effect of ultrasound only and ultrasound with microbubbles on the 21-day on-chip PDAC culture. There were no noticeable differences observed with the ultrasound only application (Figure 6.7A). With ultrasound and microbubbles, what was observed was an increase in the ATTO 488 fluorescent intensity (Figure 6.7B). Without microbubbles, the viability of the on-chip PDAC cultures with ultrasound only application was 93 %. With microbubbles, the viability of the on-chip PDAC cultures with ultrasound was 90 % (Figure 6.5). This further demonstrated that there was no effect on the on-chip PDAC cultures with ultrasound only application. The effect of ultrasound with microbubbles on the culture viability was likely to do with the preparation of the lipid solution used for the microbubbles.

6.3. Effect of gemcitabine, microbubbles, and ultrasound on the PDAC culture

Studies on the use of sonoporation, the formation of small pores in cell membranes with ultrasound, to transfer therapeutics into cells, show an increase in drug uptake by cells and drug efficacy.^[210] Kotpoulis *et al.* 2014 investigated a combination of gemcitabine, ultrasound, and microbubbles on orthotopic pancreatic cancer mouse models and found a significant decrease in tumour growth with increased median survival.^[368] Dimcevski *et al.* 2016 and Kotopoulis *et al.* 2013 investigated the combination of gemcitabine, ultrasound, and microbubbles in the clinical setting and found an improved efficacy of gemcitabine, where there was an increase in PDAC patient survival.^[209, 369] McEwan *et al.* 2016 and Nesbitt *et al.* 2018 assessed the effect of gemcitabine together with microbubbles (although oxygenated; O₂MBs) and ultrasound in human xenograft SCID mice models as well as on the 2D cultures of the PDAC cancer cells MIA PaCa-2, BxPC-3, and PANC-1, and a patient-derived cell line, T110299. O₂MBs were used to increase the reactive oxygen species and sensitivity of the cancer cells to the effects of gemcitabine. They observed a significant reduction in the PDAC cancer cell viabilities and tumour growth in the mice.^[218, 219]

So far, the effect of gemcitabine, microbubbles, and ultrasound has not been investigated in 3D PDAC cultures that reflect the mechanics of the PDAC tumour. However, using 3D tumour spheroids Roovers *et al.* 2019 and Bourn *et al.* 2020 show sonoporation allows the release of doxorubicin into the deep layers of spheroids resulting in a significant reduction in cell viability.^[291, 370]

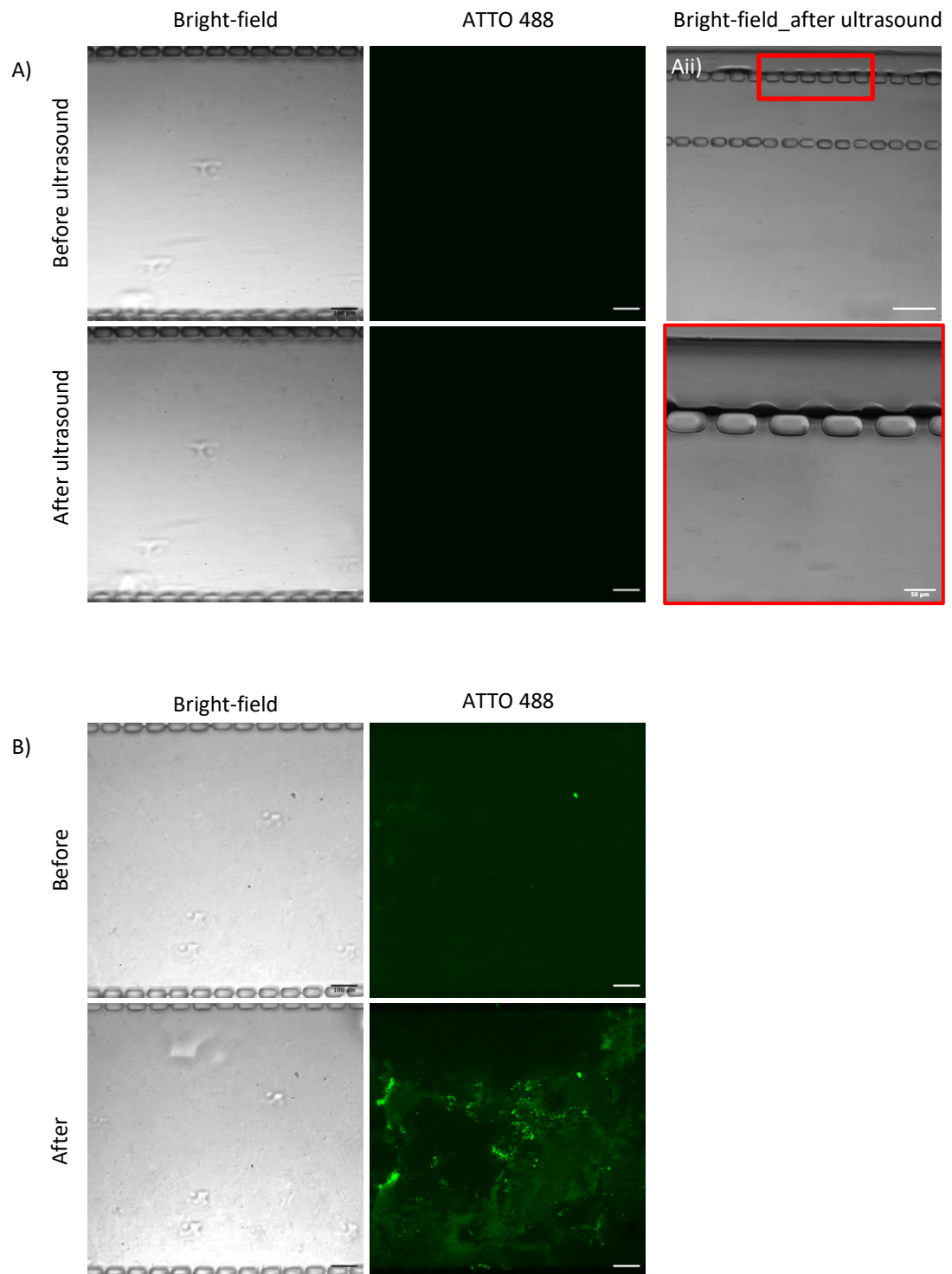


Figure 6.6. The effect of ultrasound on BME gel on-chip

Confocal images of the effect of ultrasound with and without microbubbles on BME gel only in the culture chamber of the device. A) images of the effect of ultrasound without microbubbles on $6 - 9 \text{ mg mL}^{-1}$ of BME gel. Aii) Effect of ultrasound on the BME gel around the pillars between the gel channels and media channels. The red box in the bright-field image, top, is of the magnified image below. B) Images of the effect of ultrasound with microbubbles on the $6 - 9 \text{ mg mL}^{-1}$ BME gel. Where not specified, the scale bar is $100 \mu\text{m}$.

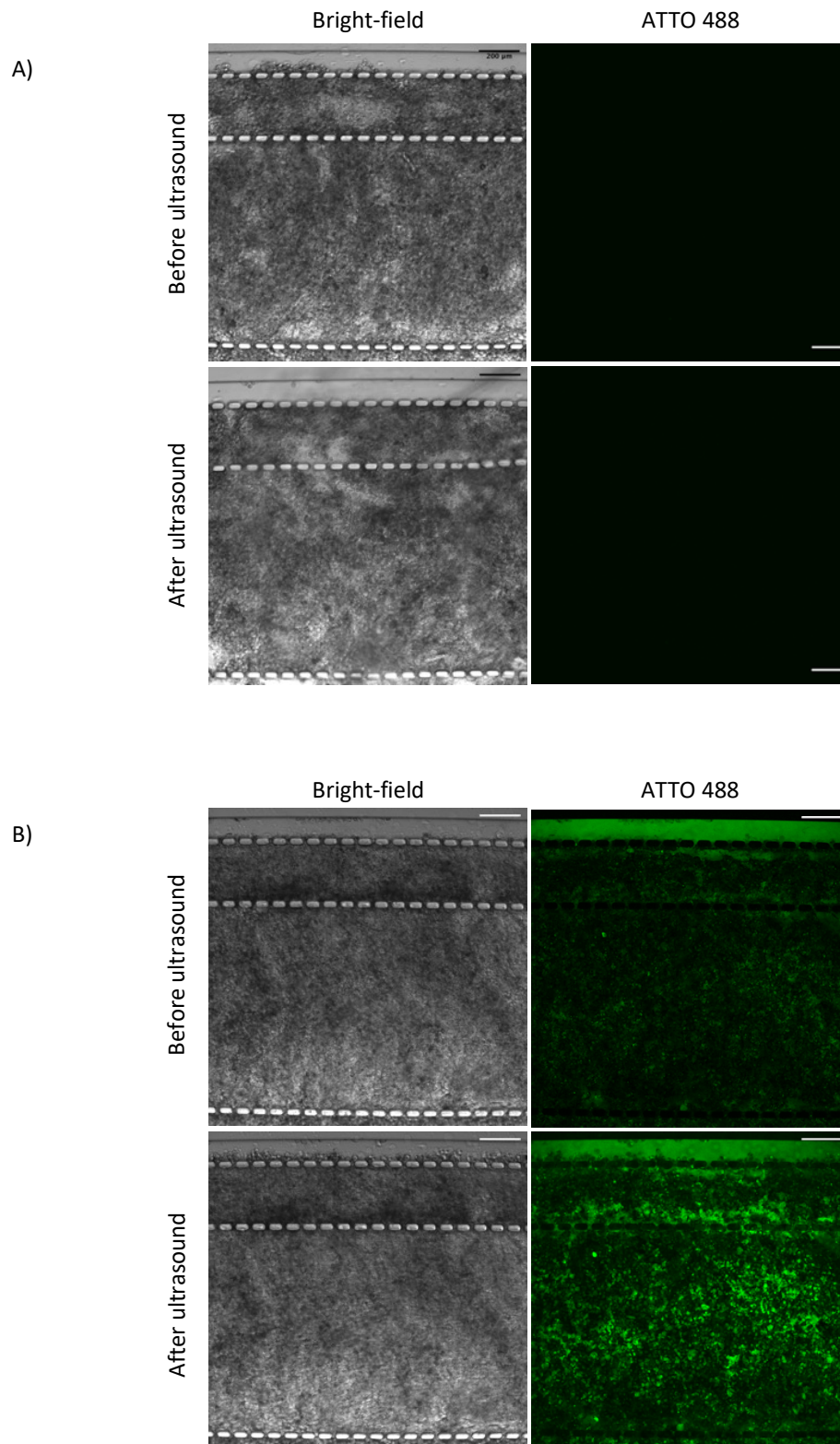


Figure 6.7. The effect of ultrasound on the 21-day on-chip PDAC culture

Confocal images of the effect of ultrasound with and without microbubbles on the on-chip PDAC culture grown for 21 days. A) images of the effect of ultrasound without microbubbles, and B) images of the effect of ultrasound with microbubbles. Scale bar, 200 μm.

Utilising the idea and effect of sonoporation in forming pores in membranes and increasing drug efficacy, microbubbles and ultrasound was exposed to the 21-day on-chip PDAC cultures to disrupt the ECM and sensitise the PDAC cells to the effects of gemcitabine. PDAC cells were seeded into the 5-channel device, cultured for 21 days with TGF- β 1 (10 ng mL⁻¹), and treated to DPPC: DSPE-PEG₂₀₀₀ microbubbles diluted in a 1: 10 ratio with DMEM/10 %FBS/31.25 μ M of gemcitabine solution. After approximately 2 hours, ultrasound was applied, and culture viability assessed (Figure 6.1). As controls, the cultures were treated with gemcitabine only, gemcitabine and microbubbles, and gemcitabine and ultrasound to compare and determine the effect of gemcitabine with microbubbles and ultrasound treatment together.

Figure 6.8 shows the percentage viability of the effect of gemcitabine only, gemcitabine with microbubbles, gemcitabine with ultrasound, and gemcitabine with microbubbles and ultrasound together normalised to controls. The percentage viabilities of the culture with the different treatments were approximately 62 %, 64 %, 69 %, and 61 %, respectively. Compared to the effect of gemcitabine only, there was no significant reduction in the cell viability for cultures treated with gemcitabine, microbubble, and ultrasound together.

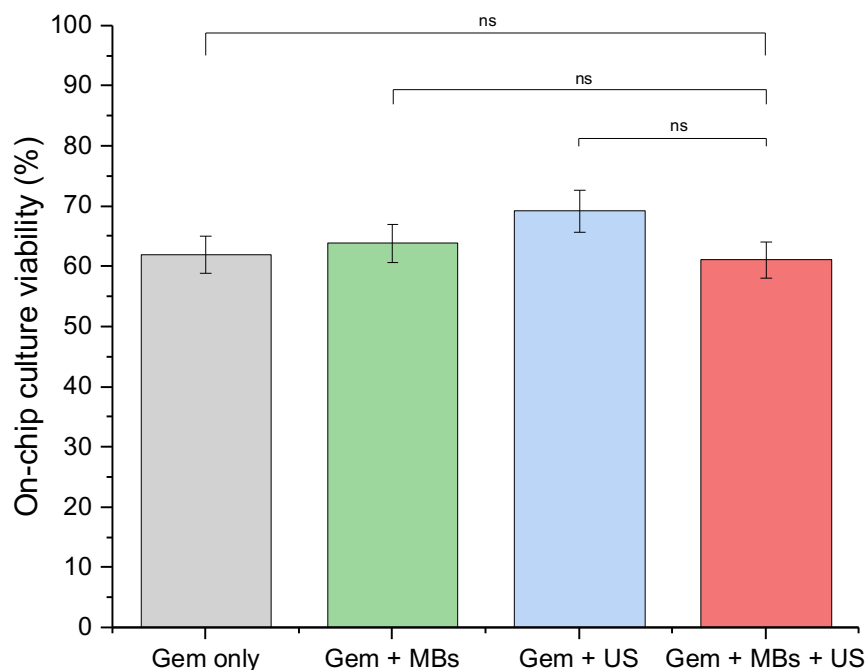


Figure 6.8. On-chip culture viability with gemcitabine, microbubbles, and ultrasound treatment

Culture viability assessment of the 21-day on-chip PDAC cultures 72 hours after treatment with 31.25 μ M of gemcitabine, microbubbles, and ultrasound. The on-chip PDAC cultures were treated with gemcitabine only (Gem only), where $n = 12$ on-chip cultures; gemcitabine and microbubbles (Gem + MBs), where $n = 7$ on-chip cultures; gemcitabine and ultrasound (Gem + US), where $n = 7$ on-chip cultures, and gemcitabine, microbubbles, and ultrasound together (Gem + MBs + US), where $n = 9$ on-chip cultures, all from three separate seeding settings. ns, $p > 0.5$, one-way ANOVA followed by Tukey's multiple comparison test.

Although microbubbles were observed in the culture chamber of the 21-day PDAC culture (Figures 6.7B; figure show the top view of the chip) with a dense, collagenous matrix and a reduced hydraulic conductivity, compared to the hydraulic conductivity measured for the BME gel only with a complex shear modulus of 10 – 15 Pa, it is likely a significantly smaller number of microbubbles entered the culture chamber from the media channels. This then resulted in not enough microbubbles to interact and disrupt the ECM and sensitise the cells to the effect of gemcitabine under ultrasound exposure. Therefore, a small reduction in the culture viability with gemcitabine, microbubble, and ultrasound treatment together.

To compare, the effect of the gemcitabine, with microbubble, and ultrasound treatment was also assessed on the 2D culture of the PDAC cells. As described in section 3.11.8, PDAC cells were seeded into a 96-well plate and ibidi μ -Slide microfluidic devices, cultured until $\geq 70\%$ confluency, and treated with gemcitabine only, microbubbles only, ultrasound only, gemcitabine and microbubbles together, gemcitabine and ultrasound together, and gemcitabine, microbubbles, and ultrasound treatment together.

Figure 6.9 shows the results of the ATP viability assessment of the 2D PDAC cultures with the different treatment conditions. Although there was no significant difference between the effect of the gemcitabine only treatment and the gemcitabine, microbubbles, and ultrasound treatment together, the percentage viability of 55 % and 45 %, respectively, indicated that the mechanics of the on-chip PDAC cultures (*i.e.*, dense, collagenous matrix with reduced hydraulic conductivity) resulted in their percentage viabilities of 62 % and 61 % with gemcitabine treatment only and gemcitabine, microbubble, and ultrasound treatment together, respectively.

6.4. Effect of therapeutic microbubbles on the PDAC culture

The sonoporation of microbubbles conjugated to drug-loaded liposomes (therapeutic microbubbles) has shown to be a useful therapeutic tool to avoid low therapeutic index – high toxicity effects in cells and tissues while maintaining high therapeutic delivery and effect.^[222, 370, 371] Similar to Ruan *et al.*, 2021 and Tucci *et al.*, 2019^[228, 229], who treated their cell cultures and mice models with conjugates of microbubbles and gemcitabine-loaded liposomes and ultrasound, here, the 21-day on-chip PDAC culture was treated with therapeutic microbubbles, a gemcitabine-loaded liposome-microbubble complex (Figure 3.11A), and ultrasound exposure. With ultrasound, the oscillating microbubbles will shed the attached

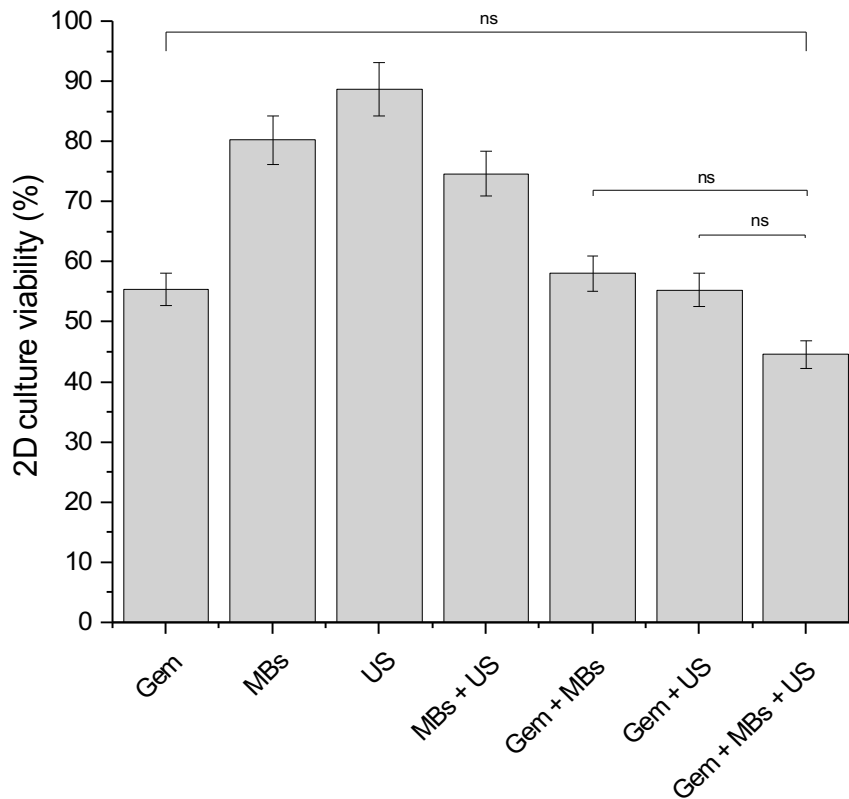


Figure 6.9. Viability assessment of 2D PDAC cultures

Culture viability assessment of PDAC cells cultured in 2D. PDAC cells were seeded into a 96-well plate and ibidi μ -Slide microfluidic devices, cultured until confluent, before treatment with 31.25 μ M of gemcitabine, microbubbles, and ultrasound. The 2D PDAC cultures were treated with gemcitabine only (Gem only), gemcitabine and microbubbles (Gem + MBs), gemcitabine and ultrasound (Gem + US), and gemcitabine, microbubbles, and ultrasound together (Gem + MBs + US), where $n = 6$ well of a 96-well plate and 8 ibidi μ -Slide channels, for each of the treatment condition, all from three separate seeding setting. ns, $p > 0.5$, one-way ANOVA followed by Tukey's multiple comparison test.

gemcitabine-loaded liposomes, which will be deposited close to the PDAC cells, and the encapsulated gemcitabine will be released from the liposomes under ultrasound exposure. With liposomes, the amount of gemcitabine in the culture chamber with the PDAC culture will be concentrated.^[222, 227] It is important to note that due to limited experimental time, the viability data presented here on the effect of therapeutic microbubbles on the 21-day on-chip PDAC culture were of one seeding setting.

Gemcitabine-loaded liposomes were made as described in section 3.11.7. The liposome size distribution and concentration were characterised, and Figure 6.10A shows the size and concentration of the gemcitabine-loaded liposomes. The mean size and concentration of the gemcitabine-loaded liposomes were 190.2 ± 1.3 nm and $1.42 \times 10^{13} \pm 5.91 \times 10^{11}$ particles

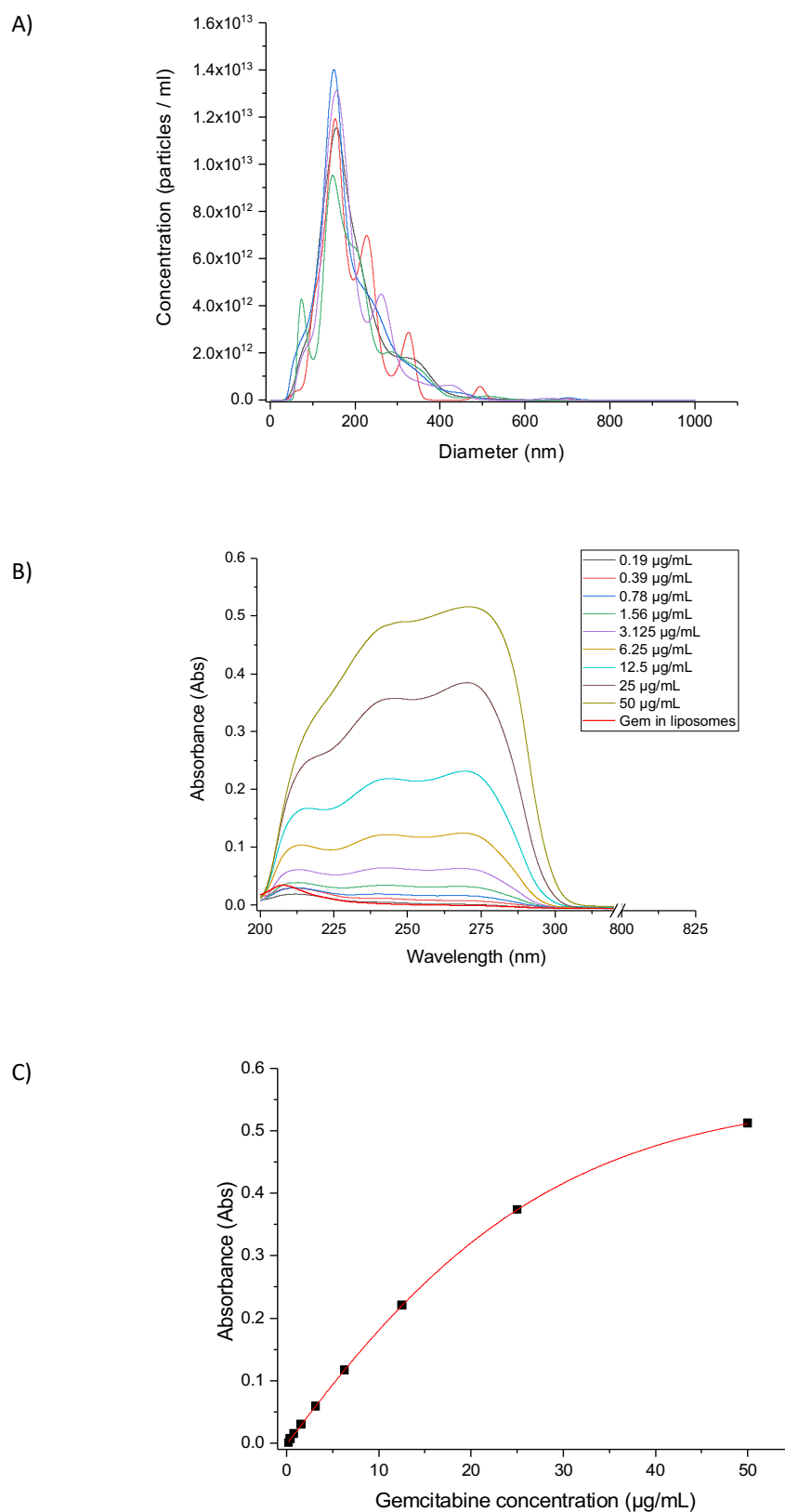


Figure 6.10. Concentration and size of the gemcitabine-loaded liposomes

A) The concentration and size characterisation of the gemcitabine-loaded liposomes with the Nanosight. The average size and concentration of the liposomes were 190.2 ± 1.3 nm and $1.42 \times 10^{13} \pm 5.91 \times 10^{11}$ particles mL^{-1} , respectively. B) UV-vis spectra of the absorbance of different gemcitabine concentrations for C) a calibration or standard curve to determine the concentration of gemcitabine encapsulated in the liposomes.

mL^{-1} , respectively. The gemcitabine concentration in the liposomes was also characterised using a UV-vis spectrometer. A standard curve with different gemcitabine concentrations was generated to determine the amount of gemcitabine in the liposomes. Figure 6.10B shows the UV-vis spectra data of absorbance versus wavelength (nm) for the different gemcitabine concentrations and of gemcitabine in the liposomes. The peak absorbance of gemcitabine for the different concentrations was 275 nm. From this, the standard curve, shown in Figure 6.10C, was generated. A peak absorbance reading for the gemcitabine-loaded liposomes was found at 208 nm. Although this did not appear to be a peak for gemcitabine, with reference to the standard curve (Figure 6.10C), this corresponded to a gemcitabine concentration of about $1.8 \mu\text{g mL}^{-1}$ ($6 \mu\text{M}$). With a total drug concentration of 5 mg mL^{-1} (16.68 mM) gemcitabine used to prepare the liposome, the EE % (using *Equation 24*) was calculated as 0.036 %. The minimal 3 hour incubation of the liposomes with gemcitabine, compared to an overnight incubation, likely resulted in less or no gemcitabine encapsulated, with a peak absorbance at 208 nm for the gemcitabine-loaded liposomes. However, the gemcitabine-loaded liposomes were used in making the therapeutic microbubbles for treatment with the on-chip PDAC culture.

The therapeutic microbubbles were made as described in section 3.11.7. After production, the size and concentration of the therapeutic microbubbles were characterised. Figure 6.11A shows a plot of the size and concentration of the therapeutic microbubbles. Figure 6.11B shows the bright-field and fluorescent images of the therapeutic microbubbles with the ATTO 590 fluorescently labelled gemcitabine-loaded liposomes surrounding the microbubbles. The mean size and concentration of the therapeutic microbubbles were $2.1 \pm 2 \mu\text{m}$ and $2.63 \times 10^9 \pm 2.85 \times 10^8$ bubbles per mL, respectively. The therapeutic microbubbles were then mixed in a 1: 10 ratio with DMEM/10 %FBS culture media and used to treat the PDAC cells grown on-chip for 21-days with and without ultrasound. As controls, the 21-day on-chip PDAC cultures were treated with therapeutic microbubbles of blank liposomes conjugated to the DPPC: DSPE-PEG₂₀₀₀: ATTO 488 microbubbles, and 2D PDAC cells were treated with the therapeutic microbubbles (gemcitabine-loaded liposomes or blank liposomes conjugated onto DPPC: DSPE-PEG₂₀₀₀: ATTO 488 microbubbles) with and without ultrasound. ATP viability assessment was performed to determine the effect of the therapeutic microbubbles on the on-chip cultures.

Figures 6.11C shows the percentage viability of the 21-day on-chip culture and the 2D PDAC cultures treated with the therapeutic microbubbles. There was no difference observed

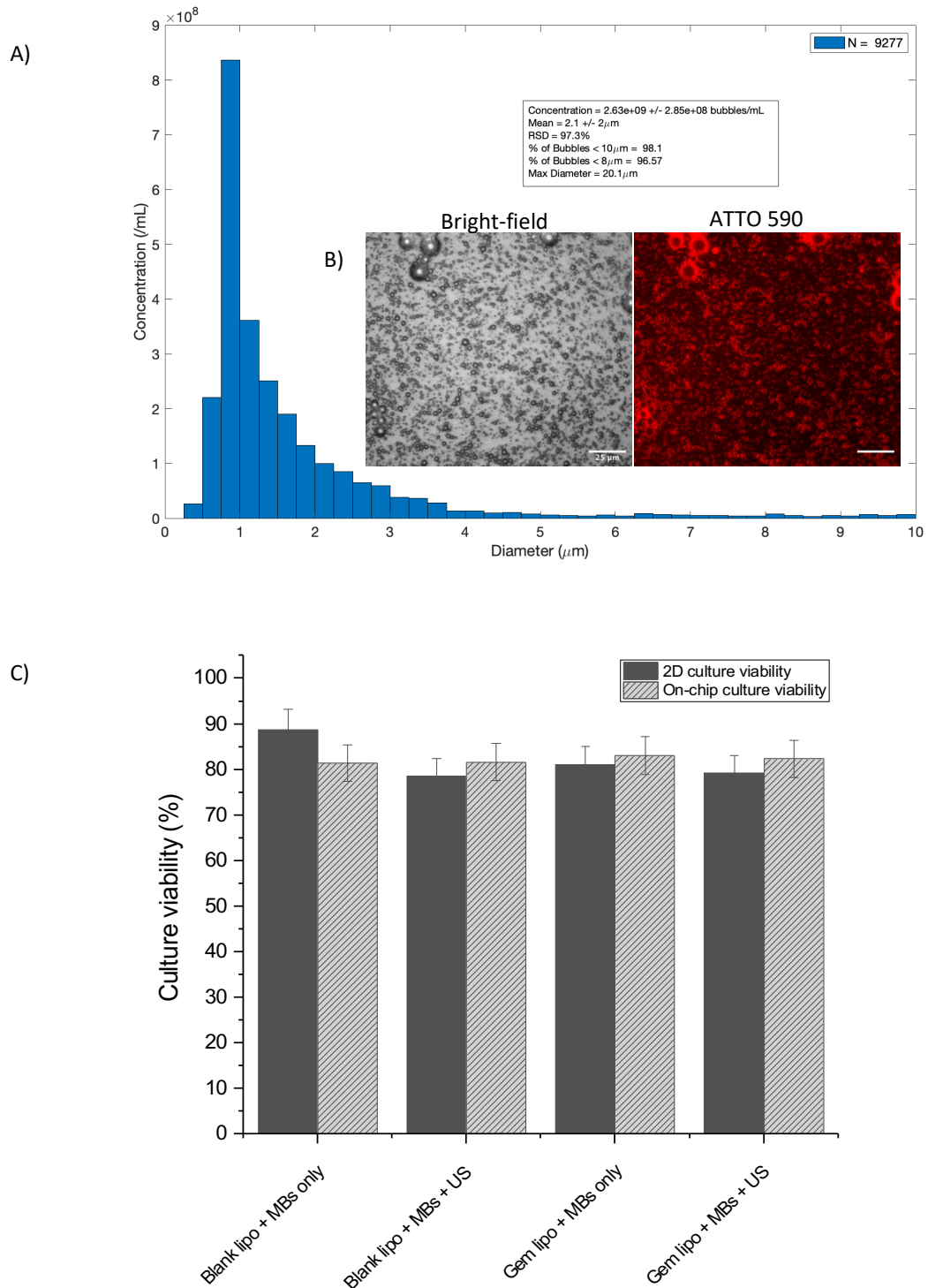


Figure 6.11. Concentration, size, and effect of the therapeutic microbubbles

A) The concentration and size of the therapeutic microbubbles. B) The bright-field and epifluorescence images of the therapeutic microbubbles with the ATTO590 fluorescently labelled gemcitabine-loaded liposomes conjugated to the microbubbles. Scale bar, 25 μm . C) Culture viability of the 2D PDAC and the 21-day on-chip PDAC cultures 72-hours after treatment with therapeutic. The therapeutic microbubbles and treatment were blank-loaded liposome-microbubble complex with and without ultrasound exposure (Blank lipo + MBs + US and Blank lipo + MBs only, respectively) and gemcitabine-loaded liposome-microbubble complex with and without ultrasound exposure (Gem lipo + MBs + US and Gem lipo + MBs only, respectively). N = 3 ibidi μ -Slide channels for each treatment group for the 2D PDAC cultures, and n = 2 on-chip cultures for each of the blank-loaded liposome treatment groups and n = 3 on-chip cultures for each of the gemcitabine-loaded liposome treatment groups for the on-chip PDAC cultures.

between the effect of the therapeutic microbubbles on the 21-day on-chip PDAC cultures and on 2D PDAC cultures and between the gemcitabine-loaded liposome-microbubble complex and the blank liposome-microbubble complex with and without ultrasound exposure. In comparison to Ruan et al., who saw a reduction in the viability of their 2D cultured bladder cancer cell lines and tumour growth in orthotopic mouse models, here, there was no therapeutic effect observed. This could be as a result of 1) less or no gemcitabine encapsulated in the liposomes. The EE % was 0.036 % (with a peak absorbance at 208 nm not corresponding to gemcitabine), and as such, there was not enough or no gemcitabine to cause a therapeutic effect on both the 2D and the on-chip culture. Any reduction in viability could have been due to effects of microbubbles and ultrasound, as seen in Figures 6.5 and 6.9. 2) As observed with the gemcitabine, microbubble, and ultrasound treatment together (Figure 6.8), the effects of the reduced interstitial flow (Figure 5.9) likely resulted in less of the therapeutic microbubbles entering into the culture chamber to cause an effect on the 21-day on-chip culture. However, this does not explain the percentage viabilities for the 2D culture. On-going ways of increasing the amount of gemcitabine encapsulated in the liposomes, for example, an overnight incubation of the liposomes with gemcitabine, are being investigated.

6.5. Conclusion

Findings of the mechanism of gemcitabine resistance include the entrapment of the drug by fibroblasts and CAF cells, competition for its uptake into cells with deoxycytidine, its active uptake into cells by hENT1, and high levels of MRPs.^[117, 166, 179, 190, 228, 372] Studies on improving drug delivery to cancer cells include the use of ultrasound-targeted delivery. The use of sonoporation to increase the efficacy of gemcitabine has been shown in 2D culture studies, mice models, and clinically in patients, where there is a decrease in 2D cell culture viability and an improvement in the survival of mice and patients. However, the effect of sonoporation has not been investigated on the microfluidic culture of PDAC, which mimics the hallmarks of the disease.

Ultrasound-targeted delivery of gemcitabine on the 21-day PDAC culture was investigated, and in comparison to the percentage viability of the culture with gemcitabine only treatment, there was no significant decrease in the viability of the cultures with gemcitabine, microbubbles, and ultrasound treatment together. The 21-day PDAC culture as shown in Figures 4.9, 5.6, 5.7, and 5.9 mimics the fibrotic stroma, mechanical stiffness, the hypoxic

environment, and reduced interstitial flow of the PDAC tumour tissue, and this likely accounted for the percentage viabilities. Other models in the literature have observed a significant effect in the efficacies of chemotherapeutic drugs with microbubbles and ultrasound, and this could be because their models do not encompass the biophysical hallmarks of the PDAC tissue. For example, Nesbitt *et al.* assessed the ultrasound-targeted delivery of gemcitabine *in vitro* with 2D cultures of PDAC cells.^[219] Shown here is how important it is to model the mechanics of the PDAC tumour tissue, in 3D, to effectively assess drug efficacy. More studies are needed to know of the mechanics of the PDAC tumour tissue and the effects on treatment outcomes to improve patient survival. Targeting of the PDAC tumour tissue with, *e.g.*, ECM depleting drugs, such as losartan, or by targeting microbubbles to the stroma will enhance the delivery of chemotherapeutic drugs to the PDAC cancer cells.

7. Conclusion and Future Studies

In this work, a microfluidic PDAC culture model, recapitulating stromal elements of the PDAC tumour tissue (*i.e.*, the presence of PSC cells and cytokines such as TGF- β), with the natural deposition of collagen type I, increasing mechanical stiffness, and reduced interstitial flow for assessment with gemcitabine, microbubbles, and ultrasound together, was presented.

Chapter 4, *The Off-chip Pancreatic Ductal Adenocarcinoma Culture*, presented off-chip 3D PDAC cultures used to investigate the culture conditions required to mimic the rigid, collagenous PDAC tumour microenvironment on-chip. The PANC-1 spheroids (cells grown in ULA plates) in the presence of PSCs and TGF- β showed increased compactness and spheroid growth (Figure 4.3, Table 4.1, and Figure 4.6). This, in addition to the PSC cells surrounding the PDAC cancer cells (Supplementary video 4), decreased the perfusion of oxygen and nutrients through the spheroids, rendering the cells to have different metabolic activities (Figure 4.4). These findings are in line with Ware *et al.* 2016 and Pednekar *et al.* 2021 on the increased compactness and growth of PDAC cancer cells with PSCs, the cellular arrangement of the PDAC cells surrounded by PSCs, and the nutrient and waste gradients of solid tumours.^[104, 129, 144] In replicating a mechanically stiff PDAC stroma, the cells were then seeded into culture dishes with BME gel to investigate collagen deposition and culture stiffness. Mechanical stiffness was measured with oscillatory shear deformation, and the PDAC cultures (PANC-1 and PSC co-culture in BME gel with TGF- β 1 supplement) were stained for collagen type I to determine whether the increased culture stiffness was due to ECM deposition by the cells. The cultures were also stained for HIF-1 alpha as with increased ECM deposition or collagenous regions, there is decreased interstitial transport, and the cells adapt to inadequate oxygen and nutrient supply by switching on alternative metabolic pathways, *i.e.*, anaerobic glycolysis, to survive. By day 21, where the PDAC cultures were in reach of *in vivo* mechanical stiffness,^[21, 46, 89] there was collagen in the culture environment and the cells expressed HIF-1 alpha (Figures 4.9, 4.15, and 4.16E). The effect of gemcitabine at varying concentrations was assessed, and the percentage viability achieved with a concentration of 250 μ M was > 60 % (Figures 4.16B – D). This demonstrated that with a rigid, stroma environment, therapeutic effectiveness is decreased. With the culture conditions optimum for the on-chip PDAC culture determined, a 21-day culture to mimic the PDAC tissue fibrotic stroma, mechanical stiffness, and resistance to gemcitabine, the PANC-1 and PSC cells were seeded on-chip for culture.

Chapter 5, *The On-chip Pancreatic Ductal Adenocarcinoma Culture*, presented a 5-channel microfluidic device (Figure 5.1) for the 21-day culture of the PANC-1 cells with PSCs and TGF- β supplement. Optimum channel dimensions and flow rates were first investigated for the design and fabrication of the 5-channel device (Tables 5.1 and 5.2 and Figure 5.1), and with the device fabricated, the cells were seeded for culture (Figure 5.4B). The on-chip culture viability was assessed, and the cultures were stained for collagen type I and HIF-1 alpha. This was to ensure that the on-chip culture emulated the growth, mechanical behaviour and stroma environment observed off-chip. The 21-day on-chip PDAC cultures were viable (Figure 5.5), and exhibited collagen and a hypoxic environment (Figures 5.6 and 5.7) mirroring the collagenous, rigid microenvironment observed off-chip. The interstitial flow nature of the cultures was evaluated by investigating their hydraulic conductivity, and as the cultures developed mechanically, mirroring the collagenous, rigid microenvironment observed off-chip, their hydraulic conductivity and thus interstitial flow decreased (Figures 5.8 and 5.9 and Table 5.3).

Chapter 6, *The effect of Gemcitabine with Microbubbles and Ultrasound on the On-chip Pancreatic Ductal Adenocarcinoma Culture*, the increase in gemcitabine success with microbubbles and ultrasound was investigated. First, the ability of microbubbles to be able to perfuse into the culture chamber with the PDAC culture, and the effect of microbubble only, ultrasound only, and microbubbles, and ultrasound together were assessed. Microbubbles were able to perfuse into the culture chamber with the PDAC culture (Figure 6.7), and the effect of microbubbles only, ultrasound only, microbubbles and ultrasound together resulted in a percentage viability of approximately > 80 % (Figures 6.5). The viabilities of the cultures with gemcitabine, microbubbles, and ultrasound treatment together resulted in a 61 % viability compared to gemcitabine only treatment, which resulted in a 62 % viability (Figure 6.8). With reduced interstitial flow, a smaller number of microbubbles were in the culture chamber to disrupt the rigid stroma and sensitise the cells to gemcitabine with ultrasound.

Here, the importance of modelling the growth, stroma, tissue stiffness, and reduced interstitial transport of the PDAC tumour tissue, *in vitro*, to effectively assess the effect of therapeutics was highlighted. To develop effective therapeutics against PDAC and improve patient survival, it is vital to encompass the correct biophysical microenvironment in *in vitro* models. The 21-day on-chip PDAC culture model is useful for evaluating novel treatments against PDAC in a biologically relevant way. Future studies could implement more cell types, cytokines, and a plethora of key factors in the PDAC tumour microenvironment to increase

model complexity and understand the contribution of the different elements of the stroma on the disease progression and drug resistance.

7.1. Future studies

7.1.1. Making the on-chip PDAC culture heterogeneous

The PDAC tumour microenvironment consists of diverse cellular and acellular components. On the cellular aspects, in addition to the CAFs and PSC cells, which are essential to the PDAC desmoplastic stroma, with the PSC cells being the predominant cellular composition, are endothelial and tumour infiltrating immune cells. On the acellular part, in addition to the fibrillar collagen type I, which predominantly makes up the fibrillar interstitial matrix of the tumour tissue, is hyaluronan, the predominant glycosaminoglycan of the PDAC stroma, contributing to the increase in interstitial fluid pressure, and signalling molecules such as interleukin (IL) -6, in addition to TGF- β .^[24, 373-375] The 21-day on-chip PDAC culture model consists of PDAC cancer cells and PSC cells. However, endothelial cells and immune cells, such as tumour-associated macrophages (TAMs), could be included to make the culture model heterogeneous and representative of the diverse cellular PDAC stroma compartment.^[373-376]

PDAC is known for its hypovascularity from the surrounding dense stroma, and endothelial cells could be included in the model to investigate and observe the collapse of vasculatures as the on-chip PDAC culture develops mechanically. The architecture of the vasculatures during the on-chip culture development, the change in interstitial flow as the vessels fragment with the development, and the effect of their impairment on the delivery and subsequent effect of gemcitabine with microbubbles, and ultrasound, can be studied. This will add knowledge on the process of vasculature collapse in the PDAC tissue and its effect on the availability of nutrients, oxygen, drugs and therapy response. Gene expression analysis could look at the levels of vascular endothelial growth factor receptors or epithelial growth factor receptors (which are highly expressed in PDAC) and the levels of interleukin secretion (e.g., IL-8) by the cells, as the endothelial cells become activated and transition into a mesenchymal subtype contributing to the CAF population.^[7, 24, 373, 377]

TAMs are the most dominant immune cell population in many tumours, including PDAC. They correlate with poor prognosis with the secretion of immunosuppressive cytokines including TGF- β , IL -6 and -10, and tumour necrosis factors (TNFs) to inhibit immune response with the

inactivation of natural killer and T effector cells and the overexpression of ligands of program death receptor 1. This facilitates the malignant progression of PDAC, its metastasis, and recurrence, as it stimulates an inflammatory response, which increases the fibrotic reaction in the PDAC stroma.^[9, 375, 376, 378-380] There are other immune cells such as tumour-associated neutrophils and regulatory T cells that contribute to the overall immunosuppressive microenvironment of the PDAC tumour, which could be added to the on-chip culture.^[9, 24, 144, 375] The addition of the immune cells could add knowledge to the mechanistic role the cells play in the immunosuppressive tumour microenvironment and therapeutic resistance.

TGF- β was included in the PDAC culture model as it promotes PDAC cancer cell growth and survival by stimulating the activities of CAFs and PSC cells to increase ECM synthesis and deposition. TGF- β also contributes to the immunosuppressive environment by stimulating cells to secrete pro-inflammatory cytokines.^[375, 376] Other signalling molecules secreted by the cancer cells, CAFs, PSCs, and the immune cells that could be added to the PDAC culture model include IL-6. High expression of IL-6 has been found in the serum of PDAC patients, and IL-6 has been associated with pro-tumorigenic signalling cascades, *i.e.*, the JAK/STAT signalling pathway, stimulating cell growth and their secretion of ECM to maintain the stroma microenvironment. IL-6 has been found to also contribute to the immune regulation of PDAC to enhance its progression.^[381] Looking at the mechanistic role of IL-6 could reveal new therapeutic opportunities to manage PDAC cancer progression.

Collagen type I gives the PDAC tumour microenvironment its rigidity, while hyaluronan (HA) retains large amounts of water molecules, resulting in a viscous gel increasing the interstitial fluid pressure of the tumour tissue and compressing vessels.^[57, 59, 65, 206] HA has been found associated with the dismal survival of PDAC patients due to its hydrodynamic properties.^[41, 44, 195, 382] The addition of HA to the model will be representative of the ECM composition of the PDAC microenvironment and also can provide insight into the high interstitial pressures and vasculature collapse when seeded with endothelial cells on-chip. Adding HA could also provide insight into the role the viscous compartment has on PDAC progression and drug response.

Furthermore, the device could be optimised to accommodate the endothelial cells, immune cells, and the addition of HA to make the PDAC culture heterogeneous and representative of the PDAC tumour microenvironment, inquiring on the role of the different components of the microenvironment on the disease advancement and its response to therapy.

7.1.2. Assessing the mechanics of the on-chip PDAC cultures

The mechanics of the on-chip PDAC cultures was assessed with the staining of collagen type I and assessment of its hydraulic conductivity (chapter 5). This was to ensure that the on-chip PDAC culture encompassed the characteristics of the rigid PDAC tumour microenvironment observed off-chip (chapter 4). With increasing collagen synthesis, is increasing cross-linking of collagen fibre, which correlates with increasing tissue stiffness.^[48, 58] The stiffness of the on-chip PDAC culture could be investigated to assess the change in the culture mechanics as it develops.

Due to the microscale of the culture model, the stiffness of the on-chip PDAC cultures can be assessed with commonly used techniques such as AFM, particle-tracking microrheology, and with Brillouin microscopy. Brillouin microscopy is a type of optical elastography, which uses laser light and thermally induced sound waves to probe the viscoelastic properties of biological samples, and its use holds promise for the early diagnosis of diseases.^[383-386] AFM is a type of scanning force microscopy at high resolution that allows the unique capability of probing and providing information on the viscoelastic properties of biological samples in real-time in a physiological environment.^[21, 387-390] Particle-tracking microrheology is a passive microrheological technique that measures the Brownian motion or trajectory of micro-sized tracers within a sample for information on the sample's mechanical properties. Fluorescent tracers or beads of approximately 1 μm in diameter can be introduced into the on-chip culture, and the displacement of these beads can be tracked and recorded.^[90, 391-394] Moreover, as shown by Ito *et al.* 2016 and Zareei *et al.* 2020,^[395, 396] the 5-channel microfluidic device could be modified for real-time analysis of the mechanics of the on-chip PDAC cultures with electrical force sensor probes or ultrasonic transducers.

7.1.3. Assessing the porous structure and size of the PDAC culture stroma

Moreover, looking at the mechanics of the on-chip PDAC cultures, the matrix or culture environment could be imaged with scanning or transmission electron microscopy. This will provide information on the porous structure of the PDAC stroma with increasing ECM deposition and on how this influences the rigidity of the culture environment and its effect on interstitial transport.

SEM will provide 3D images of the culture surface and its composition, while TEM, although with complex sample preparation, will provide 2D images with information on the inner

structure morphology of the cultures and its matrix. Pednekar *et al.* 2020^[144] used SEM to observe the porous nature of their PANC-1: PSC co-cultures showing the individual collagen fibres, the resulting porous size of the stroma, and how this influenced the penetration of silica nanoparticles used in their therapeutic assessment. Ishiwata *et al.* 2018, Shichi *et al.* 2019, and Norberg *et al.* 2020 used both SEM and TEM to examine the intercellular space and cellular junctions of their PANC-1 spheroid cultures.^[397-399]

In comparison to the SEM and TEM, second harmonic imaging (SHG), a non-invasive microscopic approach to looking at the ECM structure of cell cultures and tissues,^[38, 58, 77, 78, 400, 401] could be used to investigate the ECM of the PDAC cultures. SHG is a non-linear optical process, which is based on the interactions of laser light, radiated at half the excitation wavelength, with non-centrosymmetric structures such as fibrillar collagen. As such, SHG has emerged as a powerful label-free technique to visualise fibrillar collagen within tissues.^[58, 76-78, 400, 402] Moreover, SHG can be used in conjunction with Raman spectroscopy to determine the different ECM components in the PDAC culture environment. Wang *et al.* 2008, Mortati *et al.* 2012, and Moura *et al.* 2019 used SHG with coherent anti-stokes Raman scattering (CARS) to image not only the fibrous collagen structure of the matrix environment but also other ECM such as elastin and glycosaminoglycans.^[401, 403, 404] CARS is a type of Raman spectroscopy, which can be used to collect information on the different chemical signatures of the culture ECM, and therefore determine the make-up of the PDAC culture ECM.

Imaging the ECM composition of the PDAC culture microenvironment can provide valuable information on the matrix composition and its porous structure, and genetic and protein expression of lysyl oxidase (LOX) could be performed to support assessments on the matrix porous structure and the increasing culture rigidity. LOX oxidises lysine residues in fibrillar proteins, *i.e.*, collagen, thereby resulting in the covalent cross-linking of collagen fibres. This will help in understanding how the rigid PDAC stroma results in the ineffective transport and delivery of therapeutics to the cancer cells.

7.1.4. Assessing the rigidity sensing mechanisms of the PDAC cells

Figure 4.9 (chapter 4) presents the changes in the mechanics of the PDAC cultures as they grow and develop. It reports on increasing culture stiffness with increasing culture time, as the cells grow and remodel their microenvironment, with the production of collagen (Figure 4.15). The increasing culture stiffness with increasing culture time implies cellular responses

to the mechanical forces in the culture environment,^[21, 90] and it would be interesting to look at the mechanical feedback mechanisms of the cells – how the cells sense, communicate and respond to the increasing mechanical forces and rigidity in their microenvironment.

Cells sense and respond to the mechanical forces in their environment via integrins.^[47, 54, 328, 405, 406] Integrins facilitate cell-ECM and cell-cell signalling. They couple the ECM to the cell actin cytoskeleton and, therefore, are involved in the cell shape, orientation, and motility. The integrin protein family consist of alpha and beta subtypes and function as adhesion receptors to transduce mechanical cues into cells. Integrins are bound to the ECM through focal adhesions, and upon activation with a mechanical cue, activate intracellular signalling pathways to induce a change in the cell cytoskeleton structure for growth and survival.^[50, 359, 405, 407, 408] Below *et al.* 2021 show integrins to be important to cell-ECM interaction and the survival of their pancreatic organoids.^[344]

Integrins in the ECM of the PDAC cultures can be identified with techniques such as immunostaining and real-time quantitative PCR, and this will help to identify the mechanosensing mechanisms and their effect on the culture development. Table 7.1 shows examples of the types of integrins that could be identified.^[409-413] Identifying the integrins in the PDAC cultures can also highlight the ECM composition of the culture matrix.

*Table 7.1. Examples of the types of integrins
Types of integrin in the pancreatic ductal adenocarcinoma tumour tissue stroma*

| Integrin | Ligand/ECM component | Function/Effect of activation |
|---|-----------------------------|--|
| $\alpha_2\beta_1$ | Collagen I, IV, & V | Proliferation and migration of cancer cells |
| $\alpha_{11}\beta_1$ | Fibrillar collagens | Correlates with CAFs/PSCs expression with a role matrix remodelling and the metastatic potential of cancer cells |
| $\alpha_5\beta_1$ | Fibronectin & Collagen III | Metastatic potential and poor differentiation of cancer cells |
| $\alpha_3\beta_1$ | Laminin | Cancer cell migration and CAF maintenance |
| $\alpha_v\beta_3$ and $\alpha_v\beta_3$ | CAFs | CAF and TGF- β activation, cell migration of cancer cells |

7.1.5. Durotaxis study

The rigid microenvironment of the PDAC stroma is a potent contributor to PDAC’s malignant behaviour. This includes the metastatic potential of the cancer cells, as elevated ECM stiffness

is associated with cancer cell invasion. Referred to as durotaxis or reverse durotaxis, it has been reported that cancer cell migration is affected by rigidity gradients, where the cancer cells can move from a soft substrate region to a stiff substrate region and *vice versa*, respectively.^[326, 414, 415]

The movement of the PDAC cells can be assessed to determine if the cells, with increasing culture stiffness, migrate from the culture chamber to a region with soft hydrogel or a region with stiff hydrogel. The microfluidic device could be optimised to have channels with a soft hydrogel and or a stiff hydrogel. Investigating the direction of the PDAC cancer cell migration in response to the rigidity gradient will add understanding to the effect of the increasing rigid tumour microenvironment on PDAC cancer cell migration and invasion.

7.1.6. Stroma reduction

The stiffness of the stroma is a critical biophysical hallmark of disease progression, and targeting the ECM by preventing or reversing the stiffening of the tumour microenvironment is an emerging interest to increase drug efficacy.^[22, 42, 43, 193, 416] Figures 5.6, 5.9, and 6.8 of chapters 5 and 6 show how the rigid collagenous PDAC culture was less conducive to interstitial flow and, therefore, resistant to the effects of gemcitabine with microbubbles and ultrasound. Future studies of the PDAC culture model presented here could look at reducing the density of the rigid collagenous culture environment.

Targeting tumour tissue stiffness includes the depletion of CAFs or PSC cells with saridegib, or IPI-2, an experimental sonic hedgehog inhibitor to suppress the paracrine signalling between cancer cells and CAFs, the use of all-trans retinoic acid to regulate the cell transcription to restore the quiescence state of PSC cells, the use of pegylated hyaluronidase (PEGPH20) to reduce the ability of hyaluronan to imbibe large amounts of water molecules, and the use of collagenase and metalloproteinase 1 to degrade collagen.^[22, 42, 105, 410] In comparison to these measures of which some show unfavourable outcomes (e.g., collagenase and MMP-1 are associated with toxicity and poor tumour prognosis), angiotensin receptor antagonists or blockers (ARBs), which are approved anti-hypertensive drugs with mild and short-lived side effects and have been shown to have anti-fibrotic activity,^[193, 199, 417] can be assessed on the PDAC cultures to determine its effects on the collagen production, culture mechanical stiffness, and the efficacy of gemcitabine with and without microbubbles and ultrasound.

The renin-angiotensin-aldosterone system is essential for the regulation of blood pressure, fluid balance, and the regulation and production of the ECM via the TGF- β 1 pathway. Via the TGF- β 1 pathway, matrix degrading enzymes and proteases are suppressed to drive matrix stiffening, exacerbating tumour fibrotic stroma.^[193, 199, 418] ARBs, such as candesartan and losartan, have been shown to enhance fluid flow in the interstitial space, improving interstitial transport and therapeutic efficacy. They suppress the activity of fibroblasts and CAFs by attenuating TGF- β 1 pathway, decreasing ECM synthesis and accumulation and mechanical stiffness.^[193, 199, 417-419] With a decrease in the amounts of ECM in the PDAC culture environment, there will be an increase in the interstitial flow and transport of gemcitabine and microbubbles to the cells in the culture chamber. Moreover, ARBs could be used in conjunction with integrin inhibitors such as the integrin α 5 (ITGA5) antagonistic peptide, AV3, used by Pednekar *et al.* 2021^[144], to further suppress the activity of PSC cells.^[192]

7.2. Summary

Pancreatic ductal adenocarcinoma is the most aggressive pancreatic cancer. In addition to the genetic factors for the disease development and advancement, its desmoplastic tumour microenvironment accounts for the low efficacy of current therapeutics. It is becoming of interest to model the PDAC rigid tumour microenvironment to understand more about the disease biology for better therapeutic measures.^[144, 344] However, conventional and current models of PDAC do not encompass the biophysical characteristic of the PDAC tumour microenvironment and perform therapeutic measures when the models do not adequately capture the mechanics of the disease. In this study, the importance of having a relevant *in vitro* PDAC culture model with the biophysical characteristic of the disease is emphasized. The advantage of precise fluid control, due to the presence of laminar flow, that microfluidics provides enabled the culturing of PDAC cells within a physiologically relevant environment. The disease fibrotic stroma with increasing collagen deposition, mechanical stiffness, and reduced interstitial flow was captured on-chip, and the cultures showed resistance to the ultrasound-targeted delivery of gemcitabine. This has provided insight into the development of better therapeutic strategies against PDAC. It is important that *in vitro* cultures model the biophysical characteristics of PDAC, as presented here, to improve the development of effective therapeutic strategies for better treatment outcomes.

References

1. Kpeglo, D., Hughes, M.D.G., Dougan, L., Haddrick, M., Knowles, M.A., Evans, S.D. and Peyman, S.A. Modeling the mechanical stiffness of pancreatic ductal adenocarcinoma. *Matrix Biology Plus*. 2022, **14**.
2. Bardeesy, N. and DePinho, R.A. Pancreatic cancer biology and genetics. *Nat Rev Cancer*. 2002, **2**(12), pp.897-909.
3. Bond-Smith, G., Banga, N., Hammond, T.M. and Imber, C.J. Pancreatic adenocarcinoma. *BMJ*. 2012, **344**, p.e2476.
4. Güngör, C., Hofmann, B., T., Wolters-Eisfeld, G. and Bockhorn, M. Pancreatic cancer. *British Journal of Pharmacology*. 2014, **171**(4).
5. Siriwardena, A.K. and Siriwardena, A.M. Pancreatic cancer. *BMJ*. 2014, **349**, p.g6385.
6. Windsor, A.J. Anatomy and Physiology of the Pancreas. In: *ACS Surgery: Principles and Practice*. 2012.
7. Deer, E.L., Gonzalez-Hernandez, J., Coursen, J.D., Shea, J.E., Ngatia, J., Scaife, C.L., Firpo, M.A. and Mulvihill, S.J. Phenotype and genotype of pancreatic cancer cell lines. *Pancreas*. 2010, **39**(4), pp.425-435.
8. Rawla, P., Sunkara, T. and Gaduputi, V. Epidemiology of Pancreatic Cancer: Global Trends, Etiology and Risk Factors. *World J Oncol*. 2019, **10**(1), pp.10-27.
9. Orth, M., Metzger, P., Gerum, S., Mayerle, J., Schneider, G., Belka, C., Schnurr, M. and Lauber, K. Pancreatic ductal adenocarcinoma: biological hallmarks, current status, and future perspectives of combined modality treatment approaches. *Radiat Oncol*. 2019, **14**(1), p.141.
10. Ryan, D.P., Hong, T.S. and Bardeesy, N. Pancreatic adenocarcinoma. *N Engl J Med*. 2014, **371**(11), pp.1039-1049.
11. Bradney, M.J., Venis, S.M., Yang, Y., Konieczny, S.F. and Han, B. A Biomimetic Tumor Model of Heterogeneous Invasion in Pancreatic Ductal Adenocarcinoma. *Small*. 2020, **16**(10), p.e1905500.
12. de Wilde, R.F., Hruban, R.H., Maitra, A. and Offerhaus, G.J.A. Reporting precursors to invasive pancreatic cancer: pancreatic intraepithelial neoplasia, intraductal neoplasms and mucinous cystic neoplasm. *Diagnostic Histopathology*. 2012, **18**(1), pp.17-30.
13. Hruban, R.H. and Fukushima, N. Pancreatic adenocarcinoma: update on the surgical pathology of carcinomas of ductal origin and PanINs. *Mod Pathol*. 2007, **20** Suppl 1, pp.S61-70.
14. Hruban, R.H., Maitra A Fau - Goggins, M. and Goggins, M. Update on pancreatic intraepithelial neoplasia. 2008, (1936-2625 (Electronic)).
15. Apte, M.V., Pirola, R.C. and Wilson, J.S. Pancreatic stellate cells: a starring role in normal and diseased pancreas. *Front Physiol*. 2012, **3**, p.344.

16. Massague, J. TGFbeta in Cancer. *Cell*. 2008, **134**(2), pp.215-230.
17. Weniger, M., Honselmann, K.C. and Liss, A.S. The Extracellular Matrix and Pancreatic Cancer: A Complex Relationship. *Cancers (Basel)*. 2018, **10**(9).
18. Hosein, A.N., Brekken, R.A. and Maitra, A. Pancreatic cancer stroma: an update on therapeutic targeting strategies. *Nat Rev Gastroenterol Hepatol*. 2020, **17**(8), pp.487-505.
19. Jain, R.K., Martin, J.D. and Stylianopoulos, T. The role of mechanical forces in tumor growth and therapy. *Annu Rev Biomed Eng*. 2014, **16**, pp.321-346.
20. Nguyen, A.V., Nyberg, K. D., Scott, M. B., Welsh, A. M., Nguyen, A. H., Wu, N., Hohlbauch, S. V., Geisse, N. A., Gibb, E. A., Robertson, A. G., Donahue, T. R., & Rowat, A. C. . Stiffness of pancreatic cancer cells is associated with increased invasive potential. *Integr Biol (Camb)*. 2016, **8**(12), pp.1232–1245.
21. Rice, A.J., Cortes, E., Lachowski, D., Cheung, B.C.H., Karim, S.A., Morton, J.P. and Del Rio Hernandez, A. Matrix stiffness induces epithelial-mesenchymal transition and promotes chemoresistance in pancreatic cancer cells. *Oncogenesis*. 2017, **6**(7), p.e352.
22. Stromnes, I.M., DelGiorno, K.E., Greenberg, P.D. and Hingorani, S.R. Stromal reengineering to treat pancreas cancer. *Carcinogenesis*. 2014, **35**(7), pp.1451-1460.
23. Apte, M.V., Xu, Z., Pothula, S., Goldstein, D., Pirola, R.C. and Wilson, J.S. Pancreatic cancer: The microenvironment needs attention too! *Pancreatology*. 2015, **15**(4 Suppl), pp.S32-38.
24. Feig, C., Gopinathan, A., Neesse, A., Chan, D.S., Cook, N. and Tuveson, D.A. The pancreas cancer microenvironment. *Clin Cancer Res*. 2012, **18**(16), pp.4266-4276.
25. Longati, P., Jia, X., Eimer, J., Wagman, A., Witt, M. R., Rehnmark, S., Verbeke, C., Toftgård, R., Löhr, M., & Heuchel, R. L. . 3D pancreatic carcinoma spheroids induce a matrix-rich, chemoresistant phenotype offering a better model for drug testing. *BMC Cancer*. 2013, **13**(95).
26. Phillips, P. Pancreatic stellate cells and fibrosis. In: Grippo, P.J. and Munshi, H.G. eds. *Pancreatic Cancer and Tumor Microenvironment*. 2012.
27. Xie, D. and Xie, K. Pancreatic cancer stromal biology and therapy. *Genes Dis*. 2015, **2**(2), pp.133-143.
28. Ferdek, P.E. and Jakubowska, M.A. Biology of pancreatic stellate cells-more than just pancreatic cancer. *Pflugers Arch*. 2017, **469**(9), pp.1039-1050.
29. Frantz, C., Stewart, K.M. and Weaver, V.M. The extracellular matrix at a glance. *J Cell Sci*. 2010, **123**(Pt 24), pp.4195-4200.
30. Means, A.L. Pancreatic stellate cells: small cells with a big role in tissue homeostasis. *Lab Invest*. 2013, **93**(1), pp.4-7.

31. Bailey, J.M., Swanson, B.J., Hamada, T., Eggers, J.P., Singh, P.K., Caffery, T., Ouellette, M.M. and Hollingsworth, M.A. Sonic hedgehog promotes desmoplasia in pancreatic cancer. *Clin Cancer Res.* 2008, **14**(19), pp.5995-6004.
32. Bailey, J.M., Mohr, A.M. and Hollingsworth, M.A. Sonic hedgehog paracrine signaling regulates metastasis and lymphangiogenesis in pancreatic cancer. *Oncogene.* 2009, **28**(40), pp.3513-3525.
33. Rasheed, Z.A., Matsui, W. and Maitra, A. Pathology of pancreatic stroma in PDAC. BTI - Pancreatic Cancer and Tumor Microenvironment. 2012.
34. Liu, S.L., Cao, S.G., Li, Y., Sun, B., Chen, D., Wang, D.S. and Zhou, Y.B. Pancreatic stellate cells facilitate pancreatic cancer cell viability and invasion. *Oncol Lett.* 2019, **17**(2), pp.2057-2062.
35. Mekapogu, A.R., Pothula, S.P., Pirola, R.C., Wilson, J.S. and Apte, M.V. Multifunctional role of pancreatic stellate cells in pancreatic cancer. *Annals of Pancreatic Cancer.* 2019, **2**, pp.10-10.
36. Thomas, S.K., Lee, J. and Beatty, G.L. Paracrine and cell autonomous signalling in pancreatic cancer progression and metastasis. *EBioMedicine.* 2020, **53**, p.102662.
37. Bolm, L., Cigolla, S., Wittel, U.A., Hopt, U.T., Keck, T., Rades, D., Bronsert, P. and Wellner, U.F. The Role of Fibroblasts in Pancreatic Cancer: Extracellular Matrix Versus Paracrine Factors. *Transl Oncol.* 2017, **10**(4), pp.578-588.
38. Drifka, C.R., Eliceiri, K.W., Weber, S.M. and Kao, W.J. A bioengineered heterotypic stroma-cancer microenvironment model to study pancreatic ductal adenocarcinoma. *Lab Chip.* 2013, **13**(19), pp.3965-3975.
39. Lai Benjamin, F.L., Lu Rick, X., Hu, Y., Davenport, H.L., Dou, W., Wang, E.Y., Radulovich, N., Tsao, M.S., Sun, Y. and Radisic, M. Recapitulating pancreatic tumor microenvironment through synergistic use of patient organoids and organ-on-a-chip vasculature. *Adv Funct Mater.* 2020, **30**(48).
40. Laplane, L., Duluc, D., Larmonier, N., Pradeu, T. and Bikfalvi, A. The Multiple Layers of the Tumor Environment. *Trends Cancer.* 2018, **4**(12), pp.802-809.
41. DuFort, C.C., DelGiorno, K.E. and Hingorani, S.R. Mounting Pressure in the Microenvironment: Fluids, Solids, and Cells in Pancreatic Ductal Adenocarcinoma. *Gastroenterology.* 2016, **150**(7), pp.1545-1557 e1542.
42. Lampi, M.C. and Reinhart-King, C.A. Targeting extracellular matrix stiffness to attenuate disease: From molecular mechanisms to clinical trials. *Science Translational Medicine.* 2018, **10**(422), p.eaao0475.
43. Stylianopoulos, T., Munn, L.L. and Jain, R.K. Reengineering the Physical Microenvironment of Tumors to Improve Drug Delivery and Efficacy: From Mathematical Modeling to Bench to Bedside. *Trends Cancer.* 2018, **4**(4), pp.292-319.
44. DuFort, C.C., DelGiorno, K.E., Carlson, M.A., Osgood, R.J., Zhao, C., Huang, Z., Thompson, C.B., Connor, R.J., Thanos, C.D., Scott Brockenbrough, J., Provenzano, P.P., Frost, G.I., Michael Shepard, H. and Hingorani, S.R. Interstitial Pressure in Pancreatic

- Ductal Adenocarcinoma Is Dominated by a Gel-Fluid Phase. *Biophys J.* 2016, **110**(9), pp.2106-2119.
45. Gasparski, A.N. and Beningo, K.A. Mechanoreception at the cell membrane: More than the integrins. *Arch Biochem Biophys.* 2015, **586**, pp.20-26.
46. Piersma, B., Hayward, M.K. and Weaver, V.M. Fibrosis and cancer: A strained relationship. *Biochim Biophys Acta Rev Cancer.* 2020, **1873**(2), p.188356.
47. Baker, E.L. and Zaman, M.H. The biomechanical integrin. *J Biomech.* 2010, **43**(1), pp.38-44.
48. Micalet, A., Moeendarbary, E. and Cheema, U. 3D In Vitro Models for Investigating the Role of Stiffness in Cancer Invasion. *ACS Biomater Sci Eng.* 2021.
49. Hall, A. The cytoskeleton and cancer. *Cancer Metastasis Rev.* 2009, **28**(1-2), pp.5-14.
50. Ingber, D. Integrins as mechanochemical transducers. *Current Opinion in Cell Biology.* 1991, **3**(5), pp.841-848.
51. Khan, Z. and Marshall, J.F. The role of integrins in TGFbeta activation in the tumour stroma. *Cell Tissue Res.* 2016, **365**(3), pp.657-673.
52. Liu, T., Zhou, L., Li, D., Andl, T. and Zhang, Y. Cancer-Associated Fibroblasts Build and Secure the Tumor Microenvironment. *Front Cell Dev Biol.* 2019, **7**, p.60.
53. Antoine, E.E., Vlachos, P.P. and Rylander, M.N. Review of collagen I hydrogels for bioengineered tissue microenvironments: characterization of mechanics, structure, and transport. *Tissue Eng Part B Rev.* 2014, **20**(6), pp.683-696.
54. Burla, F., Mulla, Y., Vos, B.E., Aufderhorst-Roberts, A. and Koenderink, G.H. From mechanical resilience to active material properties in biopolymer networks. *Nature Reviews Physics.* 2019, **1**(4), pp.249-263.
55. Gelse, K., Poschl, E. and Aigner, T. Collagens--structure, function, and biosynthesis. *Adv Drug Deliv Rev.* 2003, **55**(12), pp.1531-1546.
56. Pickup, M.W., Mouw, J.K. and Weaver, V.M. The extracellular matrix modulates the hallmarks of cancer. *EMBO Rep.* 2014, **15**(12), pp.1243-1253.
57. Provenzano, P.P. and Hingorani, S.R. Hyaluronan, fluid pressure, and stromal resistance in pancreas cancer. *Br J Cancer.* 2013, **108**(1), pp.1-8.
58. Robinson, B.K., Cortes, E., Rice, A.J., Sarper, M. and Del Rio Hernandez, A. Quantitative analysis of 3D extracellular matrix remodelling by pancreatic stellate cells. *Biol Open.* 2016, **5**(6), pp.875-882.
59. Sato, N., Kohi, S., Hirata, K. and Goggins, M. Role of hyaluronan in pancreatic cancer biology and therapy: Once again in the spotlight. *Cancer Sci.* 2016, **107**(5), pp.569-575.
60. Shoulders, M.D. and Raines, R.T. Collagen structure and stability. *Annu Rev Biochem.* 2009, **78**, pp.929-958.

61. Wenger, M.P., Bozec, L., Horton, M.A. and Mesquida, P. Mechanical properties of collagen fibrils. *Biophys J.* 2007, **93**(4), pp.1255-1263.
62. Balhouse, B., Ivey, J. and Verbridge, S. Engineered Microenvironments for Cancer Study. In: Baldacchini, T. ed. *In Micro and Nano Technologies, Three-Dimensional Microfabrication Using Two-photon Polymerization: Fundamentals, Technology, and Applications* Elsevier Inc., 2016, pp.417-445.
63. Munson, J.M. and Shieh, A.C. Interstitial fluid flow in cancer: implications for disease progression and treatment. *Cancer Manag Res.* 2014, **6**, pp.317-328.
64. Polacheck, W.J., Charest, J.L. and Kamm, R.D. Interstitial flow influences direction of tumor cell migration through competing mechanisms. *Proc Natl Acad Sci U S A.* 2011, **108**(27), pp.11115-11120.
65. Sato, N., Cheng, X.B., Kohi, S., Koga, A. and Hirata, K. Targeting hyaluronan for the treatment of pancreatic ductal adenocarcinoma. *Acta Pharm Sin B.* 2016, **6**(2), pp.101-105.
66. Saito, N., Adachi, H., Tanaka, H., Nakata, S., Kawada, N., Oofusa, K. and Yoshizato, K. Interstitial fluid flow-induced growth potential and hyaluronan synthesis of fibroblasts in a fibroblast-populated stretched collagen gel culture. *Biochim Biophys Acta Gen Subj.* 2017, **1861**(9), pp.2261-2273.
67. McEwan, C., Owen, J., Stride, E., Fowley, C., Nesbitt, H., Cochrane, D., Coussios, C.C., Borden, M., Nomikou, N., McHale, A.P. and Callan, J.F. Oxygen carrying microbubbles for enhanced sonodynamic therapy of hypoxic tumours. *J Control Release.* 2015, **203**, pp.51-56.
68. Burroughs, S.K., Kaluz, S., Wang, D., Wang, K., Van Meir, E.G. and Wang, B. Hypoxia inducible factor pathway inhibitors as anticancer therapeutics. *Future Med Chem.* 2013, **5**(5), pp.553-572.
69. Daniel, S.K., Sullivan, K.M., Labadie, K.P. and Pillarisetty, V.G. Hypoxia as a barrier to immunotherapy in pancreatic adenocarcinoma. *Clin Transl Med.* 2019, **8**(1), p.10.
70. Masoud, G.N. and Li, W. HIF-1 α pathway: role, regulation and intervention for cancer therapy. *Acta Pharm Sin B.* 2015, **5**(5), pp.378-389.
71. Rohwer, N. and Cramer, T. Hypoxia-mediated drug resistance: novel insights on the functional interaction of HIFs and cell death pathways. *Drug Resist Updat.* 2011, **14**(3), pp.191-201.
72. Spivak-Kroizman, T.R., Hostetter, G., Posner, R., Aziz, M., Hu, C., Demeure, M.J., Von Hoff, D., Hingorani, S.R., Palculict, T.B., Izzo, J., Kiriakova, G.M., Abdelmelek, M., Bartholomeusz, G., James, B.P. and Powis, G. Hypoxia triggers hedgehog-mediated tumor-stromal interactions in pancreatic cancer. *Cancer Res.* 2013, **73**(11), pp.3235-3247.
73. Yamasaki, A., Yanai, K. and Onishi, H. Hypoxia and pancreatic ductal adenocarcinoma. *Cancer Lett.* 2020, **484**, pp.9-15.

74. Petrova, V., Annicchiarico-Petruzzelli, M., Melino, G. and Amelio, I. The hypoxic tumour microenvironment. *Oncogenesis*. 2018, **7**(1), p.10.
75. Shi, Y., Glaser, K.J., Venkatesh, S.K., Ben-Abraham, E.I. and Ehman, R.L. Feasibility of using 3D MR elastography to determine pancreatic stiffness in healthy volunteers. *J Magn Reson Imaging*. 2015, **41**(2), pp.369-375.
76. Bancelin, S., Aime, C., Gusachenko, I., Kowalczyk, L., Latour, G., Coradin, T. and Schanne-Klein, M.C. Determination of collagen fibril size via absolute measurements of second-harmonic generation signals. *Nat Commun*. 2014, **5**, p.4920.
77. Boerboom, R.A., Krahn, K.N., Megens, R.T., van Zandvoort, M.A., Merkx, M. and Bouten, C.V. High resolution imaging of collagen organisation and synthesis using a versatile collagen specific probe. *J Struct Biol*. 2007, **159**(3), pp.392-399.
78. Couture, C.A., Bancelin, S., Van der Kolk, J., Popov, K., Rivard, M., Legare, K., Martel, G., Richard, H., Brown, C., Laverty, S., Ramunno, L. and Legare, F. The Impact of Collagen Fibril Polarity on Second Harmonic Generation Microscopy. *Biophys J*. 2015, **109**(12), pp.2501-2510.
79. Guimarães, C.F., Gasperini, L., Marques, A.P. and Reis, R.L. The stiffness of living tissues and its implications for tissue engineering. *Nature Reviews Materials*. 2020, **5**(5), pp.351-370.
80. Payen, T., Oberstein, P., Saharkhiz, N., Palermo, C., Sastra, S., Han, Y., Nabavizadeh, A., Sagalovskiy, I., Orelli, B., Rosario, V., Desrouilleres, D., Remotti, H., Kluger, M., Schrope, B., Chabot, J., Iuga, A., Konofagou, E. and Olive, K. Harmonic motion imaging of pancreatic tumor stiffness indicates disease state and treatment response. *Clin Cancer Res*. 2020, **26**(6), pp.1297–1308.
81. Abou-Saleh, R.H., Hernandez-Gomez, M.C., Amsbury, S., Paniagua, C., Bourdon, M., Miyashima, S., Helariutta, Y., Fuller, M., Budtova, T., Connell, S.D., Ries, M.E. and Benitez-Alfonso, Y. Interactions between callose and cellulose revealed through the analysis of biopolymer mixtures. *Nat Commun*. 2018, **9**(1), p.4538.
82. Chang, Y.R., Raghunathan, V.K., Garland, S.P., Morgan, J.T., Russell, P. and Murphy, C.J. Automated AFM force curve analysis for determining elastic modulus of biomaterials and biological samples. *J Mech Behav Biomed Mater*. 2014, **37**, pp.209-218.
83. Frey, M.T., Engler, A., Discher, D.E., Lee, J. and Wang, Y. Microscopic Methods for Measuring the Elasticity of Gel Substrates for Cell Culture: Microspheres, Microindenters, and Atomic Force Microscopy. In: *Methods in Cell Biology*. 2007, pp.47-65.
84. Lekka, M., Gil, D., Pogoda, K., Dulinska-Litewka, J., Jach, R., Gostek, J., Klymenko, O., Prauzner-Bechcicki, S., Stachura, Z., Wiltowska-Zuber, J., Okon, K. and Laidler, P. Cancer cell detection in tissue sections using AFM. *Arch Biochem Biophys*. 2012, **518**(2), pp.151-156.
85. MacCurtain, B.M., Quirke, N.P., Thorpe, S.D. and Gallagher, T.K. Pancreatic Ductal Adenocarcinoma: Relating Biomechanics and Prognosis. *Journal of Clinical Medicine*. 2021, **10**(12).

86. Radmacher, M. Studying the Mechanics of Cellular Processes by Atomic Force Microscopy. In: *Methods in Cell Biology*. 2007, pp.347-372.
87. Stylianou, A. and Stylianopoulos, T. Atomic Force Microscopy Probing of Cancer Cells and Tumor Microenvironment Components. *BioNanoScience*. 2015, **6**(1), pp.33-46.
88. Vyas, V., Solomon, M., D'Souza, G.G.M. and Huey, B.D. Nanomechanical Analysis of Extracellular Matrix and Cells in Multicellular Spheroids. *Cell Mol Bioeng*. 2019, **12**(3), pp.203-214.
89. Wex, C., Frohlich, M., Brandstadter, K., Bruns, C. and Stoll, A. Experimental analysis of the mechanical behavior of the viscoelastic porcine pancreas and preliminary case study on the human pancreas. *J Mech Behav Biomed Mater*. 2015, **41**, pp.199-207.
90. Wullkopf, L., West, A.V., Leijnse, N., Cox, T.R., Madsen, C.D., Oddershede, L.B. and Erler, J.T. Cancer cells' ability to mechanically adjust to extracellular matrix stiffness correlates with their invasive potential. *Mol Biol Cell*. 2018, **29**(20), pp.2378-2385.
91. McKee, C.T., Last, J.A., Russell, P. and Murphy, C.J. Indentation versus tensile measurements of Young's modulus for soft biological tissues. *Tissue Eng Part B Rev*. 2011, **17**(3), pp.155-164.
92. Meyvis, T.K.L., Stubbe, B.G., Van Steenberghe, M.J., Hennink, W.E., De Smedt, S.C. and Demeester, J. A comparison between the use of dynamic mechanical analysis and oscillatory shear rheometry for the characterisation of hydrogels. *International Journal of Pharmaceutics*. 2002, **244**(1), pp.163-168.
93. Weitz, D., Wyss, H.M. and Larsen, R.J. Oscillatory Rheology Measuring the Viscoelastic Behaviour of Soft Materials. *GIT laboratory journal Europe*. 2007, **11**, pp.68-70.
94. Janmey, P.A., Georges, P.C. and Hvidt, S. Basic Rheology for Biologists. In: *Methods in Cell Biology*. 2007, pp.1, 3-27.
95. Rubiano, A., Delitto, D., Han, S., Gerber, M., Galitz, C., Trevino, J., Thomas, R.M., Hughes, S.J. and Simmons, C.S. Viscoelastic properties of human pancreatic tumors and in vitro constructs to mimic mechanical properties. *Acta Biomater*. 2018, **67**, pp.331-340.
96. Kalluri, R. and Weinberg, R.A. The basics of epithelial-mesenchymal transition. *J Clin Invest*. 2009, **119**(6), pp.1420-1428.
97. Kumar, S. and Weaver, V.M. Mechanics, malignancy, and metastasis: the force journey of a tumor cell. *Cancer Metastasis Rev*. 2009, **28**(1-2), pp.113-127.
98. Nia, H.T., Munn, L.L. and Jain, R.K. Mapping Physical Tumor Microenvironment and Drug Delivery. *Clin Cancer Res*. 2019, **25**(7), pp.2024-2026.
99. Suresh, S. Biomechanics and biophysics of cancer cells. *Acta Biomater*. 2007, **3**(4), pp.413-438.
100. Pothula, S.P., Pirola, R.C., Wilson, J.S. and Apte, M.V. Pancreatic stellate cells: Aiding and abetting pancreatic cancer progression. *Pancreatology*. 2020, **20**(3), pp.409-418.

101. Gioeli, D., Snow, C.J., Simmers, M.B., Hoang, S.A., Figler, R.A., Allende, J.A., Roller, D.G., Parsons, J.T., Wulfkuhle, J.D., Petricoin, E.F., Bauer, T.W. and Wamhoff, B.R. Development of a multicellular pancreatic tumor microenvironment system using patient-derived tumor cells. *Lab Chip*. 2019, **19**(7), pp.1193-1204.
102. Hou, S., Tiriac, H., Sridharan, B.P., Scampavia, L., Madoux, F., Seldin, J., Souza, G.R., Watson, D., Tuveson, D. and Spicer, T.P. Advanced Development of Primary Pancreatic Organoid Tumor Models for High-Throughput Phenotypic Drug Screening. *SLAS Discov*. 2018, **23**(6), pp.574-584.
103. Lazzari, G., Nicolas, V., Matsusaki, M., Akashi, M., Couvreur, P. and Mura, S. Multicellular spheroid based on a triple co-culture: A novel 3D model to mimic pancreatic tumor complexity. *Acta Biomater*. 2018, **78**, pp.296-307.
104. Ware, M.J., Colbert, K., Keshishian, V., Ho, J., Corr, S.J., Curley, S.A. and Godin, B. Generation of Homogenous Three-Dimensional Pancreatic Cancer Cell Spheroids Using an Improved Hanging Drop Technique. *Tissue Eng Part C Methods*. 2016, **22**(4), pp.312-321.
105. Adamska, A., Domenichini, A. and Falasca, M. Pancreatic Ductal Adenocarcinoma: Current and Evolving Therapies. *Int J Mol Sci*. 2017, **18**(7).
106. Baker, L.A., Tiriac, H., Clevers, H. and Tuveson, D.A. Modeling pancreatic cancer with organoids. *Trends Cancer*. 2016, **2**(4), pp.176-190.
107. Boj, S.F., Hwang, C.I., Baker, L.A., Chio, I., Engle, D.D., Corbo, V., Jager, M., Ponz-Sarvisé, M., Tiriac, H., Spector, M.S., Gracanin, A., Oni, T., Yu, K.H., van Boxtel, R., Huch, M., Rivera, K.D., Wilson, J.P., Feigin, M.E., Ohlund, D., Handly-Santana, A., Ardito-Abraham, C.M., Ludwig, M., Elyada, E., Alagesan, B., Biffi, G., Yordanov, G.N., Delcuze, B., Creighton, B., Wright, K., Park, Y., Morsink, F.H., Molenaar, I.Q., Borel Rinkes, I.H., Cuppen, E., Hao, Y., Jin, Y., Nijman, I.J., Iacobuzio-Donahue, C., Leach, S.D., Pappin, D.J., Hammell, M., Klimstra, D.S., Basturk, O., Hruban, R.H., Offerhaus, G.J., Vries, R.G., Clevers, H. and Tuveson, D.A. Organoid models of human and mouse ductal pancreatic cancer. *Cell*. 2015, **160**(1-2), pp.324-338.
108. Costa, E.C., Moreira, A.F., de Melo-Diogo, D., Gaspar, V.M., Carvalho, M.P. and Correia, I.J. 3D tumor spheroids: an overview on the tools and techniques used for their analysis. *Biotechnol Adv*. 2016, **34**(8), pp.1427-1441.
109. Clevers, H. Modeling Development and Disease with Organoids. *Cell*. 2016, **165**(7), pp.1586-1597.
110. Pape, J., Emberton, M. and Cheema, U. 3D Cancer Models: The Need for a Complex Stroma, Compartmentalization and Stiffness. *Front Bioeng Biotechnol*. 2021, **9**, p.660502.
111. Sutherland, R.M. Cell and environment interactions in tumor microregions: the multicell spheroid model. *Science*. 1988, **240**(4849), p.177.
112. Zanoni, M., Piccinini, F., Arienti, C., Zamagni, A., Santi, S., Polico, R., Bevilacqua, A. and Tesei, A. 3D tumor spheroid models for in vitro therapeutic screening: a systematic approach to enhance the biological relevance of data obtained. *Sci Rep*. 2016, **6**, p.19103.

113. Gopinathan, A., Morton, J.P., Jodrell, D.I. and Sansom, O.J. GEMMs as preclinical models for testing pancreatic cancer therapies. *Dis Model Mech.* 2015, **8**(10), pp.1185-1200.
114. Miller, D.M., Thomas, S.D., Islam, A., Muench, D. and Sedoris, K. c-Myc and cancer metabolism. *Clin Cancer Res.* 2012, **18**(20), pp.5546-5553.
115. Mukubou, H., Tsujimura, T., Sasaki, R. and Ku, Y. The role of autophagy in the treatment of pancreatic cancer with gemcitabine and ionizing radiation. *Int J Oncol.* 2010, **37**(4), pp.821-828.
116. Amrutkar, M., Vethe, N.T., Verbeke, C.S., Aasrum, M., Finstadsveen, A.V., Santha, P. and Gladhaug, I.P. Differential Gemcitabine Sensitivity in Primary Human Pancreatic Cancer Cells and Paired Stellate Cells Is Driven by Heterogenous Drug Uptake and Processing. *Cancers (Basel).* 2020, **12**(12).
117. Bjanec, T., Kotopoulis, S., Murvold, E.T., Kamceva, T., Gjertsen, B.T., Gilja, O.H., Schjott, J., Riedel, B. and McCormack, E. Ultrasound- and Microbubble-Assisted Gemcitabine Delivery to Pancreatic Cancer Cells. *Pharmaceutics.* 2020, **12**(2).
118. Cekanova, M. and Rathore, K. Animal models and therapeutic molecular targets of cancer: utility and limitations. *Drug Des Devel Ther.* 2014, **8**, pp.1911-1921.
119. Chinwalla, A., Cook, L. and Delehaunty, K.e.a. Initial sequencing and comparative analysis of the mouse genome. *Nature.* 2002, **420**, pp.520-562.
120. Church, D.M., Goodstadt, L., Hillier, L.W., Zody, M.C., Goldstein, S., She, X., Bult, C.J., Agarwala, R., Cherry, J.L., DiCuccio, M., Hlavina, W., Kapustin, Y., Meric, P., Maglott, D., Birtle, Z., Marques, A.C., Graves, T., Zhou, S., Teague, B., Potamousis, K., Churas, C., Place, M., Herschleb, J., Runnheim, R., Forrest, D., Amos-Landgraf, J., Schwartz, D.C., Cheng, Z., Lindblad-Toh, K., Eichler, E.E., Ponting, C.P. and Mouse Genome Sequencing, C. Lineage-specific biology revealed by a finished genome assembly of the mouse. *PLoS Biol.* 2009, **7**(5), p.e1000112.
121. Behrens, D., Walther, W. and Fichtner, I. Pancreatic cancer models for translational research. *Pharmacol Ther.* 2017, **173**, pp.146-158.
122. Erstad, D.J., Sojoodi, M., Taylor, M.S., Ghoshal, S., Razavi, A.A., Graham-O'Regan, K.A., Bardeesy, N., Ferrone, C.R., Lanuti, M., Caravan, P., Tanabe, K.K. and Fuchs, B.C. Orthotopic and heterotopic murine models of pancreatic cancer and their different responses to FOLFIRINOX chemotherapy. *Disease models & mechanisms.* 2018, **11**(7), p.dmm034793.
123. Murtaugh, L.C. Pathogenesis of pancreatic cancer: lessons from animal models. *Toxicol Pathol.* 2014, **42**(1), pp.217-228.
124. Perez-Mancera, P.A., Guerra, C., Barbacid, M. and Tuveson, D.A. What we have learned about pancreatic cancer from mouse models. *Gastroenterology.* 2012, **142**(5), pp.1079-1092.
125. Song, A.J. and Palmiter, R.D. Detecting and Avoiding Problems When Using the Cre-lox System. *Trends Genet.* 2018, **34**(5), pp.333-340.

126. Ariston Gabriel, A.N., Jiao, Q., Yvette, U., Yang, X., Al-Ameri, S.A., Du, L., Wang, Y.S. and Wang, C. Differences between KC and KPC pancreatic ductal adenocarcinoma mice models, in terms of their modeling biology and their clinical relevance. *Pancreatology*. 2020, **20**(1), pp.79-88.
127. Li, J., Qian, W., Qin, T., Xiao, Y., Cheng, L., Cao, J., Chen, X., Ma, Q. and Wu, Z. Mouse-Derived Allografts: A Complementary Model to the KPC Mice on Researching Pancreatic Cancer In Vivo. *Comput Struct Biotechnol J*. 2019, **17**, pp.498-506.
128. Herreros-Villanueva, M., Hijona, E., Cosme, A. and Bujanda, L. Mouse models of pancreatic cancer. *World J Gastroenterol*. 2012, **18**(12), pp.1286-1294.
129. Ware, M.J., Keshishian, V., Law, J.J., Ho, J.C., Favela, C.A., Rees, P., Smith, B., Mohammad, S., Hwang, R.F., Rajapakshe, K., Coarfa, C., Huang, S., Edwards, D.P., Corr, S.J., Godin, B. and Curley, S.A. Generation of an in vitro 3D PDAC stroma rich spheroid model. *Biomaterials*. 2016, **108**, pp.129-142.
130. MacArthur Clark, J. The 3Rs in research: a contemporary approach to replacement, reduction and refinement. *Br J Nutr*. 2018, **120**(s1), pp.S1-S7.
131. Huh, D., Kim, H.J., Fraser, J.P., Shea, D.E., Khan, M., Bahinski, A., Hamilton, G.A. and Ingber, D.E. Microfabrication of human organs-on-chips. *Nat Protoc*. 2013, **8**(11), pp.2135-2157.
132. Menon, N.V., Chuah, Y.J., Cao, B., Lim, M. and Kang, Y. A microfluidic co-culture system to monitor tumor-stromal interactions on a chip. *Biomicrofluidics*. 2014, **8**(6), p.064118.
133. Meyvantsson, I. and Beebe, D.J. Cell culture models in microfluidic systems. *Annu Rev Anal Chem (Palo Alto Calif)*. 2008, **1**, pp.423-449.
134. Nashimoto, Y., Okada, R., Hanada, S., Arima, Y., Nishiyama, K., Miura, T. and Yokokawa, R. Vascularized cancer on a chip: The effect of perfusion on growth and drug delivery of tumor spheroid. *Biomaterials*. 2020, **229**, p.119547.
135. Hoarau-Véchet, J., Rafii, A., Touboul, C. and Pasquier, J. Halfway between 2D and Animal Models: Are 3D Cultures the Ideal Tool to Study Cancer-Microenvironment Interactions? *International Journal of Molecular Sciences*. 2018, **19**(1).
136. Nath, S. and Devi, G.R. Three-dimensional culture systems in cancer research: Focus on tumor spheroid model. *Pharmacol Ther*. 2016, **163**, pp.94-108.
137. Tomas-Bort, E., Kieler, M., Sharma, S., Candido, J.B. and Loessner, D. 3D approaches to model the tumor microenvironment of pancreatic cancer. *Theranostics*. 2020, **10**(11), pp.5074-5089.
138. Weiswald, L.B., Bellet, D. and Dangles-Marie, V. Spherical cancer models in tumor biology. *Neoplasia*. 2015, **17**(1), pp.1-15.
139. Wen, Z., Liao, Q., Hu, Y., You, L., Zhou, L. and Zhao, Y. A spheroid-based 3-D culture model for pancreatic cancer drug testing, using the acid phosphatase assay. *Braz J Med Biol Res*. 2013, **46**(7), pp.634-642.

140. Puls, T.J., Tan, X., Whittington, C.F. and Voytik-Harbin, S.L. 3D collagen fibrillar microstructure guides pancreatic cancer cell phenotype and serves as a critical design parameter for phenotypic models of EMT. *PLoS One*. 2017, **12**(11), p.e0188870.
141. Hou, S., Tiriach, H., Sridharan, B. P., Scampavia, L., Madoux, F., Seldin, J., Souza, G. R., Watson, D., Tuveson, D., & Spicer, T. P. . Advanced Development of Primary Pancreatic Organoid Tumor Models for High-Throughput Phenotypic Drug Screening. *SLAS discovery : advancing life sciences R & D*. 2018, **23**(6), pp.574–584.
142. Boedtkjer, E. and Pedersen, S.F. The Acidic Tumor Microenvironment as a Driver of Cancer. *Annu Rev Physiol*. 2020, **82**, pp.103-126.
143. Lin, B., Chen, H., Liang, D., Lin, W., Qi, X., Liu, H. and Deng, X. Acidic pH and High-H₂O₂ Dual Tumor Microenvironment-Responsive Nanocatalytic Graphene Oxide for Cancer Selective Therapy and Recognition. *ACS Appl Mater Interfaces*. 2019, **11**(12), pp.11157-11166.
144. Pednekar, K.P., Heinrich, M.A., van Baarlen, J. and Prakash, J. Novel 3D microtissues Mimicking the Fibrotic Stroma in Pancreatic Cancer to Study Cellular Interactions and Stroma-Modulating Therapeutics. *Cancers (Basel)*. 2021, **13**(19).
145. Huang, L., Holtzinger, A., Jagan, I., BeGora, M., Lohse, I., Ngai, N., Nostro, C., Wang, R., Muthuswamy, L.B., Crawford, H.C., Arrowsmith, C., Kalloger, S.E., Renouf, D.J., Connor, A.A., Cleary, S., Schaeffer, D.F., Roehrl, M., Tsao, M.S., Gallinger, S., Keller, G. and Muthuswamy, S.K. Ductal pancreatic cancer modeling and drug screening using human pluripotent stem cell- and patient-derived tumor organoids. *Nat Med*. 2015, **21**(11), pp.1364-1371.
146. Tsai, S., McOlash, L., Palen, K., Johnson, B., Duris, C., Yang, Q., Dwinell, M.B., Hunt, B., Evans, D.B., Gershan, J. and James, M.A. Development of primary human pancreatic cancer organoids, matched stromal and immune cells and 3D tumor microenvironment models. *BMC Cancer*. 2018, **18**(1), p.335.
147. de Souza, N. Organoids. *Nature Methods*. 2018, **15**(1), pp.23-23.
148. Grapin-Botton, A. Three-dimensional pancreas organogenesis models. *Diabetes Obes Metab*. 2016, **18** Suppl 1, pp.33-40.
149. Mehling, M. and Tay, S. Microfluidic cell culture. *Curr Opin Biotechnol*. 2014, **25**, pp.95-102.
150. Sackmann, E.K., Fulton, A.L. and Beebe, D.J. The present and future role of microfluidics in biomedical research. *Nature*. 2014, **507**(7491), pp.181-189.
151. Bhatia, S.N. and Ingber, D.E. Microfluidic organs-on-chips. *Nat Biotechnol*. 2014, **32**(8), pp.760-772.
152. Carvalho, M.R. Colorectal tumor-on-a-chip system: A 3D tool for precision onco-nanomedicine. *Science Advances*. 2019, **5**.
153. Gupta, N., Liu, J.R., Patel, B., Solomon, D.E., Vaidya, B. and Gupta, V. Microfluidics-based 3D cell culture models: Utility in novel drug discovery and delivery research. *Bioeng Transl Med*. 2016, **1**(1), pp.63-81.

154. Halldorsson, S., Lucumi, E., Gomez-Sjoberg, R. and Fleming, R.M.T. Advantages and challenges of microfluidic cell culture in polydimethylsiloxane devices. *Biosens Bioelectron.* 2015, **63**, pp.218-231.
155. Lai, B.F.L., Huyer, L.D., Lu, R.X.Z., Drecun, S., Radisic, M. and Zhang, B. InVADE: Integrated Vasculature for Assessing Dynamic Events. *Advanced Functional Materials.* 2017, **27**(46).
156. Nikolaev, M., Mitrofanova, O., Broguiere, N., Geraldo, S., Dutta, D., Tabata, Y., Elci, B., Brandenburg, N., Kolotuev, I., Gjorevski, N., Clevers, H. and Lutolf, M.P. Homeostatic mini-intestines through scaffold-guided organoid morphogenesis. *Nature.* 2020, **585**(7826), pp.574-578.
157. Tsai, H.F., Trubelja, A., Shen, A.Q. and Bao, G. Tumour-on-a-chip: microfluidic models of tumour morphology, growth and microenvironment. *J R Soc Interface.* 2017, **14**(131).
158. Velve-Casquillas, G., Le Berre, M., Piel, M. and Tran, P.T. Microfluidic tools for cell biological research. *Nano Today.* 2010, **5**(1), pp.28-47.
159. Whitesides, G.M. The origins and the future of microfluidics. *Nature.* 2006, **442**(7101), pp.368-373.
160. Brown, J.A., Pensabene, V., Markov, D.A., Allwardt, V., Neely, M.D., Shi, M., Britt, C.M., Hoilett, O.S., Yang, Q., Brewer, B.M., Samson, P.C., McCawley, L.J., May, J.M., Webb, D.J., Li, D., Bowman, A.B., Reiserer, R.S. and Wikswo, J.P. Recreating blood-brain barrier physiology and structure on chip: A novel neurovascular microfluidic bioreactor. *Biomicrofluidics.* 2015, **9**(5), p.054124.
161. Kennedy, R., Kuvshinov, D., Sdrolia, A., Kuvshinova, E., Hilton, K., Crank, S., Beavis, A.W., Green, V. and Greenman, J. A patient tumour-on-a-chip system for personalised investigation of radiotherapy based treatment regimens. *Sci Rep.* 2019, **9**(1), p.6327.
162. Kim, H.J. and Ingber, D.E. Gut-on-a-Chip microenvironment induces human intestinal cells to undergo villus differentiation. *Integr Biol (Camb).* 2013, **5**(9), pp.1130-1140.
163. Shrestha, J., Razavi Bazaz, S., Aboulkheyr Es, H., Yaghobian Azari, D., Thierry, B., Ebrahimi Warkiani, M. and Ghadiri, M. Lung-on-a-chip: the future of respiratory disease models and pharmacological studies. *Crit Rev Biotechnol.* 2020, **40**(2), pp.213-230.
164. Virumbrales-Munoz, M., Ayuso, J.M., Gong, M.M., Humayun, M., Livingston, M.K., Lugo-Cintron, K.M., McMinn, P., Alvarez-Garcia, Y.R. and Beebe, D.J. Microfluidic lumen-based systems for advancing tubular organ modeling. *Chem Soc Rev.* 2020, **49**(17), pp.6402-6442.
165. Lee, J.H., Kim, S.K., Khawar, I.A., Jeong, S.Y., Chung, S. and Kuh, H.J. Microfluidic co-culture of pancreatic tumor spheroids with stellate cells as a novel 3D model for investigation of stroma-mediated cell motility and drug resistance. *J Exp Clin Cancer Res.* 2018, **37**(1), p.4.
166. Kramer, B., Haan, L., Vermeer, M., Olivier, T., Hankemeier, T., Vulto, P., Joore, J. and Lanz, H.L. Interstitial Flow Recapitulates Gemcitabine Chemoresistance in A 3D

- Microfluidic Pancreatic Ductal Adenocarcinoma Model by Induction of Multidrug Resistance Proteins. *Int J Mol Sci.* 2019, **20**(18).
167. Zhang, H., Whalley, R.D., Ferreira, A.M. and Dalgarno, K. High throughput physiological micro-models for in vitro pre-clinical drug testing: a review of engineering systems approaches. *Progress in Biomedical Engineering.* 2020, **2**(2).
168. Hadden, M., Mittal, A., Samra, J., Zreiqat, H., Sahni, S. and Ramaswamy, Y. Mechanically stressed cancer microenvironment: Role in pancreatic cancer progression. *Biochim Biophys Acta Rev Cancer.* 2020, **1874**(2), p.188418.
169. Conroy, T., Hammel, P., Hebbar, M., Ben Abdelghani, M., Wei, A.C., Raoul, J.L., Chone, L., Francois, E., Artru, P., Biagi, J.J., Lecomte, T., Assenat, E., Faroux, R., Ychou, M., Volet, J., Sauvanet, A., Breysacher, G., Di Fiore, F., Cripps, C., Kavan, P., Texereau, P., Bouhier-Leporrier, K., Khemissa-Akouz, F., Legoux, J.L., Juzyna, B., Gourguou, S., O'Callaghan, C.J., Jouffroy-Zeller, C., Rat, P., Malka, D., Castan, F., Bachet, J.B., Canadian Cancer Trials, G. and the Unicancer, G.I.P.G. FOLFIRINOX or Gemcitabine as Adjuvant Therapy for Pancreatic Cancer. *N Engl J Med.* 2018, **379**(25), pp.2395-2406.
170. de Sousa Cavalcante, L. and Monteiro, G. Gemcitabine: metabolism and molecular mechanisms of action, sensitivity and chemoresistance in pancreatic cancer. *Eur J Pharmacol.* 2014, **741**, pp.8-16.
171. Eskander, M.F., Bliss, L.A. and Tseng, J.F. Pancreatic adenocarcinoma. *Curr Probl Surg.* 2016, **53**(3), pp.107-154.
172. Erkan, M., Hausmann, S., Michalski, C.W., Fingerle, A.A., Dobritz, M., Kleeff, J. and Friess, H. The role of stroma in pancreatic cancer: diagnostic and therapeutic implications. *Nat Rev Gastroenterol Hepatol.* 2012, **9**(8), pp.454-467.
173. Liu, Q., Liao, Q. and Zhao, Y. Chemotherapy and tumor microenvironment of pancreatic cancer. *Cancer Cell Int.* 2017, **17**, p.68.
174. Gall, T.M., Wasan, H. and Jiao, L.R. Pancreatic cancer: current understanding of molecular and genetic aetiologies. *Postgrad Med J.* 2015, **91**(1080), pp.594-600.
175. Azad, A., Yin Lim, S., D'Costa, Z., Jones, K., Diana, A., Sansom, O.J., Kruger, P., Liu, S., McKenna, W.G., Dushek, O., Muschel, R.J. and Fokas, E. PD-L1 blockade enhances response of pancreatic ductal adenocarcinoma to radiotherapy. *EMBO Mol Med.* 2017, **9**(2), pp.167-180.
176. Gong, R. and Ren, H. Targeting chemokines/chemokine receptors: a promising strategy for enhancing the immunotherapy of pancreatic ductal adenocarcinoma. *Signal Transduct Target Ther.* 2020, **5**(1), p.149.
177. Maitra, A. Pancreatic cancer hidden in plain sight. *Nature.* 2020.
178. Conroy, T.D., F.; Ychou, M.; Bouché, O.; Guimbaud, R.; Bécouarn, Y.; Adenis, A.; Raoul, J. L.; Gourguou-Bourgade, S.; de la Fouchardière, C.; Bennouna, J.; Bachet, J. B.; Khemissa-Akouz, F.; Péré-Vergé, D.; Delbaldo, C.; Assenat, E.; Chauffert, B.; Michel, P.; Montoto-Grillot, C.; Ducreux, M., ... PRODIGE Intergroup. FOLFIRINOX versus Gemcitabine for Metastatic Pancreatic Cancer. *N Engl J Med.* 2011, **364**(19), pp.1817–1825.

179. Hessmann, E., Patzak, M.S., Klein, L., Chen, N., Kari, V., Ramu, I., Bapiro, T.E., Frese, K.K., Gopinathan, A., Richards, F.M., Jodrell, D.I., Verbeke, C., Li, X., Heuchel, R., Lohr, J.M., Johnsen, S.A., Gress, T.M., Ellenrieder, V. and Neesse, A. Fibroblast drug scavenging increases intratumoural gemcitabine accumulation in murine pancreas cancer. *Gut*. 2018, **67**(3), pp.497-507.
180. Ko, A.H., LoConte, N., Tempero, M.A., Walker, E.J., Kate Kelley, R., Lewis, S., Chang, W.C., Kantoff, E., Vannier, M.W., Catenacci, D.V., Venook, A.P. and Kindler, H.L. A Phase I Study of FOLFIRINOX Plus IPI-926, a Hedgehog Pathway Inhibitor, for Advanced Pancreatic Adenocarcinoma. *Pancreas*. 2016, **45**(3), pp.370-375.
181. Singh, R.R. and O'Reilly, E.M. New Treatment Strategies for Metastatic Pancreatic Ductal Adenocarcinoma. *Drugs*. 2020, **80**(7), pp.647-669.
182. Amrutkar, M. and Gladhaug, I.P. Pancreatic Cancer Chemoresistance to Gemcitabine. *Cancers (Basel)*. 2017, **9**(11).
183. Mini, E., Nobili, S., Caciagli, B., Landini, I. and Mazzei, T. Cellular pharmacology of gemcitabine. *Ann Oncol*. 2006, **17 Suppl 5**, pp.v7-12.
184. Alvarellos, M.L., Lamba, J., Sangkuhl, K., Thorn, C.F., Wang, L., Klein, D.J., Altman, R.B. and Klein, T.E. PharmGKB summary: gemcitabine pathway. *Pharmacogenet Genomics*. 2014, **24**(11), pp.564-574.
185. Liang, C., Shi, S., Meng, Q., Liang, D., Ji, S., Zhang, B., Qin, Y., Xu, J., Ni, Q. and Yu, X. Complex roles of the stroma in the intrinsic resistance to gemcitabine in pancreatic cancer: where we are and where we are going. *Exp Mol Med*. 2017, **49**(12), p.e406.
186. Borst, P., Evers, R., Kool, M. and Wijnholds, J. The multidrug resistance protein family. *Biochimica et Biophysica Acta (BBA) - Biomembranes*. 1999, **1461**(2), pp.347-357.
187. Kruh, G.D. and Belinsky, M.G. The MRP family of drug efflux pumps. *Oncogene*. 2003, **22**(47), pp.7537-7552.
188. Zhang, Y.K., Wang, Y.J., Gupta, P. and Chen, Z.S. Multidrug Resistance Proteins (MRPs) and Cancer Therapy. *AAPS J*. 2015, **17**(4), pp.802-812.
189. Che, P.P., Gregori, A., Firuzi, O., Dahele, M., Sminia, P., Peters, G.J. and Giovannetti, E. Pancreatic cancer resistance conferred by stellate cells: looking for new preclinical models. *Exp Hematol Oncol*. 2020, **9**, p.18.
190. Dalin, S., Sullivan, M.R., Lau, A.N., Grauman-Boss, B., Mueller, H.S., Kreidl, E., Fenoglio, S., Luengo, A., Lees, J.A., Vander Heiden, M.G., Lauffenburger, D.A. and Hemann, M.T. Deoxycytidine Release from Pancreatic Stellate Cells Promotes Gemcitabine Resistance. *Cancer Res*. 2019, **79**(22), pp.5723-5733.
191. Sperb, N., Tsesmelis, M. and Wirth, T. Crosstalk between Tumor and Stromal Cells in Pancreatic Ductal Adenocarcinoma. *Int J Mol Sci*. 2020, **21**(15).
192. Kuninty, P.R., Bansal, R., De Geus, S.W.L., Mardhian, D.F., Schnittert, J., van Baarlen, J., Storm, G., Bijlsma, M.F., van Laarhoven, H.W., Metselaar, J.M., Kuppen, P.J.K., Vahrmeijer, A.L., Östman, A., Sier, C.F.M. and Prakash, J. ITGA5 inhibition in pancreatic

- stellate cells attenuates desmoplasia and potentiates efficacy of chemotherapy in pancreatic cancer. *Science Advances*. 2019, **5**(9), pp.eaax2770-eaax2770.
193. Chauhan, V.P., Martin, J.D., Liu, H., Lacorre, D.A., Jain, S.R., Kozin, S.V., Stylianopoulos, T., Mousa, A.S., Han, X., Adstamongkonkul, P., Popovic, Z., Huang, P., Bawendi, M.G., Boucher, Y. and Jain, R.K. Angiotensin inhibition enhances drug delivery and potentiates chemotherapy by decompressing tumour blood vessels. *Nat Commun*. 2013, **4**, p.2516.
194. Alvarez, R., Musteanu, M., Garcia-Garcia, E., Lopez-Casas, P.P., Megias, D., Guerra, C., Munoz, M., Quijano, Y., Cubillo, A., Rodriguez-Pascual, J., Plaza, C., de Vicente, E., Prados, S., Taberner, S., Barbacid, M., Lopez-Rios, F. and Hidalgo, M. Stromal disrupting effects of nab-paclitaxel in pancreatic cancer. *Br J Cancer*. 2013, **109**(4), pp.926-933.
195. Jacobetz, M.A., Chan, D.S., Neesse, A., Bapiro, T.E., Cook, N., Frese, K.K., Feig, C., Nakagawa, T., Caldwell, M.E., Zecchini, H.I., Lolkema, M.P., Jiang, P., Kultti, A., Thompson, C.B., Maneval, D.C., Jodrell, D.I., Frost, G.I., Shepard, H.M., Skepper, J.N. and Tuveson, D.A. Hyaluronan impairs vascular function and drug delivery in a mouse model of pancreatic cancer. *Gut*. 2013, **62**(1), pp.112-120.
196. Provenzano, P.P., Cuevas, C., Chang, A.E., Goel, V.K., Von Hoff, D.D. and Hingorani, S.R. Enzymatic targeting of the stroma ablates physical barriers to treatment of pancreatic ductal adenocarcinoma. *Cancer Cell*. 2012, **21**(3), pp.418-429.
197. Ozdemir, B.C., Pentcheva-Hoang, T., Carstens, J.L., Zheng, X., Wu, C.C., Simpson, T.R., Laklai, H., Sugimoto, H., Kahlert, C., Novitskiy, S.V., De Jesus-Acosta, A., Sharma, P., Heidari, P., Mahmood, U., Chin, L., Moses, H.L., Weaver, V.M., Maitra, A., Allison, J.P., LeBleu, V.S. and Kalluri, R. Depletion of carcinoma-associated fibroblasts and fibrosis induces immunosuppression and accelerates pancreas cancer with reduced survival. *Cancer Cell*. 2014, **25**(6), pp.719-734.
198. Stromnes, I.M., Schmitt, T.M., Hulbert, A., Brockenbrough, J.S., Nguyen, H., Cuevas, C., Dotson, A.M., Tan, X., Hotes, J.L., Greenberg, P.D. and Hingorani, S.R. T Cells Engineered against a Native Antigen Can Surmount Immunologic and Physical Barriers to Treat Pancreatic Ductal Adenocarcinoma. *Cancer Cell*. 2015, **28**(5), pp.638-652.
199. Diop-Frimpong, B., Chauhan, V.P., Krane, S., Boucher, Y. and Jain, R.K. Losartan inhibits collagen I synthesis and improves the distribution and efficacy of nanotherapeutics in tumors. *Proc Natl Acad Sci U S A*. 2011, **108**(7), pp.2909-2914.
200. Stylianopoulos, T., Martin, J.D., Chauhan, V.P., Jain, S.R., Diop-Frimpong, B., Bardeesy, N., Smith, B.L., Ferrone, C.R., Hornicek, F.J., Boucher, Y., Munn, L.L. and Jain, R.K. Causes, consequences, and remedies for growth-induced solid stress in murine and human tumors. *Proc Natl Acad Sci U S A*. 2012, **109**(38), pp.15101-15108.
201. Olive, K.P., Jacobetz, M.A., Davidson, C.J., Gopinathan, A., McIntyre, D., Honess, D., Madhu, B., Goldgraben, M.A., Caldwell, M.E., Allard, D., Frese, K.K., Denicola, G., Feig, C., Combs, C., Winter, S.P., Ireland-Zecchini, H., Reichelt, S., Howat, W.J., Chang, A., Dhara, M., Wang, L., Ruckert, F., Grutzmann, R., Pilarsky, C., Izeradjene, K., Hingorani, S.R., Huang, P., Davies, S.E., Plunkett, W., Egorin, M., Hruban, R.H., Whitebread, N., McGovern, K., Adams, J., Iacobuzio-Donahue, C., Griffiths, J. and Tuveson, D.A.

- Inhibition of Hedgehog signaling enhances delivery of chemotherapy in a mouse model of pancreatic cancer. *Science*. 2009, **324**(5933), pp.1457-1461.
202. Jones, L.E., Humphreys, M.J., Campbell, F., Neoptolemos, J.P. and Boyd, M.T. Comprehensive Analysis of Matrix Metalloproteinase and Tissue Inhibitor Expression in Pancreatic Cancer. *Clinical Cancer Research*. 2004, **10**, pp.2832-2845.
203. Heldin, C.H., Rubin, K., Pietras, K. and Ostman, A. High interstitial fluid pressure - an obstacle in cancer therapy. *Nat Rev Cancer*. 2004, **4**(10), pp.806-813.
204. Chauhan, V.P., Martin, J.D., Liu, H., Lacorre, D.A., Jain, S.R., Kozin, S.V., Stylianopoulos, T., Mousa, A.S., Han, X., Adstamongkonkul, P., Popovic, Z., Huang, P., Bawendi, M.G., Boucher, Y. and Jain, R.K. Angiotensin inhibition enhances drug delivery and potentiates chemotherapy by decompressing tumour blood vessels. *Nat Commun*. 2013, **4**.
205. Nakai, Y., Isayama, H., Ijichi, H., Sasaki, T., Sasahira, N., Hirano, K., Kogure, H., Kawakubo, K., Yagioka, H., Yashima, Y., Mizuno, S., Yamamoto, K., Arizumi, T., Togawa, O., Matsubara, S., Tsujino, T., Tateishi, K., Tada, M., Omata, M. and Koike, K. Inhibition of renin-angiotensin system affects prognosis of advanced pancreatic cancer receiving gemcitabine. *British Journal of Cancer*. 2013, **103**(11), pp.1644-1648.
206. Kudo, D., Suto, A. and Hakamada, K. The Development of a Novel Therapeutic Strategy to Target Hyaluronan in the Extracellular Matrix of Pancreatic Ductal Adenocarcinoma. *Int J Mol Sci*. 2017, **18**(3).
207. Ambika Rajendran, M. Ultrasound-guided Microbubble in the Treatment of Cancer: A Mini Narrative Review. *Cureus*. 2018, **10**(9), p.e3256.
208. Browning, R. and Stride, E. Microbubble-Mediated Delivery for Cancer Therapy. *Fluids*. 2018, **3**(4).
209. Dimcevski, G., Kotopoulos, S., Bjanec, T., Hoem, D., Schjott, J., Gjertsen, B.T., Biermann, M., Molven, A., Sorbye, H., McCormack, E., Postema, M. and Gilja, O.H. A human clinical trial using ultrasound and microbubbles to enhance gemcitabine treatment of inoperable pancreatic cancer. *J Control Release*. 2016, **243**, pp.172-181.
210. Roovers, S., Segers, T., Lajoinie, G., Deprez, J., Versluis, M., De Smedt, S.C. and Lentacker, I. The Role of Ultrasound-Driven Microbubble Dynamics in Drug Delivery: From Microbubble Fundamentals to Clinical Translation. *Langmuir*. 2019, **35**(31), pp.10173-10191.
211. Sirsi, S. and Borden, M. Microbubble Compositions, Properties and Biomedical Applications. *Bubble Sci Eng Technol*. 2009, **1**(1-2), pp.3-17.
212. Tsutsui, J.M., Xie, F. and Porter, R.T. The use of microbubbles to target drug delivery. *Cardiovasc Ultrasound*. 2004, **2**, p.23.
213. Abou-Saleh, R.H., Peyman, S.A., Johnson, B.R., Marston, G., Ingram, N., Bushby, R., Coletta, P.L., Markham, A.F. and Evans, S.D. The influence of intercalating perfluorohexane into lipid shells on nano and microbubble stability. *Soft Matter*. 2016, **12**(34), pp.7223-7230.

214. Chen, H.H., J.H. Ultrasound-targeted microbubble destruction for chemotherapeutic drug delivery to solid tumors. *J Ther Ultrasound*. 2013, (1), p.10.
215. Ibsen, S., Schutt, C.E. and Esener, S. Microbubble-mediated ultrasound therapy: a review of its potential in cancer treatment. *Drug Des Devel Ther*. 2013, **7**, pp.375-388.
216. Peyman, S.A., Abou-Saleh, R.H. and Evans, S.D. Research spotlight: microbubbles for therapeutic delivery. *Ther Deliv*. 2013, **4**(5), pp.539-542.
217. Stride, E., Segers, T., Lajoinie, G., Cherkaoui, S., Bettinger, T., Versluis, M. and Borden, M. Microbubble Agents: New Directions. *Ultrasound Med Biol*. 2020, **46**(6), pp.1326-1343.
218. McEwan, C., Kamila, S., Owen, J., Nesbitt, H., Callan, B., Borden, M., Nomikou, N., Hamoudi, R.A., Taylor, M.A., Stride, E., McHale, A.P. and Callan, J.F. Combined sonodynamic and antimetabolite therapy for the improved treatment of pancreatic cancer using oxygen loaded microbubbles as a delivery vehicle. *Biomaterials*. 2016, **80**, pp.20-32.
219. Nesbitt, H., Sheng, Y., Kamila, S., Logan, K., Thomas, K., Callan, B., Taylor, M.A., Love, M., O'Rourke, D., Kelly, P., Beguin, E., Stride, E., McHale, A.P. and Callan, J.F. Gemcitabine loaded microbubbles for targeted chemo-sonodynamic therapy of pancreatic cancer. *J Control Release*. 2018, **279**, pp.8-16.
220. Bressand, D., Novell, A., Girault, A., Raoul, W., Fromont-Hankard, G., Escoffre, J.M., Lecomte, T. and Bouakaz, A. Enhancing Nab-Paclitaxel Delivery Using Microbubble-Assisted Ultrasound in a Pancreatic Cancer Model. *Mol Pharm*. 2019, **16**(9), pp.3814-3822.
221. Akbarzadeh, A., Rezaei-Sadabady, R., Davaran, S., Joo, S.W., Zarghami, N., Hanifehpour, Y., Samiei, M., Kouhi, M. and Nejati-Koshki, K. Liposome: classification, preparation, and applications. *Nanoscale research letters*. 2013, **8**(1), pp.102-102.
222. Celano, M., Calvagno, M.G., Bulotta, S., Paolino, D., Arturi, F., Rotiroti, D., Filetti, S., Fresta, M. and Russo, D. Cytotoxic effects of gemcitabine-loaded liposomes in human anaplastic thyroid carcinoma cells. *BMC Cancer*. 2004, **4**, p.63.
223. Crommelin, D.J.A., van Hoogevest, P. and Storm, G. The role of liposomes in clinical nanomedicine development. What now? Now what? *J Control Release*. 2020, **318**, pp.256-263.
224. Sercombe, L., Veerati, T., Moheimani, F., Wu, S.Y., Sood, A.K. and Hua, S. Advances and Challenges of Liposome Assisted Drug Delivery. *Front Pharmacol*. 2015, **6**, p.286.
225. Habib, S. and Singh, M. Recent Advances in Lipid-Based Nanosystems for Gemcitabine and Gemcitabine-Combination Therapy. *Nanomaterials (Basel)*. 2021, **11**(3).
226. Kim, D.H., Im, B.N., Hwang, H.S. and Na, K. Gemcitabine-loaded DSPE-PEG-PheoA liposome as a photomediated immune modulator for cholangiocarcinoma treatment. *Biomaterials*. 2018, **183**, pp.139-150.

227. Li, P.W., Luo, S., Xiao, L.Y., Tian, B.L., Wang, L., Zhang, Z.R. and Zeng, Y.C. A novel gemcitabine derivative-loaded liposome with great pancreas-targeting ability. *Acta Pharmacol Sin.* 2019, **40**(11), pp.1448-1456.
228. Ruan, J.L., Browning, R.J., Yildiz, Y.O., Bau, L., Kamila, S., Gray, M.D., Folkes, L., Hampson, A., McHale, A.P., Callan, J.F., Vojnovic, B., Kiltie, A.E. and Stride, E. Evaluation of Loading Strategies to Improve Tumor Uptake of Gemcitabine in a Murine Orthotopic Bladder Cancer Model Using Ultrasound and Microbubbles. *Ultrasound Med Biol.* 2021, **47**(6), pp.1596-1615.
229. Tucci, S.T., Kheirloom, A., Ingham, E.S., Mahakian, L.M., Tam, S.M., Foiret, J., Hubbard, N.E., Borowsky, A.D., Baikoghli, M., Cheng, R.H. and Ferrara, K.W. Tumor-specific delivery of gemcitabine with activatable liposomes. *J Control Release.* 2019, **309**, pp.277-288.
230. Xu, H., Paxton, J., Lim, J., Li, Y., Zhang, W., Duxfield, L. and Wu, Z. Development of high-content gemcitabine PEGylated liposomes and their cytotoxicity on drug-resistant pancreatic tumour cells. *Pharm Res.* 2014, **31**(10), pp.2583-2592.
231. Baumgart, F. Stiffness — an unknown world of mechanical science? *Injury.* 2000, **31**, pp.14-84.
232. Maccabi, A., Shin, A., Namiri, N.K., Bajwa, N., St John, M., Taylor, Z.D., Grundfest, W. and Saddik, G.N. Quantitative characterization of viscoelastic behavior in tissue-mimicking phantoms and ex vivo animal tissues. *PLoS One.* 2018, **13**(1), p.e0191919.
233. Li, Y., Khuu, N., Prince, E., Tao, H., Zhang, N., Chen, Z., Gevorkian, A., McGuigan, A.P. and Kumacheva, E. Matrix Stiffness-Regulated Growth of Breast Tumor Spheroids and Their Response to Chemotherapy. *Biomacromolecules.* 2021, **22**(2), pp.419-429.
234. Taubenberger, A.V., Girardo, S., Traber, N., Fischer-Friedrich, E., Krater, M., Wagner, K., Kurth, T., Richter, I., Haller, B., Binner, M., Hahn, D., Freudenberg, U., Werner, C. and Guck, J. 3D Microenvironment Stiffness Regulates Tumor Spheroid Growth and Mechanics via p21 and ROCK. *Adv Biosyst.* 2019, **3**(9), p.e1900128.
235. Chary, S. and Jain, R. Direct measurement of interstitial convection and diffusion of albumin in normal and neoplastic tissues by fluorescent photobleaching. *Proc Natl Acad Sci U S A.* 1989, **86**(14), pp.5385-5389.
236. Jain, R.K. Transport of Molecules in the Tumor Interstitium: A Review. *Cancer Research.* 1987, **47**(12), p.3039.
237. Levick, J.R. FLOW THROUGH INTERSTITIUM AND OTHER FIBROUS MATRICES. *Quarterly Journal of Experimental Physiology.* 1987, **72**(4), pp.409-437.
238. Liu, L.J. and Schlesinger, M. Interstitial hydraulic conductivity and interstitial fluid pressure for avascular or poorly vascularized tumors. *J Theor Biol.* 2015, **380**, pp.1-8.
239. Netti, P.A., Berk, D.A., Swartz, M.A., Grodzinsky, A.J. and Jain, R.K. Role of Extracellular Matrix Assembly in Interstitial Transport in Solid Tumors. *Cancer Research.* 2000, **60**(9), p.2497.

240. Baxter, L.T. and Jain, R.K. Transport of fluid and macromolecules in tumors. I. Role of interstitial pressure and convection. *Microvascular Research*. 1989, **37**(1), pp.77-104.
241. Kurth, F., Györvary, E., Heub, S., Ledroit, D., Paoletti, S., Renggli, K., Revol, V., Verhulsel, M., Weder, G. and Loizeau, F. Organs-on-a-chip engineering. In: *Organ-on-a-chip* Elsevier, 2020, pp.47-130.
242. Tschumperlin, D.J. and Lagares, D. Mechano-therapeutics: Targeting Mechanical Signaling in Fibrosis and Tumor Stroma. *Pharmacol Ther*. 2020, **212**, p.107575.
243. Coluccio, M.L., Perozziello, G., Malara, N., Parrotta, E., Zhang, P., Gentile, F., Limongi, T., Raj, P.M., Cuda, G., Candeloro, P. and Di Fabrizio, E. Microfluidic platforms for cell cultures and investigations. *Microelectronic Engineering*. 2019, **208**, pp.14-28.
244. Huang, Y.L., Segall, J.E. and Wu, M. Microfluidic modeling of the biophysical microenvironment in tumor cell invasion. *Lab Chip*. 2017, **17**(19), pp.3221-3233.
245. Inamdar, N.K. and Borenstein, J.T. Microfluidic cell culture models for tissue engineering. *Curr Opin Biotechnol*. 2011, **22**(5), pp.681-689.
246. Polacheck, W.J., Li, R., Uzel, S.G. and Kamm, R.D. Microfluidic platforms for mechanobiology. *Lab Chip*. 2013, **13**(12), pp.2252-2267.
247. Sontheimer-Phelps, A., Hassell, B.A. and Ingber, D.E. Modelling cancer in microfluidic human organs-on-chips. *Nat Rev Cancer*. 2019, **19**(2), pp.65-81.
248. Trujillo-de Santiago, G., Flores-Garza, B.G., Tavares-Negrete, J.A., Lara-Mayorga, I.M., Gonzalez-Gamboa, I., Zhang, Y.S., Rojas-Martinez, A., Ortiz-Lopez, R. and Alvarez, M.M. The Tumor-on-Chip: Recent Advances in the Development of Microfluidic Systems to Recapitulate the Physiology of Solid Tumors. *Materials (Basel)*. 2019, **12**(18).
249. Beebe, D.J., Mensing, G.A. and Walker, G.M. Physics and applications of microfluidics in biology. *Annu Rev Biomed Eng*. 2002, **4**, pp.261-286.
250. Toepke, M.W. and Beebe, D.J. PDMS absorption of small molecules and consequences in microfluidic applications. *Lab Chip*. 2006, **6**(12), pp.1484-1486.
251. Young, E.W. and Beebe, D.J. Fundamentals of microfluidic cell culture in controlled microenvironments. *Chem Soc Rev*. 2010, **39**(3), pp.1036-1048.
252. Komeya, M., Hayashi, K., Nakamura, H., Yamanaka, H., Sanjo, H., Kojima, K., Sato, T., Yao, M., Kimura, H., Fujii, T. and Ogawa, T. Pumpless microfluidic system driven by hydrostatic pressure induces and maintains mouse spermatogenesis in vitro. *Sci Rep*. 2017, **7**(1), p.15459.
253. Beer, M., Kuppalu, N., Stefanini, M., Becker, H., Schulz, I., Manoli, S., Schuette, J., Schmees, C., Casazza, A., Stelzle, M. and Arcangeli, A. A novel microfluidic 3D platform for culturing pancreatic ductal adenocarcinoma cells: comparison with in vitro cultures and in vivo xenografts. *Sci Rep*. 2017, **7**(1), p.1325.
254. Convery, N. and Gadegaard, N. 30 years of microfluidics. *Micro and Nano Engineering*. 2019, **2**, pp.76-91.

255. LaNasa, P.J. and Upp, E.L. Basic Flow Measurement Laws. In: *Fluid Flow Measurement (Third Edition)*. Elsevier, 2014, pp.19-29.
256. Shashi Menon, E. Chapter Five - Fluid Flow in Pipes. In: Shashi Menon, E. ed. *Transmission Pipeline Calculations and Simulations Manual*. Boston: Gulf Professional Publishing, 2015, pp.149-234.
257. Silva, P.N., Green, B.J., Altamentova, S.M. and Rocheleau, J.V. A microfluidic device designed to induce media flow throughout pancreatic islets while limiting shear-induced damage. *Lab Chip*. 2013, **13**(22), pp.4374-4384.
258. Bruus, H. Chapter 1. Governing Equations in Microfluidics. In: *Microscale Acoustofluidics*. 2014, pp.1-28.
259. Rapp, B.E. Fluids. In: *Microfluidics: Modelling, Mechanics and Mathematics*. 2017, pp.243-263.
260. Versluis, M., Stride, E., Lajoinie, G., Dollet, B. and Segers, T. Ultrasound Contrast Agent Modeling: A Review. *Ultrasound Med Biol*. 2020, **46**(9), pp.2117-2144.
261. Yildirim, T., Yaparathne, S., Graf, J., Garcia-Segura, S. and Apul, O. Electrostatic forces and higher order curvature terms of Young–Laplace equation on nanobubble stability in water. *npj Clean Water*. 2022, **5**(1).
262. Quaia, E. Microbubble ultrasound contrast agents: an update. *Eur Radiol*. 2007, **17**(8), pp.1995-2008.
263. Wischhusen, J. and Padilla, F. Ultrasound Molecular Imaging with Targeted Microbubbles for Cancer Diagnostics: From Bench to Bedside. *Irbm*. 2019, **40**(1), pp.3-9.
264. Pereno, V., Lei, J., Carugo, D. and Stride, E. Microstreaming inside Model Cells Induced by Ultrasound and Microbubbles. *Langmuir*. 2020, **36**(23), pp.6388-6398.
265. Peyman, S.A., McLaughlan, J.R., Abou-Saleh, R.H., Marston, G., Johnson, B.R., Freear, S., Coletta, P.L., Markham, A.F. and Evans, S.D. On-chip preparation of nanoscale contrast agents towards high-resolution ultrasound imaging. *Lab Chip*. 2016, **16**(4), pp.679-687.
266. Segers, T. and Versluis, M. Acoustic bubble sorting for ultrasound contrast agent enrichment. *Lab Chip*. 2014, **14**(10), pp.1705-1714.
267. Daeichin, V., van Rooij, T., Skachkov, I., Ergin, B., Specht, P.A., Lima, A., Ince, C., Bosch, J.G., van der Steen, A.F., de Jong, N. and Kooiman, K. Microbubble Composition and Preparation for High-Frequency Contrast-Enhanced Ultrasound Imaging: In Vitro and In Vivo Evaluation. *IEEE Trans Ultrason Ferroelectr Freq Control*. 2017, **64**(3), pp.555-567.
268. Peyman, S.A., Abou-Saleh, R.H., McLaughlan, J.R., Ingram, N., Johnson, B.R., Critchley, K., Freear, S., Evans, J.A., Markham, A.F., Coletta, P.L. and Evans, S.D. Expanding 3D geometry for enhanced on-chip microbubble production and single step formation of liposome modified microbubbles. *Lab Chip*. 2012, **12**(21), pp.4544-4552.

269. Tinkov, S., Bekeredjian, R., Winter, G. and Coester, C. Microbubbles as ultrasound triggered drug carriers. *J Pharm Sci.* 2009, **98**(6), pp.1935-1961.
270. Abou-Saleh, R.H., Delaney, A., Ingram, N., Batchelor, D.V.B., Johnson, B.R.G., Charalambous, A., Bushby, R.J., Peyman, S.A., Coletta, P.L., Markham, A.F. and Evans, S.D. Freeze-Dried Therapeutic Microbubbles: Stability and Gas Exchange. *ACS Applied Bio Materials.* 2020, **3**(11), pp.7840-7848.
271. Lichtman, J.W. and Conchello, J.A. Fluorescence microscopy. *Nat Methods.* 2005, **2**(12), pp.910-919.
272. Sanderson, M.J., Smith, I., Parker, I. and Bootman, M.D. Fluorescence microscopy. *Cold Spring Harb Protoc.* 2014, **2014**(10), p.pdb top071795.
273. Webb, D.J. and Brown, C.M. Epi-fluorescence microscopy. *Methods Mol Biol.* 2013, **931**, pp.29-59.
274. Thorn, K. A quick guide to light microscopy in cell biology. *Mol Biol Cell.* 2016, **27**(2), pp.219-222.
275. Lavrentovich, O.D. Confocal Fluorescence Microscopy. In: *Characterization of Materials.* 2012, pp.1-15.
276. Paddock, S. *Confocal Microscopy: Methods and Protocols.* 2014.
277. Corporation, L.T. Tracking cells through time and space. *BioProbe* 66. 2011.
278. O'Farrell, N., Houlton, A. and Horrocks, B.R. Silicon nanoparticles: applications in cell biology and medicine. *International journal of nanomedicine.* 2006, **1**(4), pp.451-472.
279. Chen, W., Wong, C., Vosburgh, E., Levine, A.J., Foran, D.J. and Xu, E.Y. High-throughput image analysis of tumor spheroids: a user-friendly software application to measure the size of spheroids automatically and accurately. *J Vis Exp.* 2014, (89).
280. Lowe, J.S. and Anderson, P.G. Support Cells and the Extracellular Matrix. In: *Stevens Lowes Human Histology.* 2015, pp.55-70.
281. Fang, Y. and Eglén, R.M. Three-Dimensional Cell Cultures in Drug Discovery and Development. *SLAS discovery : advancing life sciences R & D.* 2017, **22**(5), pp.456-472.
282. Frappart, P.O. and Hofmann, T.G. Pancreatic Ductal Adenocarcinoma (PDAC) Organoids: The Shining Light at the End of the Tunnel for Drug Response Prediction and Personalized Medicine. *Cancers (Basel).* 2020, **12**(10).
283. Lin, C.C. and Korc, M. Designer hydrogels: Shedding light on the physical chemistry of the pancreatic cancer microenvironment. *Cancer Lett.* 2018, **436**, pp.22-27.
284. Tibbitt, M.W. and Anseth, K.S. Hydrogels as extracellular matrix mimics for 3D cell culture. *Biotechnol Bioeng.* 2009, **103**(4), pp.655-663.
285. Wu, J., Li, P., Dong, C., Jiang, H., Bin, X., Gao, X., Qin, M., Wang, W., Bin, C. and Cao, Y. Rationally designed synthetic protein hydrogels with predictable mechanical properties. *Nat Commun.* 2018, **9**(1), p.620.

286. Singh, V., Barbosa, F.L., Torricelli, A.A., Santhiago, M.R. and Wilson, S.E. Transforming growth factor β and platelet-derived growth factor modulation of myofibroblast development from corneal fibroblasts in vitro. *Exp Eye Res.* 2014, **120**, pp.152 - 160.
287. Tomlinson, D.C., Freestone, S.H., Grace, O.C. and Thomson, A.A. Differential effects of transforming growth factor-beta1 on cellular proliferation in the developing prostate. *Endocrinology.* 2004, **145**(9), pp.4292-4300.
288. Abnaof, K., Mallela, N., Walenda, G., Meurer, S., Seré, K., Lin, Q., Smeets, B., Hoffmann, K., Wagner, W., Zenke, M., Weiskirchen, R. and Fröhlich, H. TGF- β stimulation in human and murine cells reveals commonly affected biological processes and pathways at transcription level. *BMC Systems Biology.* 2014, **8**(1).
289. Papageorgis, P. and Stylianopoulos, T. Role of TGFbeta in regulation of the tumor microenvironment and drug delivery (review). *Int J Oncol.* 2015, **46**(3), pp.933-943.
290. Carpino, G., Renzi, A., Cardinale, V., Franchitto, A., Onori, P., Overi, D., Rossi, M., Berloco, P.B., Alvaro, D., Reid, L.M. and Gaudio, E. Progenitor cell niches in the human pancreatic duct system and associated pancreatic duct glands: an anatomical and immunophenotyping study. *J Anat.* 2016, **228**(3), pp.474-486.
291. Bourn, M.D., Batchelor, D.V.B., Ingram, N., McLaughlan, J.R., Coletta, P.L., Evans, S.D. and Peyman, S.A. High-throughput microfluidics for evaluating microbubble enhanced delivery of cancer therapeutics in spheroid cultures. *J Control Release.* 2020, **326**, pp.13-24.
292. Liu, T., Lin, B. and Qin, J. Carcinoma-associated fibroblasts promoted tumor spheroid invasion on a microfluidic 3D co-culture device. *Lab Chip.* 2010, **10**(13), pp.1671-1677.
293. Sugimoto, M., Kitagawa, Y., Yamada, M., Yajima, Y., Utoh, R. and Seki, M. Micropassage-embedding composite hydrogel fibers enable quantitative evaluation of cancer cell invasion under 3D coculture conditions. *Lab Chip.* 2018, **18**(9), pp.1378-1387.
294. Annabi, N., Selimovic, S., Acevedo Cox, J.P., Ribas, J., Afshar Bakooshi, M., Heintze, D., Weiss, A.S., Cropek, D. and Khademhosseini, A. Hydrogel-coated microfluidic channels for cardiomyocyte culture. *Lab Chip.* 2013, **13**(18), pp.3569-3577.
295. Maoz, B.M., Herland, A., FitzGerald, E.A., Grevesse, T., Vidoudez, C., Pacheco, A.R., Sheehy, S.P., Park, T.E., Dauth, S., Mannix, R., Budnik, N., Shores, K., Cho, A., Nawroth, J.C., Segre, D., Budnik, B., Ingber, D.E. and Parker, K.K. A linked organ-on-chip model of the human neurovascular unit reveals the metabolic coupling of endothelial and neuronal cells. *Nat Biotechnol.* 2018, **36**(9), pp.865-874.
296. Jain, A., Graveline, A., Waterhouse, A., Vernet, A., Flaumenhaft, R. and Ingber, D.E. A shear gradient-activated microfluidic device for automated monitoring of whole blood haemostasis and platelet function. *Nat Commun.* 2016, **7**, p.10176.
297. Hassell, B.A., Goyal, G., Lee, E., Sontheimer-Phelps, A., Levy, O., Chen, C.S. and Ingber, D.E. Human Organ Chip Models Recapitulate Orthotopic Lung Cancer Growth, Therapeutic Responses, and Tumor Dormancy In Vitro. *Cell Rep.* 2017, **21**(2), pp.508-516.

298. Martinez-Duarte, R., & Madou, M.J. . SU-8 Photolithography and Its Impact on Microfluidics. 2011.
299. Tan, S.H., Nguyen, N.T., Chua, Y.C. and Kang, T.G. Oxygen plasma treatment for reducing hydrophobicity of a sealed polydimethylsiloxane microchannel. *Biomicrofluidics*. 2010, **4**(3), p.32204.
300. Asif, A., Kim, K.H., Jabbar, F., Kim, S. and Choi, K.H. Real-time sensors for live monitoring of disease and drug analysis in microfluidic model of proximal tubule. *Microfluidics and Nanofluidics*. 2020, **24**(6).
301. Microfluidics, D. *Shear stress in microfluidic devices– Darwin Microfluidics*. [Online]. 2017. [Accessed].
302. Abou-Saleh, R.H., Armistead, F.J., Batchelor, D.V.B., Johnson, B.R.G., Peyman, S.A. and Evans, S.D. Horizon: Microfluidic platform for the production of therapeutic microbubbles and nanobubbles. *Rev Sci Instrum*. 2021, **92**(7), p.074105.
303. Batchelor, D. DamienBatchelor/UoL_MicrobubbleCount: First public release of MATLAB Microbubble Code (Version v1.0.1). *Zenodo*. 2020.
304. Ding, N., Wang, Y., Wang, X., Chu, W., Yin, T., Gou, J., He, H., Zhang, Y., Wang, Y. and Tang, X. Improving plasma stability and antitumor effect of gemcitabine via PEGylated liposome prepared by active drug loading. *Journal of Drug Delivery Science and Technology*. 2020, **57**.
305. Cruz, D.J., Bonotto, R.M., Gomes, R.G., da Silva, C.T., Taniguchi, J.B., No, J.H., Lombardot, B., Schwartz, O., Hansen, M.A. and Freitas-Junior, L.H. Identification of novel compounds inhibiting chikungunya virus-induced cell death by high throughput screening of a kinase inhibitor library. *PLoS Negl Trop Dis*. 2013, **7**(10), p.e2471.
306. Carreño, E.A., Alberto, A.V.P., de Souza, C.A.M., de Mello, H.L., Henriques-Pons, A. and Anastacio Alves, L. Considerations and Technical Pitfalls in the Employment of the MTT Assay to Evaluate Photosensitizers for Photodynamic Therapy. *Applied Sciences*. 2021, **11**(6).
307. Hamid, R., Rotshteyn, Y., Rabadi, L., Parikh, R. and Bullock, P. Comparison of alamar blue and MTT assays for high through-put screening. *Toxicol In Vitro*. 2004, **18**(5), pp.703-710.
308. Sui, Y. and Wu, Z. Alternative statistical parameter for high-throughput screening assay quality assessment. *J Biomol Screen*. 2007, **12**(2), pp.229-234.
309. Zhang, J.-H., Chung, T.D.Y. and Oldenburg, K.R. A Simple Statistical Parameter for Use in Evaluation and Validation of High Throughput Screening Assays. *Journal of Biomolecular Screening*. 1999, **4**(2), pp.67-73.
310. Zhang, X.D. Illustration of SSMD, z score, SSMD*, z* score, and t statistic for hit selection in RNAi high-throughput screens. *J Biomol Screen*. 2011, **16**(7), pp.775-785.
311. Ahmed, S., Bradshaw, A.D., Gera, S., Dewan, M.Z. and Xu, R. The TGF-beta/Smad4 Signaling Pathway in Pancreatic Carcinogenesis and Its Clinical Significance. *J Clin Med*. 2017, **6**(1).

312. Emon, B., Bauer, J., Jain, Y., Jung, B. and Saif, T. Biophysics of Tumor Microenvironment and Cancer Metastasis - A Mini Review. *Comput Struct Biotechnol J*. 2018, **16**, pp.279-287.
313. Jin, G., Hong, W., Guo, Y., Bai, Y. and Chen, B. Molecular Mechanism of Pancreatic Stellate Cells Activation in Chronic Pancreatitis and Pancreatic Cancer. *J Cancer*. 2020, **11**(6), pp.1505-1515.
314. Meng, X.M., Nikolic-Paterson, D.J. and Lan, H.Y. TGF-beta: the master regulator of fibrosis. *Nat Rev Nephrol*. 2016, **12**(6), pp.325-338.
315. Nicolas-Boluda, A., Vaquero, J., Vimeux, L., Guilbert, T., Barrin, S., Kantari-Mimoun, C., Ponzo, M., Renault, G., Deptula, P., Pogoda, K., Bucki, R., Cascone, I., Courty, J., Fouassier, L., Gazeau, F. and Donnadieu, E. Tumor stiffening reversion through collagen crosslinking inhibition improves T cell migration and anti-PD-1 treatment. *Elife*. 2021, **10**.
316. Schnittert, J., Bansal, R. and Prakash, J. Targeting Pancreatic Stellate Cells in Cancer. *Trends Cancer*. 2019, **5**(2), pp.128-142.
317. Shields, M.A., Dangi-Garimella, S., Redig, A.J. and Munshi, H.G. Biochemical role of the collagen-rich tumour microenvironment in pancreatic cancer progression. *Biochem J*. 2012, **441**(2), pp.541-552.
318. Fujiwara, M., Kanayama, K., Hirokawa, Y.S. and Shiraishi, T. ASF-4-1 fibroblast-rich culture increases chemoresistance and mTOR expression of pancreatic cancer BxPC-3 cells at the invasive front in vitro, and promotes tumor growth and invasion in vivo. *Oncol Lett*. 2016, **11**(4), pp.2773-2779.
319. Bynigeri, R.R., Jakkampudi, A., Jangala, R., Subramanyam, C., Sasikala, M., Rao, G.V., Reddy, D.N. and Talukdar, R. Pancreatic stellate cell: Pandora's box for pancreatic disease biology. *World J Gastroenterol*. 2017, **23**(3), pp.382-405.
320. Xue, R., Jia, K., Wang, J., Yang, L., Wang, Y., Gao, L. and Hao, J. A Rising Star in Pancreatic Diseases: Pancreatic Stellate Cells. *Front Physiol*. 2018, **9**, p.754.
321. Dardare, J., Witz, A., Merlin, J.L., Gilson, P. and Harle, A. SMAD4 and the TGFbeta Pathway in Patients with Pancreatic Ductal Adenocarcinoma. *Int J Mol Sci*. 2020, **21**(10).
322. Principe, D.R., Timbers, K.E., Atia, L.G., Koch, R.M. and Rana, A. TGFbeta Signaling in the Pancreatic Tumor Microenvironment. *Cancers (Basel)*. 2021, **13**(20).
323. Shen, W., Tao, G.Q., Zhang, Y., Cai, B., Sun, J. and Tian, Z.Q. TGF-beta in pancreatic cancer initiation and progression: two sides of the same coin. *Cell Biosci*. 2017, **7**, p.39.
324. Nair, M., Best, S.M. and Cameron, R.E. Crosslinking Collagen Constructs: Achieving Cellular Selectivity Through Modifications of Physical and Chemical Properties. *Applied Sciences*. 2020, **10**(19).
325. Sheu, M.-T., Huang, J.-C., Yeh, G.-C. and Ho, H.-O. Characterization of collagen gel solutions and collagen matrices for cell culture. *Biomaterials*. 2001, **22**(13), pp.1713-1719.

326. Chang, C.Y. and Lin, C.C. Hydrogel Models with Stiffness Gradients for Interrogating Pancreatic Cancer Cell Fate. *Bioengineering (Basel)*. 2021, **8**(3).
327. Zakaria, M.A., Rajab, N.F., Chua, E.W., Selvarajah, G.T. and Masre, S.F. The Roles of Tissue Rigidity and Its Underlying Mechanisms in Promoting Tumor Growth. *Cancer Invest*. 2020, **38**(8-9), pp.445-462.
328. Bonnans, C., Chou, J. and Werb, Z. Remodelling the extracellular matrix in development and disease. *Nat Rev Mol Cell Biol*. 2014, **15**(12), pp.786-801.
329. Papalazarou, V., Salmeron-Sanchez, M. and Machesky, L.M. Tissue engineering the cancer microenvironment-challenges and opportunities. *Biophys Rev*. 2018, **10**(6), pp.1695-1711.
330. Grasso, C., Jansen, G. and Giovannetti, E. Drug resistance in pancreatic cancer: Impact of altered energy metabolism. *Crit Rev Oncol Hematol*. 2017, **114**, pp.139-152.
331. Bein, A., Shin, W., Jalili-Firoozinezhad, S., Park, M.H., Sontheimer-Phelps, A., Tovaglieri, A., Chalkiadaki, A., Kim, H.J. and Ingber, D.E. Microfluidic Organ-on-a-Chip Models of Human Intestine. *Cell Mol Gastroenterol Hepatol*. 2018, **5**(4), pp.659-668.
332. Huang, C.P., Lu, J., Seon, H., Lee, A.P., Flanagan, L.A., Kim, H.Y., Putnam, A.J. and Jeon, N.L. Engineering microscale cellular niches for three-dimensional multicellular co-cultures. *Lab Chip*. 2009, **9**(12), pp.1740-1748.
333. Jeon, J.S., Bersini, S., Gilardi, M., Dubini, G., Charest, J.L., Moretti, M. and Kamm, R.D. Human 3D vascularized organotypic microfluidic assays to study breast cancer cell extravasation. *Proc Natl Acad Sci U S A*. 2015, **112**(1), pp.214-219.
334. Liu, W., Tian, C., Yan, M., Zhao, L., Ma, C., Li, T., Xu, J. and Wang, J. Heterotypic 3D tumor culture in a reusable platform using pneumatic microfluidics. *Lab Chip*. 2016, **16**(21), pp.4106-4120.
335. Huber, D., Oskooei, A., Casadevall, I.S.X., Andrew, d. and Kaigala, G.V. Hydrodynamics in Cell Studies. *Chem Rev*. 2018, **118**(4), pp.2042-2079.
336. Jeong, S.Y., Lee, J.H., Shin, Y., Chung, S. and Kuh, H.J. Co-Culture of Tumor Spheroids and Fibroblasts in a Collagen Matrix-Incorporated Microfluidic Chip Mimics Reciprocal Activation in Solid Tumor Microenvironment. *PLoS One*. 2016, **11**(7), p.e0159013.
337. Tourovskaia, A., Figueroa-Masot, X. and Folch, A. Differentiation-on-a-chip: a microfluidic platform for long-term cell culture studies. *Lab Chip*. 2005, **5**(1), pp.14-19.
338. Follain, G., Herrmann, D., Harlepp, S., Hyenne, V., Osmani, N., Warren, S.C., Timpson, P. and Goetz, J.G. Fluids and their mechanics in tumour transit: shaping metastasis. *Nat Rev Cancer*. 2020, **20**(2), pp.107-124.
339. Zhu, X., Yi Chu, L., Chueh, B.-h., Shen, M., Hazarika, B., Phadke, N. and Takayama, S. Arrays of horizontally-oriented mini-reservoirs generate steady microfluidic flows for continuous perfusion cell culture and gradient generation. *Analyst*. 2004, **129**(11), pp.1026-1031.

340. Fares, J., Fares, M.Y., Khachfe, H.H., Salhab, H.A. and Fares, Y. Molecular principles of metastasis: a hallmark of cancer revisited. *Signal Transduct Target Ther.* 2020, **5**(1), p.28.
341. Roussos, E.T., Condeelis, J.S. and Patsialou, A. Chemotaxis in cancer. *Nat Rev Cancer.* 2011, **11**(8), pp.573-587.
342. Yang, L., Banada, P.P., Bhunia, A.K. and Bashir, R. Effects of Dielectrophoresis on Growth, Viability and Immuno-reactivity of *Listeria monocytogenes*. *J Biol Eng.* 2008, **2**, p.6.
343. Nagelkerke, A., Bussink, J., Rowan, A.E. and Span, P.N. The mechanical microenvironment in cancer: How physics affects tumours. *Semin Cancer Biol.* 2015, **35**, pp.62-70.
344. Below, C.R., Kelly, J., Brown, A., Humphries, J.D., Hutton, C., Xu, J., Lee, B.Y., Cintas, C., Zhang, X., Hernandez-Gordillo, V., Stockdale, L., Goldsworthy, M.A., Geraghty, J., Foster, L., O'Reilly, D.A., Schedding, B., Askari, J., Burns, J., Hodson, N., Smith, D.L., Lally, C., Ashton, G., Knight, D., Mironov, A., Banyard, A., Eble, J.A., Morton, J.P., Humphries, M.J., Griffith, L.G. and Jorgensen, C. A microenvironment-inspired synthetic three-dimensional model for pancreatic ductal adenocarcinoma organoids. *Nat Mater.* 2021.
345. Berger Fridman, I., Ugolini, G.S., VanDelinder, V., Cohen, S. and Konry, T. High throughput microfluidic system with multiple oxygen levels for the study of hypoxia in tumor spheroids. *Biofabrication.* 2021, **13**(3).
346. Byrne, M.B., Leslie, M.T., Gaskins, H.R. and Kenis, P.J.A. Methods to study the tumor microenvironment under controlled oxygen conditions. *Trends Biotechnol.* 2014, **32**(11), pp.556-563.
347. Grist, S.M., Nasser, S.S., Laplatine, L., Schmok, J.C., Yao, D., Hua, J., Chrostowski, L. and Cheung, K.C. Long-term monitoring in a microfluidic system to study tumour spheroid response to chronic and cycling hypoxia. *Sci Rep.* 2019, **9**(1), p.17782.
348. Palacio-Castaneda, V., Kooijman, L., Venzac, B., Verdurmen, W.P.R. and Le Gac, S. Metabolic Switching of Tumor Cells under Hypoxic Conditions in a Tumor-on-a-chip Model. *Micromachines (Basel).* 2020, **11**(4).
349. Refet-Mollof, E., Najyb, O., Chermat, R., Glory, A., Lafontaine, J., Wong, P. and Gervais, T. Hypoxic Jumbo Spheroids On-A-Chip (HOnAChip): Insights into Treatment Efficacy. *Cancers (Basel).* 2021, **13**(16).
350. Harris, A.L. Hypoxia--a key regulatory factor in tumour growth. *Nat Rev Cancer.* 2002, **2**(1), pp.38-47.
351. Laitala, A. and Erler, J.T. Hypoxic Signalling in Tumour Stroma. *Front Oncol.* 2018, **8**, p.189.
352. Måseide, K., Kandel, R.A., Bell, R.S., Catton, C.N., O'Sullivan, B., Wunder, J.S., Pintilie, M., Hedley, D. and Hill, R.P. Carbonic Anhydrase IX as a Marker for Poor Prognosis in Soft Tissue Sarcoma. *Clinical Cancer Research.* 2004, **10**(13), p.4464.

353. Muz, B., de la Puente, P., Azab, F. and Azab, A.K. The role of hypoxia in cancer progression, angiogenesis, metastasis, and resistance to therapy. *Hypoxia (Auckl)*. 2015, **3**, pp.83-92.
354. Maxwell, P.H., Pugh, C.W. and Ratcliffe, P.J. Activation of the HIF pathway in cancer. *Current Opinion in Genetics & Development*. 2001, **11**(3), pp.293-299.
355. Weidemann, A. and Johnson, R.S. Biology of HIF-1alpha. *Cell Death Differ*. 2008, **15**(4), pp.621-627.
356. Tao, J., Yang, G., Zhou, W., Qiu, J., Chen, G., Luo, W., Zhao, F., You, L., Zheng, L., Zhang, T. and Zhao, Y. Targeting hypoxic tumor microenvironment in pancreatic cancer. *J Hematol Oncol*. 2021, **14**(1), p.14.
357. Thomas, D. and Radhakrishnan, P. Tumor-stromal crosstalk in pancreatic cancer and tissue fibrosis. *Mol Cancer*. 2019, **18**(1), p.14.
358. Yuen, A. and Diaz, B. The impact of hypoxia in pancreatic cancer invasion and metastasis. *Hypoxia (Auckl)*. 2014, **2**, pp.91-106.
359. Levental, K.R., Yu, H., Kass, L., Lakins, J.N., Egeblad, M., Erler, J.T., Fong, S.F., Csiszar, K., Giaccia, A., Weninger, W., Yamauchi, M., Gasser, D.L. and Weaver, V.M. Matrix crosslinking forces tumor progression by enhancing integrin signaling. *Cell*. 2009, **139**(5), pp.891-906.
360. Saatci, O., Kaymak, A., Raza, U., Ersan, P.G., Akbulut, O., Banister, C.E., Sikirzhytski, V., Tokat, U.M., Aykut, G., Ansari, S.A., Dogan, H.T., Dogan, M., Jandaghi, P., Isik, A., Gundogdu, F., Kosemehmetoglu, K., Dizdar, O., Aksoy, S., Akyol, A., Uner, A., Buckhaults, P.J., Riazalhosseini, Y. and Sahin, O. Targeting lysyl oxidase (LOX) overcomes chemotherapy resistance in triple negative breast cancer. *Nat Commun*. 2020, **11**(1), p.2416.
361. Winkler, J., Abisoye-Ogunniyan, A., Metcalf, K.J. and Werb, Z. Concepts of extracellular matrix remodelling in tumour progression and metastasis. *Nat Commun*. 2020, **11**(1), p.5120.
362. Swabb, E.A., Wei, J. and Gullino, P.M. Diffusion and Convection in Normal and Neoplastic Tissues. *Cancer Research*. 1974, **34**(10), p.2814.
363. Malfanti, A., Miletto, I., Bottinelli, E., Zonari, D., Blandino, G., Berlier, G. and Arpicco, S. Delivery of Gemcitabine Prodrugs Employing Mesoporous Silica Nanoparticles. *Molecules*. 2016, **21**(4), p.522.
364. Fischer, T., Hayn, A. and Mierke, C.T. Fast and reliable advanced two-step pore-size analysis of biomimetic 3D extracellular matrix scaffolds. *Sci Rep*. 2019, **9**(1), p.8352.
365. Drescher, S. and van Hoogevest, P. The Phospholipid Research Center: Current Research in Phospholipids and Their Use in Drug Delivery. *Pharmaceutics*. 2020, **12**(12).
366. Li, J., Wang, X., Zhang, T., Wang, C., Huang, Z., Luo, X. and Deng, Y. A review on phospholipids and their main applications in drug delivery systems. *Asian Journal of Pharmaceutical Sciences*. 2015, **10**(2), pp.81-98.

367. Cafarelli, A., Verbeni, A., Poliziani, A., Dario, P., Menciassi, A. and Ricotti, L. Tuning acoustic and mechanical properties of materials for ultrasound phantoms and smart substrates for cell cultures. *Acta Biomater.* 2017, **49**, pp.368-378.
368. Kotopoulis, S., Delalande, A., Popa, M., Mamaeva, V., Dimcevski, G., Gilja, O.H., Postema, M., Gjertsen, B.T. and McCormack, E. Sonoporation-enhanced chemotherapy significantly reduces primary tumour burden in an orthotopic pancreatic cancer xenograft. *Mol Imaging Biol.* 2014, **16**(1), pp.53-62.
369. Kotopoulis, S., Dimcevski, G., Gilja, O.H., Hoem, D. and Postema, M. Treatment of human pancreatic cancer using combined ultrasound, microbubbles, and gemcitabine: a clinical case study. *Med Phys.* 2013, **40**(7), p.072902.
370. Roovers, S., Deprez, J., Priwitaningrum, D., Lajoinie, G., Rivron, N., Declercq, H., De Wever, O., Stride, E., Le Gac, S., Versluis, M., Prakash, J., De Smedt, S.C. and Lentacker, I. Sonoprinting liposomes on tumor spheroids by microbubbles and ultrasound. *J Control Release.* 2019, **316**, pp.79-92.
371. Yan, F., Li, L., Deng, Z., Jin, Q., Chen, J., Yang, W., Yeh, C.K., Wu, J., Shandas, R., Liu, X. and Zheng, H. Paclitaxel-liposome-microbubble complexes as ultrasound-triggered therapeutic drug delivery carriers. *J Control Release.* 2013, **166**(3), pp.246-255.
372. Ohlund, D., Handly-Santana, A., Biffi, G., Elyada, E., Almeida, A.S., Ponz-Sarvisé, M., Corbo, V., Oni, T.E., Hearn, S.A., Lee, E.J., Chio, I., Hwang, C.I., Tiriác, H., Baker, L.A., Engle, D.D., Feig, C., Kultti, A., Egeblad, M., Fearon, D.T., Crawford, J.M., Clevers, H., Park, Y. and Tuveson, D.A. Distinct populations of inflammatory fibroblasts and myofibroblasts in pancreatic cancer. *J Exp Med.* 2017, **214**(3), pp.579-596.
373. Group Young Researchers In Inflammatory, C., Wandmacher, A.M., Mehdorn, A.S. and Sebens, S. The Heterogeneity of the Tumor Microenvironment as Essential Determinant of Development, Progression and Therapy Response of Pancreatic Cancer. *Cancers (Basel).* 2021, **13**(19).
374. Murakami, T., Hiroshima, Y., Matsuyama, R., Homma, Y., Hoffman, R.M. and Endo, I. Role of the tumor microenvironment in pancreatic cancer. *Ann Gastroenterol Surg.* 2019, **3**(2), pp.130-137.
375. Truong, L.H. and Pauklin, S. Pancreatic Cancer Microenvironment and Cellular Composition: Current Understandings and Therapeutic Approaches. *Cancers (Basel).* 2021, **13**(19).
376. Karamitopoulou, E. Tumour microenvironment of pancreatic cancer: immune landscape is dictated by molecular and histopathological features. *Br J Cancer.* 2019, **121**(1), pp.5-14.
377. Craven, K.E., Gore, J. and Korc, M. Overview of pre-clinical and clinical studies targeting angiogenesis in pancreatic ductal adenocarcinoma. *Cancer Lett.* 2016, **381**(1), pp.201-210.
378. Knudsen, E.S., Vail, P., Balaji, U., Ngo, H., Botros, I.W., Makarov, V., Riaz, N., Balachandran, V., Leach, S., Thompson, D.M., Chan, T.A. and Witkiewicz, A.K. Stratification of Pancreatic Ductal Adenocarcinoma: Combinatorial Genetic, Stromal, and Immunologic Markers. *Clin Cancer Res.* 2017, **23**(15), pp.4429-4440.

379. Yang, S., Liu, Q. and Liao, Q. Tumor-Associated Macrophages in Pancreatic Ductal Adenocarcinoma: Origin, Polarization, Function, and Reprogramming. *Front Cell Dev Biol.* 2020, **8**, p.607209.
380. Ye, H., Zhou, Q., Zheng, S., Li, G., Lin, Q., Wei, L., Fu, Z., Zhang, B., Liu, Y., Li, Z. and Chen, R. Tumor-associated macrophages promote progression and the Warburg effect via CCL18/NF- κ B/VCAM-1 pathway in pancreatic ductal adenocarcinoma. *Cell Death Dis.* 2018, **9**(5), p.453.
381. van Duijneveltdt, G., Griffin, M.D.W. and Putoczki, T.L. Emerging roles for the IL-6 family of cytokines in pancreatic cancer. *Clin Sci (Lond).* 2020, **134**(16), pp.2091-2115.
382. Tahkola, K., Ahtiainen, M., Mecklin, J.P., Kellokumpu, I., Laukkanen, J., Tammi, M., Tammi, R., Vayrynen, J.P. and Bohm, J. Stromal hyaluronan accumulation is associated with low immune response and poor prognosis in pancreatic cancer. *Sci Rep.* 2021, **11**(1), p.12216.
383. Antonacci, G., Beck, T., Bilenca, A., Czarske, J., Elsayad, K., Guck, J., Kim, K., Krug, B., Palombo, F., Prevedel, R. and Scarcelli, G. Recent progress and current opinions in Brillouin microscopy for life science applications. *Biophys Rev.* 2020, **12**(3), pp.615-624.
384. McGlynn, J.A., Wu, N. and Schultz, K.M. Multiple particle tracking microrheological characterization: Fundamentals, emerging techniques and applications. *Journal of Applied Physics.* 2020, **127**(20).
385. Prevedel, R., Bevilacqua, C. and Diz-Muñoz, A. Brillouin microscopy – measuring mechanics in biology using light. In, 2006.
386. Prevedel, R., Diz-Munoz, A., Ruocco, G. and Antonacci, G. Brillouin microscopy: an emerging tool for mechanobiology. *Nat Methods.* 2019, **16**(10), pp.969-977.
387. Lekka, M. Discrimination Between Normal and Cancerous Cells Using AFM. *BioNanoScience.* 2016, **6**, pp.65-80.
388. Malik, R., Luong, T., Cao, X., Han, B., Shah, N., Franco-Barraza, J., Han, L., Shenoy, V.B., Lelkes, P.I. and Cukierman, E. Rigidity controls human desmoplastic matrix anisotropy to enable pancreatic cancer cell spread via extracellular signal-regulated kinase 2. *Matrix Biol.* 2019, **81**, pp.50-69.
389. Roa, J.J., Oncins, G., Diaz, J., Sanz, F. and Segarra, M. Calculation of Young's modulus value by means of AFM. *Recent Pat Nanotechnol.* 2011, **5**(1), pp.27-36.
390. Stylianou, A., Lekka, M. and Stylianopoulos, T. AFM assessing of nanomechanical fingerprints for cancer early diagnosis and classification: from single cell to tissue level. *Nanoscale.* 2018, **10**(45), pp.20930-20945.
391. Cicuta, P. and Donald, A.M. Microrheology: a review of the method and applications. *Soft Matter.* 2007, **3**(12), pp.1449-1455.
392. Jones, D.P., Hanna, W., Cramer, G.M. and Celli, J.P. In situ measurement of ECM rheology and microheterogeneity in embedded and overlaid 3D pancreatic tumor stroma co-cultures via passive particle tracking. *Journal of Innovative Optical Health Sciences.* 2017, **10**(06).

393. Wirtz, D. Particle-tracking microrheology of living cells: principles and applications. *Annu Rev Biophys.* 2009, **38**, pp.301-326.
394. Wu, P.-H., Gambhir, S.S., Hale, C.M., Chen, W.-C., Wirtz, D. and Smith, B.R. Particle tracking microrheology of cancer cells in living subjects. *Materials Today.* 2020, **39**, pp.98-109.
395. Ito, K., Sakuma, S., Kimura, M., Takebe, T., Kaneko, M. and Arai, F. Temporal Transition of Mechanical Characteristics of HUVEC/MSC Spheroids Using a Microfluidic Chip with Force Sensor Probes. *Micromachines (Basel).* 2016, **7**(12).
396. Zareei, A., Jiang, H., Chittiboyina, S., Zhou, J., Marin, B.P., Lelievre, S.A. and Rahimi, R. A lab-on-chip ultrasonic platform for real-time and nondestructive assessment of extracellular matrix stiffness. *Lab Chip.* 2020, **20**(4), pp.778-788.
397. Ishiwata, T., Hasegawa, F., Michishita, M., Sasaki, N., Ishikawa, N., Takubo, K., Matsuda, Y., Arai, T. and Aida, J. Electron microscopic analysis of different cell types in human pancreatic cancer spheres. *Oncol Lett.* 2018, **15**(2), pp.2485-2490.
398. Norberg, K.J., Liu, X., Fernandez Moro, C., Strell, C., Nania, S., Blumel, M., Balboni, A., Bozoky, B., Heuchel, R.L. and Lohr, J.M. A novel pancreatic tumour and stellate cell 3D co-culture spheroid model. *BMC Cancer.* 2020, **20**(1), p.475.
399. Shichi, Y., Sasaki, N., Michishita, M., Hasegawa, F., Matsuda, Y., Arai, T., Gomi, F., Aida, J., Takubo, K., Toyoda, M., Yoshimura, H., Takahashi, K. and Ishiwata, T. Enhanced morphological and functional differences of pancreatic cancer with epithelial or mesenchymal characteristics in 3D culture. *Sci Rep.* 2019, **9**(1), p.10871.
400. Drifka, C.R.L., A. G.; Mathewson, K.; Keikhosravi, A.; Eickhoff, J. C.; Liu, Y.; Weber, S. M.; Kao, W. J.; & Eliceiri, K. W. Highly aligned stromal collagen is a negative prognostic factor following pancreatic ductal adenocarcinoma resection. *Oncotarget.* 2016, **7**(46), pp.76197–76213.
401. Moura, C.C., Bourdakos, K.N., Tare, R.S., Oreffo, R.O.C. and Mahajan, S. Live-imaging of Bioengineered Cartilage Tissue using Multimodal Non-linear Molecular Imaging. *Sci Rep.* 2019, **9**(1), p.5561.
402. Costa Moura, C., Lanham, S.A., Monfort, T., Bourdakos, K.N., Tare, R.S., Oreffo, R.O.C. and Mahajan, S. Quantitative temporal interrogation in 3D of bioengineered human cartilage using multimodal label-free imaging. *Integr Biol (Camb).* 2018, **10**(10), pp.635-645.
403. Mortati, L., Divieto, C. and Sassi, M.P. CARS and SHG microscopy to follow collagen production in living human corneal fibroblasts and mesenchymal stem cells in fibrin hydrogel 3D cultures. *Journal of Raman Spectroscopy.* 2012, **43**(5), pp.675-680.
404. Wang, H.-W., Le, T.T. and Cheng, J.-X. Label-free Imaging of Arterial Cells and Extracellular Matrix Using a Multimodal CARS Microscope. *Optics communications.* 2008, **281**(7), pp.1813-1822.
405. Kechagia, J.Z., Ivaska, J. and Roca-Cusachs, P. Integrins as biomechanical sensors of the microenvironment. *Nat Rev Mol Cell Biol.* 2019, **20**(8), pp.457-473.

406. Muiznieks, L.D. and Keeley, F.W. Molecular assembly and mechanical properties of the extracellular matrix: A fibrous protein perspective. *Biochim Biophys Acta*. 2013, **1832**(7), pp.866-875.
407. Marciano, D.K., Denda, S. and Reichardt, L.F. Methods for Identifying Novel Integrin Ligands. In: *Integrins*. 2007, pp.223-237.
408. Schwartz, M.A. Integrins and extracellular matrix in mechanotransduction. *Cold Spring Harb Perspect Biol*. 2010, **2**(12), p.a005066.
409. Alberts B, J.A., Lewis J, et al. Integrins. In: *Molecular Biology of the Cell*. 4th ed. New York: Garland Science, 2002.
410. Perez, V.M., Kearney, J.F. and Yeh, J.J. The PDAC Extracellular Matrix: A Review of the ECM Protein Composition, Tumor Cell Interaction, and Therapeutic Strategies. *Front Oncol*. 2021, **11**, p.751311.
411. Schnittert, J., Bansal, R., Mardhian, D.F., Van Baarlen, J., Östman, A. and Prakash, J. Integrin α 11 in pancreatic stellate cells regulates tumor stroma interaction in pancreatic cancer. *The FASEB Journal*. 2019, **33**(5), pp.6609-6621.
412. Takada, Y., Ye, X. and Simon, S. The integrins. *Genome Biol*. 2007, **8**(5), p.215.
413. Zeltz, C., Primac, I., Erusappan, P., Alam, J., Noel, A. and Gullberg, D. Cancer-associated fibroblasts in desmoplastic tumors: emerging role of integrins. *Seminars in Cancer Biology*. 2020, **62**, pp.166-181.
414. Lachowski, D., Cortes, E., Pink, D., Chronopoulos, A., Karim, S.A., J, P.M. and Del Rio Hernandez, A.E. Substrate Rigidity Controls Activation and Durotaxis in Pancreatic Stellate Cells. *Sci Rep*. 2017, **7**(1), p.2506.
415. Nikolaou, S. and Machesky, L.M. The stressful tumour environment drives plasticity of cell migration programmes, contributing to metastasis. *J Pathol*. 2020, **250**(5), pp.612-623.
416. Liu, J.R., Liao, S., Diop-Frimpong, B., Chen, W.M., Goel, S., Kamila, N., Ancukiewicz, M., Boucher, Y., Jain, R.K. and Xu, L. TGF- β blockade improves the distribution and efficacy of therapeutics in breast carcinoma by normalizing the tumor stroma. *Proc Natl Acad Sci U S A*. 2012, **109**(41), pp.16618–16623.
417. Kim, M.Y., Cho, M.Y., Baik, S.K., Jeong, P.H., Suk, K.T., Jang, Y.O., Yea, C.J., Kim, J.W., Kim, H.S., Kwon, S.O., Yoo, B.S., Kim, J.Y., Eom, M.S., Cha, S.H. and Chang, S.J. Beneficial effects of candesartan, an angiotensin-blocking agent, on compensated alcoholic liver fibrosis - a randomized open-label controlled study. *Liver Int*. 2012, **32**(6), pp.977-987.
418. Fang, Q.Q., Wang, X.F., Zhao, W.Y., Ding, S.L., Shi, B.H., Xia, Y., Yang, H., Wu, L.H., Li, C.Y. and Tan, W.Q. Angiotensin-converting enzyme inhibitor reduces scar formation by inhibiting both canonical and noncanonical TGF-beta1 pathways. *Sci Rep*. 2018, **8**(1), p.3332.
419. Nakai, Y., Isayama, H., Ijichi, H., Sasaki, T., Sasahira, N., Hirano, K., Kogure, H., Kawakubo, K., Yagioka, H., Yashima, Y., Mizuno, S., Yamamoto, K., Arizumi, T., Togawa, O., Matsubara, S., Tsujino, T., Tateishi, K., Tada, M., Omata, M. and Koike, K. Inhibition

of renin-angiotensin system affects prognosis of advanced pancreatic cancer receiving gemcitabine. *Br J Cancer*. 2010, **103**(11), pp.1644-1648.

Appendix

Hydrostatic pressure driven flow by gravity code

Defining the cross section of culture media channel

1. $W = 100 \cdot 10^{-6}$; %culture media channel width (unit in metres, m)
2. $w1 = w \cdot 10^6$; %unit in microns, um
3. $h = 100 \cdot 10^{-6}$; %culture media channel height (unit in metres, m)
4. $herr = 2 \cdot 10^{-6}$; %error in channel height (unit in metres, m)
5. $h1 = h \cdot 10^6$; %unit in microns, um
6. $L = 43000 \cdot 10^{-6}$; %culture media channel length of the 5-channel device (unit in m)
7. $L1 = L \cdot 10^3$; %unit in millimetres, mm

Defining values in relation to culture media fluid level and reservoirs

8. $\rho = 993.3$; %density of water (unit in kg per m⁻³) at 37 C [culture media]
9. $n = 6.922 \cdot 10^{-4}$; %dynamic viscosity of water (unit in Pa.s) at 37 C [culture media]
10. $\pi = 3.1415$; %ratio of the reservoir circumference to its diameter
11. $g = 9.81$; %gravitational acceleration (unit in metres per second⁻²)
12. $d = 10 \cdot 10^{-3}$; %reservoir inner diameter about 12 mm, rounded to 10 mm (unit in m)
13. $d1 = 10$; %unit in millimetres, mm
14. $HCM1 = 20$; %culture media height level in inlet reservoir with about 2 mL of culture media (unit in mm)
15. $HCM2 = 2$; %culture media height level in outlet reservoir with about 200 uL of culture media (unit in mm)
16. $dH0 = (HCM1 - HCM2) \cdot 10^{-3}$; %difference in culture media height level between inlet and outlet reservoir (unit in m)
17. $dHPc = (20 - 10) \cdot 10^{-3}$; %height for Pc calculations, when culture media in reservoirs equilibrate (unit in m)
18. $Pc = \rho \cdot g \cdot dHPc$; %capillary pressure (unit in Pa) with dHPc determined experimentally when culture media in inlet and outlet reservoir equilibrates

Defining values for the figure plots

19. $\%t = 0:0.1:500000$; time varies for 0 - 500000 seconds in steps of 0.1
20. $x = 168$; %x axis in hours
21. $t = 0:1:(x \cdot 3600)$; %time in seconds
22. $thrs = t/3600$; %time in hours

Defining values and calculations for the hydrostatic pressure driven flow by gravity between the reservoirs

23. $R_{hyd} = (12 * n * L / ((h^3) * w)) * (((1 - (0.63 * h / w))^{\wedge} - 1))$; %hydraulic resistance for rectangular channel, the culture media channel
24. $R_{hyderr} = (12 * n * L / ((herr^3) * w)) * (((1 - (0.63 * herr / w))^{\wedge} - 1))$;
25. $Q_0 = ((\rho * g * dH_0) - P_c) / R_{hyd}$; %flow = hydraulic pressure/hydraulic resistance
26. $Q = Q_0 * 10^{\wedge} 9 * \exp((-2 * \rho * g * t) / (R_{hyd} * \pi * ((d/2)^{\wedge} 2)))$; %volumetric flow rate = flow/hydraulic resistance*cylinder (reservoirs) volume (unit in uL/sec)
27. $Phyd = (Q / 10^{\wedge} 9) * R_{hyd}$; %hydraulic pressure = flow velocity*hydraulic resistance (unit Pa)
28. $Q_{min} = Q * 60$; %volumetric flow rate of culture media (unit in uL/min)
29. $V = \text{cumtrapz}(t, Q)$; %volume of culture media at time t with a volumetric flow rate of Q (unit in uL)
30. $H_1 = HCM_1 - (V / (\pi * ((d_1/2)^{\wedge} 2)))$; %change in culture media height level with flow out the inlet reservoir (unit in mm)
31. $H_2 = HCM_2 + (V / (\pi * ((d_1/2)^{\wedge} 2)))$; %change in culture media height level with flow into the outlet reservoir (unit in mm)
32. $dH = H_1 - H_2$; %difference in culture media height level between inlet and outlet reservoir
33. $dH_{err} = dH * (herr/h)$;
34. $y = [\text{thrs}; dH]$; %for figure plot of culture media volumetric flow rate against time in hours

Culture media volumetric flow rate through culture media channel figure plot

35. `figure(1)`
36. `plot(thrs, Q*60, 'LineWidth', 1)`
37. `xlabel('Time (hours)')`
38. `xticks([0 24 48 72 96 120 144 168])`
39. `ylabel('Volumetric flow rate (\muL / min)')`
40. `title('Culture media volumetric flow rate (\muL / min) v Time (hours)')`
41. `legend('Culture media channel length: 40mm')`
42. `ax = gca;`
43. `ax.FontSize = 9.5;`
44. `saveas(figure(1), ['Culture media volumetric flow rate, DH= ', num2str(HCM1), 'mm, w= ', num2str(w1), 'um, h= ', num2str(h1), 'um ', 'L= ', num2str(L1), 'mm.tiff'])`

Culture media pressure difference between the inlet and outlet reservoirs figure plot

45. `figure(2)`
46. `plot(thrs, Phyd, 'LineWidth', 1)`

```
47. xlabel ('Time (hours)')
48. xticks ([0 24 48 72 96 120 144 168])
49. ylabel ('Pressure difference (Pa)')
50. ylim ([0 100])
51. title ('Pressure difference between reservoirs (Pa) v Time (hours)')
52. legend ('Culture media channel length: 43mm')
53. ax = gca;
54. ax.FontSize = 9.5;
55. saveas (figure(2), ['Pressure difference between reservoirs, DH= ', num2str(HCM1), 'mm,
    w= ', num2str(w1), 'um, h= ', num2str(h1), 'um ', ' L= ', num2str(L1), 'mm.tiff'])
```

Culture media height level difference between the inlet and outlet reservoirs figure plot

```
56. figure(3)
57. plot (thrs, dH, 'LineWidth', 1)
58. xlabel ('Time (hours)')
59. xticks ([0 24 48 72 96 120 144 168])
60. ylabel ('Culture media height difference (mm)')
61. ylim ([10 20])
62. title ('Culture media height difference between reservoirs (mm) v Time (hours)')
63. legend ('Culture media channel length: 43mm')
64. ax = gca;
65. ax.FontSize = 9.5;
66. saveas (figure(3), ['Culture media height level difference between reservoirs, DH= ',
    num2str(HCM1), 'mm, w= ', num2str(w1), 'um, h= ', num2str(h1), 'um ', ' L= ', num2str(L1),
    'mm.tiff'])
```

Saving culture media height level difference between the inlet and outlet reservoirs as text file

```
67. fileID = fopen ('Culture media height level difference between reservoirs.txt', 'w');
68. fprintf (fileID, 'Culture media height level difference between reservoirs\r\n', y);
69. fprintf (fileID, '%f %f\r\n', y);
70. fclose ('all');
```

Supplementary videos

Supplementary video 1: Off-chip PSC spheroid culture. Video shows early time points of the spheroid culture of the PSC cells, where the cells were observed aggregating into a spheroid structure. The video was acquired with the IncuCyte® S3 Live-Cell Analysis System at MDC, as described in section 3.2.4.

Supplementary video 2: Off-chip PANC-1 spheroid culture. Video shows early time points of the spheroid culture of the PANC-1 cells, where the cells were observed aggregating into a spheroid structure. The video was acquired with the IncuCyte® S3 Live-Cell Analysis System at MDC, as described in section 3.2.4.

Supplementary video 3: Off-chip spheroid culture of the PDAC cells. Video shows early time points of the spheroid culture of the PDAC cells, where the cells were observed aggregating into a spheroid structure. The video was acquired with the IncuCyte® S3 Live-Cell Analysis System at MDC, as described in section 3.2.4.

Supplementary video 4: Off-chip PDAC culture of labelled PANC-1 cells with unlabelled PSCs. Video shows the PANC-1 cells at the centre of the PSC cells. The video was acquired with the IncuCyte® S3 Live-Cell Analysis System at MDC, as described in section 3.2.4.

Supplementary video 5: Live-cell imaging of the PDAC cells with TGF- β 1 supplement in the 5-channel microfluidic device. Video shows early time points of the on-chip culture, where the cells are aggregating into 3D, forming structural networks. The video was acquired with the IncuCyte® S3 Live-Cell Analysis System at MDC, as described in section 3.2.4.

Supplementary video 6: Live-cell imaging of the PDAC cells with TGF- β 1 supplement in the 5-channel microfluidic device. Video shows early time points of the on-chip culture, where the cells are aggregating into 3D, forming structural networks. The video was acquired with the IncuCyte® S3 Live-Cell Analysis System at MDC, as described in section 3.2.4.

Supplementary video 7: The flow of fluorescein in media solution through BME gel on-chip. The perfusion of the solution through 6 – 9 mg mL⁻¹ BME gel in the culture chamber of the 5-channel device was captured with an epifluorescence microscope to assess the hydraulic conductivity (as described in section 3.10) and therefore the interstitial flow nature of the BME gel only on-chip.

Supplementary video 8: The flow of fluorescein in media solution through the 21-day on-chip PDAC culture. The perfusion of the solution through the 21-day on-chip PDAC culture in the culture chamber of the 5-channel device was captured with an epifluorescence microscope to assess the hydraulic conductivity (as described in section 3.10) and therefore the interstitial flow nature of the 21-day on-chip PDAC culture.

Supplementary video 9: Bright-field view of the flow of microbubbles, passing between the pillars, into the 5-channel device with 6 – 9 mg mL⁻¹ BME gel in the culture chamber. Assessment of the flow of microbubbles on-chip with BME gel is as described in section 3.11.4.

Supplementary video 10: Close up ATTO 488 fluorescent view of the flow of microbubbles (from **Supplementary video 9**) into the 5-channel device with 6 – 9 mg mL⁻¹ BME gel in the culture chamber. Assessment of the flow of microbubbles on-chip with BME gel is as described in section 3.11.4.

Supplementary video 11: Bright-field view of the flow of microbubbles into the 5-channel device with the 21-day on-chip PDAC culture. Assessment of the flow of microbubbles on-chip with BME gel only is as described in section 3.11.4.

Supplementary video 12: ATTO 488 fluorescent view of the flow of microbubbles into the 5-channel microfluidic device with the 21-day on-chip PDAC culture. Assessment of the flow of microbubbles on-chip with BME gel only is as described in section 3.11.4.

Papers

- Paper #1: Modeling the Mechanical Stiffness of Pancreatic Ductal Adenocarcinoma.
Accepted. Matrix Biology Plus. 2022